X-ray study of clusters of galaxies up to the virial radius with *Suzaku*

Hiroki Akamatsu

Department of Physics, Tokyo Metropolitan University
1-1 Minami-Ohsawa, Hachioji, Tokyo 192-0397, Japan

February 24, 2012

首都大学東京　博士（理学）学位論文（課程博士）

論文名

「すざく」衛星による銀河団外縁部までのX線放射の研究（英文）

著　者　　赤松 弘規

審査担当者

主　査　　石崎 欣尚

委　員　　大橋 隆哉

委　員　　政井 邦昭

委　員　　松下 恭子

上記の論文を合格と判定する

平成 24 年 3 月 25 日

首都大学東京大学院理工学研究科教授会

研究科長　岡部 豊

DISSERTATION FOR A DEGREE OF
DOCTOR OF PHILOSOPHY IN SCIENCE
TOKYO METROPOLITAN UNIVERSITY

TITLE :

X-ray study of clusters of galaxies up to the virial radius with Suzaku

AUTHOR : Hiroki Akamatsu

EXAMINED BY

Examiner in chief Yoshitaka Ishisaki

Examiner Takaya Ohashi

Examiner

Examiner Kyoko Matsushita

QUALIFIED BY THE GRADUATE SCHOOL
OF SCIENCE AND ENGINEERING
TOKYO METROPOLITAN UNIVERSITY

Dean Yutaka Okabe

Date March 25, 2012

Abstract

Clusters of galaxies, containing 10-1000 of galaxies, are the largest virialized structures in the Universe. They consist of galaxies, X-ray emitting hot gas (ICM: intracluster medium) with temperature reaching $10^7 \sim 10^8$ K, and the dark matter. The ICM temperature inferred from a cluster X-ray spectrum therefore indicates the depth of the cluster potential well, and the emission-line strengths in the spectrum indicate the abundances of elements like iron, oxygen, and silicon in the ICM. Clusters of galaxies are regarded as useful probes to study the cosmic evolution by several reasons: 1) since the dynamical timescale of clusters is close to the Hubble time, clusters retain the cosmological initial conditions well, 2) clusters can be described by a simple model consisting of dark matter, hot gas, and galaxies, and also the shape is almost spherical, thus they are easy to deal with and 3) though a part of metals produced in galaxies flow out into ICM, they do not escape away from clusters.

In understanding the dynamical evolution of clusters of galaxies, it is important to investigate the physical conditions of ICM in the cluster outskirts, whuch can be regarded as the front line of cluster evolution. For this purpose, we analyzed data from 15 Suzaku observations of clusters of galaxies, which include 9 relaxed and 6 merging system with the little including 4 radio relic clusters. They have redshifts $z < 0.2$. Based on the spatially resolved energy spectra, we obtained precise temperature and density profiles beyond the virial radius in a systematic way. As a result, the ICM temperatures in the relaxed systems commonly show decrease from the centers to the outskirt regions and show flatter profiles in merging systems. Those difference in the temperature profile reflect stage of the dynamical evolution of clusters of galaxies. In the radio relic clusters, we found that the temperature, electron density and pressure show significant drops across the radio relics, suggesting the existence of shock fronts at radio relics. The derived Mach numbers based on Rankine-Hugoniot jump condition span the range of 2-3, and the value are consistent with the Mach numbers derived from radio observations. In the relaxed clusters, the temperature drops from the peak level (reaching w at around $\sim$ 0.1 r_{200}) to the value at r_{200} by a factor of 2$\sim$5, which agrees with the results from numerical simulations of the cluster formation based on the ΛCDM framework. Observed entropy profiles show a flatting around outskirts except for the low temperature system. The deviation of the observed entropy profile from the numerical simulation shows ahint of the temperature dependence. Those features support the view that large systems are still evolving and their outskirts are still in a dynamically non-equilibrium state.

CONTENTS

List of Figures

List of Tables

Chapter 1

Introduction

Cluster of galaxies, being the largest virialized system in the universe, are contained a few hundred of galaxies and filled with IntraCluster Medium (ICM), which consists of X-ray emitting hot plasma with typical temperatures of a few times 10^7 K. The dynamical timescale of cluster of galaxies is expressed as

$$t_{dyn} \sim \sqrt{\frac{R^3}{GM}} \sim 4\mathrm{Gyr}, \tag{1.1}$$

which shorter than age of universe (13.6 Gyr), but can expect that cluster hold to the information of initial condition of universe. In addition above advantage, cluster has simple structure consisting of Dark matter, ICM and galaxies. Hence, cluster of galaxies are good candle to study the cosmological problems.

X-ray observation is powerful tool to find cluster of galaxies and studies in detailed those formation and evolution via higher SN (Signal to Noise ratio) than optical observation. In the optical observations, identification of cluster of galaxies is count up of galaxies, whose emissivity dependence of number of galaxies is n_{gal}. A line-of-sight S/N ratio in optical range is scaled as,

$$(\frac{S}{N})_{opt} \sim \frac{n_{gal,cls} R_{cls}}{n_{gal,univ} R_{univ}} \sim 1, \tag{1.2}$$

where $n_{gal,cls} \sim 10/(h^{-1}\mathrm{Mpc})^3$ and $n_{gal,univ} \sim 10^{-2}/(h^{-1}\mathrm{Mpc})^3$ are number density in cluster and universe, respectively. On the other hand, in the X-ray range, emissivity of ICM is depend on n^2_{gal}. A line-of-sight S/N ratio in optical range is scaled as,

$$(\frac{S}{N})_X \sim \frac{n^2_{gal,cls} R_{cls}}{n^2_{gal,univ} R_{univ}} \sim 1000. \tag{1.3}$$

The SN of X-ray observation is about 1000 times higher than optical one. For this reason, X-ray observation is important for identification of cluster of galaxies.

The temperature profile of ICM have a lot of information to understand the evolution of clusters. The primary energy source of the ICM is considered to be the kinetic energy released through the gas infall into the gravitational potential of the dark matter. The heating mechanism is, however, not yet fully understood. Based on numerical simulations, the Cold Dark Matter scenario of the cosmic structure formation predicts that clusters of galaxies are formed via collisions and mergers of smaller groups and clusters.

In the study of the dynamical evolution of clusters, we will focus on the cluster outer regions since they are expected to contain important information on the formation process. The cluster outskirts are connected to the surrounding large-scale structure, where the gas is falling towards the cluster potential and possibly subject to shock heating. Some numerical simulations (Ettori et al. 2004; Borgani et al. 2004) predicted that the intracluster gas temperature drops to about 50% of the central temperature around r_{200} under hydrostatic equilibrium. Those results reproduced observed temperature profiles to about $0.5r_{200}$ (De Grandi & Molendi 2002; Vikhlinin et al. 2005; Pratt et al. 2007). In particular, recent XMM-Newton (Pratt et al. 2007) results showed temperature profiles out to $0.8r_{200}$. Once disturbed by the subcluster collisions, it should take long time for the gas to settle due to the low density and large spatial size. Therefore, the outskirts of merging clusters offer us opportunities to look into the gas in its transition to the thermal and ionization equilibriums.

This thesis reports results from *Suzaku* observations 15 cluster of galaxies, which include 6 merging system, up to their virial radius. Thanks to low and stable background level of *Suzaku* XIS, we are able to measure the temperature profile to further outer regions than previous X-ray satellite. In this thesis, we will use H_0 = 70 km s^{-1} Mpc^{-1}, $\Omega_M = 0.27$ and $\Omega_\Lambda = 0.73$. We adopted the solar abundance defined by Anders & Grevesse (1989) and the Galactic N_H by Dickey & Lockman (1990). The errors are in the 90% confidence for a single parameter.

Chapter 2

Review of Clusters of Galaxies

2.1 Hierarchical structure formation

At present, the hierarchical clustering scenario is widely supported, because it is naturally expected from the cold dark matter model. Also, the fact that the galaxies at redshifts ~ 7 have been observed, whereas the most distant observed clusters is at $z \sim 1.5$, indicates that small systems have been formed first.

According to the bottom-up scenario, large-scale structures of the universe have formed from infinitesimally small density perturbations at the early universe through the gravitational interaction, and we can recognize three fundamental building blocks: stars, galaxies, and clusters of galaxies. A number of numerical simulations for the structure formation have shown producing the large-scale structures and clusters of galaxies. This result is recognized as a strong support to the hierarchical clustering scenario. Following an early work by White's 700-body simulations (1976), calculations such as the one by Eke et al. (1998) include N-body/gas-dynamical simulations which are designed to investigate the evolution of clusters. Borgani & Guzzo (2001) compared the evolution of universe in different universe models of $\Omega_m = 0.3$ of low Ω_m cosmology and $\Omega_m = 1$ of Einstein-deSitter (EdS) cosmology in figure 2.1. Despite the similar pattern produced at the present time ($z = 0$), the past pattern of the universe is very different. This evolutionary difference represents one of the motivations for the deep X-ray searches of clusters down to a very faint flux levels. Clusters at $z \simeq 0.5$ are no longer considered as exceptions, and even a few examples at $z > 1$ are now known. The main result reached these surveys is the evidence for a weak evolution of the bulk of the cluster population out to $z \simeq 1$, again consistent with the picture of a low-Ω_m universe.

Hierarchical clustering for the hot gas and dark matter from matter aggregates that have reached an approximate dynamical equilibrium giving them their characteristic shapes, and indicates that the clusters are formed through sub-cluster mergers and/or absorption of groups of galaxies. Thus, the evolution of the galaxy cluster population is tightly connected to the evolution of the large-scale structures and the universe as a whole. It is for this reason that observations of galaxy clusters can be used to trace the evolution of the universe and to test cosmological models.

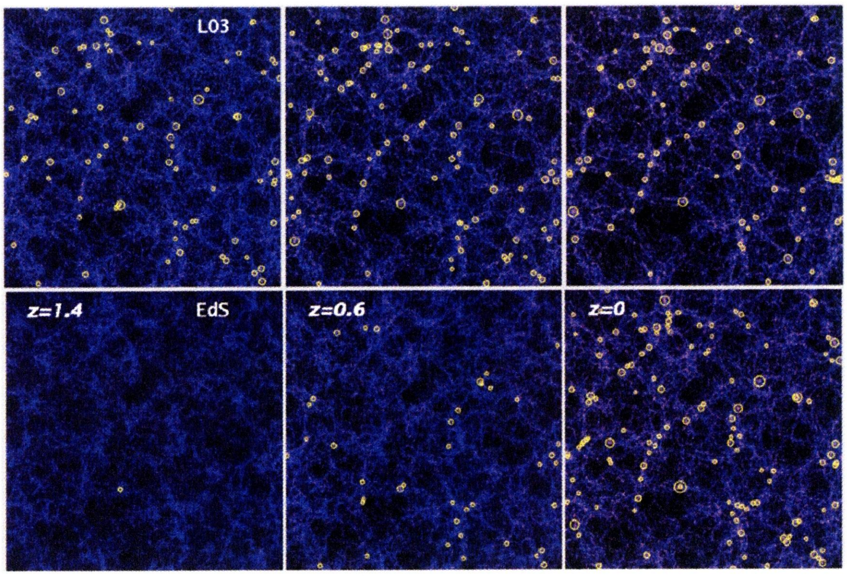

Fig. 2.1: Evolution of gravitational clustering simulated using an N-body code for two different models (Borgani & Guzzo 2001). Each of the three red shift snapshots shows a region with sides of $250h^{-1}$Mpc and thickness of $75h^{-1}$ Mpc comoving with the cosmic expansion. The upper panels describe a flat low-density model with $\Omega_m = 0.3$ and $\Omega_\Lambda = 0.7$, and the lower panels show an Einstein-de-Sitter model (EdS) with $\Omega_m = 1$. In both cases the amplitude of the power spectrum is consistent with the number density of nearby galaxy clusters and with the large-scale CMB anisotropies. Yellow circles mark the positions of galaxy clusters with $kT > 3$ keV. The size of the circles is proportional to temperature.

2.2 Clusters of galaxies

Galaxy clusters, the largest virialized system in our universe, contain rich information of cosmic evolution in the intracluster medium (ICM) and the cluster galaxy populations. Clusters of galaxies are not isolate entities in the universe and they are connected to filamentary cosmic web. Theoretical predictions indicate the way this web is evolving. ICM reaches typical temperatures of a few times 10^7 K via accretion from large scale filaments and subcluster merger. ICM is visible through spatially extended thermal X-ray emission. The ICM temperature inferred from a cluster X-ray spectrum therefore indicates the depth of the cluster potential well, and the emission-line strengths in that spectrum indicate the abundances of elements like iron, oxygen, and silicon in the ICM.

Clusters of galaxies are regarded as useful probes to study the evolution of the university by several reasons: 1) since the dynamical timescale of clusters is close to the Hubble time, clusters retain the cosmological initial conditions well, 2) clusters can be approximated by a model consisting of dark matter, hot gas, and galaxies, and also the shape is almost spherical, thus they are easy to deal with, 3) though a part of metals produced in galaxies run away into ICM, they do not escape from the clusters.

2.3 X-ray emission process in clusters of galaxies

The X-ray spectrum emitted from an ionized plasma of the low density ($\sim 10^{-3}$ cm^{-3}) ICM is described with a combination of thermal bremsstrahlung (free-free) emission and line emission from heavy elements. In the temperature range of typical cluster (1 keV $< kT <$ 10 keV) the total emission is dominated by the free-free emission if the abundance of heavy elements does not exceed the solar value very much. The emissivity of the free-free emission at a frequency ν from a hot plasma with an electron temperature of T_g is given by

$$\begin{aligned} \epsilon_\nu &= \frac{2^5 \pi e^6}{3 m_e c^3}\left(\frac{2\pi}{2 m_e k}\right)^{1/2} n_e \sum_i Z_i^2 n_i g_{ff}(Z, T_g, \nu) \times T_g^{-1/2} \exp(-h\nu/kT_g) & (2.1) \\ &= \Lambda(T, Z, \nu) n_e^2 & (2.2) \end{aligned}$$

where Z_i and n_i are the charge and number density of the ion i, respectively, and n_e is the electrons number density (e.g. Rybicki & Lightman 1979). The Gaunt factor is a correction factor for quantum mechanical effects and is approximately $g_{ff} \sim 0.9(h\nu/kT)^{-0.3}$. The emissivity in a given bandpass, $\nu_1 < \nu < \nu_2$, is then

$$\begin{aligned} \epsilon^{ff} &= \int_{\nu_1}^{\nu_2} \epsilon_\nu^{ff} d\nu & (2.3) \\ &= \Lambda(T, Z) n_e^2. & (2.4) \end{aligned}$$

The $\Lambda(T, Z)$ is the cooling function, with T and Z representing the plasma temperature and the heavy element abundance, respectively. Figure 2.2 shows the cooling function as a function of the plasma temperature assuming the cosmic abundances. The contribution of the bremsstrahlung continuum to Λ increases as $\propto T^{1/2}$.

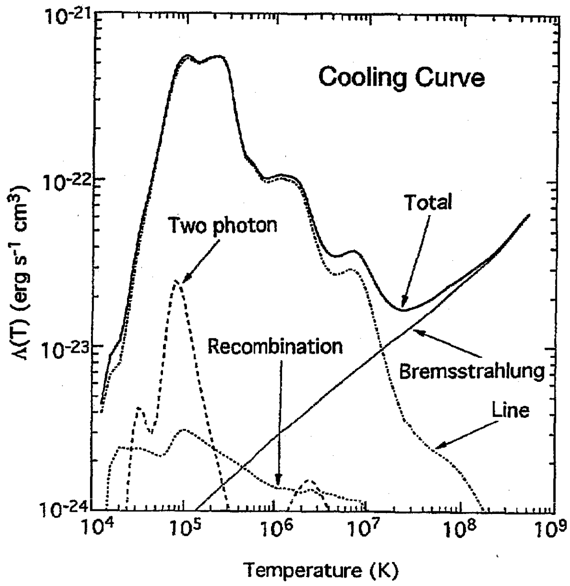

Fig. 2.2: Temperature dependence of the cooling function with its components for optically thin plasma containing cosmic abundances of elements (Gehrels & Williams (1993)).

We can obtain the total X-ray luminosity by integrating equation (2.4). It is useful to define the emission integral as

$$EI = \int n_e^2 dV, \tag{2.5}$$

where V is the volume of the cluster. If we assume that ICM has a spatially-uniform temperature and abundance in the volume V, and that the ICM density is constant over the projected sky area S, then the luminosity L_X is given as

$$\begin{aligned} L_X &= \int \epsilon^{ff} dV \qquad (2.6)\\ &= EI \times \Lambda(T, Z) \qquad (2.7)\\ &= EM \times S \times \Lambda(T, Z). \qquad (2.8)\end{aligned}$$

The EM is the emission measure defined as

$$EM = \int n_e^2 dl, \tag{2.9}$$

where l is the depth of the plasma along the line of sight. The emission integral determines the normalization of the spectrum, and the shape of the spectrum depends only on the temperature T and the heavy element abundance Z, and EI (or EM if S is known) from the observed X-ray spectra.

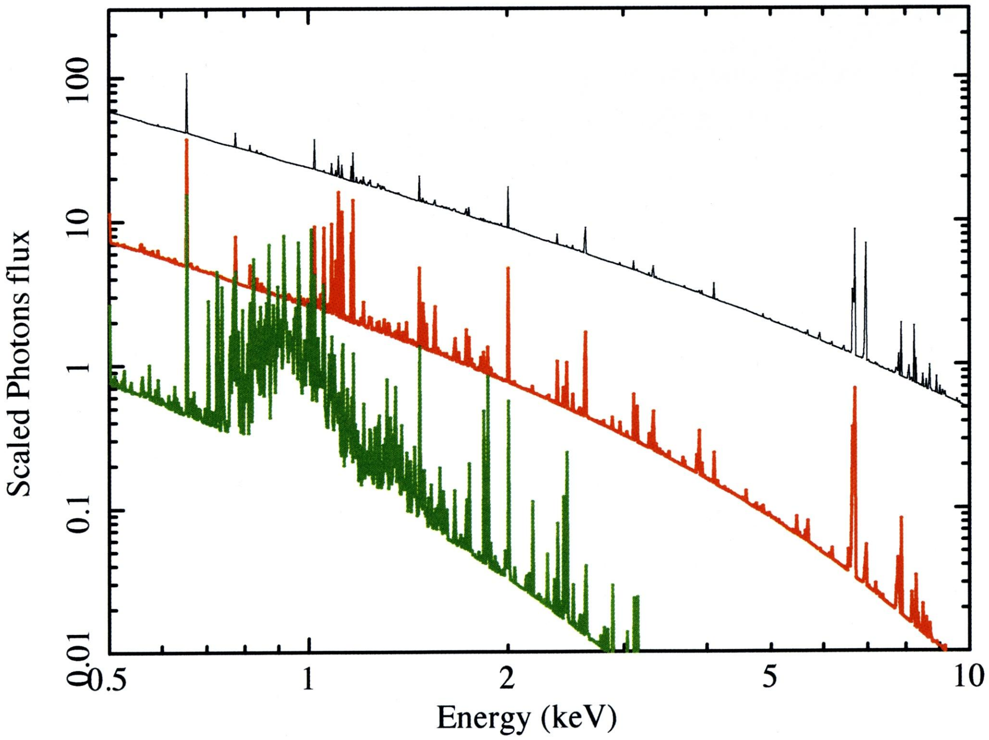

Fig. 2.3: Calculated X-ray spectra from optically thin hot plasma with various temperatures. The Apec plasma emission code is used, assuming a metal abundance of 0.5 solar.Black, red and green curves show the 10, 3,1 keV thermal plasma. Vertical scale is arbitrary.

Emission of atomic lines becomes significant when the ICM temperature falls below a few keV. Since the temperature of the ICM is of the same order as the K-shell ionization potentials of heavy elements such as O, Ne, Mg, Si, S and Fe, these elements become mainly He/H-like ions and are completely ionized. These ions are collisionally excited, and then emit their resonance K-lines. In lower temperature clusters, in which Fe ions are not only He-like but also of a low ionization status, the spectrum exhibits resonance L-lines at ~ 1 keV. We show predicted X-ray spectra for various temperature in figure 2.3.

The emission lines and continuum spectra from the ionization equilibrium plasma have been calculated by various authors, e.g. Raymond & Smith (1977), Kaastra & Mewe (1993), and so on. In this thesis, we use the APEC code v1.10[1], which reproduces emission spectra from collisionally-ionized diffuse gas, include in the XSPEC data analysis package.

2.4 Intra cluster medium (ICM)

Observed through X-rays, the clusters of galaxies are shining brightly not only by galaxies but more strongly by the intracluster space, which is filled with highly ionized plasma namely IntraCluster Medium (ICM). Here, we present the general view of the physical condition of the ICM.

2.4.1 Hydrostatic equilibrium and gravitational mass distribution

The precise knowledge of the mass of the most massive, gravitationally confined objects is not only interesting as much, but it is also a prerequisite to many of the astrophysical and cosmological studies with clusters.

A possibility to test the mass measurement with an independent method is the comparison to the implications from the gravitational lensing effect of clusters, velocity dispersion of gas and Snyaev-Zeldvich effect.

The force balance between the gas pressure, P_g, and gravitational force, both acting on the ICM, is expressed as

$$\nabla P_g = -\rho_g \nabla \phi, \tag{2.10}$$

where ϕ is the gravitational potential and ρ_g is the gas density which can be written as $\rho_g = \mu n_g m_p$. Here, n_g is the number density including electrons and ions, $\mu = 0.59$ is the mean molecular weight, and m_p is the proton mass. The electron density of ICM, n_e is computed by assuming $n_e = 1.2 n_p$ for a fully ionized gas with hydrogen. If we assume spherically symmetry, the above equation is reduced to

$$\frac{dP_g}{dr} = -\mu n_g m_p \frac{d\phi}{dr}, \tag{2.11}$$

where r is the three dimensional radius. Because of the low density ($n_g < 10^{-2}$ cm^{-3}), the ICM can be treated as an ideal gas that follows the equation of state as

$$P_g = n_g k T_g. \tag{2.12}$$

---

[1] http://hea-www.harvard.edu/APEC

we use the hydrogen and helium mass fractions of $X = 0.7$ and $Y = 0.28$, respectively. The ion density including helium is n_i=0.92 n_e, therefore the gas pressure is calculated as

$$P_g = 1.92 n_e kT \tag{2.13}$$

The gas mass density ρ_{gas} is expressed as

$$\rho_{gas} = 1.92 \mu m_p n_e, \tag{2.14}$$

where μ =0.62 is the mean molecular weight, and m_p is the proton mass. When the time scale of scattering between ion and electron is shorter enough than that of heating or cooling, we can treat the gas to be hydrostatic matter. Assuming the hydrostatic equilibrium, the total integrated gravitational mass, $M_{<R}$, within the 3-dimensional radius of R is given by

$$\begin{aligned} M_{<R} &= -\frac{R^2}{\rho_{gas} G} \frac{dP_{gas}}{dR} && (2.15) \\ &= -\frac{kTr}{\mu m_p G} \left(\frac{d\mathrm{ln}\rho_{gas}}{d\mathrm{lnr}} + \frac{d\mathrm{ln}T}{d\mathrm{lnr}} \right). && (2.16) \end{aligned}$$

in which G is the gravitational constant. The differential mass density, $M(R)$, is given by

$$M(R) = \frac{1}{4\pi R^2} \frac{dM_{<R}}{dR} \tag{2.17}$$

So, we can derive gravitational the mass from the mass density $\rho_{gas}(r)$ of ICM, and the temperature profile $T(r)$. When we calculated equation(2.15), we derived r_{200} from the matter density profile, $\rho(r) = (dM(r)/dr)/dV$, which will also be used to define the concentration parameter of NFW profile.

2.4.2 β model

As the model which describes the density distribution of ICM, β-model is used generally, which assume that ICM under isothermal and hydrostatic equilibrium. Here, we rewrite the hydrostatic equilibrium equation equation 2.11 as below;

$$\frac{kT(r)}{\mu m_p} \frac{d\mathrm{logn_g}}{dr} = -\frac{d\phi}{dr} \tag{2.18}$$

Similarly, assuming that the galaxies are in hydrostatic equilibrium, the hydrostatic equation of the galaxies is written as,

$$\sigma^2(r) \frac{d\ \mathrm{log}\rho(\mathrm{r})}{dr} = -\frac{d\phi}{dr} \tag{2.19}$$

From equations 2.21 and 2.18, we obtain

$$n_g \propto \rho^\beta \tag{2.20}$$

where, β is an energy ratio between ICM and gravitational matter in the unit mass.

$$\beta \equiv \frac{\mu m_p \sigma^2}{kT} = 0.726 (\frac{\sigma}{10^3\ \mathrm{km/s}})^2 (\frac{T}{10^8 \mathrm{K}}) \tag{2.21}$$

Assuming the cluster is a self-gravitating system, the approximate solution of Poisson equation: $\Delta\phi(r) = 4\pi G\rho(r)$ and eq 2.21 is given by King (1962) as below;

$$\rho(r) = \rho_0[1 + (\frac{r}{r_c})^2]^{3/2} \ : \text{(King model).} \tag{2.22}$$

Then the isothermal gas distribution may be represented as

$$\rho(r) = \rho_0[1 + (\frac{r}{r_c})^2]^{3/2\beta} \ : (\beta \text{ model).} \tag{2.23}$$

The surface brightness profile of an isothermal spherical plasma with a radial density profile given by equation 7.11 is calculated by integrating the local emission per unit volume. We obtain the X-ray surface brightness $S(r)$ at projected radius r as,

$$S(r) = \Lambda(T,Z)\int n_g^2\,dl = 2\pi\Lambda(T,Z)\int_{\infty}^{+\infty} dl\, n_g(0)^2[1 + (\frac{r^2 + l^2}{r^2})]^{-3\beta} = S(0)[1 + (\frac{r}{r_c})^2]^{-3\beta+\frac{1}{2}} \tag{2.24}$$

2.4.3 Temperature structure of ICM

Since the 1990s, X-ray observations developed into wide field of view and moderate spectrum resolutions by ROSAT[2] and ASCA satellites[3]. Those experiments made it possible to obtain spatially resolved spectra of clusters, and are revealing the temperature structure.

Based on the assumption of ICM as ideal gas and the relation between pressure P and volume V;

$$PV^n = C, \tag{2.25}$$

where, n is called polytropic index and C is a constant. Then, the relation between temperature and pressure of the gas is expressed as

$$\frac{T}{P^{\frac{n-1}{n}}} = C,\ P = \rho T \tag{2.26}$$

$$T = C\cdot\rho^{\frac{n-1}{n}}\cdot T^{\frac{n-1}{n}} \tag{2.27}$$

$$T^{(1-\frac{n-1}{n})} = C\cdot\rho^{\frac{n-1}{n}} \tag{2.28}$$

$$T = C\cdot\rho^{n-1} \tag{2.29}$$

Here, we assume that the density distribution follows β-model which is an empirical assumption that the ICM is in hydrostatic equilibrium and isothermal gas sphere;

$$\rho_{gas}(r) = \rho_{gas}(0)[1 + (\frac{r}{r_c})^2]^{-\frac{3}{2}\beta}. \tag{2.30}$$

Then, the temperature of ICM can be described as below;

$$T \simeq [(1 + (\frac{r}{r_c})^2)^{-\frac{3}{2}\beta}]^{n-1}, \tag{2.31}$$

---

[2] http://www.mpe.mpg.de/xray/wave/rosat/index.php

[3] http://www.astro.isas.jaxa.jp/asca/

where n reflects the physical condition of ICM as $n = 0$ is constant pressure, $n = 1$ is isothermal, $n = \gamma$ is adiabatic and $n = \infty$ is constant volume. We show predicted ICM temperature profiles for various n in figure 2.4. Markevitch et al. (1998) analyzed spatially resolved X-ray spectra of 30 nearby clusters with ASCA and ROSAT. They reported that most of them show a similar temperature decline at large radii. Recent studies of clusters of galaxies such as Chandra (Vikhlinin et al. 2005) and XMM-Newton (Pratt et al. 2007) confirmed similar trend of temperature structure in large samples as shown in figure2.5.

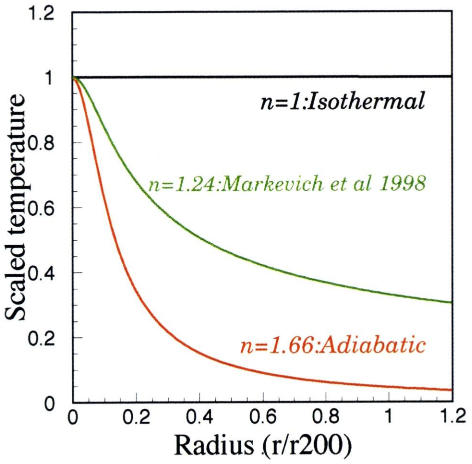

Fig. 2.4: Calculated temperature profiles.

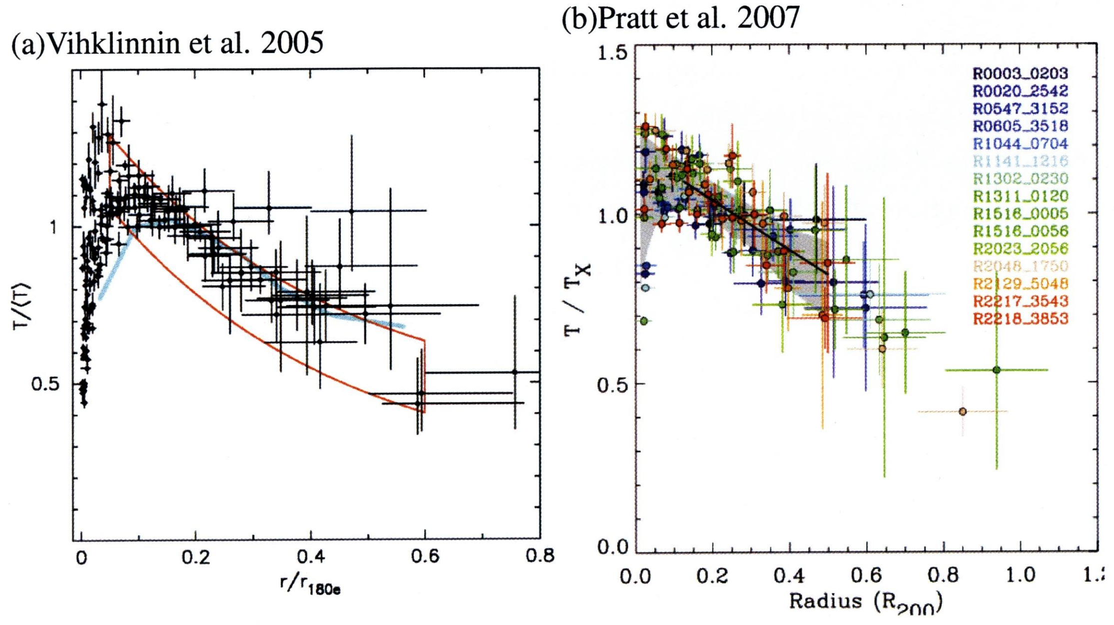
(a)Vihklinnin et al. 2005

(b)Pratt et al. 2007

Fig. 2.5: Scaled temperature profiles of galaxy clusters derived from spectroscopic observations with the Chandra (Vikhlinin et al. 2005) satellite and results obtained for a sample of clusters observed with XMM-Newton (Pratt et al. 2007).

2.4.4 Entropy

The entropy of ICM is used as an indicator of the energy acquired by the gas. Numerical simulations indicate that a self-similar growth of clusters commonly show entropy profiles approximated by $r^{1.1}$ up to r_{180}, excluding the cool core region (Voit et al. 2003). By tradition, the definition of the "entropy" of the ICM will refer to

$$K = kTn_e^{-2/3}. \qquad (2.32)$$

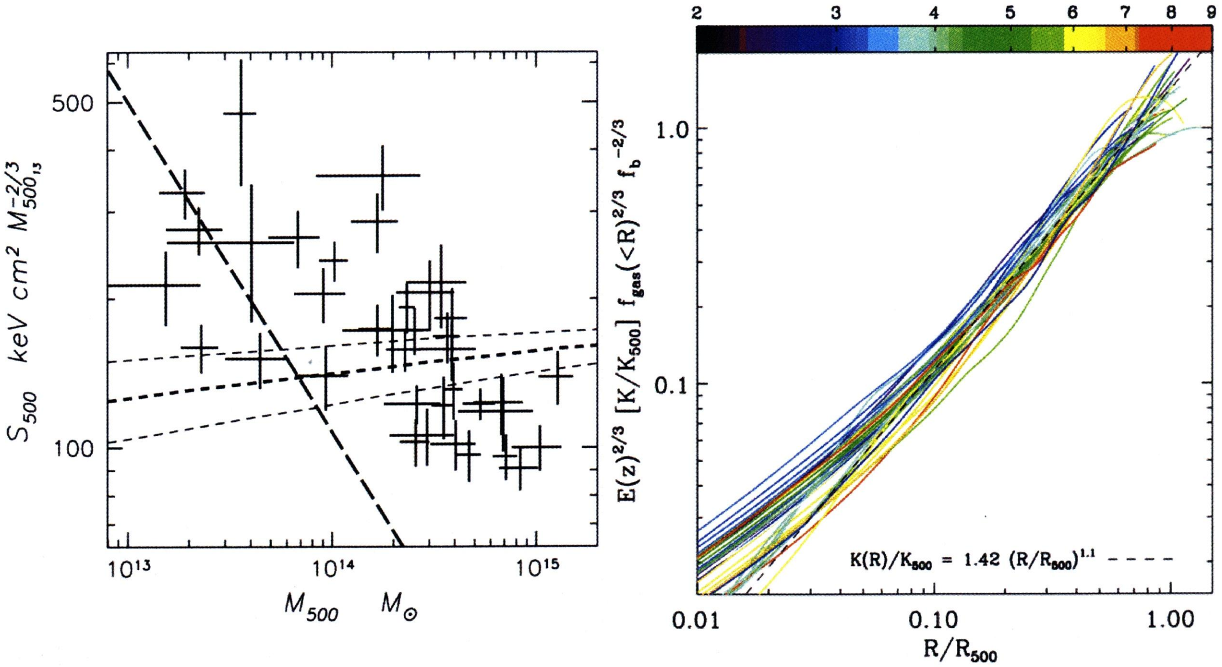

Fig. 2.6: left: The distributions of entropy in cluster central region (Finoguenov et al. 2002). right: Entropy profiles multiplied by the gas mass fraction profile. The dashed line is the predicted entropy distribution.

Specifically, the definition of thermodynamic entropy per particle for a gas of noninteracting monatomic particles is

$$s = k \ln K^{3/2} + s_0. \tag{2.33}$$

Using ASCA data, Finoguenov et al. (2002) studied entropy of groups and clusters of galaxies. They discovered the existence of variation in the level of non-gravitational heating in the central region, which called "pre-heating". The mechanism of pre-heating is still under investigating. Recent XMM-Newton results on the entropy profiles of 31 clusters showed a median slope of 0.98 out to about r_{500} which is approximately $0.5 r_{200}$ as shown in figure2.6 right (Pratt et al. 2010). The slope also showed a positive correlation with the average temperature. They also found that morphologically disturbed clusters showed a large scatter (0.5–2.0) in the slope. They found that the entropy profiles of ICM were well described by $K \propto r^{1.1}$ predicted by Voit et al. (2003). Up to abour r_{500} the results are consistent between observations and numerical simulations, however, Suzaku has extended the entropy measurements close to r_{200} for several clusters, and showed a flattening or even a decrease at $r \gtrsim 0.5\ r_{200}$ (Hoshino et al. 2010; Kawaharada et al. 2010; Akamatsu et al. 2011a; Simionescu et al. 2011). In the end of this chapter, we will summarize the recent progress of our understandings of cluster outskirts.

2.4.5 Time scale

Time scale relevant to the present clusters study are summarized below. Radiative cooling time:

$$t_{cool} = 8.5 \times 10^{10}\ yr(\frac{n_e}{10^{-3}\ \mathrm{cm}})^{-1}(\frac{T}{10^8\ K}) \tag{2.34}$$

Sound crossing time:

$$t_{sc} = \frac{R}{v_{ss}} \sim 6.6 \times 10^8 \, (\frac{T}{10^8\,K})^{-\frac{1}{2}} (\frac{R}{Mpc}) yr \tag{2.35}$$

The electron-electron conduction time:

$$t_{ee} = 4.8 \times 10^5 T_e^{3/2} n_e \ln\Lambda \tag{2.36}$$

The ion-electron conduction time:

$$t_{ie} = 2 \times 10^8 \, (\frac{n_e}{10^{-3} cm^3})^{-1} (\frac{T_e}{10^8\,K})^{\frac{3}{2}} (\frac{\ln\Lambda}{40}) \; yr \tag{2.37}$$

2.4.6 Shock heating

Recent observations revealed statistically significant substructures in the X-ray surface brightness in many clusters (e.g. Jones & Forman 1984). The observed substructures in the ICM argue for remnants or ongoing merger events. The hydro/N- body simulations show that the shocks play important roles to heat up the ICM, if the merging occurs supersonically (see e.g. Ishizaka & Mineshige 1996). We briefly discuss the transition of physical conditions in the upstream to the downstream of the shock.

The mean free paths of electrons (λ_e) and ions (λ_i) in a plasma are expressed as

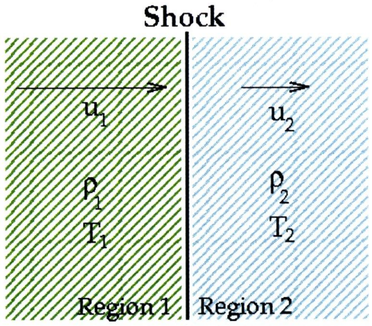

Fig. 2.7: A schematic diagram of a shock wave situation with the density ρ, velocity μ, and temperature T indicated for each region.

$$\lambda_e = \lambda_i \sim 23(\frac{n_e}{10^{-3}\mathrm{cm}^{-3}})^{-1}(\frac{T}{10^8 K})^2 \text{ kpc} \tag{2.38}$$

(Sarazin 1988, p. 156), where n_e is the number density of electrons. If the region of interest has a much larger scale than the mean free path, we may consider that the physical parameters shown in figure 2.7 satisfy the 'jump' condition. It is called as Rankine- Hugoniot jump condition (e.g. Landau & Lifshitz 1960). The mass, momentum, and energy conservation equations are expressed as

$$\rho_1 v_1 = \rho_2 v_2 \tag{2.39}$$

$$\rho_1 v_1^2 + p_1 = \rho_2 v_2^2 + p_2 \tag{2.40}$$

$$\frac{1}{2} v_1^2 + \frac{\gamma}{\gamma - 1} \frac{p_1}{\rho_1} = \frac{1}{2} v_2^2 + \frac{\gamma}{\gamma - 1} \frac{p_2}{\rho_2} \tag{2.41}$$

where ρ, v, p, indicate the density, velocity, and pressure, respectively, measured from the rest frame of the shock. The suffixes of 1 and 2 represent the upstream and downstream of the shock, respectively, and γ is the ratio of specific heats. From the above equations, we find

$$\frac{\rho_2}{\rho_1} = \frac{(\gamma + 1)\mathcal{M}_1^2}{(\gamma + 1)\mathcal{M}_1^2 + 2} \tag{2.42}$$

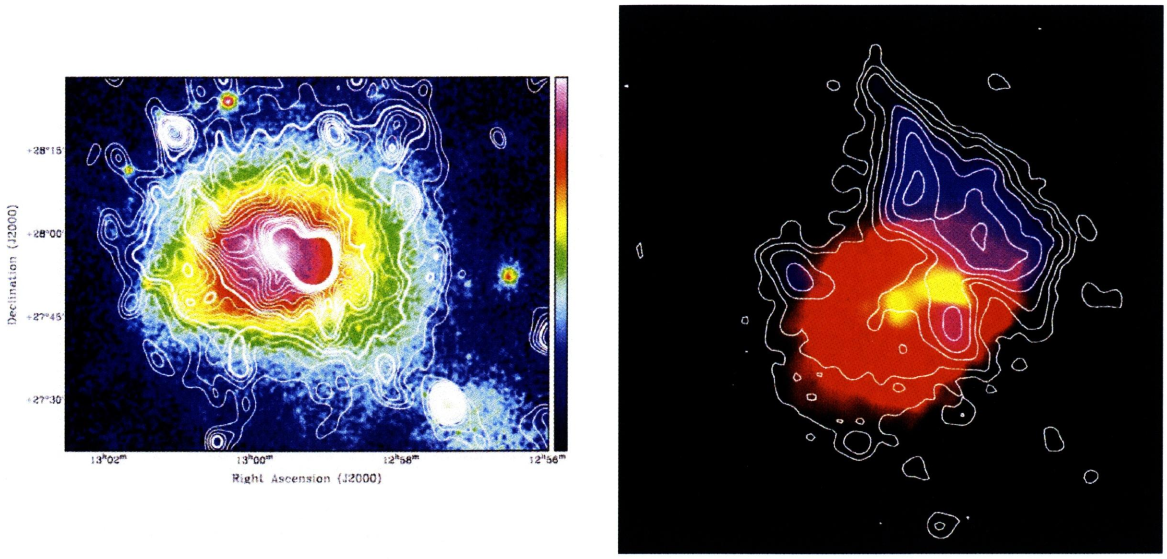

Fig. 2.8: left:350 MHz WSRT contours of the diffuse radio emission in the Coma cluster of galaxies over ROSAT diffuse X-rays. The sharp Western edge in both the radio and X-rays is likely due to shocked ICM (Brown & Rudnick 2011). right: Three-color image of the radio and X-ray emission in A2256. Contours and blue emission show the 1369 MHz synchrotron emission. The Chandra X-ray image is shown in red and green to reveal both the extended diffuse thermal emission (Clarke & Ensslin 2006)

$$\frac{p_2}{p_1} = \frac{2\gamma\mathcal{M}_1^2 - (\gamma + 1)}{(\gamma + 1)} \tag{2.43}$$

$$\frac{T_2}{T_1} = \frac{[2\gamma\mathcal{M}_1^2 - (\gamma + 1)][(\gamma + 1)\mathcal{M}_1^2 + 2]}{(\gamma + 1)\mathcal{M}_1^2} \tag{2.44}$$

where $\mathcal{M}$ indicates the Mach number. In the limit of a weak shock, $p_1 \sim p_2$, the shock wave travels with a velocity which is close to the sound speed, and is practically the same as an acoustic compression wave. On the other hand, in the limit of a strong shock, $p_2 >> p_1$ $\mathcal{M}_2$ approaches a constant value $\mathcal{M}_2 \rightarrow [(\gamma - 1)/2\gamma]^{1/2}$, and p_2 is expressed as

$$p_2 \sim \frac{2(\gamma - 1)}{(\gamma + 1)^2}\rho_2 v_1^2 \tag{2.45}$$

Thus, for the strong shock, the gas can be heated up to $kT_2 \sim (3/16)\mu m_p v_1^2$, where $\mu \sim 0.6$ is a mean molecular weight and m_p is the proton mass, assuming $\gamma = 5/3$.

2.5 Radio emission in clusters of galaxies

A number of clusters of galaxies show extended radio emission. The first detection of diffuse and extended radio emission in galaxy clusters was reported in Coma cluster. With recent progress of radio astronomy, the detections of radio emission in clusters have been grown up. Based on the morphology of radio emission, we can divide they into two prominent types below;

-*Radio halos* are extended and diffuse radio source and often locate around the central regions of clusters of galaxies. The origin of the radio halo is considered as particle acceleration caused by turbulence. However, the no firm observational evidences about turbulent have been obtained.

-Radio relics show "arc"-like shapes with a large extended scale ($\sim$ 1Mpc) located in the outskirts of clusters of galaxies. Typical radio relics show high polarizations. The origin of radio relics is considered as acceleration caused by merger shocks. Recently, Finoguenov et al. (2010) confirmed the existence of a shock front across the radio relic in Abell 3667. This is the first example of a shock front associated with a radio relic.

Origin of the radio emission in clusters has been discussed for a long time. The most likely scenario is the acceleration by turbulences or merger shocks. In the growth history of haloes, major mergers have a significant effect on the internal structure of clusters. The highest energy particles accelerated by the above processes lose their energy quickly. The steepening of the electron spectrum is a direct result of their Compton-synchrotron losses. The observed steep radio spectrum indicate validity of those acceleration scenario. However, firm observable evidences of shocks and turbulences were not reported. Thus, the origin of the radio emission has been rather poorly understood. In the next section, we will reviewed current state of observational studies of the cluster-scale shocks.

2.6 Observational studies of cluster-scale shock front

X-ray observations of merging shocks currently provide the only method for determining the velocity of the cluster gas in the plane of the sky (eg. Markevitch et al. 1998; Tamura et al. 2011). By measuring the temperature and density of the gas on either side of the shock using X-ray imaging spectroscopy, the shock velocity can be calculated from the Rankine-Hugoniot jump conditions (eq 2.43 and eq 2.44).

X-ray observations have revealed a number of merging phenomena of haloes from massive cluster scales (e.g. Markevich et al. 2002) to galaxy groups (e.g. Kawahara et al. 2011) mainly by X-ray morphology. The shock structure caused by the merger was clearly found in the Bullet cluster using *Chandra* (Markevich et al. 2002). In general, however, an identification of the shock structure in X-ray images is difficult, except in exceptionally clear merger clusters including 1E0657-56, A520, and A2146 (Clowe et al. 2006; Markevitch et al. 2005; Russell et al. 2010).

The representative example of a cluster shock have been seen in 1E0657-56 ("Bullet cluster": figure 2.9), which indicates the Mach number $\mathcal{M} \sim 3$. This highly disturbed cluster holds one of the hottest and most X-ray luminous plasma halos with $kT \sim 14$ keV. The bow shock in 1E 0657-56 offers a unique experimental setup to determine how long it takes for post-shock electrons to come to thermal equilibrium with protons in a weakly magnetized plasma. Markevitch et al. 2005 look into the heating process whether the electrons in the intra-cluster plasma are heated directly at the shock to the equilibrium temperature (instant-equilibration), or whether they equilibrate via Coulomb collisions with protons, across the shock front in 1E 0657-56. Based on observational electron temperature and Rankine-Hugoniot jump conditions,

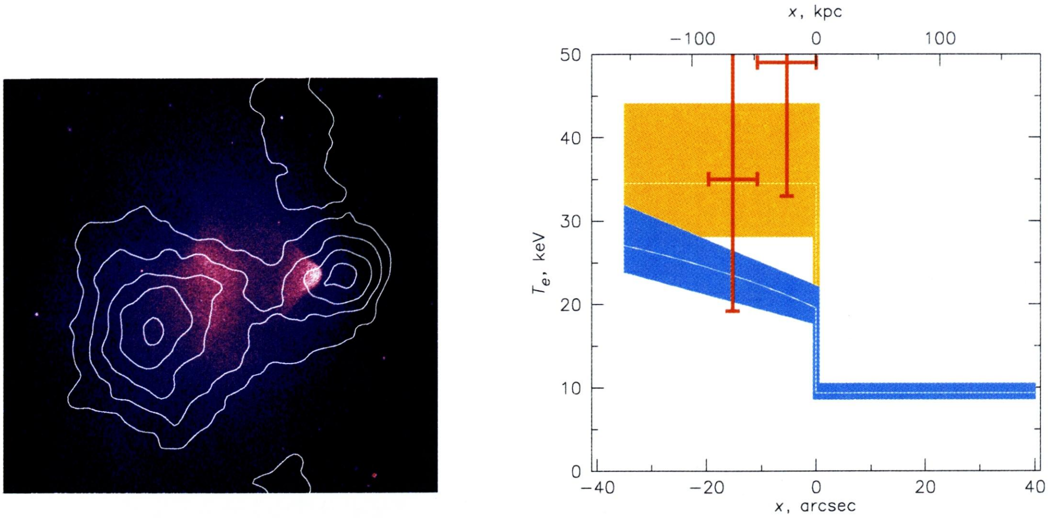

Fig. 2.9: Left: X-ray image of 1E0657-56 with contours showing total projected mass from weak lensing. The gas subcluster trails its mass peak because of ram pressure. This offset is direct proof of the existence of dark matter (Markevitch 2006). Right: Predicted T_e profiles for the shock in 1E 0657-56, for the Coulomb electron-proton equilibration timescale (blue band) and for instant equilibration (yellow band). Overlaid is the Chandra measurement (deprojected, with 1σerror bars), which indicate a shorter equilibration timescale

they determine the expected post shock adiabatic and instant-equilibration electron temperatures which they directly compare (figure 2.9). The temperatures are consistent with instant heating; equilibration on the collisional timescale is excluded. Although this is unexpected result, the measured post-shock temperature is above the range of *Chandra* ACIS energy band, we need more examples to check the possibility of instant heating.

2.7 Cluster of galaxies as cosmological probe

The growth of structure in the matter distribution of the universe has a strong dependence on the cosmological model parameters and in particular on the nature of dark matter and dark energy. Studies of galaxy clusters have proven to be crucial in helping to establish the standard model of cosmology, with a universe dominated by dark matter and dark energy. Sasaki (1996) proposed the ICM mass fraction in very massive systems can be used to constrain cosmological parameters. Recent observational studies of clusters show the consistent result with other observations that find a universe dominated by dark energy (73%), with sub-dominant dark matter (23%), and a small minority of baryonic material (4.6%) (Vikhlinin et al. 2009). Recent studies have used cluster counts or the ICM mass fraction in very massive systems (both methods described in more detail below) to constrain cosmological parameters (fig 2.10).

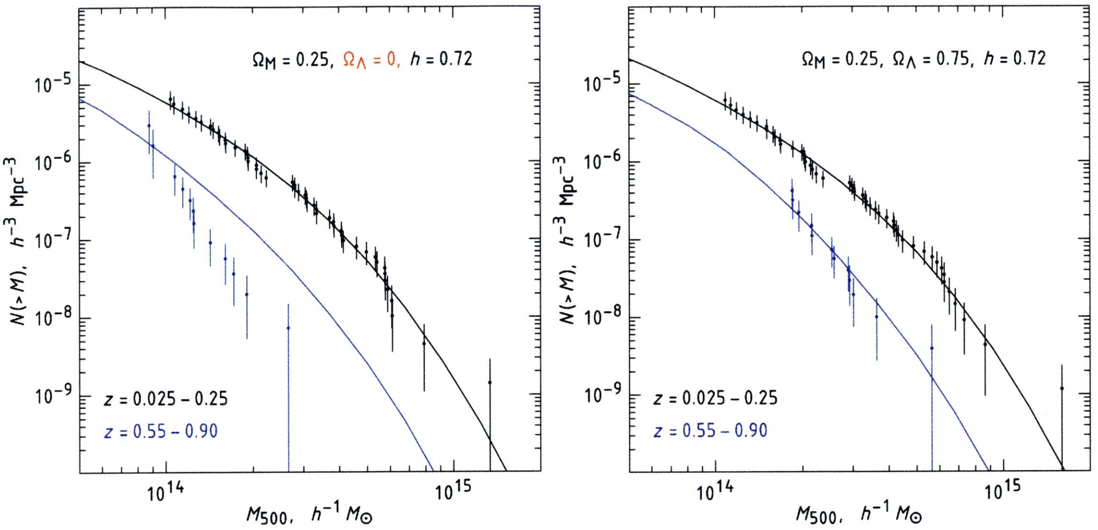

Fig. 2.10: Examples of cluster data used in recent cosmological work (Vikhlinin et al. 2009). Measured mass functions of clusters at low and high redshifts are compared with predictions of a flat, ΛCDM model and an open model without dark energy.

2.8 Previous studies of clusters of galaxies up to r_{200}

The cluster outer regions are fundamentally important as the cosmological probe because these regions record evolution of structure formation without contamination of AGN feedbacks. Also we can constrain cluster properties from the boundary conditions of cluster outskirts. Recently Basu et al. (2009) measured temperature and density profiles with SZ and X-ray observations of A2204 outer region. These observations commonly measured the temperature decreasing to about half of the averaged temperature in the range from $0.5r_{200}$ to r_{200}.

The low, stable, and well understood instrumental and particle background properties of the Suzaku satellite allowed us to perform the first pioneering studies of clusters out to and beyond their virial radii. Now that A1795 (Bautz et al. 2009), PKS0745-191 (George et al. 2008), A2204 (Reiprich et al. 2009), and A399 & A401 Fujita et al.(2008) have been studied up to r_{200} with *S uzaku*.

In particular, Kawaharada et al. (2010) observed Abell 1689 ($z = 0.1832$) out to the virial radius, combined with data sets of the projected galaxy distribution obtained from the SDSS catalog and the projected mass distribution from recent comprehensive weak and strong lensing analysis of Subaru/Suprime-Cam and *HubbleS paceT elescope*/Advanced Camera for Surveys observations. They confirm that the anisotropic gas temperature and entropy distributions in cluster outskirts beyond r_{500} which correlated with the large-scale structure of galaxies in a photometric redshift slice around the cluster. The region showing high temperature (~5.4 keV) and high entropy in the northeastern (NE) outskirts is apparently connected to an overdense filamentary structure of galaxies outside the cluster. The gas temperature and entropy profiles in the NE direction are in good agreement, out to the virial radius, with that expected from a recent XMM-Newton statistical study and with an accretion shock heating model of the ICM, respectively. On the contrary, the other outskirt regions in contact with low-density void envi-

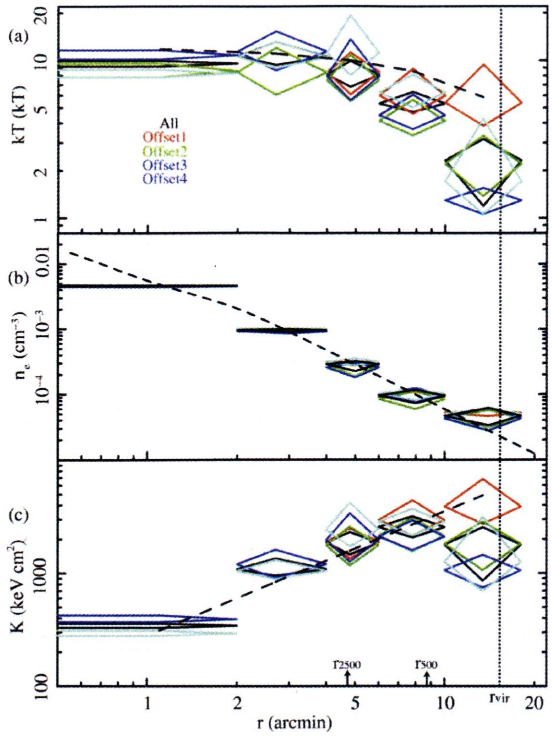

Fig. 2.11: (a) Projected temperature profiles obtained by spectral analyses of Offset1 (red), Offset2 (green), Offset3 (blue), and Offset4 (cyan) observations(Kawaharada et al. 2010). A temperature profile when all spectra of azimuthal regions at the same distance are summed is also shown in black. Dashed line is a temperature profile, $kT = 12.3 - 7.7\,(\frac{r}{15.6})$ keV, expected from the scaled temperature profile by Pratt et al. (2007). Dotted line shows the virial radius ($15'.6$). Arrows are the positions of r_{500} ($8'.7$) and r_{2500} ($4'.7$). (b) The same as panel (a), but for deprojected electron number density profiles. (c) The same as panel (a), but for entropy profiles obtained by calculating $K = kT/n^{2/3}$ from profiles in panels (a) and (b). Dashed line shows $K \sim r^{1.1}$. Normalization of dashed line is arbitrarily scaled.

ronments have low gas temperatures (~1.7 keV) and entropies, deviating from the hydrostatic equilibrium. These anisotropic ICM features associated with large-scale structure environments suggest that the thermalization of the ICM occurs faster along overdense filamentary structures than along low-density void regions.

Recent Suzaku ultra deep observations of the Perserus cluster (Simionescu et al. 2011), which are the X-ray brightest and nearby ($z = 0.018$) cluster of galaxies, provide rich information about ICM around the virial radius for the first time with unprecedented accuracy. They confirm that the entropy and pressure profiles can not be explained by the universal relation derived from the previous X-ray measurements and the baryon fraction exceeds cosmic mean value beyond $0.5r_{500}$ as shown in fig2.12. They discuss that the origin of this apparent excess of baryons at large radius arise from gas clumping. In the x-rays, the directly measurable quantity from the intensity of the bremsstrahlung emission is the average of the square of the electron density, $< n_e^2 >$, rather than $< n_e >^2$. They covect the effect of gas clumping and confirm the agreement of measured entropy and pressure profiles and the universal relation. However, However, the amount of clumping depends on a large number of physical processes in the ICM which are currently uncertain; for example, viscosity, conduction, star formation feedback, and magnetic fields. Although their results were obtained for just one galaxy cluster, it is expected

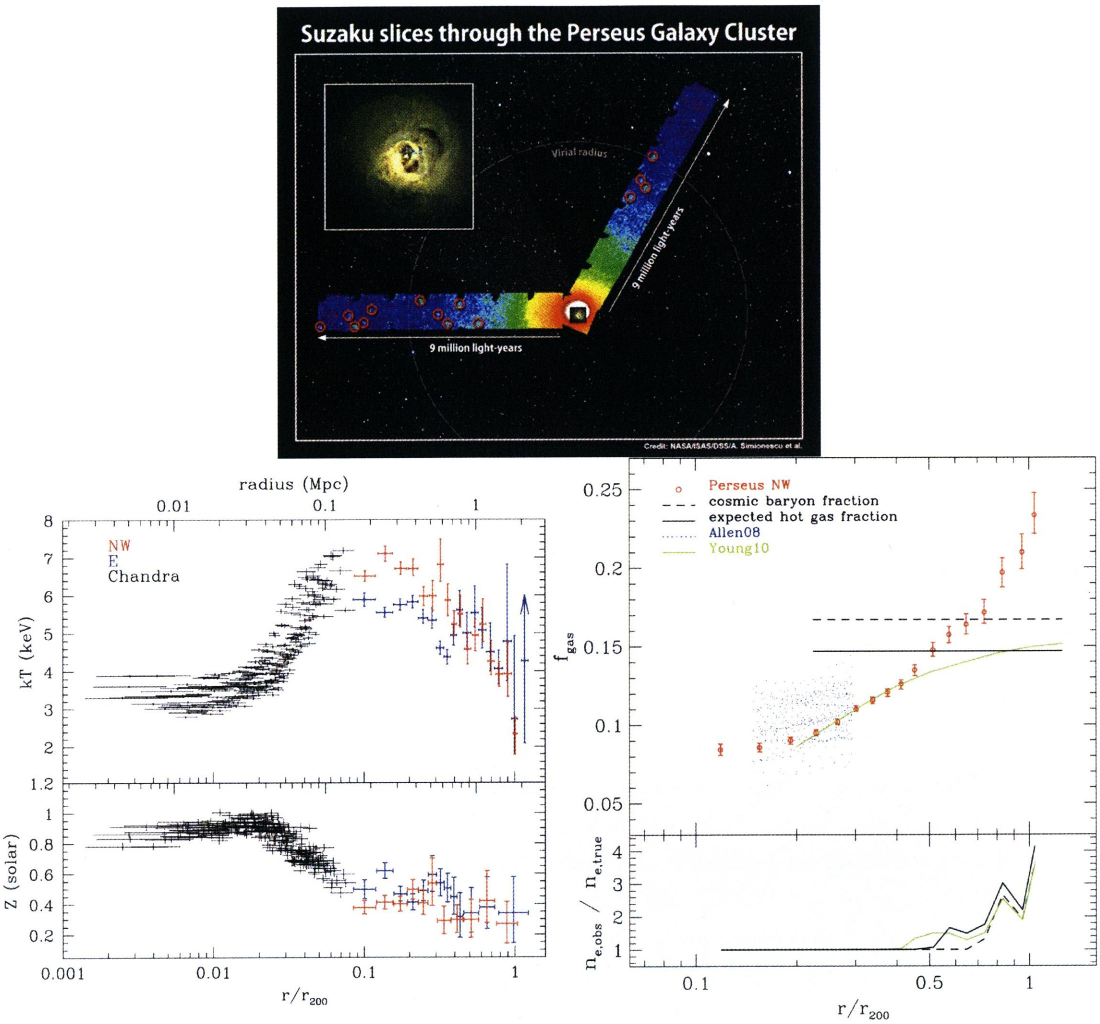

Fig. 2.12: Upper panel:Suzaku explored faint X-ray emission of hot gas across two swaths of the Perseus Galaxy Cluster (Simionescu et al. 2011). Bluer colors indicate less intense X-ray emission. The dashed circle is virial radius. Red circles indicate X-ray sources not associated with the cluster. Inset: An image of the cluster's bright central region taken by NASA's Chandra X-ray Observatory is shown.

that the observed physical processes are common.

In the outer regions of clusters of galaxies, it is possible that gas conditions are not in hydrostatic equilibrium and spherical symmetry because these regions are connected to large scale filaments and are considered to be as the accretion shock region. The physical state of the gas with low density and low temperatures can be described by polytropic relations between gas pressure and density with polytropic index. However, because thermal conductance between electrons and ions is rather low, Takizawa (1998) and Rudd & Nagai (2009) predict inconsistency between electron and ion temperatures in the outer one third of the shock radius of a cluster based on one dimensional and three dimensional simulations for some individual clusters. They also find the entropy profiles to turn to be flattening. Wong et al. (2009) found out the signatures of non-equipartition based on X-ray and SZ observations and discussed the effect of electron shock heating efficiency in the outer regions, because the effect of non-equipartition is important if shock heating efficiency of electrons is low and the equillibraion afterward is due to Coulomb collisions alone. There are possibilities that we have not observed the real averaged temperature which is not equal to the electron temperature.

Chapter 3

Instrumentation

3.1 The *Suzaku* Satellite

3.1.1 Mission Description

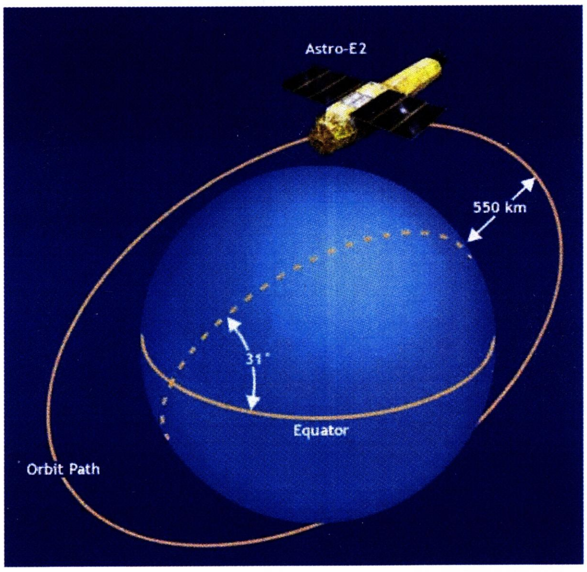

Fig. 3.1: The 96 minute *Suzaku* orbit (The *Suzaku* technical Discription).

Suzaku, the Japanese 5th X-ray astronomical satellite, was launched on July, 2005 (Mitsuda et al. 2007; Serlemitsos et al. 2007; Koyama et al. 2007; **?**). *Suzaku* is placed in a near-circular orbit with an apogee of 568 km, an inclination of 31.9 degrees, and an orbital period of about 96 minutes. The maximum slew rate of the spacecraft is 6 degrees/min, and settling to the final attitude takes ~ 10 minutes, using the star trackers.

A Brief Introduction of *Suzaku*

The scientific payload of *Suzaku* (Fig. 3.2) initially consisted of three distinct co-aligned scientific instruments. There are four X-ray sensitive imaging CCD cameras (X-ray Imaging Spectrometers, or XISs), three front-side illuminated (FI; energy range 0.4-12 keV corresponding to

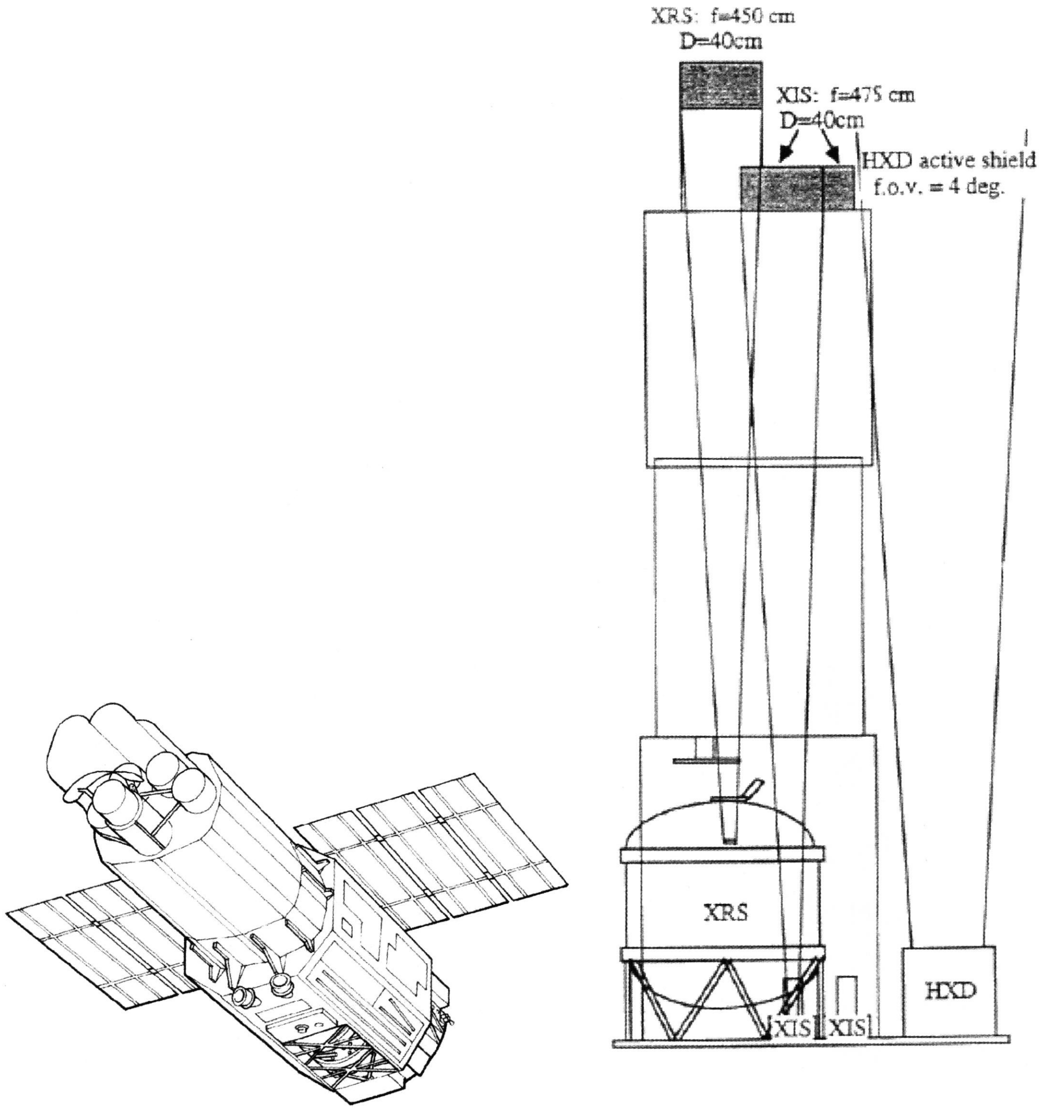

Fig. 3.2: Left: Schematic picture of the *Suzaku* satellite. Right: A side view of the instruments and telescopes on *Suzaku* (Serlemitsos et al. 2007).

XIS0, XIS2 and XIS3) and one back-side illuminated (BI; energy range 0.2-12 keV for XIS1), capable of moderate energy resolution. Each XIS is located in the focal plane of a dedicated X-ray telescope. The second instrument is the non-imaging, collimated Hard X-ray Detector (HXD), which extends the bandpass of the observatory to much higher energies with its 10–600 keV pointed bandpass. The X–Ray Spectrometer (XRS) is no longer operational.

All of the instruments on *Suzaku* operate simultaneously. Each of the co-aligned XRTs features an X-ray mirror with an angular resolution (expressed as Half-Power Diameter, or HPD) of $\sim 2'$ (Fig. 3.3). Figure 3.3 shows the total effective area of the XIS+XRT. K-shell absorption edges from the oxygen (0.54 keV) and aluminum (1.56 keV) in the blocking filters are present, as well as a number of weak M-shell features between 2–3 keV arising from the gold coated on the front surface of the XRT reflector.

The four XISs are true imagers, with a large field of view ($\sim 18' \times 18'$), and moderate spectral resolution.

Table 3.1: Overview of *Suzaku* capabilities

S/C	Orbit Apogee	568 km
	Orbital Period	96 minutes
	Observing Efficiency	$\sim 45\%$
XRT	Focal length	4.75 m
	Field of View	$17'$ at 1.5 keV
		$13'$ at 8 keV
	Plate scale	0.724 arcmin/mm
	Effective Area	440 cm^2 at 1.5 keV
		250 cm^2 at 8 keV
	Angular Resolution	$2'$ (HPD)
XIS	Field of View	$17.8' \times 17.8'$
	Bandpass	0.2–12 keV
	Pixel grid	1024×1024
	Pixel size	24 μm× 24 μm
	Energy Resolution	$\sim$ 130 eV at 6 keV
	Effective Area	340 cm^2 (FI), 390 cm^2 (BI) at 1.5 keV
	(incl XRT-I)	150 cm^2 (FI), 100 cm^2 (BI) at 8 keV
	Time Resolution	8 s (Normal mode), 7.8 ms (P-Sum mode)
HXD	Field of View	$4.5^\circ \times 4.5^\circ$ ($\geq$ 100 keV)
	Field of View	$34' \times 34'$ ($\leq$ 100 keV)
	Bandpass	10 – 600 keV
	- PIN	10 – 60 keV
	- GSO	30 – 600 keV
	Energy Resolution (PIN)	$\sim$ 3.0 keV (FWHM)
	Energy Resolution (GSO)	$7.6/\sqrt{E_{MeV}}$ % (FWHM)
	Effective area	$\sim$ 160 cm^2 at 20 keV, $\sim$ 260 cm^2 at 100 keV
	Time Resolution	61 μs
HXD-WAM	Field of View	2π (non-pointing)
	Bandpass	50 keV – 5 MeV
	Effective Area	800 cm^2 at 100 keV / 400 cm^2 at 1 MeV
	Time Resolution	31.25 ms for GRB, 1 s for All-Sky-Monitor

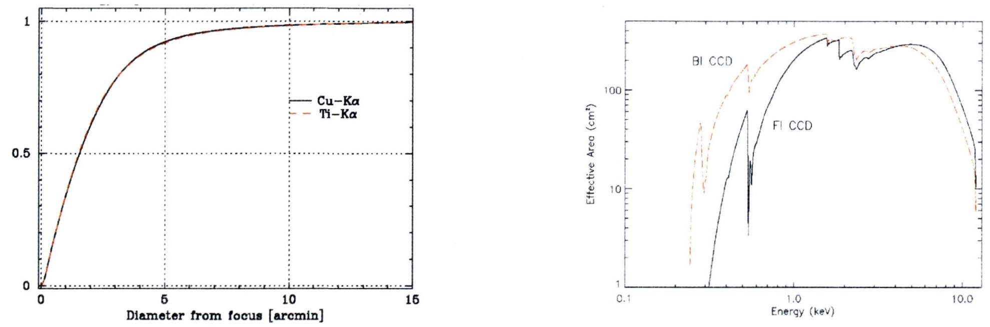

Fig. 3.3: Left: XIS Effective area of one XRT + XIS system, for the FI and BI CCDs. no contamination. Right: The Encircled Energy Function (EEF) showing the fractional energy within a given radius for one quadrant of the XRT-I telescopes on *Suzaku* at 4.5 and 8.0 keV(Serlemitsos et al. 2007).

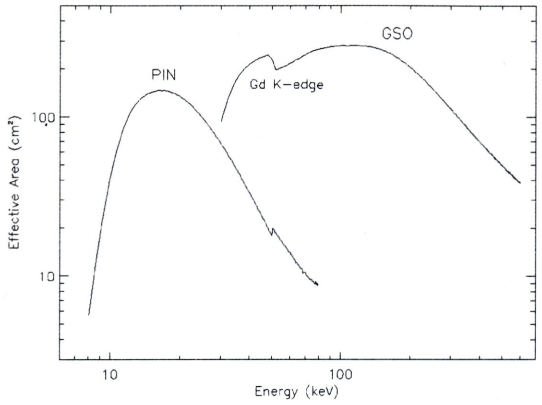

Fig. 3.4: Total effective area of the HXD detectors, PIN and GSO, as a function of energy (**?**).

The HXD is a non-imaging instrument with an effective area of ~ 260 cm^2, featuring a compound-eye configuration and an extremely low background. It extends the bandpass of the mission with its nominal sensitivity over the 10 – 600 keV band (cf. Fig. 3.4). The HXD consists of two types of sensors: 2 mm thick silicon PIN diodes sensitive over 10 – 60 keV, and GSO crystal scintillators placed behind the PIN diodes covering 30 – 600 keV. The HXD field of view is actively collimated to 4.5° × 4.5° by the well-shaped BGO scintillators, which, in combination with the GSO scintillators, are arranged in the so-called phoswich configuration. At energies below ~ 100 keV, an additional passive collimation further reduces the field of view to $34' \times 34'$. The energy resolution is ~ 3.0 keV (FWHM) for the PIN diodes, and $7.6/\sqrt{E}$ % (FWHM) for the scintillators (where E is energy in MeV). The HXD time resolution for both sensors is 61 μs. While the HXD is intended mainly to explore the faintest hard X-ray sources, it can also tolerate very bright sources up to ~ 10 Crab. The HXD also has an all-sky monitor (the Wide-band All-sky Monitor (WAM), which can detect GRB and other sources (3.1). In this paper, we do not use HXD.

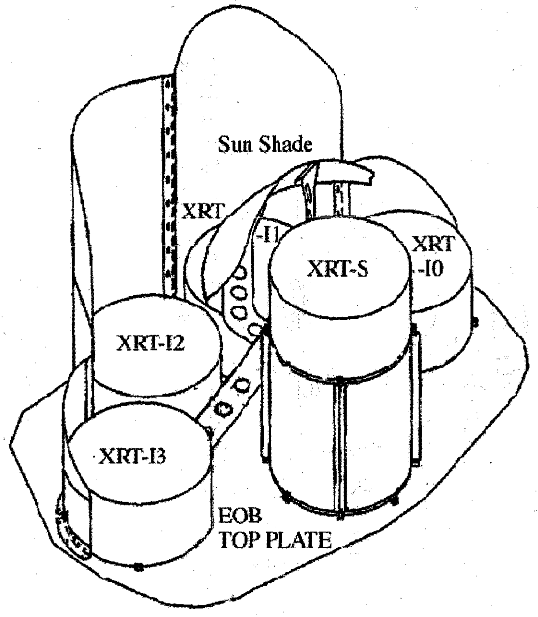

Fig. 3.5: Layout of the XRTs on the *Suzaku* spacecraft (Serlemitsos et al. 2007).

3.1.2 X–Ray Telescopes (XRTs)

Suzaku has five light-weight thin-foil X–Ray Telescopes (XRTs). The XRTs have been developed jointly by NASA/GSFC, Nagoya University, Tokyo Metropolitan University, and ISAS/JAXA. These are grazing-incidence reflective optics consisting of compactly nested, thin conical elements. Because of the reflectors' small thickness, they permit high density nesting and thus provide large collecting efficiency with a moderate imaging capability in the energy range of 0.2-12 keV, all accomplished in telescope units under 20 kg each.

Four XRTs onboard *Suzaku* (XRT-I) are used for the XIS, and the other XRT (XRT-S) is for the XRS. The XRTs are arranged on the top plate of the Extensible Optical Bench (EOB) in the manner shown in Figure 3.5. The external dimensions of the 4 XRT-Is are the same (See Table 3.2, which also includes a comparison with the ASCA telescopes).

The HPD of the XRTs range from $1.8'$ to $2.3'$, which is the diameter within which half of the focused X-ray is enclosed. The angular resolution does not significantly depend on the energy of the incident X-ray in the energy range of *Suzaku*, 0.2-12 keV. The effective areas are typically 440 cm^2 at 1.5 keV and 250 cm^2 at 8 keV. The focal lengths are 4.75 m for the XRT-I. Individual XRT quadrants have their component focal lengths deviated from the design values by a few cm. The optical axis of the quadrants of each XRT are aligned within $2'$ from the mechanical axis. The field of view (the diameter for a half of the effective area) for XRT-Is is about $17'$ at 1.5 keV and $13'$ at 8 keV.

Table 3.2: Telescope dimensions and design parameters of XRT-I, compared with ASCA XRT.

	Suzaku XRT-I	ASCA
Number of telescopes	4	4
Focal length	4.75 m	3.5 m
Inner Diameter	118 mm	120 mm
Outer Diameter	399 mm	345 mm
Height	279 mm	220 mm
Mass/Telescope	19.5 kg	9.8 kg
Number of nested shells	175	120
Reflectors/Telescope	1400	960
Geometric area/Telescope	873 cm^2	558 cm^2
Reflecting surface	Gold	Gold
Substrate material	Aluminum	Aluminum
Substrate thickness	155 μm	127 μm
Reflector slant height	101.6 mm	101.6 mm

Basic Components of XRT

The *Suzaku* XRTs consist of closely nested thin-foil reflectors, reflecting X-ray at small grazing angles. An XRT is a cylindrical structure, having the following layered components: 1. a thermal shield at the entrance aperture to help maintain a uniform temperature; 2. a pre-collimator mounted on metal rings for stray light elimination; 3. a primary stage for the first X-ray reflection; 4. a secondary stage for the second X-ray reflection; 5. a base ring for structural integrity and interface with the EOB. All these components, except the base rings, are constructed in 90° segments. Four of these quadrants are coupled together by interconnect-couplers and also by the top and base rings (Figure 3.6). The telescope housings are made of aluminum for an optimal strength to mass ratio.

Including the alignment bars, collimating pieces, screws and washers, couplers, retaining plates, housing panels and rings, each XRT-I consists of over 4112 mechanically separated parts. In total, nearly 7000 qualified reflectors were used and over 1 million cm^2 of gold surface was coated.

Reflectors Each reflector consists of a substrate also made of aluminum and an epoxy layer that couples the reflecting gold surface to the substrate. The reflectors are nominally 178 μm in thickness. In shape, each reflector is a 90° segment of a section of a cone. The cone angle is designed to be the angle of on-axis incidence for the primary stage and 3 times that for the secondary stage. They are 101.6 mm in slant length and with radii extending approximately from 60 mm at the inner part to 200 mm at the outer part. All reflectors are positioned with grooved alignment bars, which hold the foils at their circular edges. There are 13 alignment bars at each face of each quadrant, separated at approximately 6.4° apart.

In the *Suzaku* XRTs, the conical approximation of the Wolter-I type geometry is used. This

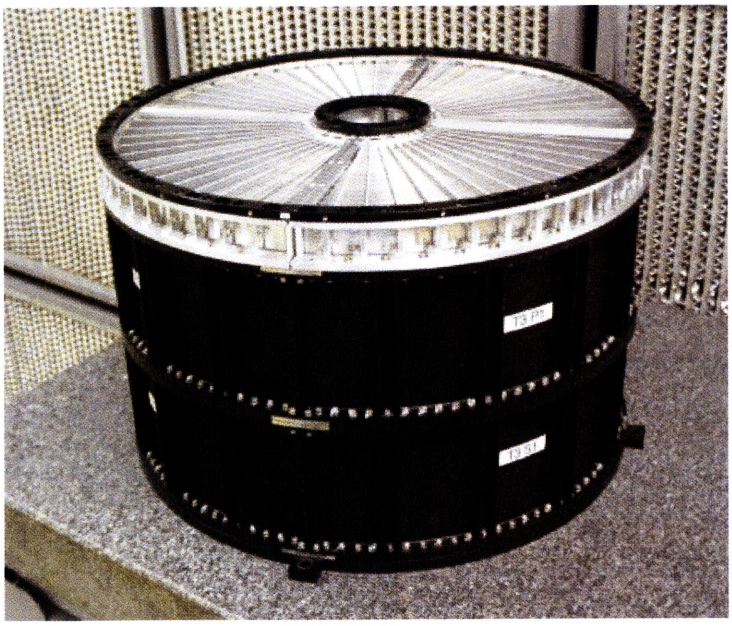

Fig. 3.6: A *Suzaku* X–Ray Telescope (Serlemitsos et al. 2007).

approximation fundamentally limits the angle resolution achievable. More significantly, the combination of the figure error in the replication mandrels and the imperfection in the thermoforming process (to about 4 micrometers in the low frequency components of the figure error in the axial direction) limits the angular resolution to about 1 minute of arc (Misaki et al. 2004).

Pre-collimator The pre-collimator, which blocks off stray light that otherwise would enter the detector at a larger angle than intended, consists of concentrically nested aluminum foils similar to that of the reflector substrates (Mori et al. 2005). They are shorter, 22 mm in length, and thinner, 120 μm in thickness. They are positioned in a fashion similar to that of the reflectors, by 13 grooved aluminum plates at each circular edge of the pieces. They are installed on top of their respective primary reflectors along the axial direction. Due to their smaller thickness, they do not significantly reduce the entrance aperture in that direction more than the reflectors already do. Pre-collimator foils do not have reflective surfaces (neither front nor back). The relevant dimensions are listed in Table 3.3.

Thermal Shields The *Suzaku* XRTs are designed to function in a thermal environment of 20±7.5 °C (figure 3.7). The thermal shield is mechanically sustained by a frame made of aluminum, with a thickness of 4 mm. The frame has thirteen spokes which are along the alignment bars of the XRT. A stainless steel mesh with a wire pitch, width and thickness of 3 mm, 0.1 mm and 0.15 mm, respectively. Finally, polyethylene teleftalate (PET) film as thin as 0.24 μm, coated with aluminum layer with thickness of 30 nm on the surface oriented to the space, is adhered to the mesh with epoxy. The reflectors, due to its composite nature and thus its mismatch in coefficients of thermal expansion, suffer from thermal distortion that degrades the angular resolution of the telescopes in temperature outside this range. Thermal gradient also distorts the telescope in a larger scale. Even though sun shields and other heating elements on the spacecraft

Table 3.3: Design parameters for pre-collimator

	XRT-I
Number of Collimators	4
Height	32 mm
Blade Substrate	Aluminum
Blade Thickness	120 μm
Blade Height	22 mm
Height from Blade Top to Reflector Top	30 mm
Number of nested shells	175
Blade/Telescope	700
Mass/Collimator	2.7 kg

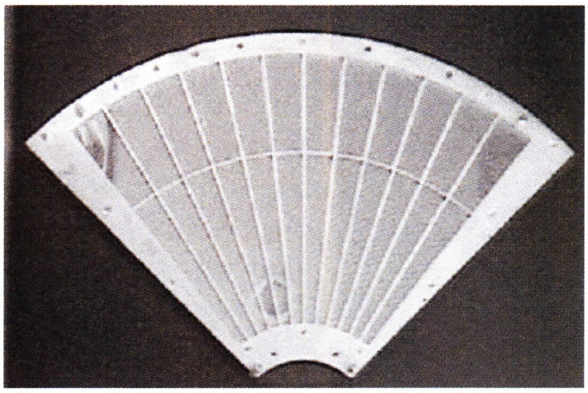

Fig. 3.7: A thermal shield (Serlemitsos et al. 2007).

help in maintaining a reasonable thermal environment, thermal shields are integrated on top of the pre-collimator stage to provide the needed thermal control.

XRT Performance in Orbit

Focal Positions and Angular Resolutions Verification of the imaging capability of the XRTs has been made with the data of SS Cyg in quiescence taken during 2005 November 2 01:02UT–23:39UT. The total exposure time was 41.3 ks. SS cyg is selected for this purpose because it is a point source and moderately bright (3.6, 5.9, 3.7 and 3.5 c s^{-1} for XIS0 through XIS3), and hence, it is needless to care about pile-up even at the image core. A constant value, evaluated from source-free corner regions was subtracted as a background, from all the pixels. The data taken only during the star-tracker calibration is on was used. Fig. 3.8 shows the images and the point spread functions (PSFs) of all the XRT-I+XIS modules. The HPD is obtained to be $1'\!.8$, $2'\!.3$, $2'\!.0$, and $2'\!.0$ for XRT-I0, 1, 2 and 3, respectively. These values are in general consistent with those expected from ground-based calibration measurements.

Figure 3.9 shows the focal position of the XRT-Is, that the source is focused when the satellite points at the XIS aimpoint. The focal positions locate roughly within $0'\!.5$ from the detector center with an deviation of $\sim 0'\!.3$. This implies that the fields of view of the XIS

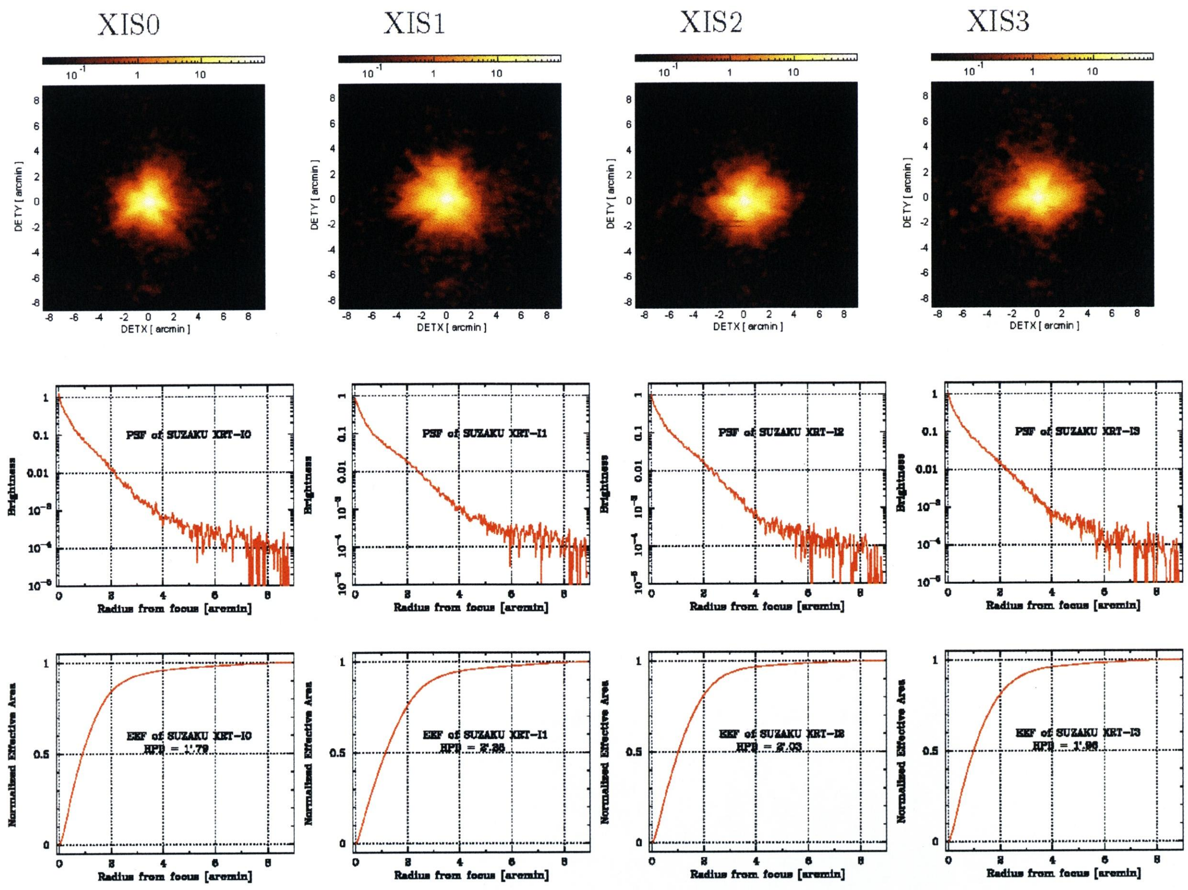

Fig. 3.8: Image, Point-Spread Function (PSF), and EEF of the four XRT-I modules in the focal plane (Serlemitsos et al. 2007). All the images are binned with 2×2 pixels followed by being smoothed with a Gaussian with a sigma of 3 pixels, where the pixel size is 24 μm. The EEF is normalized to unity at the edge of the CCD chip (a square of $17'.8$ on a side). With this normalization, the HPD of the XRT-I0 through I3 is $1'.8$, $2'.3$, $2'.0$ and $2'.0$, respectively.

coinsides each other within $\sim 0'.3$.

Optical Axes, Effective Area and Vignetting Functions A series of offset observations of the Crab observations were carried out in August and September at various off-axis angles of $0'$, $3'.5$, $7'$. The intensity of the Crab nebula is evaluated for each pointing and for each XIS module separately. By finding the maximum throughput angle, we also have obtained a direction of the optical axis of each telescope. The result is shown in Fig. 3.10 The optical axes locate roughly within $1'$ from the XIS aim point. This implies that the efficiency of all the XRT-Is is more than 97 % even at 10 keV when we observe a point source on the XIS aimpoint.

The vignetting curves calculated by the ray-tracing simulator are compared with the observed intensities of the Crab Nebula at various off-axis angles in 3.11. These figures roughly show that effective area is calibrated to within $\sim$ 10% over the XIS field of view. We expect most of these deviations can be attributed to scattering of the optical axis orientations of the four quadrants within a telescope.

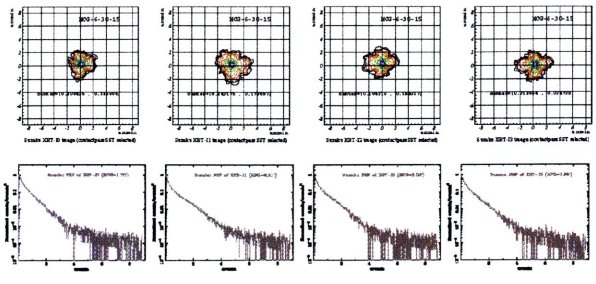

Fig. 3.9: Images and PSFs are shown in the upper, middle, and lower panels for the XIR-I0 through XRT-I3 from left to right. In each image drawn are ten contours in logarithmic spacing with the outermost contour being 1% surface brightness of the peak. the position of the maximum surface brightness is written as a caption in each panel in a unit of arcmin. Its typical error is ±0.1′. Each PSF is normalized by the number of total photons collected over the entire XIS aperture.

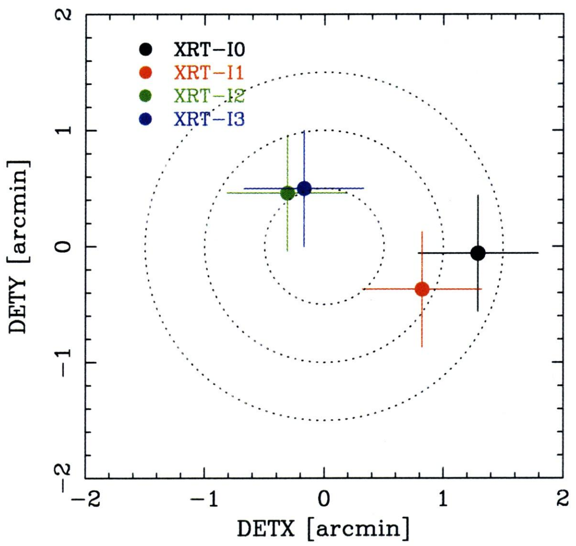

Fig. 3.10: Locations of the optical axis of each XRT-I module in the focal plane determined from the observations of the Crab Nebula in 2005 August-September. This figure implies that the image on each XIS detector becomes brightest when a target star is placed at the position of the corresponding cross. The dotted circles are drawn every 30″ in radius from the XIS-default position.

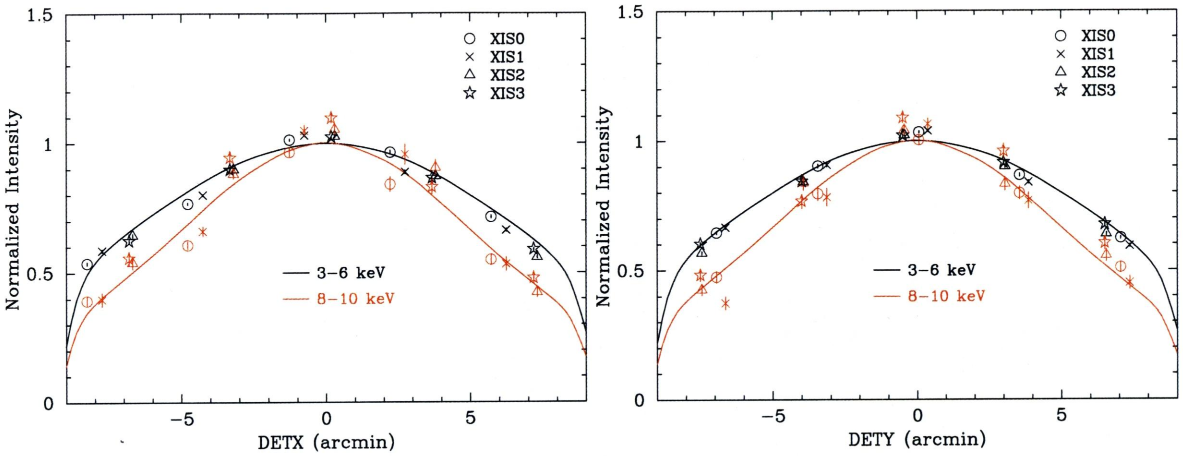

Fig. 3.11: Vignetting of the four XRT-I modules using the data of the Crab Nebula taken during 2005 August 22–27 in the two energy bands 3–6 keV and 8–10 keV. The model curves are calculated with the ray-tracing simulator with the spectral parameters of $N_{\rm H}$ = 0.33×10^{22} cm^{-2}, photon index = 2.09, and the normalization = 9.845 photons cm^{-2} s^{-1} keV^{-1} at 1 keV. Note that the abrupt drop of the model curves at $\sim$ 8′ is due to the source approaching the detector edge. The excess of the data points of XIS1 is probably due to insufficient calibration of the BI CCD.

Stray Light The mechanism of the stray light is written in References (Serlemitsos et al. 2007) in detail. Here we show some important aspects. Stray light is due to reflection paths that are different from the normal two reflection (primary reflection and then secondary reflection) path. There are four main stray paths.

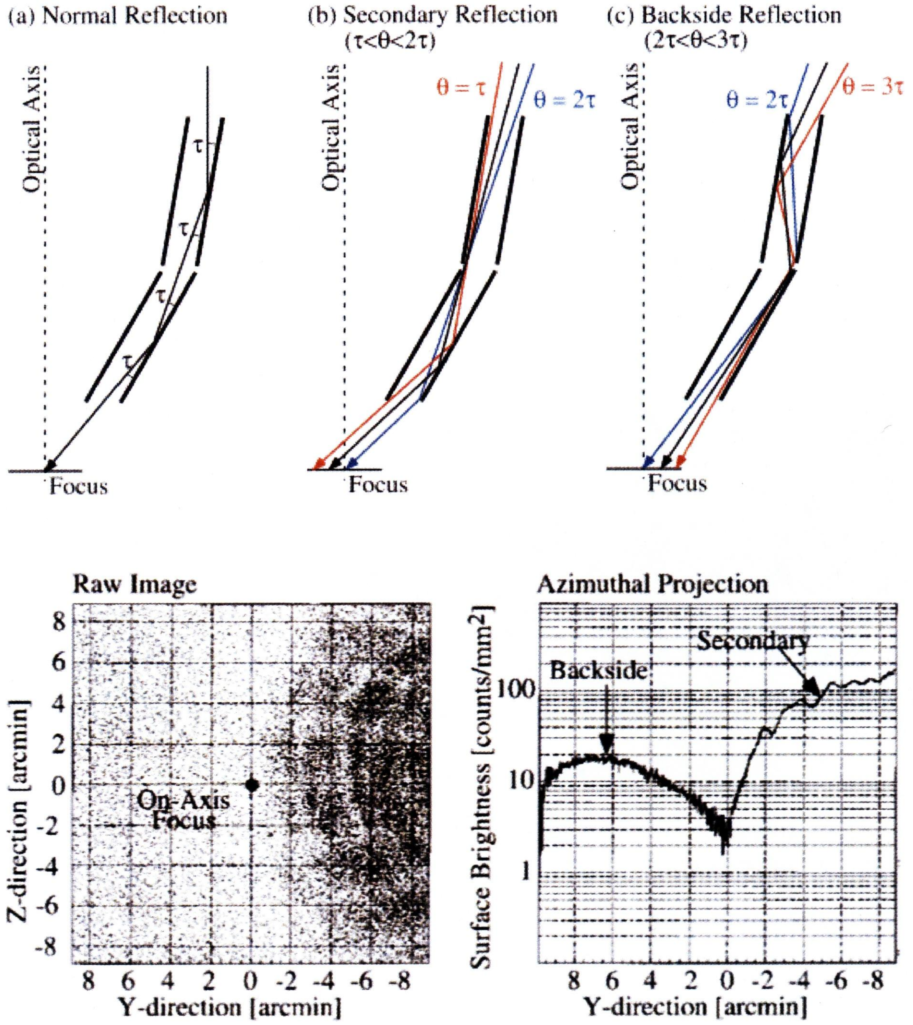

Fig. 3.12: Upper panel: Paths of stray lights of the secondary reflection (middle) and the backside reflection (right), along with the normal reflection path (left). The red and blue lines of the middle and right panels indicate the boundary of the area affected by the stray in each reflection path. Note that the object, i.e., the origin of the stray, is in the right side and so focused on the left side. Hence, the stray image due to the secondary reflection appears on the same side of that of the normal reflection, while that of the backside reflection on the opposite side. Lower panel: Image of a 30′ off object (left) and projected surface brightness profile (right) without precollimators. The object is 30′ off to the right. The stray in the right side is due to secondary reflection, while that in the left is backside reflection. As can be seen in the right panel, the surface brightness of the secondary reflection is an order of magnitude larger than the backside reflection.

- Secondary reflection. An X-ray is only reflected at the secondary reflector, without reflection by a primary reflector
- Backside reflection. An X-ray is reflected at backside of the primary reflector, then reflected by primary and secondary reflectors. So, in this path, the X-ray is reflected three times.
- Primary reflection. An X-ray is only reflected at the primary reflector, without reflection by a secondary reflector.
- No reflection. An X-ray passes through the mirror without reflection.
- Other paths such as precollimator-backside and noormal two-reflection exist. The contribution is, however, negligible.

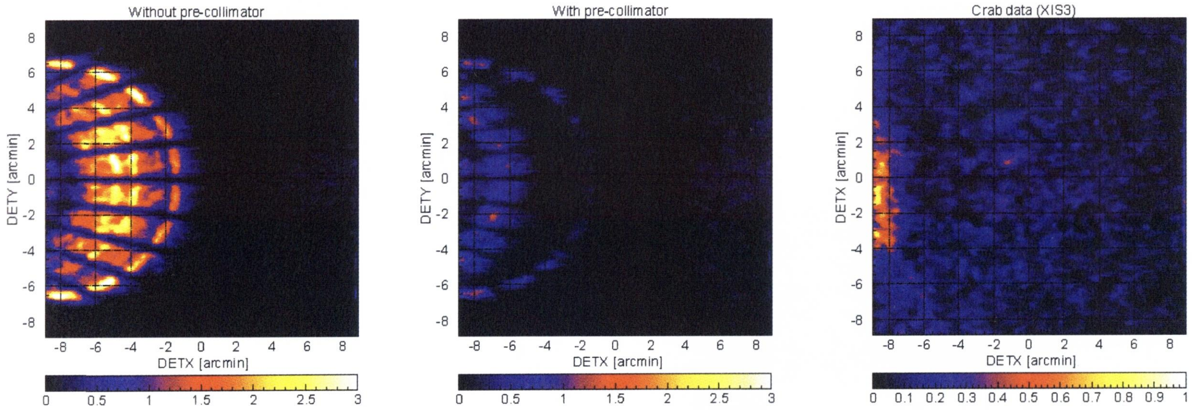

Fig. 3.13: Focal plane images formed by stray light (Serlemitsos et al. 2007). The left and middle panels show simulated images of a monochromatic point-like source of 4.51 keV locating at (DETX, DETY)=($-20'$,$0'$) in the cases of without and with the pre-collimator, respectively. The radial dark lanes are the shades of the alignment bars. The right panels is the in-flight stray image of the Crab Nebula in the 2.5−5.5 keV band located at the same off-axis angle. The unit of the color scale of this panel is counts per 16 pixels over the entire exposure time of 8428.8 s. The counting rate from the whole image is 0.78 ± 0.01 c s^{-1} including background. Note that the intensity of the Crab Nebula measured with XIS3 at the XIS-default position is 458 ± 3 c s^{-1} in the same 2.5-5.5 keV band. All the images are binned with 4×4 pixels followed by being smoothed with a Gaussian with a sigma of 2 pixels, where the pixel size is 24 μm.

In-flight stray-light observations were carried out with Crab at off-axis angles of $20'$ (4 pointings), $50'$ (4 pointing) and $120'$ (4 pointing) in August and September. Fig. 3.13 shows an example of $20'$-off image of XRT-I3 together with simulation results of the same off-axis angle for the cases with and without the pre-collimator. It is seen that the pre-collimator works for reducing the stray light in orbit. Figure 3.14 shows angular responses of the XRT-I at 1.5 and 4.5 keV up to 2 degrees. The effective area is normalized at on-axis. The integration

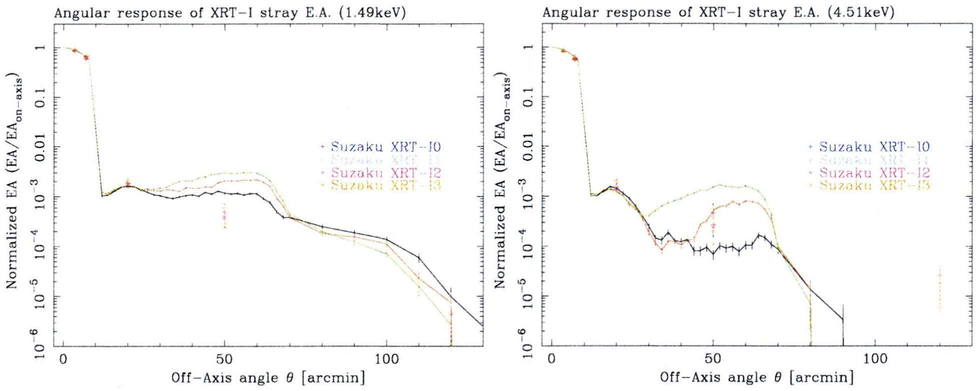

Fig. 3.14: Angular responses of the XRT-I at 1.5 (left) and 4.5 keV (right) up to 2 degrees (Serlemitsos et al. 2007). The effective area is normalized at on-axis. The integration area is corresponding to the detector size of XIS ($17'.8 \times 17'.8$). The three solid lines in the plots correspond to different parameters of ray-tracing program while the crosses are the normalized effective area using the Crab pointings.

area is corresponding to the detector size of XIS ($17'.8 \times 17'.8$). The plots are necessary to plan observations of diffuse sources or faint emissions near bright sources, such as outskirts of cluster of galaxies.

The three solid lines in the plots correspond to different parameters of ray-tracing program while the crosses are the normalized effective area using the Crab pointings. For example, the effective area of the stray lights at 1.5 keV is $\sim 10^{-3}$ at angles smaller than 70 arcmin off axis and $< 10^{-3}$ at angles larger than 70 arcmin off. The measured flux of stray lights are in good agreement with that of raytracing within an order.

On flight calibration of the stray light The stray light of XRT is caused by the reflection that is different from the normal primary-secondary reflection. There are four main stray light path: secondary- only reflection, backside reflection, primary-only reflection and no reflection. In practice, the two dominant paths of stray light are secondary-only and backside reflection.

Simulation tool: *xissim* ver 2009-01-08, **CALDB:** 2011-03-09, **xspec:** ver12.6.0
Mirror file: ae_xrt*_mirror_20080303.fits, **reflect file:** ae_xrt*_reflect_20080303.fits,
backpropfile file: ae_xrt*_pcol_20080303.fits, **xiscontani file:** ae_xi*_contami_20091201.fits

Table 3.4: Input spectrum parameters (Kirsch et al. 2005 SPIE)

Model:phaabs*powerlaw				
Energy band (keV)	Photon flux(photons)	$N_H(10^{22}\mathrm{cm}^{-2})$	Γ	$\mathrm{Flux}_{2-10\mathrm{keV}}$ (ergs /s/cm^2)
2-10	3.43	0.376	2.108	2.20×10^{-8}

23 Crab-offset observations in initial calibration phase (2005) and in AO- 5 phase (2010). Two images from observations and one simulated image is shown in Appendix 1. From the observations (not all images are shown) and comparison to *xissim* simulation, Following characteristics are identified.

- In the 20'-offset pointings, we see red bright spots along a circle of ~20'. This is like primary-only contribution. The position of the spots are slightly different among sen-

Table 3.5: Input parameters for *xissim*

Image:Point source						
Euler angle	Pointing coordinate	Exposure time	Mirror file	reflect file	backprof file	xis_contami file
Header value of observation data FITs			CALDB:2011-03-09			
Parameters of backgrand components (Galactic and CXB)						
N_H	CXB		Galactic			
10^{22}cm^{-2}	Γ	Photon_Flux	kT	kT	Photon_Flux	
0.315	1.41	0.00229	0.113 keV	0.326 keV	0.0161	

Table 3.6: Observation log of Crab during SWG and AO5 (PI: Y. Takei)

Number	Name	Obs ID	(RA, DEC)	Rare Exp time[ks]
1	CRAB_20OFF_0DEG	100010040	(83.652, 21.699)	7.5
2	CRAB_20OFF_90DEG	100010050	(83.272 , 22.020)	6.3
3	CRAB_20OFF_180DEG	100010030	(83.612 , 22.371)	8.1
4	CRAB_20OFF_270DEG	100010100	(83.582 , 22.871)	6.6
5	CRAB_50OFF_0DEG	100022010	(83.664 , 21.206)	12.0
6	CRAB_50OFF_90DEG	100022020	(82.734 , 22.011)	8.6
7	CRAB_50OFF_180DEG	100010090	(83.990 , 22.057)	7.5
8	CRAB_50OFF_270DEG	100022030	(84.530 , 22.069)	0.14
9	CRAB_80OFF_0DEG	105012010	(83.695 , 20.686)	19.2
10	CRAB_80OFF_22.5DEG	105013010	(83.153 , 20.762)	19.0
11	CRAB_80OFF_45DEG	105014010	(82.666 , 21.031)	20.6
12	CRAB_50OFF_45DEG	105015010	(83.020 , 21.413)	11.3
13	CRAB_50OFF_135DEG	105016010	(82.958 , 22.581)	6.5
14	CRAB_50OFF_225DEG	105017010	(84.234 , 22.644)	12.4
15	CRAB_50OFF_315DEG	105018010	(84.297 , 21.469)	14.4
16	CRAB_65OFF_0DEG	105019010	(83.686 , 20.937)	9.7
17	CRAB_65OFF_45DEG	105020010	(82.848 , 21.216)	9.5
18	CRAB_65OFF_90DEG	105021010	(82.463 , 21.974)	10.9
19	CRAB_65OFF_135DEG	105022010	(82.761 , 22.752)	9.2
20	CRAB_65OFF_180DEG	105023010	(83.574 , 23.102)	11.5
21	CRAB_65OFF_225DEG	105024010	(84.392 , 22.846)	9.4
22	CRAB_65OFF_270DEG	105025010	(84.797 , 22.095)	8.9
23	CRAB_65OFF_315DEG	105026010	(84.491 , 21.288)	11.4

sors. Except for the primary-only features, *xissim* models the observation fairly good; the radial profile shows in most of the regions only $< \times 2$ discrepancy.

- In the 50′ offset and 65′ offset pointings, the source-side (i.e., secondary-only contribution) images show big azimuth angle variation; e.g., no symmetry in 90′ rotation, large variation among sensors. The prediction of *xissim* underestimate the level of brighter direction while it is fairly well in the other directions.
- On the other hand, the anti-source half (i.e., backside contribution) show a good 90° rotation symmetry and good agreement among sensors; within 40% difference. Simulation by *xissim* in general overpredicts the surface brightness radial profiles from *xissim* often show opposite contrast to observation.
- Stray light is remarkably smaller in the diagonal direction compared to perpendicular direction (Figure 5.2.1), because the structure of XRT creates shaded strips. It would be advantageous to locate possible stray sources at a diagonal side.
- In the 80 offset pointings, no secondary-only reflection is observed (as expected). The backside contribution is overestimated by *xissim.*
- Secondary reflection shows sector-to-sector variation. A sector covers 7.5 deg azimuthal angle. As an example, the right panel of FIgure 3 exhibits an anomalously bright sector.
- Due to overestimate of backside reflection and underestimate of secondary-only reflection, radial profiles from *xissim* often show opposite contrast to observation.
- In the 80′ offset pointings, no secondary-only reflection is observed (as expected). The backside contribution is overestimated by *xissim.*

3.1.3 X-ray Imaging Spectrometer (XIS)

Overview of the XIS

Suzaku has four X-ray Imaging Spectrometers (XISs), which are shown in Figure 3.16. These employ X-ray sensitive silicon charge-coupled devices (CCDs), which are operated in a photon-counting mode, similar to that used in the ASCA SIS, *Chandra* ACIS, and *XMM-Newton* EPIC. In general, X-ray CCDs operate by converting an incident X-ray photon into a charge cloud, with the magnitude of charge proportional to the energy of the absorbed X-ray. This charge is then shifted out onto the gate of an output transistor via an application of time-varying electrical potential. This results in a voltage level (often referred to as "pulse height") proportional to the energy of the X-ray photon.

The four *Suzaku* XISs are named XIS0, XIS1, XIS2 and XIS3, each located in the focal plane of an X-ray Telescope; those telescopes are known respectively as XRT-I0, XRT-I1, XRT-I2, and XRT-I3. Each CCD camera has a single CCD chip with an array of 1024 × 1024

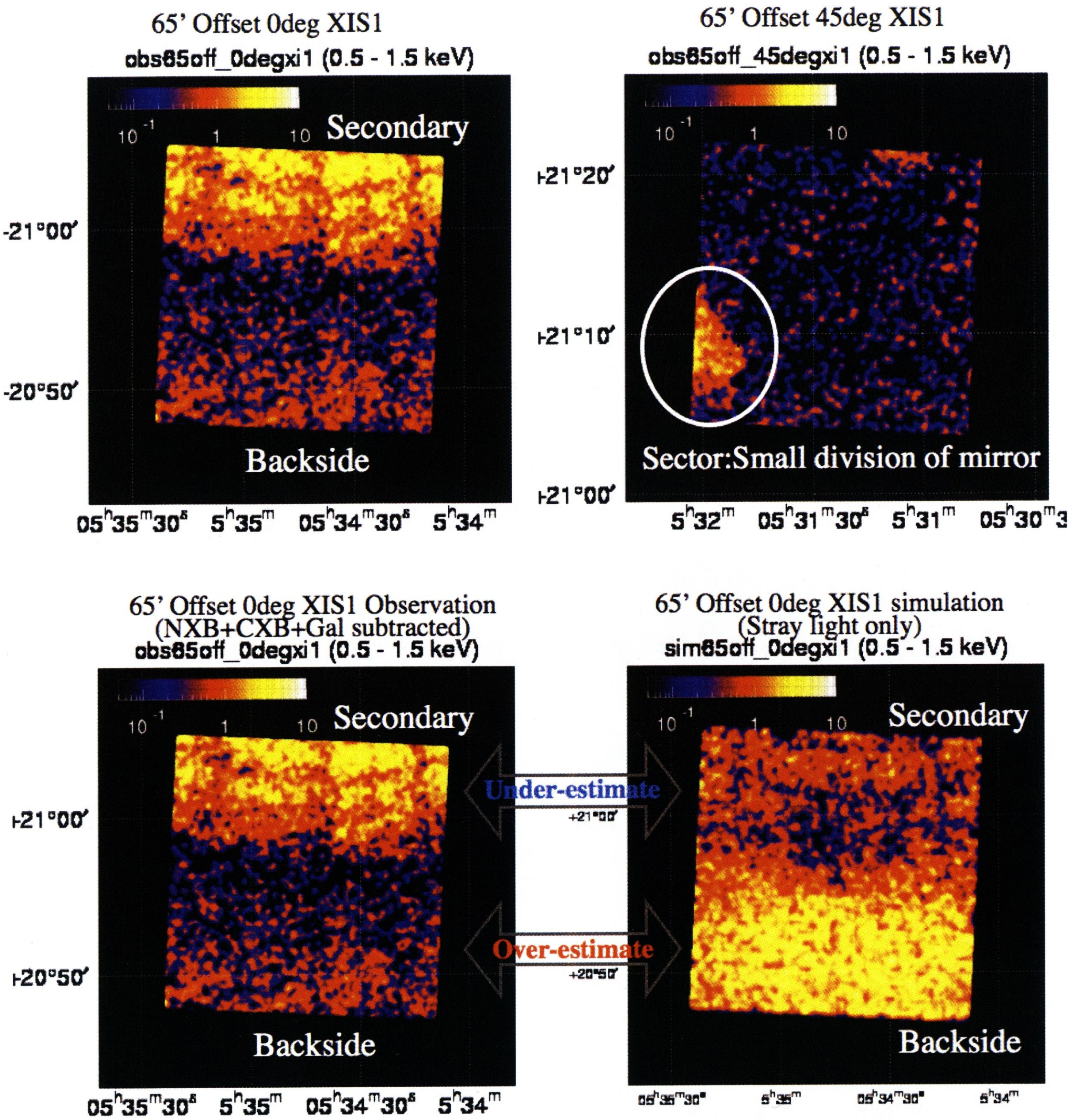

Fig. 3.15: Upper panel: Observed XIS image of Crab 65′ offset region. Lower panel: Comparison between observed Crab offset image and simulated image.

picture elements ("pixels"), and covers an 17.8′ × 17.8′ region on the sky. Each pixel is 24 μm square, and the size of the CCD is 25 mm × 25 mm. One of the XISs, XIS1, uses a back-side illuminated (BI) CCDs, while the other three use front-side illuminated (FI) CCDs. The XIS has been partially developed at MIT (CCD sensors, analog electronics, thermo-electric coolers, and temperature control electronics), while the digital electronics and a part of the sensor housing were developed in Japan, jointly by Kyoto University, Osaka University, Rikkyo University, Ehime University, and ISAS.

A CCD has a gate structure on one surface to transfer the charge packets to the readout gate. The surface of the chip with the gate structure is called the "front side". A front-side

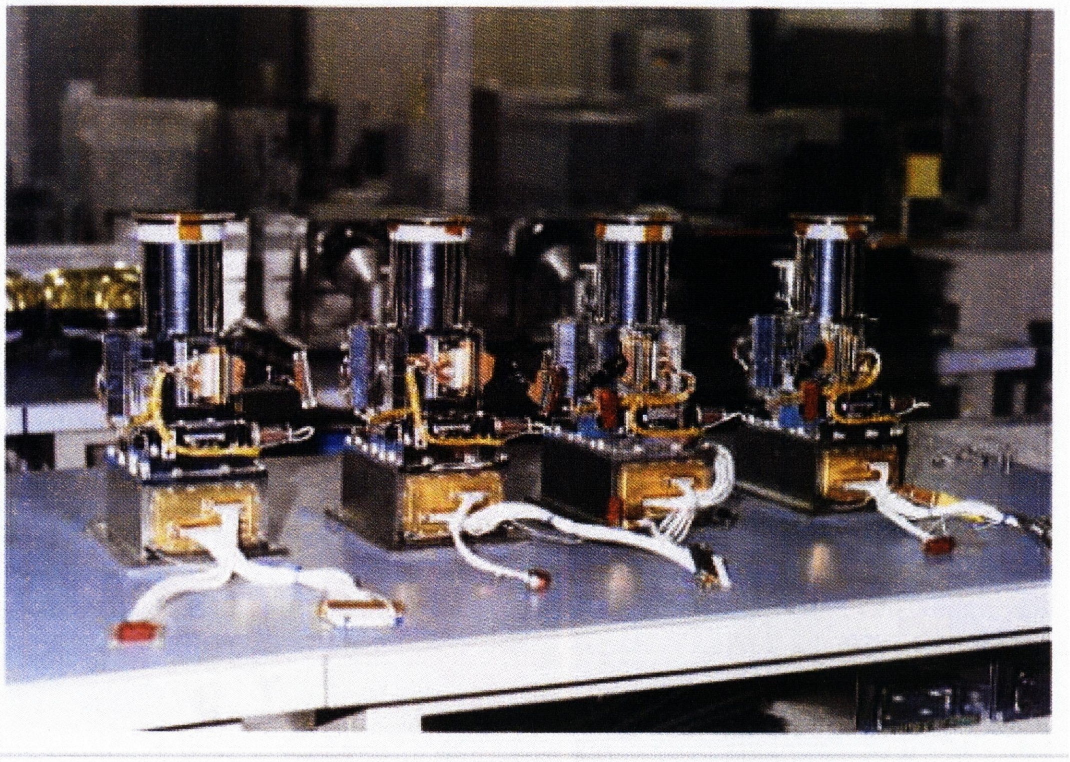

Fig. 3.16: The four XIS detectors before installation onto *Suzaku* (Koyama et al. 2007).

illuminated CCD (FI CCD) detects X-ray photons that pass through its gate structures, i.e. from the front side. Because of the additional photo-electric absorption at the gate structure, the low-energy quantum detection efficiency (QDE) of the FI CCD is rather limited. Conversely, a back-side illuminated CCD (BI CCD) receives photons from "back," or the side without the gate structures. For this purpose, the undepleted layer of the CCD is completely removed in the BI CCD, and a thin layer to enhance the electron collection efficiency is added in the back surface. A BI CCD retains a high QDE even in sub-keV energy band because of the absence of gate structure on the photon-detection side. However, a BI CCD tends to have a slightly thinner depletion layer, and the QDE is therefore slightly lower in the high energy band. The decision to use only one BI CCD and three FI CCDs was made because of both the slight additional risk involved in the new technology BI CCDs and the need to balance the overall efficiency for both low and high energy photons.

To minimize the thermal noise, the sensors need to be kept at $\sim -90°$C during observations. This is accomplished by thermo-electric coolers (TECs), controlled by TEC Control Electronics, or TCE. The Analog Electronics (AE) drives the CCD clocks, reads and amplifies the data from the CCDs, performs the analog-to-digital conversion, and routes the signals to the Digital Electronics (DE). The AE and TCE are located in the same housing, and together, they are called the AE/TCE. *Suzaku* has two AE/TCEs; AE/TCE01 is used for XIS-S0 and S1, and AE/TCE23 is used for XIS-S2 and S3. The digital electronics system for the XISs consists of two Pixel Processing Units (PPU) and one Main Processing Unit (MPU); PPU01 is associated with AE/TCE01, and PPU23 is associated with AE/TCE23. The PPUs receive the raw data from

AE, carry out event detection, and send event data to the MPU. The MPU edits and packets the event data, and sends them to the satellite's main digital processor.

To reduce contamination of the X-ray signal by optical and UV light, each XIS has an Optical Blocking Filter (OBF) located in front of it. The OBF is made of polyimide with a thickness of 1000 Å, coated with a total of 1200 Å of aluminum (400 Å on one side and 800 Å on the other side). To facilitate the in-flight calibration of the XISs, each CCD sensor has two ^{55}Fe calibration sources. One is installed on the door to illuminate the whole chip, while the other is located on the side wall of the housing and is collimated in order to illuminate two corners of the CCD. The door-mounted source will be used for initial calibration only; once the door is opened, it will not illuminate the CCD. The collimated source can easily be seen in two corners of each CCD. A small number of these X-rays scatter onto the entire CCD. In addition to the emission lines created by these sources, we can utilize a new feature of the XIS CCDs, "charge injection capability," to assist with calibration. This allows an arbitrary amount of charge to be input to the pixels at the top row of the imaging region (exposure area), i.e. the far side from the frame-store region. The charge injection capability may be used to measure the CTI (charge transfer inefficiency) of each column, or even to reduce the CTI. How the charge injection capability will be used is still in progress as of this writing.

Pulse Height Determination, Residual Dark-current Distribution, and Hot Pixels

When a CCD pixel absorbs an X-ray photon, the X-ray is converted to an electric charge, which in turn produces a voltage at the analog output of the CCD. This voltage ("pulse-height") is proportional to the energy of the incident X-ray. In order to determine the true pulse-height corresponding to the input X-ray energy, it is necessary to subtract the *Dark Levels* and correct possible *optical Light Leaks.*

Dark Levels are non-zero pixel pulse-heights caused by leakage currents in the CCD. In addition, optical and UV light may enter the sensor due to imperfect shielding ("light leak"), producing pulse heights that are not related to X-rays. In the case of the ASCA SIS, these were handled via a single mechanism: Dark Levels of 16×16 pixels were sampled and their (truncated) average was calculated for every exposure. Then the same average Dark Level was used to determine the pulse-height of each pixel in the sample. After the launch of ASCA, it was found that the Dark Levels of different pixels were actually different, and their distribution around the average did not necessarily follow a Gaussian. The non-Gaussian distribution evolved with time (referred to as Residual Dark-current Distribution or RDD), and resulted in a degradation of the energy resolution due to incorrect Dark Levels.

For the *Suzaku* XIS, Dark Levels and Light Leaks are calculated separately in normal mode. Dark Levels are defined for each pixel; those are expected to be constant for a given observation. The PPU calculates the Dark Levels in the Dark Initial mode (one of the special diagnostic modes of the XIS); those are stored in the Dark Level RAM.

The average Dark Level is determined for each pixel, and if the dark level is higher than the hot-pixel threshold, this pixel is labeled as a *hot pixel.* Dark Levels can be updated by the Dark Update mode, and sent to the telemetry by the Dark Frame mode. Unlike the case of ASCA, Dark Levels are not determined for every exposure, but the same Dark Levels are used for many exposures unless they are initialized or updated. Analysis of the ASCA data showed that Dark Levels tend to change mostly during the SAA passage of the satellite. Dark Update mode may be employed several times a day after the SAA passage.

Hot pixels are pixels which always output over threshold pulse-heights even without input signals. Hot pixels are not usable for observation, and their output has to be disregarded during scientific analysis. The ASCA SIS did not identify hot pixels on-board, and all the hot pixel data were telemetered and removed during the data analysis procedure. The number of hot pixels increased with time, and eventually occupied significant parts of the telemetry. In the case of XIS, hot pixels are detected on-board by the Dark Initial/Update mode, and their positions and pulse-heights are stored in the Hot-pixel RAM and sent to the telemetry. Thus, hot pixels can be recognized on-board, and they are excluded from the event detection processes. It is also possible to specify the hot pixels manually. There are, however, some pixels which output over threshold pulse-heights intermittently. Such pixels are called flickering pixels. It is difficult to identify and remove the flickering pixels on board; they are inevitably output to the telemetry and need to be removed during the ground processing. Flickering pixels sometimes cluster around specific columns, which makes it relatively easy to identify.

The Light Leaks are calculated on board with the pulse height data after the subtraction of the Dark Levels. A truncated average is calculated for 64 × 64 pixels (this size may be changed in the future) in every exposure and its running average produces the Light Leak. Thus, the Light Leak is basically the same as the Dark Level in ASCA SIS.

The Dark Levels and the Light Leaks are merged in the parallel-sum (P-Sum) mode, so Dark Update mode is not available in P-Sum mode. The Dark Levels, which are defined for each pixel as the case of the normal mode, are updated every exposure. It may be considered that the Light Leak is defined for each pixel in P-Sum mode.

On-board Event Analysis

The main purpose of the on-board processing of the CCD data is to reduce the total amount transmitted to ground. For this purpose, the PPU searches for a characteristic pattern of charge distribution (called an event) in the pre-processed (post- Dark Levels and Light Leaks subtraction) frame data. When an X-ray photon is absorbed in a pixel, the photoionized electrons can spread into at most four adjacent pixels. An event is recognized when a valid pulse-height (one between the Event Lower and Upper Thresholds) is found that exceeds the pulse-heights in the eight adjacent pixels (e.g. it is the peak value in the 3 × 3 pixel grid).

The coordinates of the central pixel are considered the location of the event. Pulse-height data for the adjacent 5 × 5 square pixels are sent to the Event RAM as well as the pixel location.

The MPU reads the Event RAM and edits the data to the telemetry format. The amount of information sent to telemetry depends on the editing mode of the XIS. All the editing modes (in normal mode) are designed to send the pulse heights of at least 4 central pixels of an event to the telemetry, because the charge cloud produced by an X-ray photon can spread into at most 4 pixels. Information of the surrounding pixels may or may not output to the telemetry depending on the editing mode. The 5×5 mode outputs the most detailed information to the telemetry, i.e. all 25 pulse-heights from the 5×5 pixels containing the event. The size of the telemetry data per event is reduced by a factor of 2 in 3×3 mode.

Photon pile-up

The XIS is essentially a position-sensitive integrating instrument, with the nominal interval between readouts of 8 s. If during the integration time one or more photons strike the same CCD pixel, or one of its immediate neighbors, these cannot be correctly detected as independent photons: this is the phenomenon of photon pile-up. Here, the modest angular resolution of the *Suzaku* XRT is an advantage: the central 3×3 pixel area receives 2% of the total counts of a point source, and ~10% of the counts fall within ~0.15 arcmin of the image center. We calculated the count rate at which 50% of the events within the central 3×3 pixels are piled-up (the pile-up fraction goes down as we move out of the image center; this fraction is <5% for the 0.15 arcmin radius) — although we offer no formal justification for this particular limit, this is compatible with our ASCA SIS experience (i.e., at this level, the pile-up effects do not dominate the systematic uncertainties).

XIS Background Rate

All four XISs have low backgrounds, due to a combination of the *Suzaku* orbit and the instrumental design. Below 1 keV, the high sensitivity and energy resolution of the XIS-S1 combined with this low background means that *Suzaku* is the superior instrument for observing soft sources with low surface brightness. At the same time, the large effective area at Fe K (comparable to the XMM pn) combined with this low background make *Suzaku* a powerful tool for investigating hot and/or high energy sources as well.

In the XIS, the background originates from the cosmic X-ray background (CXB) combined with charged particles (the non-X-ray background, or NXB). Currently, flickering pixels are a negligible component of the background. When observing the dark earth (*i.e.* the NXB), the background rate between 1-12 keV in is 0.11 cts/s in the FI CCDs and 0.40 cts/s in the BI CCD; see Figure 3.17:left. Note that these are the fluxes after the grade selection is applied with only grade 0, 2, 3, 4 and 6 selected. There are also fluorescence features arising from the calibration source as well as material in the XIS and XRTs. The Mn lines are due to the scattered X-rays from the calibration sources. As shown in Table 3.7 the Mn lines are almost negligible except for XIS-S0. The O lines are mostly contamination from the day earth (3.1.3). The other lines are fluorescent lines from the material used for the sensor. Table 3.7 shows the current best estimates for the strength of these emission features, along with their 90% upper and lower limits.

The background rate on the FI chips (including all the grades) is normally less than 400 counts/frame (50 cts/s) when no class discriminator is applied. On the BI chip, the rate is normally less than 150 counts/frame (18.75 cts/s). The background rate on the FI chips is

Table 3.7: Major XIS Background Emission Lines

Line	Energy keV	XIS-S0 10^{-9} ct/s/pix	XIS-S1 10^{-9} ct/s/pix	XIS-S2 10^{-9} ct/s/pix	XIS-S3 10^{-9} ct/s/pix
O K	0.5249	18.5 ± 0.5	$69.3^{+2.7}_{-2.6}$	$14.3^{+1.5}_{-1.3}$	$14.1^{+1.1}_{-1.2}$
Al K	1.846	1.98 ± 0.23	3.01 ± 0.51	$1.50^{+0.31}_{-0.28}$	$1.57^{+0.25}_{-0.23}$
Si K	2.307	$0.299^{+0.2080}_{-0.2074}$	2.21 ± 0.45	$0.0644(< 0.282)$	$0.543^{+0.212}_{-0.213}$
Au M	2.1229	0.581 ± 0.234	$1.13^{+0.280}_{-0.291}$	$0.359^{+0.211}_{-0.212}$	$6.69^{+2.91}_{-2.90}$
Mn Kα	5.898	$8.35^{+0.36}_{-0.34}$	0.648 ± 0.289	$0.299^{+0.209}_{-0.2086}$	$0.394^{+0.181}_{-0.18}$
Mn Kβ	6.490	$1.03^{+0.22}_{-0.216}$	$0.294(< 0.649)$	$0.00(< 0.111)$	$0.428^{+0.225}_{-0.226}$
Ni Kα	7.470	7.20 ± 0.31	6.24 ± 0.53	$3.78^{+0.26}_{-0.25}$	$7.13^{+0.36}_{-0.37}$
Ni Kβ	8.265	0.583 ± 0.183	$1.15^{+0.5}_{-0.489}$	0.622 ± 0.206	$0.983^{+0.247}_{-0.249}$
Au Lα	9.671	$3.52^{+0.27}_{-0.28}$	$3.28^{+1.16}_{-0.99}$	$1.88^{+0.31}_{-0.28}$	$3.54^{+0.36}_{-0.35}$
Au Lβ	11.514	$2.25^{+0.73}_{-0.59}$	2.91 ± 1.29	$0.752^{+0.428}_{-0.304}$	$2.67^{+0.61}_{-0.53}$

Note: Typical accumulation time are 110-160 ks

expected to reduce significantly when the class discriminator is applied. But little change is anticipated for the BI chip. Since 5×5, 3×3, and 2×2 modes require on average 40, 20, and 10 bytes per event, the minimum telemetry required for any source is $\sim$ 58 kbits/s for 5×5 mode, $\sim$ 31 kbits/s for 3×3, and $\sim$ 17 kbits/s for 2×2 mode, if no class discriminator is used.

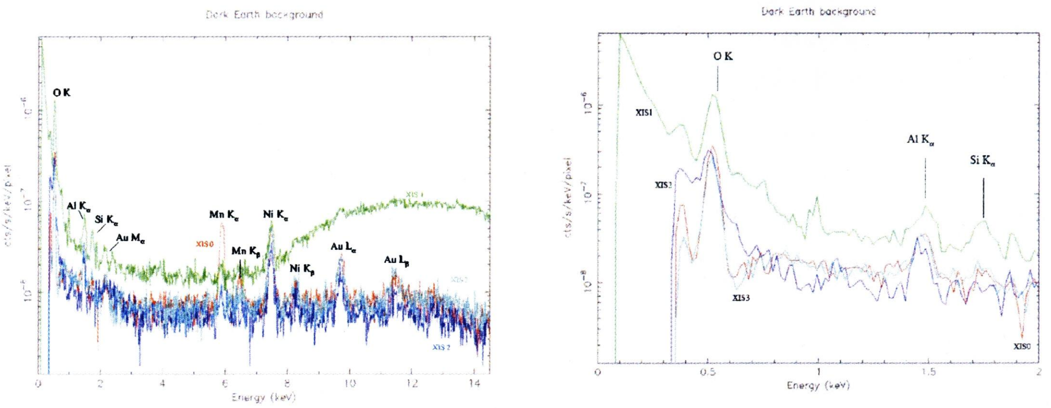

Fig. 3.17: Left: The XIS background rate for each of the four XIS detectors, with prominent fluorescent lines marked. These spectra are based on $\sim 110 - 160$ ksec of observations towards the dark Earth. These spectra does not included Cosmic X-ray background (CXB). Right: The XIS background rate for each of the four XIS detectors, showing only energies between 0.1-2.0 keV. Below 0.3 keV the background rate for the FI chips cannot be determined due to their low effective area.

Out-of-time events X-ray photons detected during the frame-store transfer do not correspond to the true image, but instead appear as a streak or blur in the readout direction. These events are called out-of-time events., and they are an intrinsic feature of CCD detectors. Similar streaks are seen from bright sources observed with *Chandra* and *XMM-Newton*. Out-of-time events produce a tail in the image, which can be an obstacle to detecting a low surface brightness feature in an image around a bright source. Thus the out-of-time events reduce the dynamic range of the detector. Since XIS spends 25 ms in the frame-store transfer, about 0.3% ($= 0.025/8 \times 100$) of all events will be out-of-time events. However, because the orientation of the CCD chip is different among the sensors, one can in principle distinguish a true feature of low surface brightness and the artifact due to the out-of-time events by comparing the images from two or more XISs.

Day Earth Contamination When the XIS field of view is close to the day earth (i.e. Sun lit Earth), fluorescent lines from the atmosphere contaminate low-energy part of the XIS data, especially in the BI chip. Most prominent is the oxygen line, but the nitrogen line may be also noticed (Fig. 3.17:right). These lines are mostly removed when we apply the standard data screening criteria (XIS FOV is at least 20 degree away from the day earth) during the ground processing. However, small amount of contamination can remain. This contamination may be further reduced if we subtract appropriate background. This subtraction, however, may be imperfect. Thus, when neutral oxygen or nitrogen lines are detected in the XIS data, contamination from day earth should be suspected.

Radiation Damage and On-board Calibration of the XIS

The performance of X-ray CCDs gradually degrades in the space environment due to the radiation damage. This generally causes an increase in the dark current and a decrease of the charge transfer efficiency (CTE). In the case of XIS, the increase of the dark current is expected to be small due to the low (–90°C) operating temperature of the CCD. However, a decrease in CTE is unavoidable. Thus, continuous calibration of CCD on orbit is essential to the good performance of the XIS. For this purpose, we use a radio isotope source and charge injection as explained below:
(i) Each XIS carries ^{55}Fe calibration sources near the two corners of the chip, which will be used to monitor the instrument gain.
(ii) Each XIS CCD is equipped with charge injection capability, which may be useful to measure and even suppress CTI.

Nonetheless, it is difficult to predict based on existing data how well we can calibrate the long-term performance change of XIS on orbit.

On-ground Event Selection

Internal (non X-ray) background events can be effectively removed using the pattern on CCD pixels (GRADE), the position (STATUS) and time of an event. The definition of GRADE is shown in Figure 3.18. Most of X-ray events take GRADE = 0, 2, 3, 4, or 6. On the other hand, most of the events of other GRADEs are dominated by non X-ray events, and should be excluded. STATUS parameter stores the information of pixel quality of an event. Known

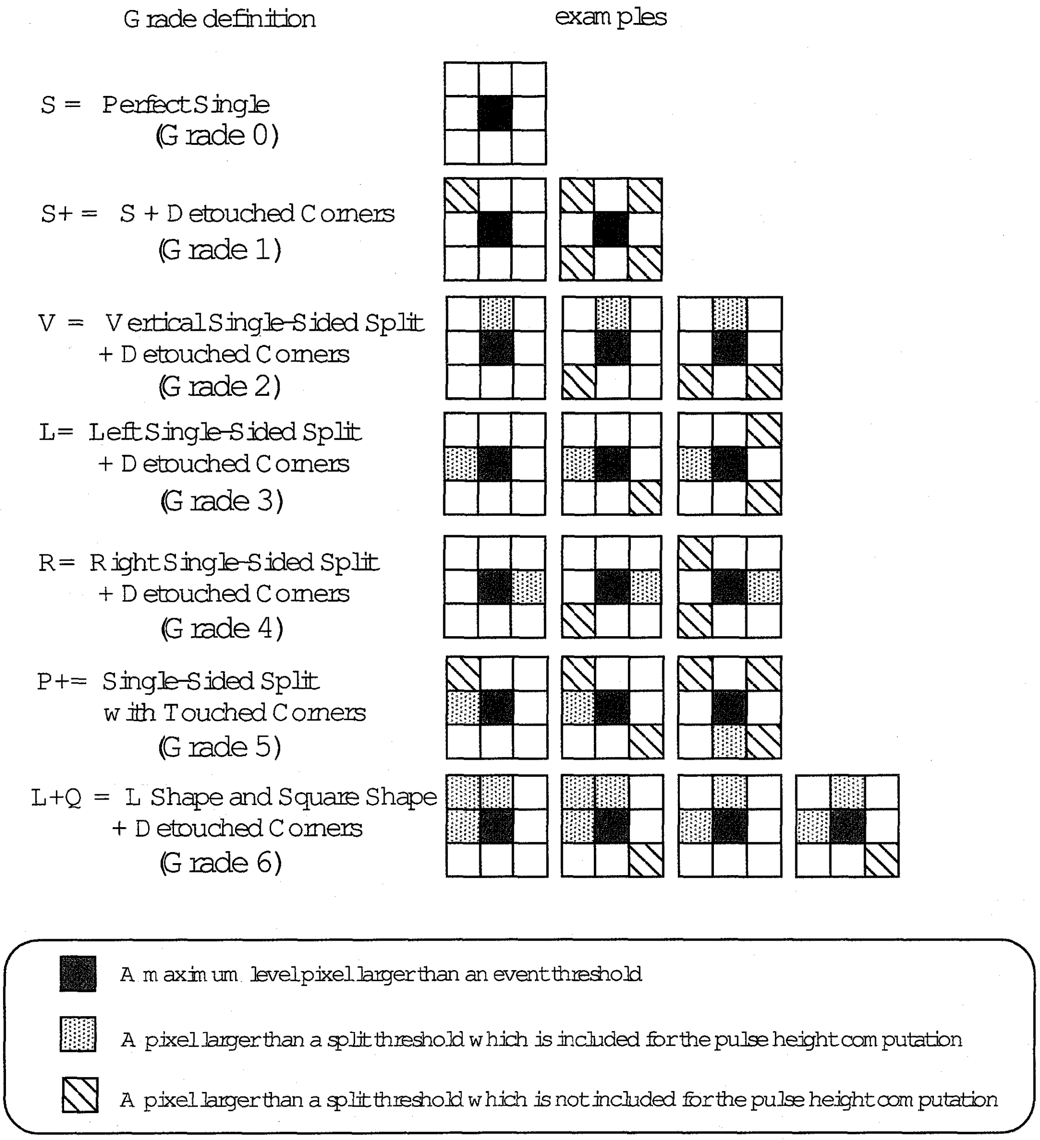

Fig. 3.18: Definition of GRADE of CCD events.

hot pixels, bad CTE columns, flickering pixels, and pixels on the segment boundaries can be removed by selecting the events with STATUS< 131072. The parameters used in good time interval (GTI) selection are shown in Table 3.8. The signal to noise ratio can be improved with an appropreate GTI criteria, indicated in Table 3.8.

Table 3.8: Parameters used in GTI selection of *Suzaku*

Parameter	Definition	Recommended value to use
SAA	Whether the satellite was in the SAA^a or not	eq.0
T_SAA	Time after the last SAA duration (s)	> 255
ELV	Elevetion angle from the Earth limb (degree)	> 5
DYE_ELV	Elevation angle from the day Earth limb (degree)	> 20
COR	Cut off rigidity of the cosmic ray (GeV/c/particle)	> 8

^{a}: South Atlantic anomaly

Contamination Crrection

The OBF has been gradually contaminated in time by out-gassing from the satellite. The contamination rate af- ter the XIS door-open is unexpectedly high, and the rate is different from sensor to sensor. Moreover, the thickness of the contamination varies with position on the OBF.

The contamination has caused a significant reduction in low-energy response since launch. We therefore need to include additional, time-varying low energy absorption in the response function. This is given as a function of both the observation date after the XIS door-open, and of de- tector coordinates (specifying the position on the OBF). For this purpose, we measured the on-axis extra absorp- tion by observing a SNR 1E0102–72 and an isolated neu- tron star RX J1856.5–3754. At the time of writing, we have not conclusively determined the chemical composi- tion for the contamination material(s). From the overall spectral shape in the low energy absorption for all the available X-ray sources and the best guess for the out- gassing source in *Suzaku*, we assume that the contami- nant contains predominantly C and O with the number ratio C/O 6. Figure 3.19 shows the time histories of the contamination accumulated on the OBF. Empirically, the time dependence of the contamination thickness is assumed to follow the exponential form as; $N_c = a - b \times \exp -day/c$, where N_c is the carbon column density in units of 10^{18} cm^{-2} (C/O = 6). To measure the off-axis absorption, we used diffuse X-rays from the bright Earth rim and the Cygnus Loop. The former emits characteristic K lines of $\mathrm{N_I}$ and $\mathrm{O_I}$ (neutral atoms) and the latter provides K lines from $\mathrm{C_{VI}}$, $\mathrm{N_{VII}}$, $\mathrm{O_{VII}}$ and $\mathrm{O_{VIII}}$ (He-like or H-like atoms). Since the for-mer can be observed frequently, we trace the time history of off-axis absorption over successive one-month periods after the XIS door-open (13 August, 2005). With the two reasonable assumptions that (1) the N:O line ratio is uniform over the field of view and (2) the contamination is azimuthally constant, we can derive the radial profile of the difference of contamination thickness from the center value. We show the radial profiles of the column density of carbon in figure 15 for one month and five months after the door-open. This radial profile is approximated by a function of $1/[1 + \{r/a(t)\}^{b(t)}]$. The time dependent parameters, $a(t)$ and $b(t)$ are determined and up-dated regularly.

3.1.4 Uncertainties of Metal Abundance

We must consider three uncertaities for metal abundance, especially oxygen and magnesium, analizing the spectra of XIS.

1. Systematic uncertainties (NXB and CXB level, gain and CTI correction and so on.)
2. Our Galactic components
3. Contamination on XIS

(1): We check the effects by changing the NXB and CXB levels by ±10%. (2): Because the O VII and O VIII lines emitted from ICM are coupled with these emitted from our Galaxy, the estimation of the emission from our Galaxy is very impotant to decide the oxygen abundance of ICM. (3): As descibed in 3.1.3, because the observed spectra are absorbed by the contaminant

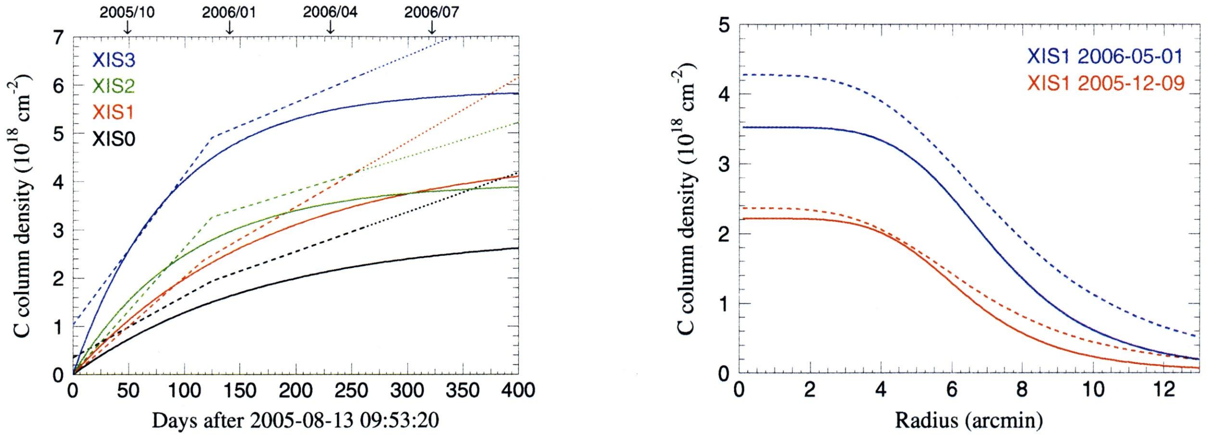

Fig. 3.19: Left: The time history of the contamination of all four XIS detectors, measured at the center of the OBF. The dotted and solid line denoted the models used by CALDB file of 2006-5-24 and 2006-10-24 version, respectively. Right: The radial prole of the contamination of the BI (XIS1).

on XIS, the effect are taken into account with the arfs, and we also check the uncertainty of the arfs by changing the amount of contaminant by 10 ~ 20%.

It is the negligible effects for the central brightness region of the cluster, however it is the severe effects, especially (2) and (3), for the faint region such as the outskirts of the cluster. Especialy the soft X-ray band (below ~1 keV), the effects of (2) and (3) are impotant. Thus, we are careful to analyze the spectra for the decision of the oxygen and magnesium abundance. In addtion, the abundance may vary whether we use a one or multi temperature model.

Chapter 4

Observations and Data Reduction

4.1 Sample selection

In order to obtain a statistically significant sample of clusters suitable for our aims, we based our selection on the Suzaku archival data catalogue. We selected all clusters satisfying the following criteria:
1): Suzaku observed beyond 0.5 r_{200}
2): $0.03 < z < 0.3$
3): Total exposure time > 30 ks
Here, we adopt the definition of the virial radius as

$$r_{200} = 2.77 h_{70}^{-1} (\langle T \rangle / 10\,\mathrm{keV})^{1/2}\,\mathrm{Mpc}/E(z), \tag{4.1}$$

where $E(z) = (\Omega_\mathrm{M}(1+z)^3 + 1 - \Omega_\mathrm{M})^{1/2}$ (Henry et al. 2009). The lower limit of z was chosen in order to ensure a good coverage with Suzaku XIS FOV. The limit in the exposure time is required to ensure a good quality of the X-ray spectrum in the cluster outskirts. We obtained a total of 15 clusters. The source list is summarized in Sec4.2. In this thesis, we employ the solar abundances given by Anders & Grevesse (1989) and Galactic hydrogen column density given by Dickey & Lockman (1990). Unless otherwise stated, the errors correspond to 90% confidence for a single parameter.

4.2 Sample clusters

We selected Suzaku observations of 15 cluster sample where outer regions ($r > 0.5r_{200}$) were observed by XIS. These cluster information and their observations log are listed in tables 4.1 and 4.2, respectively.

At first, we will calculate the virial radius of each cluster from the average gas temperature determined by previous observations, which are summarized in table 4.1. We give (1) ID number, (2) cluster name, (3) redshift, (4) physical scale, (5) angular diameter, (6) β, (7)scale radius r_c, (8) hydrogen column density, (9) average temperature, (10) expected virial radius r_{200}, (11) information of the merging event and (12) references. The ICM temperatures in our sample range from 2 keV to 11 keV. Four clusters show "radio relics", which are located far from the cluster centers and show certain features such as their steep radio spectral indices ($\alpha \sim 1$) and a general filamentary morphology. Hereafter, these are called as radio relic clusters. 8 clusters are merging clusters including the above radio relic clusters. Detailed information on individual clusters is summarized in the later sections.

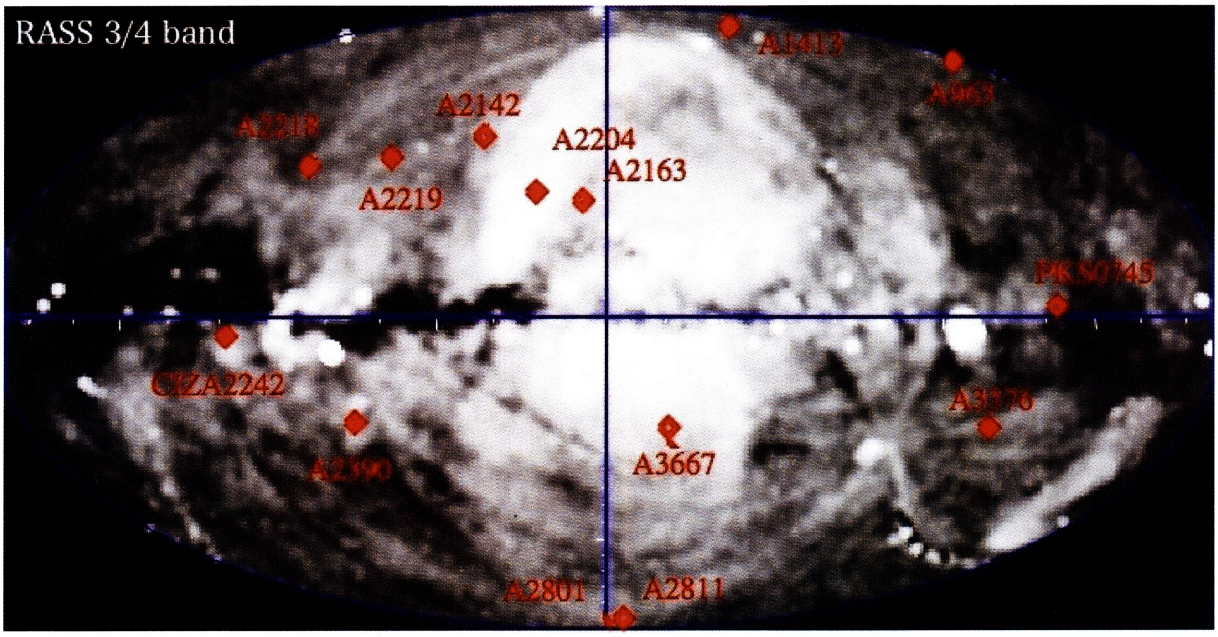

Fig. 4.1: RASS 3/4 band image. Target clusters are shown in red diamonds.

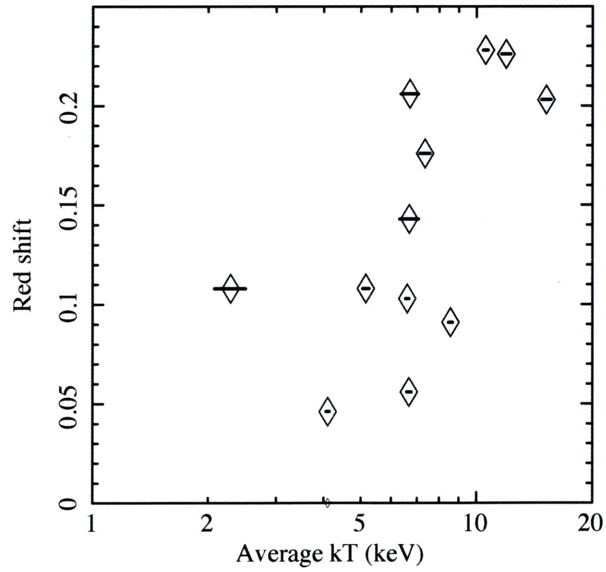

Fig. 4.2: Redshift distribution of our sample clusters.

Table 4.1: Informations of target clusters

ID	Cluster	z	arcmin kpc	D_a Mpc	β	r_c [arcmin]	N_{H} [$10^{20}\mathrm{cm}^{-2}$]	k$< T >$ [keV]	r_{200} [arcmin(Mpc)]	Merger	Ref.
1	A3376	0.046	53.7	179	0.40	2.09	4.58	4.7	34.6 (1.86)	Yes	1
2	A3667	0.056	66.2	213	0.54	2.97	4.46	7.0	34.1 (2.26)	Yes	2
3	A2142	0.091	100.1	337	0.85	4.50	3.78	8.7	24.7 (2.48)	Yes	3
4	PKS0745	0.103	113.4	362	0.52	0.27	41.8	6.5	18.8 (2.13)	No	7
5	A2811	0.108	117.0	402	0.82	1.60	1.54	5.0	14.7 (2.01)	No	4
6	A2801	0.108	117.0	402	0.80	0.88	1.70	2.0	10.2 (1.36)	No	4
7	A1413	0.143	170.3	512	0.51	0.55	1.83	7.3	14.6 (2.16)	No	2
8	A2204	0.152	182.1	539	0.50	0.13	5.67	6.7	11.6 (2.11)	No	7
9	A2218	0.176	210.5	608	0.58	0.93	2.60	7.6	10.5 (2.22)	Yes	6
10	CIZA2242	0.192	227.0	663	–	–	33.41	7.8	10.2 (2.24)	Yes	–
11	A2163	0.203	198.4	681	0.47	1.45	10.8	11.0	10.8 (2.63)	Yes	7
12	A963	0.206	200.6	690	0.50	0.35	1.26	6.8	8.62 (2.12)	No	7
13	A2219	0.226	215.6	741	0.56	0.87	1.75	9.2	8.8 (2.37)	Yes	7
14	A2390	0.228	217.0	745	0.46	0.21	6.21	9.2	8.7 (2.37)	No	7
15	Zwcl2341	0.270	246.6	849	–	–	0.98	4.5	6.55 (1.64)	Yes	–

1:Cavagnolo et al. 2009, 2:Knopp et al. 1996, 3:Henry & Briel 1996, 4:Sato et al. 2010,
5:Pratt et al. 2005, 6:?, 7:Ota & Mitsuda 2003

Table 4.2: Suzaku observation log

Cluster		Obs.ID	(R.A, DEC)	Obs. date	Exposure* (ks)	Exposure† (ks)
A3376	East	100034010	(90.56, -39.94)	2005-10-06	110.4	78.0
	Center	00011010	(90.05, -39.98)	2005-11-07	120.0	99.9
A3667	Center	801096010	(303.13, -56.79)	2006-05-06	20.9	17.9
	Off1	801095010	(302.80, -56.55)	2006-05-06	17.3	11.9
	Off2	801094010	(302.55, -56.35)	2006-05-03	94.3	66.9
	SE	805036010	(303.44, -57.03)	2010-04-12	53.6	45.0
A2142	Center	801055010	(239.54, 27.30)	2007-01-04	51.5	45.2
	Off1	802030010	(239.39, 27.38)	2007-08-04	37.6	26.7
	Off2	802031010	(239.23, 27.55)	2007-09-15	57.6	41.4
	Off3	802032010	(239.04, 27.73)	2007-08-29	23.8	20.4
PKS0745	F1	802062010	(116.88, -19.30)	2007-05-11	32.0	24.8
	F2	802062020	(116.65, -19.22)	2007-05-11	31.2	21.7
	F3	802062030	(116.97, -19.09)	2007-05-12	30.8	22.8
	F4	802062040	(117.11, -19.39)	2007-05-13	32.9	28.1
	F5	802062050	(116.79, -19.52)	2007-05-14	33.4	27.8
A2811	Center	800005010	(10.48, -28.56)	2005-11-28	30.7	25.9
	Off1	800006010	(10.19, -28.74)	2005-11-28	33.9	28.8
A2801		800008010	(9.66, -29.13)	2005-11-27	34.8	28.0
A1413	F1	805059010	(178.85, 23.21)	2010-05-29	40.2	33.0
	F2	805060010	(178.64, 23.41)	2010-05-30	40.9	32.8
	F3	805061010	(179.02, 23.41)	2010-05-31	40.9	33.4
	F4	800001010	(178.83, 23.66)	2005-11-15	108.0	88.5
A2204	F1	805056010	(248.37, 5.45)	2010-09-01	40.7	34.2
	F2	805057010	(248.11, 5.39)	2010-08-27	39.7	32.6
	F3	805058010	(248.32, 5.71)	2010-08-28	36.1	29.5
	F4	801091010	(248.10, 5.63)	2006-09-17	49.0	49.0
A2218		800019010	(249.03, 66.20)	2005-10-26	31.9	30.4
A2163		803071010	(243.82, -6.24)	2008-08-18	135.8	113.2
A963	East	802011010	(154.42, 39.07)	2007-11-23	29.1	21.2
	North	802010010	(154.26, 39.19)	2007-11-24	29.1	25.3
	South	802012010	(154.26, 38.95)	2007-11-28	27.7	24.3
CIZA2218		806001010	(340.74, 53.16)	2011-07-28	122.9	102.1
A2219		804011010	(250.05, 46.72)	2009-04-03	106.4	73.7
A2390		804012010	(328.39, 17.71)	2009-05-04	96.5	89.5

∗:COR2 > 0 GV †:COR2 > 6 GV

4.3 Data reduction

4.3.1 Procedure of analysis

We used HEAsoft ver 6.4.1 and CALDB version 2010-06-21 for all the Suzaku data analysis presented here. We started the event screening from the cleaned event file, We extracted pulse-height spectra in annular regions from the XIS event files. Here, we describe the procedure used for the spectral analysis of each cluster. However, we explain background analysis in the latter chapter.

1. The observation data were screened with ELV > 5 deg and COR2 > 6 GV.
2. From the observed images, we excluded bright point sources to avoid contamination by them using *wavdetect* tool in CIAO package.
3. The spectra were extracted from the annular regions centered on the cluster X-ray peaks.
4. For each annular regions, the Non X-ray background (NXB) model spectrum was created using *xisnxbgen* (Tawa et al. 2008). These NXB spectra were subtracted from the observed spectra which were extracted in step 3.
5. We generated the Redistribution Matrix File (RMF) for the epoch of the cluster observation using the *xisrmfgen* (version 2009-02-28).
6. We analyzed the point source spectra and estimated the flux contamination by all of them in FOV.
7. By assuming the surface brightness profiles, we created simulated cluster images for ARF generations.
8. We generated uniform ARFs for CXB, and the galactic components, and the cluster ARFs for each region by *xissimarfgen* (version 2010-11-05) with 2M photons.
9. We carried out fitting with all the background model components (CXB and the galactic components), for all detectors (FI+BI).

4.3.2 X-ray image

We extracted XIS X-ray images from screened events described above section. The images were extracted in the energy range of 0.5-8.0 keV for all XIS band. We can use the exposure map which was calculated using *xisexpmapgen* in FTOOL. The exposure map contains the effective exposure times of the pixels, which gradually declines toward the periphery. The non X-ray background (NXB) images were estimated from the database of Suzaku night-earth observations using the procedure of Tawa et al. (2008). We accumulated the data for the same detector area and the same distribution of COR2 for each observation, using the FTOOL *xisnxbgen*. The night-earth data cover 150 days before and after the period of each observation. To increase the signal-to-noise ratio by keeping the NXB count rate low, we selected durations in which COR2 was > 6 or 8 GV. Finally, we subtracted the NXB image from observed exposure corrected image. The images were smoothed by a Gaussian filter with a 2-dimensional gaussian with σ = 16 pixel =17″. For example, figure 4.3 shows the raw observed image, exposure map, NXB image and NXB subtracted and exposure corrected images of CIZA2242, respectively.

(a) Raw oserved image (b) Exposure map

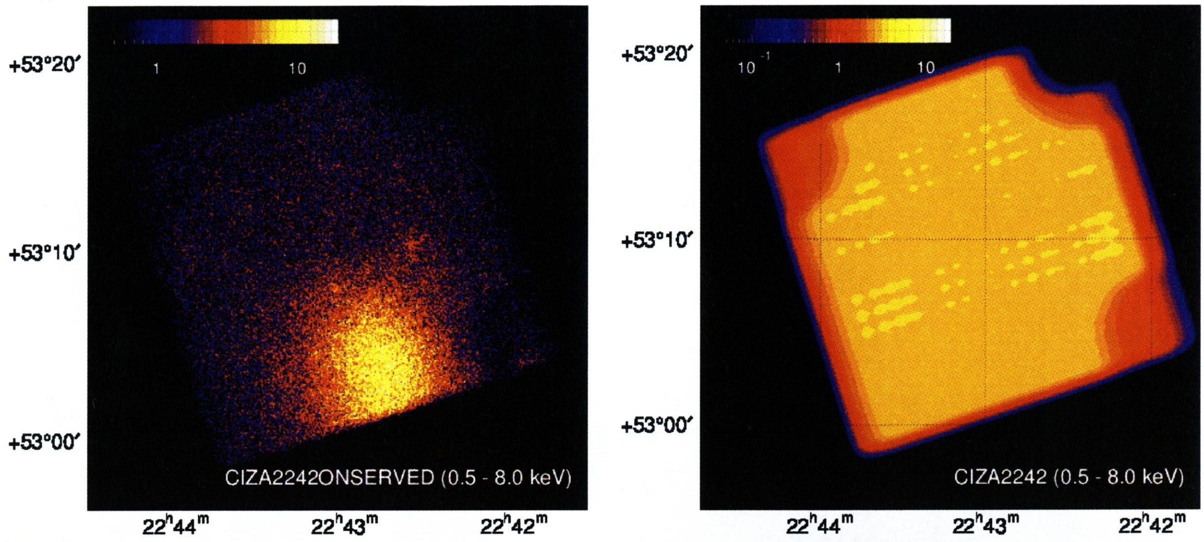

(c) NXB image (d) NXB subtracted exposure corrected image

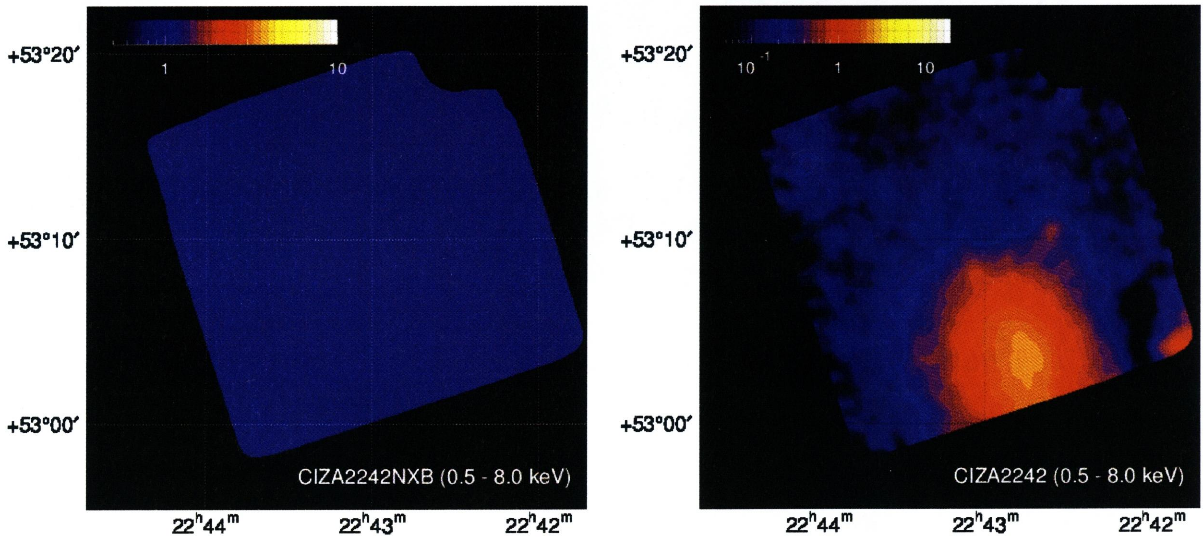

Fig. 4.3: (a)Raw observed image for the CIZA2242 cluster observation. Calibration sources are masked and the data of XIS 0,1, 3 are combined. (b)Exposure map images for the CIZA2242. These images were casted onto the sky, at the position of CIZA2242. (c)NXB image in 0.5-8.0 keV band. (d) NXB subtracted Suzaku FI+BI image in 0.5-8.0 keV band smoothed by a 2-dimensional gaussian with σ = 16 pixel =17″ . The image is corrected for the exposure time but not for the vignetting.

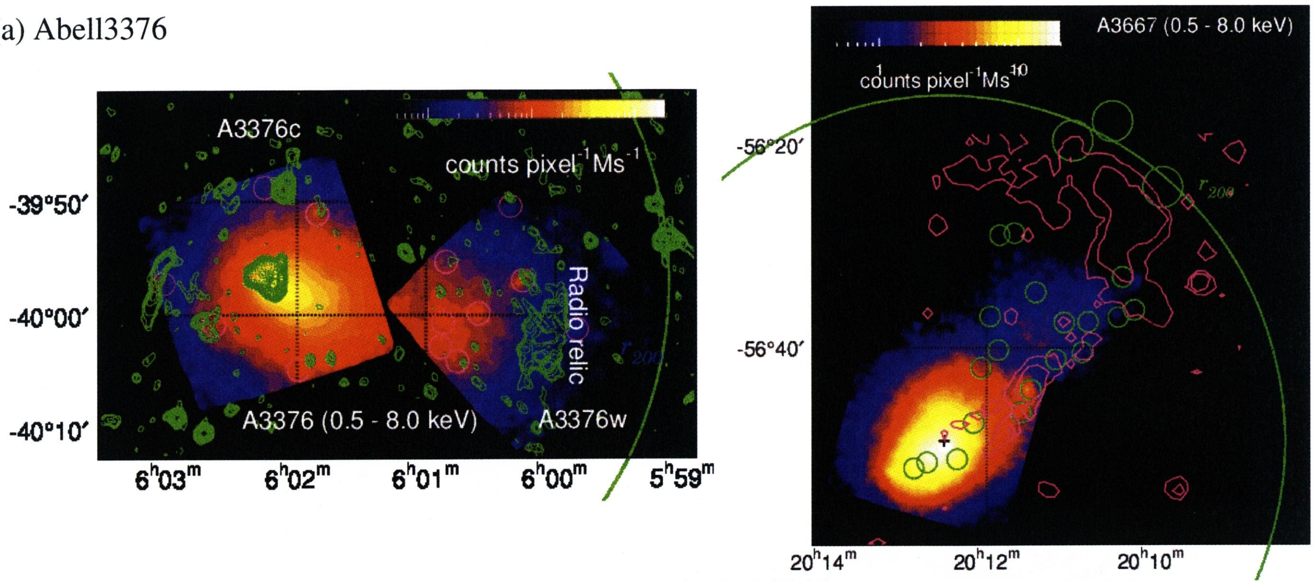

(a) Abell3376

(b) Abell3667

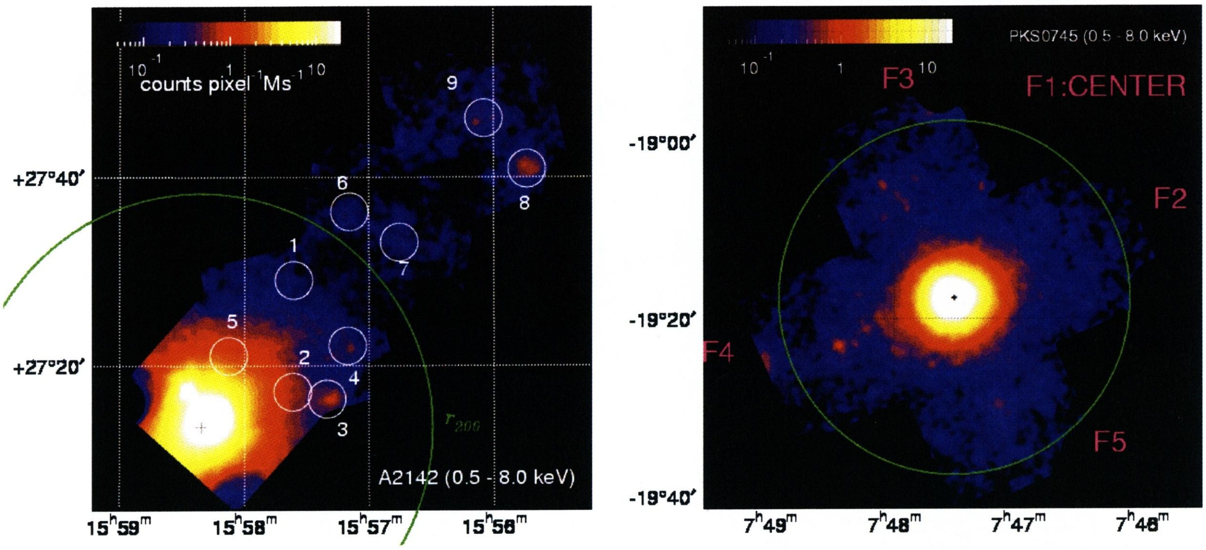

(c) Abell2142

(d) PKS0745

Fig. 4.4: NXB subtracted Suzaku FI+BI image of the smaple clusters in 0.5-8.0 keV band smoothed by a 2-dimensional gaussian with σ = 16 pixel =17″ . The images are corrected for exposure time but not for vignetting. Large green circle shows the virial radius of each cluster.

(e) Abell2801

(f) Abell2811

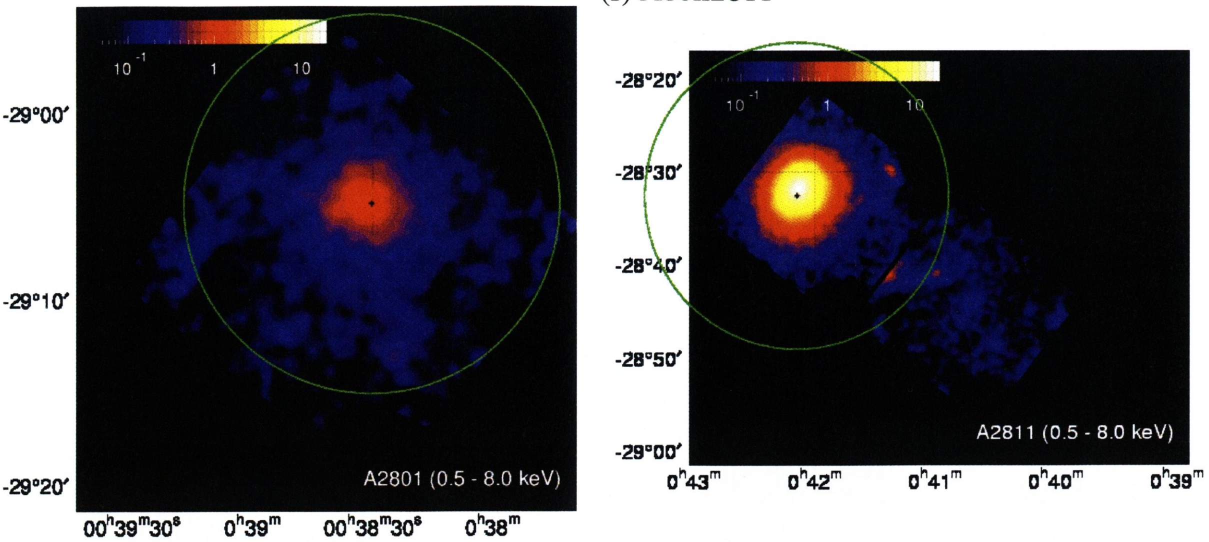

(g) Abell1413

(h) Abell2204

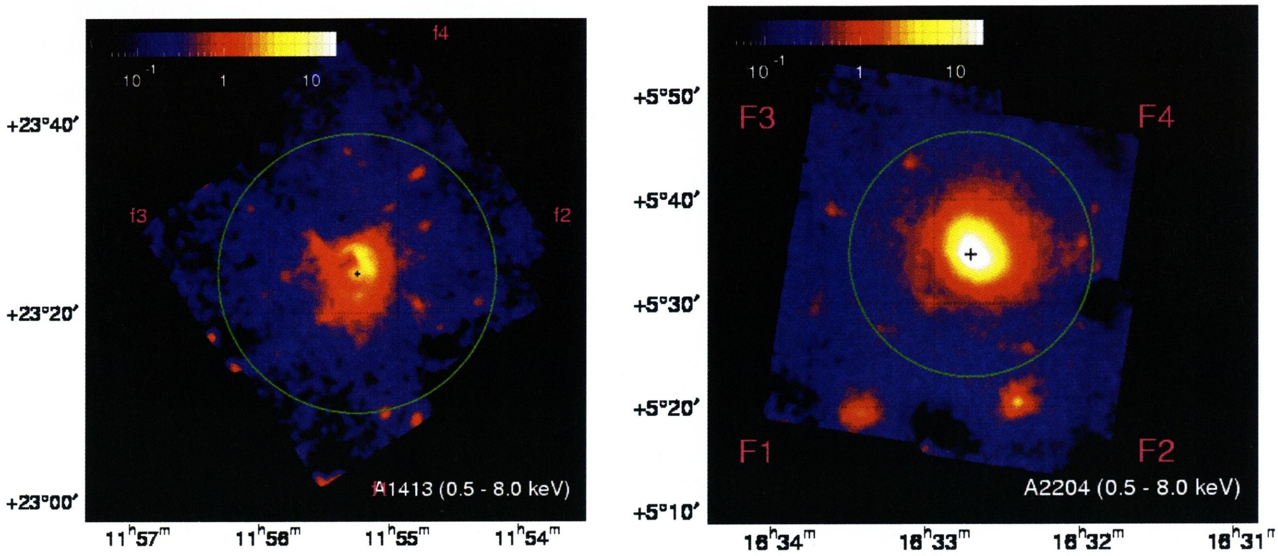

Fig. 4.5: Continued.

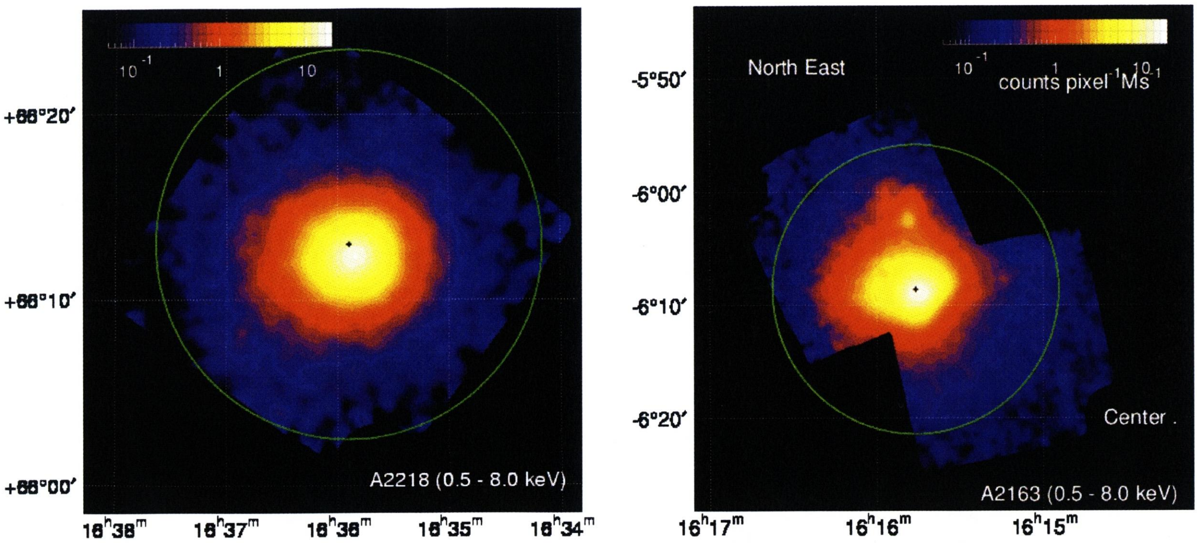

(a) A2218 (b) A2163

(c) A963 (d) A2219

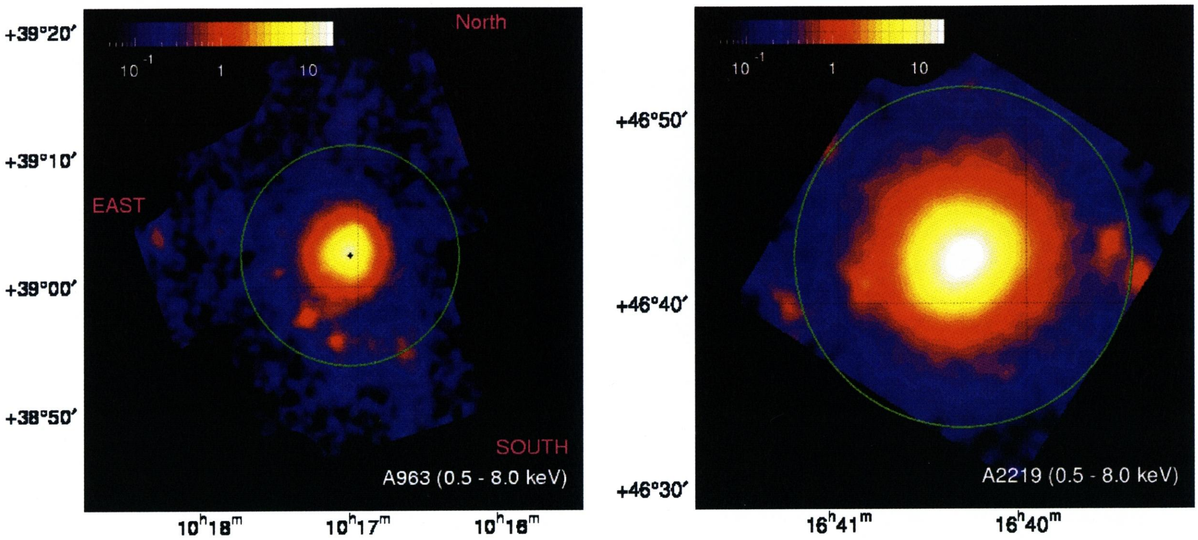

Fig. 4.6: Continued.

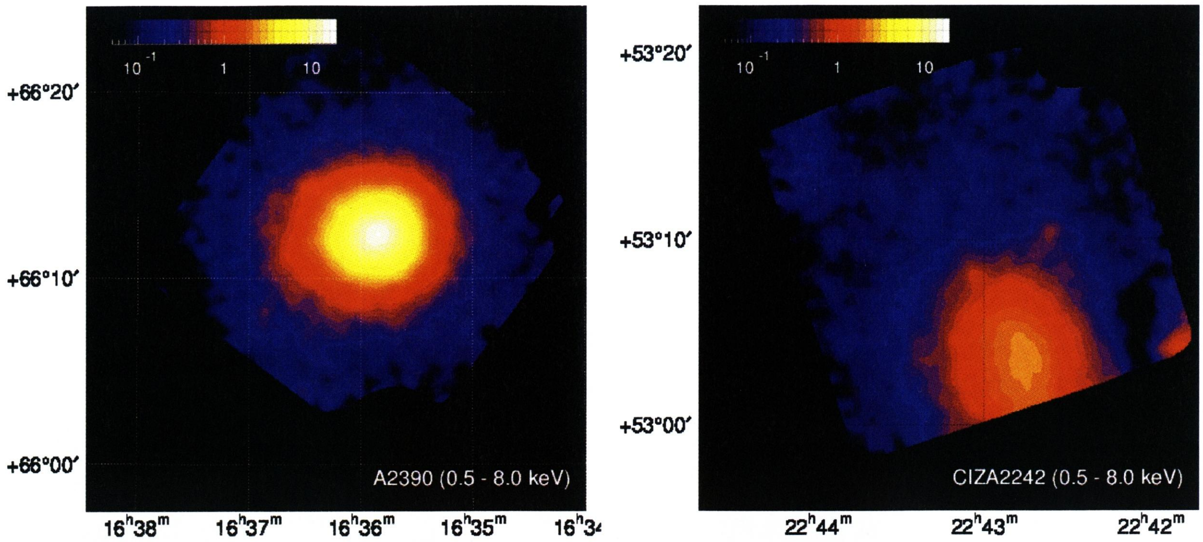

(a) A2390

(b) CIZA2241

(c) Zwcl2341

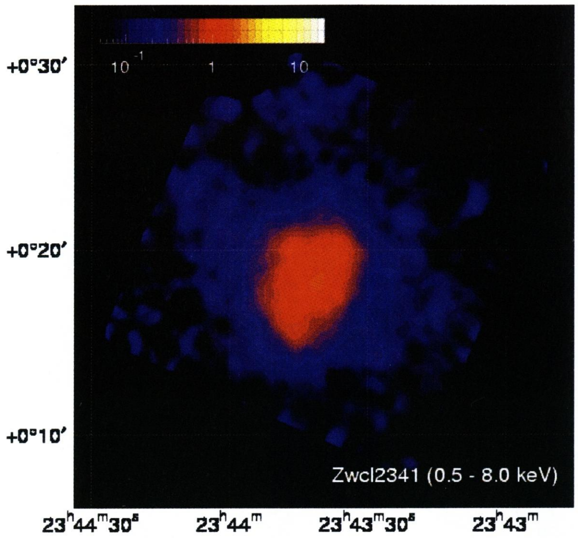

Fig. 4.7: Continued.

4.3.3 Point source elimination

Since we are interested in the nature of the ICM in cluster outskirts, we should remove the point sources (background or foreground AGN, binary sources, and galaxies) from the images. To exclude the point source contamination, we use *wavdetect* tool in CIAO package version 4.3.0[1] to identify the point-like sources. We adopt the value of the *sigthresh* parameter as 5×10^{-6} in *wavdetect*, which is the significance threshold for the source detection. This command operates on the input in two stages. First it detects possible source pixels in a dataset by repeatedly correlating it with " Mexican Hat " wavelet functions with different scale sizes. Pixels with sufficiently large positive correlation values are removed from the image as assumed sources, and subsequent correlations are performed at the same scale. The second stage generates a source list from information from the first stage at each wavelet scale.

The typical lowest detected 2–10 keV flux of these sources was $S_c = 5 \times 10^{-14}$ erg cm^{-2} s^{-1}. Since this flux limit is lower than the level of $S_c = 2 \times 10^{-13}$ erg cm^{-2} s^{-1} by Kushino et al. (2002), we basically adopted the CXB intensity as 5.97×10^{-8} erg cm^{-2} s^{-1}sr^{-1} after these point source were subtracted. For instance, we show the results of point source analysis of our method as below. Table 4.3 is taken from the previous published paper (Akamatsu et al. 2011a).

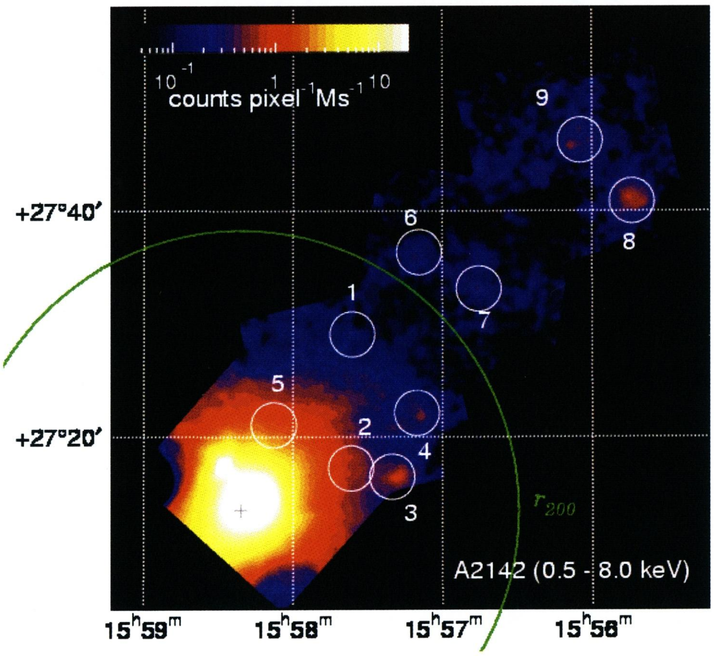

Fig. 4.8: NXB subtracted Suzaku FI+BI image in 0.5-8.0 keV band smoothed by a 2-dimensional gaussian with σ = 16 pixel =17″ . The image is corrected for the exposure time but not for the vignetting. Large green circle show the virial radius of the cluster. Small white circles show the detected point sources.

---

[1] http://cxc.harvard.edu/ciao/

Table 4.3: Informations of point source in two XMM and Suzaku observations of A2142 center, OFFSET1, OFFSET2 OFFSET3.

		XMM-Newton(MOS1+MOS2)			Suzaku		
No.*	(α, δ) †	Photon Index	Flux‡	χ^2/d.o.f	Photon Index	Flux‡	χ^2/d.o.f
1	(239.401, 27.485)	$1.44^{+0.22}_{-0.21}$	$1.28^{+0.72}_{-0.34}$	108.9/ 63	$1.96^{+0.29}_{-0.23}$	$1.02^{+0.37}_{-0.30}$	53.0 / 52
2	(239.393, 27.287)	$1.42^{+0.63}_{-0.68}$	$0.31^{+0.56}_{-0.31}$	35.6 / 23	$1.69^{+0.14}_{-0.14}$	$1.40^{+0.52}_{-0.48}$	59.0 / 53
3	(239.334, 27.275)	$2.21^{+0.64}_{-0.50}$	$1.27^{+0.46}_{-0.18}$	34.0 / 31	$2.08^{+0.15}_{-0.13}$	$1.88^{+0.46}_{-0.42}$	75.0 / 53
4	(239.283, 27.366)	—	—	— / —	$1.64^{+0.23}_{-0.18}$	$2.32^{+0.59}_{-0.59}$	74.0 / 52
5	(239.532, 27.351)	—	—	— / —	$0.94^{+0.54}_{-0.74}$	$2.28^{+6.51}_{-1.79}$	58.0 / 51
6	(239.295, 27.605)	—	—	— / —	$1.89^{+0.19}_{-0.18}$	$0.89^{+0.19}_{-0.18}$	70.0 / 54
8	(238.922, 27.686)	—	—	— / —	$1.93^{+0.10}_{-0.10}$	$3.23^{+0.41}_{-0.39}$	60.0 / 54
9	(239.012, 27.773)	—	—	— / —	$1.63^{+0.15}_{-0.14}$	$1.65^{+0.28}_{-0.26}$	52.0 / 54

∗:Serial number for point source. †:Position of the point source.

‡:The 2.0–10.0 keV flux in units of 10^{-13} erg cm^{-2} s^{-1}

4.4 Individual cluster properties

4.4.1 Abell 3376: Akamatsu et al. 2011b

A3376 (z = 0.046) is considered to be experiencing a binary subcluster merger. Previous BeppoSAX/PDS observation reported 2.7 σ detection of hard X-ray signal (Nevalainen et al. 2004). However, Suzaku HXD observation gave an upper limit, which did not exclude the BeppoSAX flux (Kawano et al. 2009). The detection of the hard X-ray signal was still controversial. The striking feature of A3376 is a pair of Mpc-scale radio relics. Previous studies showed the global mean temperature to be 4.0 keV and the existence of a pair of Mpc-scale radio relics revealed by 1.4 GHz VLA NVSS observations (Bagchi et al. 2006).
Suzaku carried out two pointing observations of Abell 3376 along the merger axis in October and November 2005, designated as A 3376c, A 3376w for the center and the west relics.

4.4.2 Abell 3667: Akamatsu et al. 2011c

Abell 3667 (z = 0.0556) is a very bright merging cluster with irregular morphology and an average temperature of 7.0 ± 0.5 keV (Knopp et al. 1996). Briel et al. (2004) studied the ICM characteristics in the cluster central region and showed that the ICM emission was elongated to the northwest direction. The most striking feature of A3667 is a discontinuity in the X-ray surface brightness, namely a “cold front”, which was found with Chandra (Vikhlinin et al. 2001). Another features of A3667 are the two extended, symmetrically located regions of diffuse radio emission revealed with the 843 MHz ATCA observatory (Australia Telescope Compact Array: Rötttgering et al. 1997). From Suzaku XIS/HXD observations of A3667, Nakazawa et al. (2009) measured the cluster emission up to 40′ and set upper limits on the non-thermal X-ray emission in the XIS spectra to be 7.3×10^{-13} erg cm^{-2} s^{-1} when extrapolated to 10-40 keV. Nakazawa et al. (2009) also observed very high temperature components ($kT \sim$ 14 keV) in the cluster center. Since their main interest was to look into the non-thermal phenomenon, the global ICM properties in the cluster outskirts remain to be further explored. The presence of these structures naturally indicates that A3667 is a merging system and the subcluster infall seems to be occurring along the northwest–southeast direction. Actually, the overall cluster emission is elongated in this direction. Suzaku performed 3 pointing observations of Abell 3667 along the northwest merger axis in May 2006. Figure 4.4(b) show the NXB subtracted X-ray image of A3667 with the SUMMS 842 MHz radio contours.

4.4.3 Abell 2142: Akamatsu et al. 2011a

A 2142 (z = 0.0909) is a bright cluster of galaxies, having a high ICM temperature of $kT \approx$ 9 keV. This object is also known as the first cluster in which the cold fronts have been detected (?). The cold fronts in the south and the northwest are $0\overset{\prime}{.}7$ (or 70 kpc) and $2\overset{\prime}{.}7$ (or 270 kpc) off of the cluster center, respectively, and a sharp surface-brightness drop by a factor of about 2 is seen. Since the temperature and density distributions suggest that the pressure is constant across the cold front, it is considered as a contact discontinuity. The presence of these structures naturally indicates that A2142 is a merger and the subcluster infall seems to be occurring along the northwest–southeast direction. The overall cluster emission is also elongated in this direction. This is likely to coincide with the large-scale structure, and the matter density seems to be enhanced along the filament. A2142 is also suitable for the search of redshifted emission lines from the WHIM. Given the cluster redshift of ~ 0.1, the OVII line (the rest-frame energy of 0.65 keV) is shifted to 0.57 keV and then falls into a gap between the Galactic OVII line energy and the instrumental line features. Therefore, it makes it possible to distinguish the WHIM emission from the local one. In addition, because the redshift of A2142 is not too high, the oxygen line from the WHIM can be measured with good sensitivity. With these purposes, we have carried out Suzaku observations of the northwest offset regions of A2142.

Suzaku performed four pointing observations in 2007 with the XIS instrument around Abell 2142. The central pointing observation was performed in June, and the other three in September to October. The cold front feature indicates that there is an ongoing merger in the north-west to south-east direction. This suggests that matter would be falling in along this merger axis, possibly from a large-scale filament. We allocated the observed regions to be successively offset towards the north-west direction. The regions are designated as Center, Offset1, Offset2, and Offset3 with the exposure times 51.4 ks, 37 ks, 58 ks, and 24 ks, respectively. The observation log is shown in table 4.2. The outermost observation reaches twice the virial radius ($49'.2 \sim 4.92$ Mpc) from the cluster center, in which we planned to search for emission from the warm-hot intergalactic medium (WHIM).

4.4.4 PKS0745-191

PKS0745-191 ($z = 0.103$) is a X-ray bright relaxed and cool core cluster. Previous X-ray measurements show the average ICM temperature in the energy range 6-8 keV depending on the spectral modeling. In the central region, there are still arguments about the discrepancy of mass estimation between X-ray and weak lensing studies (Chen et al. 2003). Suzaku observed PKS0745 from 2007 May 11 to 14 in five separate fields for roughly 32 ks each. George et al. (2008) already reported the results of Suzaku observations. They detected ICM emission beyond the virial radius and showed the flatness in the entropy profile. However, recent result from the analysis of the ROSAT archival data (Eckert et al. 2011a) indicated that the ROSAT surface-brightness profile was statistically inconsistent (7.7σ significance) with the Suzaku result around and beyond r_{200}. They conclude that the difference in the surface brightness between ROSAT and Suzaku data is most likely explained by the existence of additional foreground components at the low Galactic latitude of the source, which were not taken into account in the Suzaku background modeling.

4.4.5 Abell 2811 & Abell 2801

A2811 & A2801 ($z = 0.108$) belong to Sculptor supercluster, which contains 23 clusters. It is located near the south galactic pole. The Sculptor supercluster has been observed with

ROSAT and ASCA (Obayashi et al. 1998). Suzaku carried out four pointing observations of A2801, A2804 and A2811 in the Sculptor supercluster to investigate the Warm Hot Intragalactic Medium (WHIM) emission. Sato et al. (2010) already reported the analysis results of Suzaku observations. We re-analyzed A2801 and A2811 data by focusing on the ICM properties.

The XIS images are shown in Figure 4.6(e)(f). Since those clusters are adjacent with each other, we adopt the same background components (table 5.1) in the spectral analysis. We extract the spectrum from $0'.0$, $2'.0$,$4'.0$, $7'.0$ and $10'.0$ centered on $(00^{h}38^{m}30^{s}.31, -29^{\circ}04^{m}52^{s})$ $0'.0$, $2'.0$,$4'.0$, $7'.0$ and $10'.0$ centered on $(00^{h}38^{m}30^{s}.31, -29^{\circ}04^{m}52^{s})$ for A2811 and A2801, respectively.

4.4.6 Abell 1413

A1413 (z = 0.142) is a well known relaxed cluster with the average temperature $k\langle T\rangle$=7 keV (Pratt et al. 2005). Previous X-ray studies by Pratt et al. (2005) and Vikhlinin et al. (2005) revealed the evidence of a cooling core. Pratt et al. (2005) reported ICM temperature profile of A1413 showed gradual decrease from 7 keV to 4 keV and the temperature profile was well described by a polytropic model with $\gamma = 1.07 \pm 0.01$. Recently, Hoshino et al. (2010) confirmed those results with the Suzaku observation in the north direction and found the entropy profile to show a slight deviation from the prediction of numerical simulations (Tozzi & Norman 2001; Voit et al. 2003). They discussed the origin of the deviation and proposed the possibility of difference between electron and ion temperatures in the cluster outskirt.

4.4.7 Abell 2204

A2204 (z = 0.152) is a typical X-ray bright and regular morphology cluster (Buote & Tsai 1996). In the past Chandra and XMM-newton era, A2204 was considered as having a strong cooling flow which means A2204 has a highly peaked soft X-ray surface brightness profile. Recent studies by Chandra (Sanders et al. 2005; Sanders et al. 2009) reveal the core of the cluster has a complex morphological structure, made up of a high-density core ($n_e \sim 0.2$ cm^{-3}) with flat surface brightness. More recently, Reiprich et al. (2009) detected ICM emission up to the virial radius in the northwest direction using Suzaku observation.

4.4.8 Abell 2218

A2218 (z=0.176) is well known for weak and strong lensing cluster. A2218 shows a remarkable discrepancy between mass estimates derived from the X-ray and the strong lensing analyses (Miralda-Escude & Babul 1995). Previous X-ray studies (ROSAT, Chandra:Neumann Bohringer 1999; Machacek et al. 2002) suggested complicated X-ray structure near the core. Recently, XMM-Newton derived gas density and temperature profiles out to a large radius (Pratt et al. 2005). Another feature of A2218 is the report of a merger event within the line-of-sight. Suzaku observed A2218 twice during the SWG term to investigate the WHIM emission, for which the results are already reported by Takei et al. (2007). Since their main science was WHIM search, they did not derive the radial profiles of the ICM properties.

4.4.9 Abell 2163

A2163 (z=0.203) is the hottest and X-ray luminous cluster in our sample (kT=15 keV). It possesses a giant bright radio halo. Previous X-ray and weak lensing studies show a signature of merger event in the cluster (Squires et al. 1997). Using ASCA data, Markevitch & Vikhlinin (2001) show the average ICM temperature of A2163 is $\mathrm{k}\langle T\rangle = 12.3^{+1.3}_{-1.1}$ keV and temperature profile drop from 12 keV to 5 keV. Recent XMM-Newton and Chandra observations (Bourdin et al. 2011) reveal that A2163 has an E-W elongated morphology and a substructure located in northern region namely A2163B. From those observations, A2163 is considered as early stage of major merger. Another feature of A2163 is its high ICM temperature, which can be used as cosmological probes.

4.4.10 Abell 963

A963 (z = 0.206) has two blue arcs associated with the cD galaxy (Lavery & Henry 1988). A963 shows an elliptical and relaxed morphology with some possible very small-scale structure in the core. A963 became known by the discrepancy between X-ray and weak lensing mass estimations within the central region (Metcalfe et al. 2003; Shan et al. 2010).

4.4.11 Abell 2219

A2219 (z = 0.22) is an X-ray luminous cluster (Allen et al. 1992) and shows elliptical and elongated morphology in the northwest-southeast direction. A2219 has a bright optical arc and shows significant difference between weak-lensing and X-ray mass estimations (Smail et al. 1995). More recently, Bezecourt et al. (2000) report that strong and weak lensing observations are combined to give a consistent mass model of the cluster over the radius range 100 h_{50}^{-1} kpc to 1.5h_{50}^{-1} Mpc. The resultant mass within 1Mpc is 8.3×10^{14} $\mathrm{M}_{\odot}$.

4.4.12 Abell 2390

A2390 (z = 0.228) has the best lensing data of all regular, relaxed clusters of galaxies, in addition to exceptionally high quality optical-dynamical data. Previous X-ray studies show average ICM temperature in the range 9 to 12 keV and show an agreement between the mass determined from the X-ray data and the mass determined from the models for the gravitational arc and the weak lensing results (Boehringer et al. 1998). The resultant X-ray mass reaches $1.9^{+1.1}_{-0.8} \times 10^{15}\mathrm{M}_{\odot}$ at 1.79 Mpc.

4.4.13 CIZA2242: Akamatsu & Kawahara 2011

CIZA2242 was discovered in the Clusters in the Zone of Avoidance (CIZA) survey (Kocevski et al. 2007). van Weeren et al. (2010) reported a Mpc scale radio relic located in the northern outskirts, at a distance of 1.2 Mpc from the cluster center. The radio relic is extremely narrow with a width of 55 kpc. The spectral index at the front of relic is -0.6 ± 0.05, which correspond to the Mach number $\mathcal{M} = 4.5^{+1.3}_{-0.9}$. While this shock wave is the strongest than the other shocks, X-ray data are only available by ROSAT observations so far. The 120 ksec observation of CIZA2242 by SUZAKU was performed in 2011/7/28 with an additional 60 ksec offset observation.

4.4.14 Zwcl2341N & Zwcl2341S

Zwcl2341 (z = 0.270) has two Mpc-scale structures of diffuse radio emission, which were discovered in 1.4 GHz New VLA All the Sky Survey (NVSS) (Bagchi et al. 2002) at the north (~1100 kpc, Zwcl2341N) and south (~1100 kpc Zwcl2341S*sim*) of the clusters. Recently, GMRT observation revealed that those radio emissions exhibited "arc"-like shapes (van Weeren et al. 2009). The spectal indices of the relics are -0.49±0.18 for Zwcl2341N and -0.76±0.17 for Zwcl2341S corresponding to the Mach number $\mathcal{M} > 3.57$ and 2.95 ± 1.39, respectively. Previous Chandra and XMM-Newton observations (van Weeren et al. 2009) show that X-ray emission extends over ~ 3.3 Mpc in the north-south direction. Due to its low X-ray brightness, the X-ray information around the radio relics is still limited.

4.5 Radio relic clusters

The formation theory of galaxy clusters and groups is now well established: the high density peaks that exist within the primordial matter latter grow in time to groups and clusters by both accretions of surrounding matters and mergers of clumps. In growth history of haloes, major mergers have a significant effect on the internal structure of clusters. X-ray observation have revealed a lot of merging phenomena of haloes from massive clusters scale (e.g. Markevich et al. 2002) to galaxy groups (e.g. Kawahara et al. 2011) mainly by X-ray morphology. The shock structure by the merger was clearly found in the Bullet cluster using *Chandra* (Markevich et al. 2002). In general, however, an identification of the shock structure in X-ray images is difficult, except in incredible merger clusters including 1E0657-56, A520, and A2146 (Clowe et al. 2006; Markevitch et al. 2005; Russell et al. 2010). Recent progress in radio astronomy has revealed interesting arc structures in merging clusters, namely the radio relic (Ferrari et al. 2008). The radio relic is believed as a tracer of the shock structure by the syncrotron radiation. Finoguenov et al. (2010) performed X-ray observation by XMM-Newton of the one of the radio relic clusters, Abell 3667 and found a sharp temperature decrement across the radio relic. Akamatsu et al. (2011b) confirmed their results by Suzaku satellite.

Here we present a systematic X-ray analysis of 6 radio relics of 4 clusters observed by Suzaku, including a new observation of a strong radio relic cluster, CIZA 2242.8-5301 (hereafter CIZA 2242), recently discovered by the Giant Metrewave Radio Telescope (GMRT) observation (Swarup 1991), new analysis of archival data of Zwcl 2341.1-0000 (hereafter Zwcl2341) and Abell3667SE , and compilation of previous results of Abell3667NE (Akamatsu et al. 2011b) and Abell3376 (Akamatsu et al. 2011c).

Table 4.4: Basic properties of the radio relic clusters

	redshift	physical length for 1′ (kpc)	Temperature (keV)	N_H (10^{20} cm^{-2})	Radio references	
CIZA2242	0.192	190	8.4	33.4	van Weeren et al. 2010	
Abell3376	0.046	54	4.2	5.8	Bagchi et al. 2006	$*$
Abell3667NW	0.056	66	6.0	4.7	Rötttgering et al. 1997	†
Abell3667SE	0.056	66	6.0	4.7	Rötttgering et al. 1997	
Zwcl2341N	0.270	246	5.7	3.4	van Weeren et al. 2009	
Zwcl2341S	0.270	246	5.7	3.4	van Weeren et al. 2009	

$*$:Akamatsu et al. 2011c

†:Akamatsu et al. 2011b

(a)CIZA2242 (van Weeren et al. 2010)

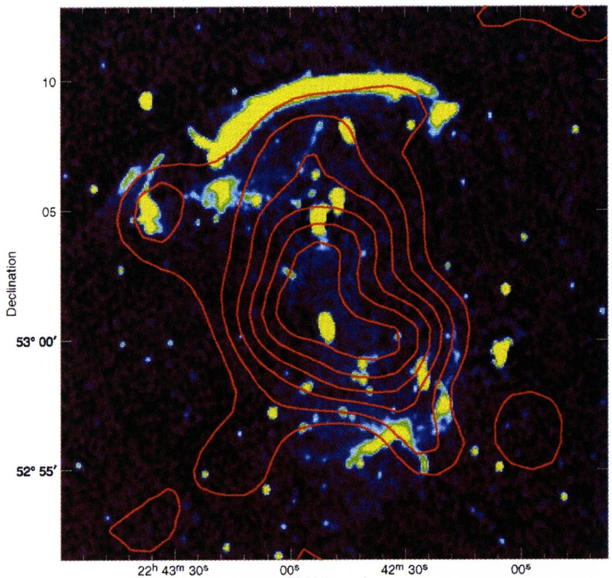

(b)Abell3376(Bagchi et al. 2006)

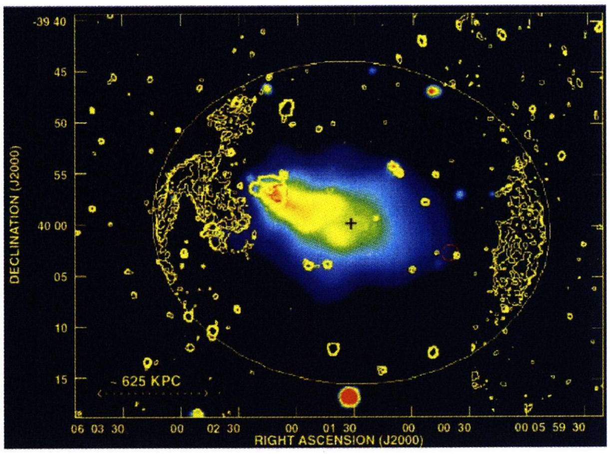

(c)Abell3667(Rötttgering et al. 1997)

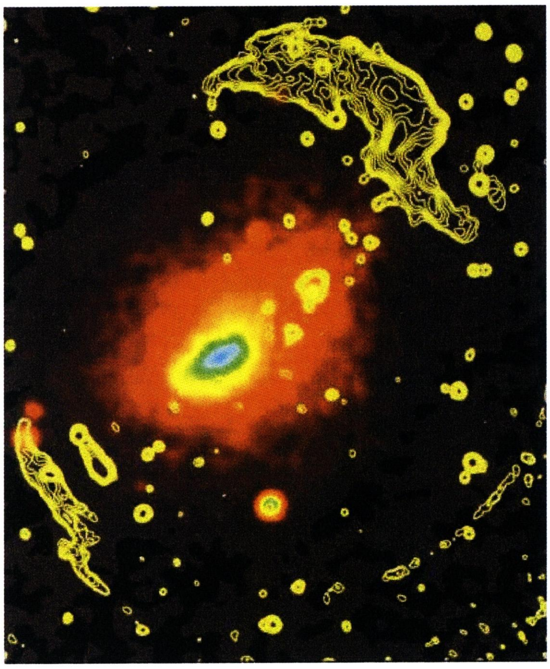

(d)Zwcl2341(van Weeren et al. 2009)

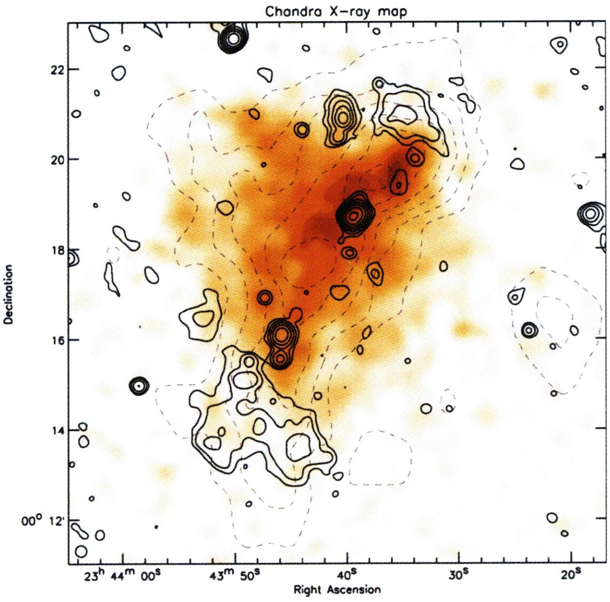

Fig. 4.9: X-ray images of (a)CIZA2242, (b)A3376, (c)A3667 and (d)Zwcl2341 in the energy band 0.5-8.0 keV, after subtraction of the NXB without vignetting correction and after smoothing by a 2-dimensional Gaussian with σ = 16 pixel =17″.

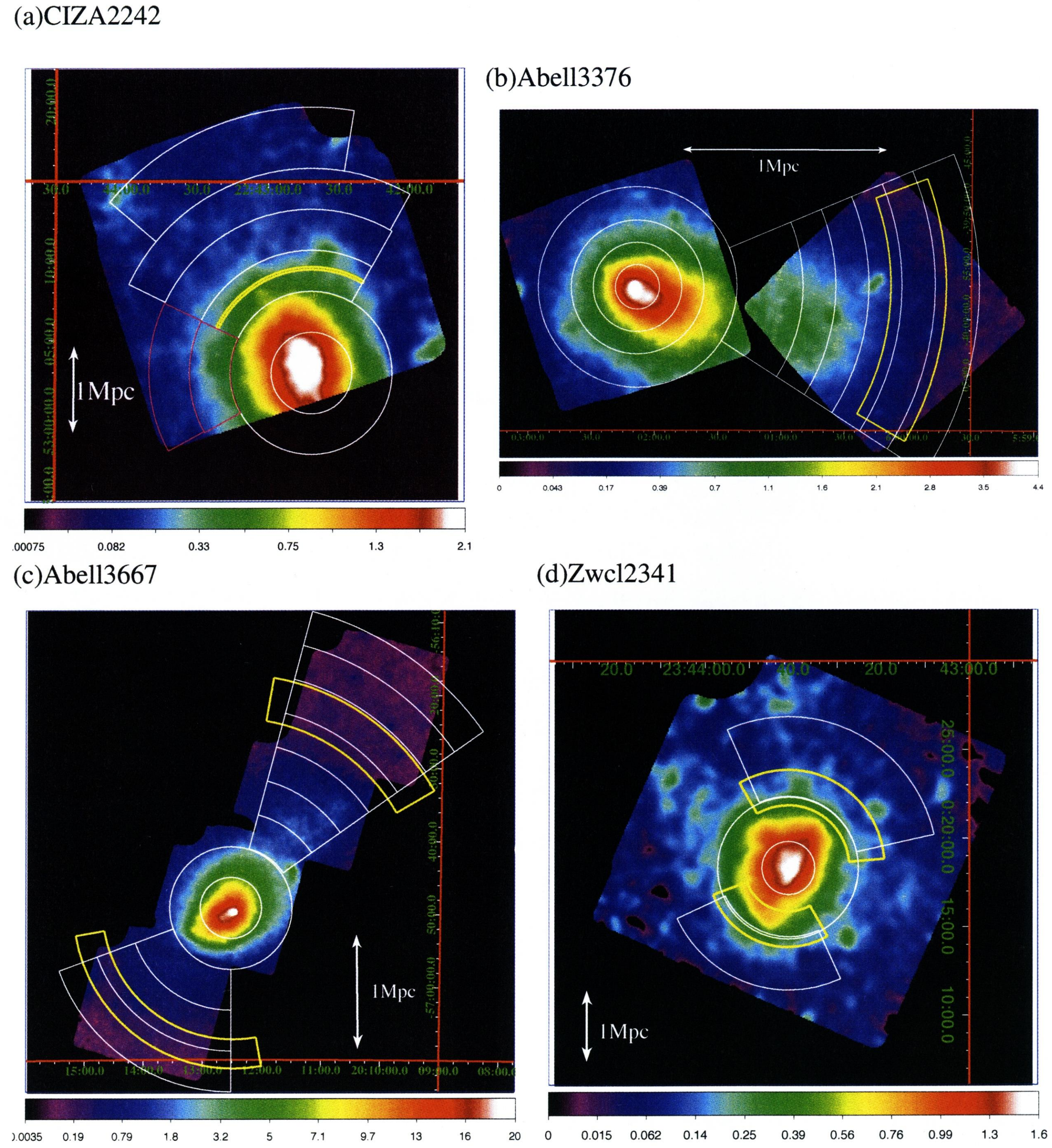

Fig. 4.10: X-ray images of (a)CIZA2242, (b)A3376, (c)A3667 and (d)Zwcl2341 in the energy band 0.5-8.0 keV, after subtraction of the NXB without vignetting correction and after smoothing by a 2-dimensional Gaussian with σ = 16 pixel =17″. White and Yellow annuli indicate the spectral analysis regions and the radio relic region. Magenta annuli in panel (a) is used for the analysis of the region perpendicular to the merger axis.

Chapter 5

Spectral analysis

Based on the X-ray images in the 0.5-8 keV band for the FI & BI sensors, we accumulated the pulse-hight spectra from circular regions centered at the peak. To avoid contamination from adjacent regions, we set the minimum width of annular to $2'$. We then subtracted NXB background spectra that were obtained from the database of Suzaku night-earth observations using the procedure by Tawa et al. (2008). The instrument response can be split up into two parts : a Redistribution Matrix File (RMF), which specifies the channel probability distribution for a photon of given energy, and an Ancillary Response File (ARF) which specifies the spatial distribution of the telescope effective area and window absorption. In this chapter, we will show the details of the spectral analysis such as preparations of detector response (RMF), effective area (ARF), NXB estimations and background estimations.

5.1 Spatial and spectral responses

We need to prepare the spatial and spectral responses which are necessary for reducing and analyzing our observation of data. These responses have complicated properties for extended sources. Indeed they depend on the surface brightness distribution of the source and so are unique for each annular region. Monte Carlo simulators are used to generate some of the responses. The X-ray telescope + XIS simulator is called *xissim*, and the ARF generator using the simulator is called *xissimarfgen* (Ishisaki et al. 2007). We used version 2010-11-05 of the simulator. A surface brightness distribution is necessary for *xissim* and *xissimarfgen*, because the point spread function (PSF) of the XRT produces an efficiency that is correlated among adjacent spatial cells. As an example, the resultant ARF image and those effective area distribution of A2142 0.2-0.3 r_{200} region are shown in figure 5.1.

5.2 Background estimations

Accurate estimation of the background is particularly important when constraining the ICM surface brightness and temperature in the outer region of clusters. We assumed that the background is comprised of three components: non-X-ray background (NXB), cosmic X-ray background

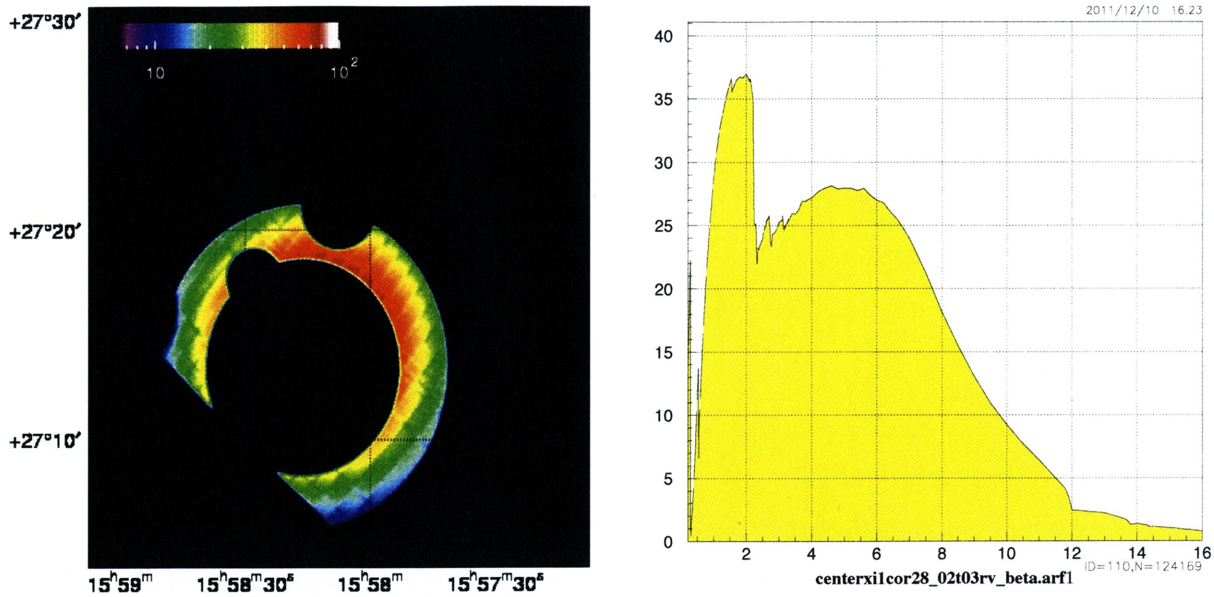

Fig. 5.1: Left: The resultant ARF image of A2142 0.2-0.3 r_{200} region generated by *xissimarfgen*. Right: The energy dependence of the effective area.

(CXB) and Galactic emission (GAL), which itself is comprised of two components. In this section we describe how we estimate all these background components.

5.2.1 Non X-ray background

The non X-ray background (NXB) spectra were estimated from the database of Suzaku night-earth observations using the procedure of Tawa et al. (2008). We accumulated the data for the same detector area and the same distribution of COR2 for each observation, using an FTOOL *xisnxbgen*. The night-earth data cover 150 days before and after the period of each observation. To increase the signal-to-noise ratio by keeping the NXB count rate low, we selected durations in which COR2 is > 6 GV. Figure 5.3 shows the background level for the Suzaku BI, FI sensors, for the A2142 observations. Black and gray crosses show the observed spectrum after the NXB subtraction and the estimated NXB spectrum, respectively. Black curve shows CXB level.

5.2.2 Galactic components

To estimate the Galactic emission, we examined the spectra from the outermost region or nearby Suzaku observations, which showed negligible ICM contribution. We employed ancillary response files (ARFs) for a spatially uniform source filling the FOV. A power-law is used to model the CXB in both spectra. The Galactic emission is represented as a two-temperature model consisting of an unabsorbed ~0.1 keV plasma (LHB; representing the local hot bubble and the solar wind charge exchange) and an absorbed ~0.3 keV plasma (MWH; representing the Milky Way halo): $apec_1 + wabs \times (apec_2 + powerlaw)$. The redshift and abundance of both the *apec* components were fixed at 0 and unity, respectively.

The best-fit parameters for each target are summarized in table 5.1. The temperatures and

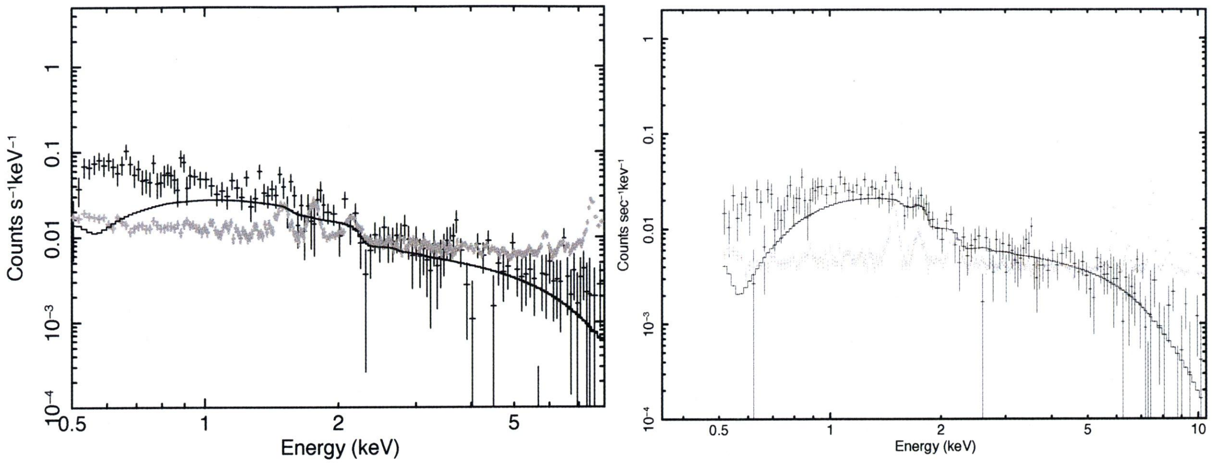

Fig. 5.2: NXB-subtracted XIS BI(left) and FI(right) spectra (Black cross) of Offset3, plotted with estimated CXB (black curve) and NXB (gray crosses) spectra described in Sec 5.2, Sec 5.2.1, respectively.

intensities are consistent with the typical Galactic emission (Yoshino et al. 2009).

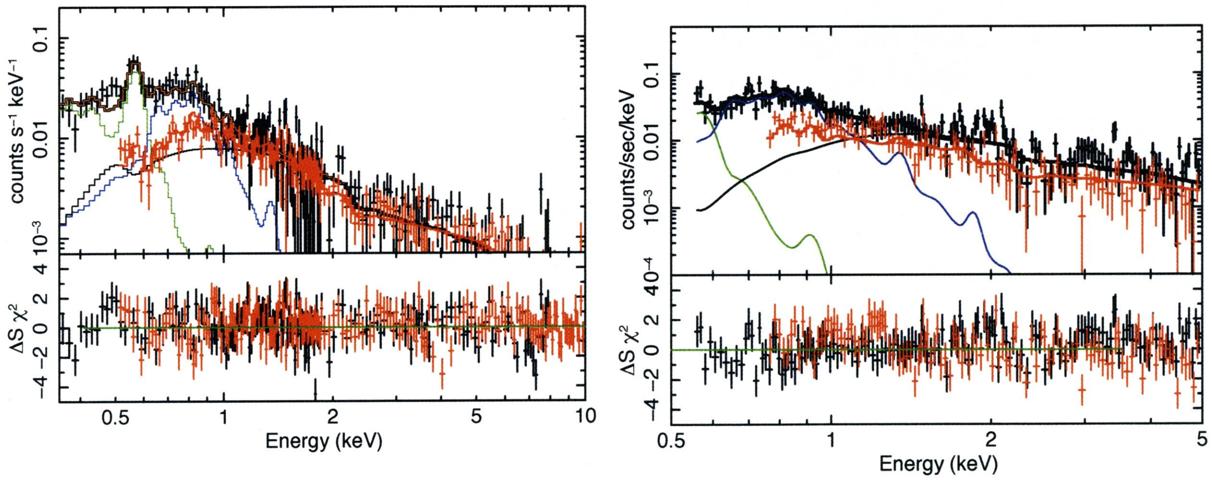

Fig. 5.3: left: The spectrum of the outermost region of A3667 used for the background estimation ($r = 37'.8 - 42'.0$), after NXB subtraction. right: The spectrum of the CIZA2242OFFSET used for the background estimation, after subtraction of NXB and the source. The XIS BI (Black) and FI (Red) spectra are fitted with CXB + Galactic components (LHB, MWH) (*apec+wabs(apec+powerlow)*). The CXB spectrum is shown with a black curve, and the LHB and MWH components are indicated by green and blue curves, respectively.

5.3 Spectral modeling and fitting

We carried out spectral fitting to the pulse-height data of each annular region separately. The NXB component was subtracted before the fit, and the fitting model included the LHB, MWH, CXB and ICM components. The spectra from the BI and FI sensors were jointly fitted with

Table 5.1: Summary of the best-fit parameters for each background observations.

	LHB		MWH		CXB Γ = 1.41
	kT(keV)	$norm^*$ ($\times 10^{-3}$)	kT(keV)	$norm^*$ ($\times 10^{-4}$)	$norm^\dagger$ ($\times 10^{-4}$)
A3376	0.08 (fix)	$11.3^{+3.4}_{-3.8}$	0.27±0.05	$4.12^{+1.91}_{-1.56}$	9.6±0.7
A3667	0.11±0.01	$6.85^{+1.70}_{-1.01}$	0.37±0.03	$11.67^{+1.20}_{-1.61}$	9.6±0.6
A2142	0.09±0.02	4.90±2.90	0.28±0.04	$5.12^{+1.89}_{-2.01}$	9.6(fix)
PKS0745	0.11±0.02	$1.83^{+0.70}_{-0.35}$	0.23±0.03	$58.74^{+1.54}_{-1.21}$	11.6±0.5
A2801	0.10±0.01	$2.15^{+0.35}_{-0.21}$	0.32±0.06	$3.67^{+1.19}_{-0.92}$	8.7±0.7
A2811	0.10±0.01	$2.15^{+0.35}_{-0.21}$	0.32±0.06	$3.67^{+1.16}_{-0.93}$	8.7±0.7
A1413	0.11±0.01	$2.74^{+0.70}_{-0.41}$	0.30±0.02	$3.64^{+1.08}_{-1.24}$	9.6±0.3
A2204	0.08 (fix)	$66.97^{+4.21}_{-3.32}$	0.27±0.03	$92.41^{+12.31}_{-11.21}$	11.9±0.7
A2218	0.08 (fix)	$4.02^{+0.39}_{-0.32}$	0.16±0.02	$8.41^{+1.33}_{-1.28}$	10.7±0.8
CIZA2242	0.08 (fix)	$1.72^{+0.23}_{-0.21}$	0.27±0.01	$4.53^{+0.59}_{-0.80}$	13.8 ±0.4
A2163	0.10±0.01	$2.67^{+0.25}_{-0.30}$	0.25±0.03	$18.52^{+2.65}_{-2.14}$	10.2±0.4
A963	0.10±0.01	$3.54^{+0.41}_{-0.45}$	0.25±0.03	$4.78^{+0.92}_{-0.61}$	11.3±0.4
A2219	0.10±0.01	$2.45^{+0.38}_{-0.31}$	0.27±0.02	$6.45^{+0.54}_{-0.32}$	12.9±0.5
A2390	0.10(fix)	$4.00^{+0.55}_{-0.67}$	0.25±0.04	$10.64^{+2.19}_{-2.87}$	11.9±0.7
Zwcl2341	0.10±0.01	$4.85^{+1.70}_{-1.01}$	0.25 ± 0.02	$1.12^{+0.37}_{-0.24}$	11.2 ±0.3

*:Normalization of the apec component scaled with a factor $1/400\pi$.

Norm=$\frac{1}{400\pi}\int n_e n_H dV/(4\pi(1+z^2)D_A^2) \times 10^{-14}$ cm^{-5} arcmin^{-2},

where D_A is the angular diameter distance to the source.

The referred CXB intensity normalization in Kushino et al. 2002 is

9.6 $\times 10^{-4}$ for $\Gamma = 1.41$ in the unit of photons keV^{-1} cm^{-2} s^{-1} at 1 keV.

the same model by minimizing the total χ^2 value. To increase the signal to noise ratio of the targeted ICM emission, we used energy ranges of 0.35–8 keV for BI and 0.5–10 keV for FI, respectively. The relative normalization between the two sensors was a free parameter in this fit to compensate for the cross-calibration errors. The photon index and normalization of the CXB, the temperatures and normalization of the LHB and MWH were fixed at the values in table 5.1. Metal abundances of the LHB and MWH components were set to be unity. The Galactic absorption column density $N_{\rm H}$ was fixed at the value of target cluster directions (Dickey & Lockman 1990). The fits were carried out with XSPEC ver12.6. In the central regions, free parameters were the temperature, normalization and metal abundance of the ICM component. In the outer regions, we fixed the metal abundance of the ICM at 0.2, which is the value observed in the outskirts of clusters (Fujita et al.(2008)). As an example, figure 5.4 shows the results of the spectral fit for all the annular regions of A2142 from Akamatsu et al. (2011a). The parameters and χ^2 values are listed in tables 5.2. We obtained fairly good fits for all the regions with reduced χ^2 values less than 1.3. Other cluster data are shown in Appendix A.

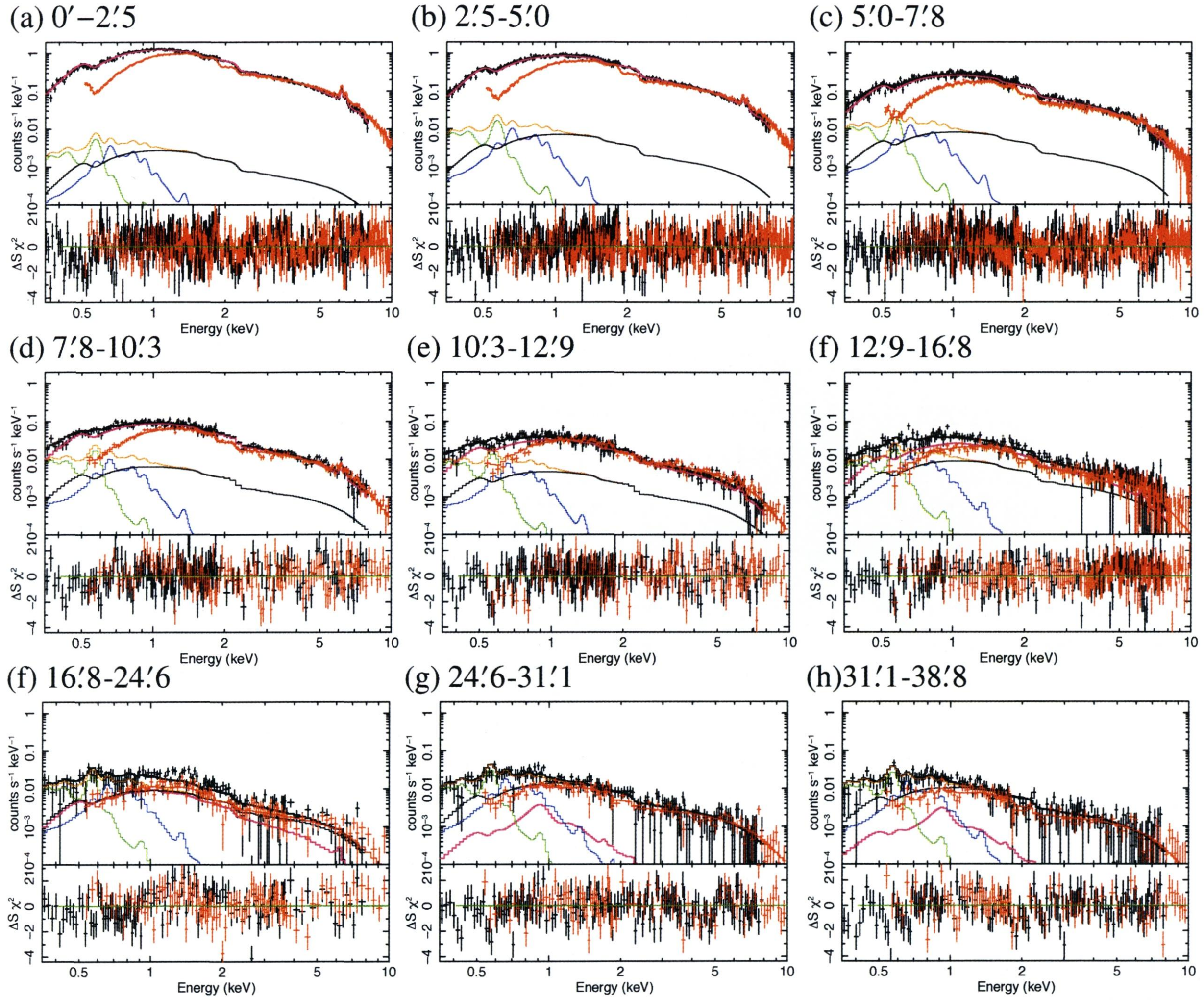
(a) 0′–2′.5 (b) 2′.5-5′.0 (c) 5′.0-7′.8

(d) 7′.8-10′.3 (e) 10′.3-12′.9 (f) 12′.9-16′.8

(f) 16′.8-24′.6 (g) 24′.6-31′.1 (h)31′.1-38′.8

Fig. 5.4: Spectral fit for the A2142 data. NXB subtracted spectrum is shown for each region. The XIS BI (Black) and FI (Red) spectra are fitted with ICM (*wabs + apec*), added with CXB and the galactic components (LHB, MWH) (*apec+wabs(apec+powerlow)*). The ICM components are shown in magenta. The CXB components are shown with a black curve, and the LHB and MWH emissions are indicated by green and blue histgrams, respectively.

Table 5.2: Best-fit parameters of the A2142 ICM with Offset3 background

Region	kT (keV)	Z ($Z_\odot$)	norm*	$S^{\dagger}_{0.4-10\mathrm{keV}}$	BI/FI	χ^2/d.o.f
$0'-2'.5$	$8.16^{+0.10}_{-0.10}$	$0.33^{+0.02}_{-0.02}$	$1.82 \pm 0.01 \times 10^5$	$7.74 \pm 0.30 \times 10^4$	0.92	712 / 604
$2'.5-5'.0$	$9.02^{+0.19}_{-0.19}$	$0.28^{+0.02}_{-0.02}$	$3.90 \pm 0.01 \times 10^4$	$1.65 \pm 0.05 \times 10^4$	0.93	691 / 604
$5'.0-7'.8$	$9.50^{+0.38}_{-0.38}$	$0.24^{+0.05}_{-0.05}$	$7.50 \pm 0.01 \times 10^3$	$3.33 \pm 0.05 \times 10^3$	1.03	681 / 604
$7'.8-10'.3$	$8.47^{+0.65}_{-0.48}$	$0.31^{+0.09}_{-0.09}$	$2.09 \pm 0.07 \times 10^3$	$9.59 \pm 0.33 \times 10^2$	1.07	309 / 270
$10'.3-12'.9$	$7.79^{+0.81}_{-0.79}$	$0.19^{+0.13}_{-0.12}$	$8.30 \pm 0.32 \times 10^2$	$3.90 \pm 0.33 \times 10^2$	1.19	338 / 270
$12'.9-16'.8$	$6.14^{+1.30}_{-0.95}$	0.2 (fix)	$6.70 \pm 0.40 \times 10^2$	$2.67 \pm 0.22 \times 10^2$	0.85	381 / 358
$16'.8-24'.6$	$3.42^{+2.14}_{-1.22}$	0.2 (fix)	$1.35 \pm 0.22 \times 10^2$	$5.18 \pm 0.22 \times 10^1$	0.92	272 / 217
$24'.6-31'.1$	$1.01^{+0.44}_{-0.29}$	0.2 (fix)	$2.00 \pm 0.11 \times 10^1$	6.40 ± 0.20	0.94	238 / 223
$31'.1-38'.8$	$1.08^{+0.28}_{-0.37}$	0.2 (fix)	1.00 ± 0.50	2.75 ± 0.20	0.88	299 / 223

*: Normalization of the apec component scaled with a factor SOURCE_RATIO_REG Ω_e from table ,
Norm=$\frac{\mathrm{SOURCE\_RATIO\_REG}}{\Omega_e} \int n_e n_H dV / (4\pi(1+z^2)D_A^2) \times 10^{-22} cm^{-5}\ arcmin^{-2}$,
where D_A is the angular diameter distance to the source.

†: 10^{-8} photons cm^{-2}s^{-1} arcmin^{-2}. Energy band is 0.4 - 10.0 keV.

Chapter 6

Results of spectral analysis

6.1 Individual cluster properties

6.1.1 Abell3376: Akamatsu et al. 2011b

Figure 7.5(a) shows the temperature profiles of A3376. The temperature within 20′ (1.2 Mpc corresponding to $0.6r_{200}$) of the cluster center shows an almost flat or rising profile with $kT \sim$ 4.0 keV, which is very much different from those seen in the relaxed clusters. The increase of temperature just inside of the radio relic (18′-21′, and 21′-24′) compared with the level in the inner region is significant by about 4σ. The temperature of A3376 suddenly drops at the radio relic region from 4.7 keV to 1.3 keV. These features strongly suggest that there is a shock heating taking place in the relic region. The surface brightness profile also shows more than an order of magnitude drop at the same region. A detailed study of A3376 radio relic has already been published by Akamatsu et al. (2011b). We refer to this paper for the images and X-ray information and look into the observed feature in the discussion.

6.1.2 Abell 3667: Akamatsu et al. 2011c

The resultant ICM temperature profile is shown in Fig. 7.5(b). The temperature within 15′ (960 kpc) from the cluster center shows a fairly constant value of ∼ 7 keV, and it gradually decreases toward the outer region down to ∼ 5 keV around the radio relic (∼ 27′). Our temperature profile also shows a remarkable drop by a factor of 2–3 in this region even considering the systematic errors. The temperature profile inside the relic shows an excess over the mean values for other clusters observed with XMM-Newton (Pratt et al. 2007) described by the following formula

$$T/T_X = 1.19 - 0.74R/R_{200}, \tag{6.1}$$

where T_X is the average temperature and R_{200} is the virial radius. We used $T_X = 7.0$ keV and $R_{200} = 34.'1$ for A3667. The temperature profile of A3667 shows good agreement with the previous XMM result for the radius range within the radio relic, as shown in Fig. 7.5(b). The observed temperatures of A3667 are somewhat higher than the average levels between 10′ and 26′. Around the radio relic region, the average profile predicts 4.0 keV but the observed temperature is 5.3 keV, which is in excess by about 30%.

The surface brightness profile shows a good agreement with the β-model ($\beta = 0.54$) up to the radio relic region. As shown in Fig. ??(b), the surface brightness also shows a drop by an order of magnitude across the relic. The surface brightness and the pressure profiles also show the significant drop as reported by other X-ray observatory (Finoguenov et al. 2010).

A detailed study of A3667NW radio relic has already been carried out by Akamatsu et al. (2011a). We refer to this paper for the images and X-ray information and will include the A3667NW feature in the discussion.

6.1.3 Abell 2142: Akamatsu et al. 2011a

Figure 7.5(c) shows the radial profile of ICM temperature, based on the result of the spectral fits. The inner 5 annular regions have the width of about $2\farcm5$, and 20–40% of the detected flux comes from the adjacent sky regions. The maximum temperature within $7'$ (700 kpc) from the cluster center is $\sim$ 9 keV, and it gradually decreases toward the outer region down to $\sim$ 4 keV around the virial radius. There is a suggestion of weak emission with $kT \sim$ 1 keV just outside of r_{200}.

Next, we derived electron density profiles using the above deprojection method. The resultant radial distribution of n_e is shown in figure 6.2 (c), along with the β-model profile from ROSAT ($\beta = 0.85, r_c = 4\farcm5$). We obtained an upper limit of the electron density in the outermost region ($31\farcm1$–$38\farcm8$) to be $< 2.0 \times 10^{-5}\mathrm{cm}^{-3}$. One can see that the β-model gives a fairly good approximation for the density profile, even though the temperature shows a large deviation from the isothermal case. Even though flatter temperature profiles are regarded as a sign of recent matter infall, steeper temperature curves such as seen in A 2142 and abrupt temperature drops, as seen in A 3667 and Virgo Cluster can also be a sign of recent heating (Finoguenov et al. 2010; Urban et al. 2011). Therefore, simple steepness of the temperature profile seems to carry somewhat degenerate information about the cluster evolution.

6.1.4 PKS 0745-191

We re-analyzed the PKS0745-191 data by focusing on the ICM properties by different background modeling from the one performed by George et al. (2008). We analyzed data from the offset observation of PKS0745 which was carried after the observations and confirmed that there was no additional thermal component but the CXB level was higher (9.43×10^{-4} photon $\mathrm{cm}^{-2}\ \mathrm{s}^{-1}\ \mathrm{keV}^{-1}$ at 1 keV) than the value in the Lockman hole (7.26×10^{-4} photon $^{-1}\ \mathrm{cm}^{-2}\ \mathrm{s}^{-1}$ keV at 1 keV) which George et al. (2008) used for the background estimations. We extracted the spectra from annular regions with boundary radii $0\farcm0$, $2\farcm5$, $5\farcm0$, $8\farcm0$, $13\farcm0$ and $18\farcm0$ centered on $(07^{\mathrm{h}}47^{\mathrm{m}}30\fs88, -19^{\circ}17^{\mathrm{m}}39^{\mathrm{s}})$, and analyzed the spectra for the sum of all the azimuthal regions.

The resultant temperature profile is shown in figure 7.5(d). Red, gray and black crosses show the results of Suzaku (this work), George et al. (2008) and XMM-Newton(Chen et al. 2003), respectively. Our results are in good agreement with the previous Suzaku results by George et al. (2008). Hence, the inconsistency between ROSAT and Suzaku results still remained.

A possible explanation of this inconsistency is the effect of stray light from the strong cool core of PKS0745. Additional observations of PKS0745 with the roll angle which reduces the contamination of the stray light are necessary.

6.1.5 Abell 2811 & Abell 2801

Figure 7.5(a) shows the radial profile of the ICM temperature in A2811 and A2801. In A2811, the temperature gradually drops from 5 keV to 2 keV. A2801 shows the lowest ICM temperature in this sample of k< T >=2.28 keV (table 6.1). The temperature profile of A2801 shows a slightly flatter slope than the other clusters. The above average temperatures are in good agreement with the previous ASCA measurements (Obayashi et al. 1998).

6.1.6 Abell 1413

In addition to the previous Suzaku data (Hoshino et al. 2010), we analyzed the new observational data, which covered all directions. We modeled the background component using the outermost region data which had negligibly-small contribution of the ICM emission. We extracted the spectra from annular regions with boundary radii $0'.0$, $2'.5$, $5'.0$, $8'.0$, $12'.0$ and $18'.0$ centered on $(11^{h}55^{m}18^{s}.90, 23^{\circ}24^{m}31^{s})$ and analyzed the spectra for the sum of all the azimuthal regions. The results are shown in Figure 7.5(g) and consistent with the previous works. The temperature gradually decreases from 8 keV to 3 keV from the center to the virial radius.

6.1.7 Abell 2204

In addition to the previous Suzaku data (Reiprich et al. 2009), we analyzed the new observational data covering all directions. We extract the spectrum from annular regions with boundary radii $0'.0$, $3'.0$, $6'.0$, $11'.0$, $16'.0$ and $18'.0$ centered on $(16^{h}32^{m}45^{s}.70, 05^{\circ}34^{m}43^{s})$, and analyzed the spectra for the sum of all the azimuthal regions. The resultant temperature profile is shown in figure 7.5(h). The temperature gradually decreases form 8 keV to 4 keV from the center to the virial radius, which is consistent with the previous X-ray studies (Snowden et al. 2008; Reiprich et al. 2009).

6.1.8 Abell 2218

We re-analyzed the archival Suzaku data of A2218 which covered up to 0.9 r_{200}. The average temperature (within $< 0.4 r_{200}$) show $k\langle T\rangle = 7.35^{+0.22}_{-0.22}$ keV. We extracted the spectra from annular regions with boundary radii $0'.0$, $2'.0$, $4'.0$, $7'.0$ and $10'.0$, centered on $(16^{h}35^{m}54^{s}.88, 66^{\circ}12^{m}18^{s})$. The resultant temperature profile is shown in figure 7.5(i). Our results are consistent with the previous X-ray studies (Neumann Bohringer 1999; Pratt et al. 2005), indicating that the ICM temperature gradually decreases from 8 keV to 3 keV from the center to the virial radius,

6.1.9 Abell 2163

Suzaku observed A2163 along the north and south direction which covered beyond r_{200}. The average temperature (within $< 0.4r_{200}$) is $k\langle T\rangle = 15.17^{+0.41}_{-0.42}$ keV. The temperature profiles of the two directions show significant decreases from 15 keV to 5-8 keV from the center to the outskirts as shown in figure 7.5(k), which is consistent with the previous X-ray studies.

6.1.10 Abell 963

Suzaku observed A963 with 3 pointings covering north, east and south directions beyond the virial radius. The exposure times are 30 ks for all the observations. We extracted the spectra from annular regions with boundary radii $0'.0$, $2'.0$, $4'.0$, $7'.0$ and $11'.0$, centered on $(10^{h}17^{m}03^{s}.00, 39^{\circ}02^{m}30^{s})$, and analyzed the spectra for the sum of all the azimuthal regions. The average temperature of A963 (within $< 0.4r_{200}$) is $k\langle T\rangle = 6.81^{+0.35}_{-0.27}$ keV. The temperature profile show decrease from 7 keV to 3 keV from the center to the outskirt as shown in figure 7.5(l).

6.1.11 Abell 2219

Suzaku carried out observation of A2219 during April 2009 with 100 ks exposure. We extract the spectra from the radii $0'.0$, $2'.0$, $5'.0$, $9'.0$, centered on $(16^{h}39^{m}25^{s}.47, 46^{\circ}41^{m}40^{s})$. The average temperature of A2219 (within $0.4r_{200}$) show $k\langle T\rangle = 11.93^{+0.32}_{-0.25}$ keV. We obtained ICM emission up to the virial radius. The temperature profile show monotonic decrease from 12 keV to 6 keV from the center to the outskirt as shown in figure 7.5(m).

6.1.12 Abell2390

Suzaku carried out observations of A2390 beyond the virial radius during 2009 May with 100 ks exposure. We extracted the spectra from the radii $0'.0$, $2'.0$,$4'.0$, $7'.0$ and $10'.0$ centered on $(21^{h}53^{m}35^{s}.97, 17^{\circ}41^{m}28^{s})$. The average temperature of A2390 (within $0.4r_{200}$) is $k\langle T\rangle = 10.56^{+0.15}_{-0.15}$ keV. We obtained ICM emission up to the virial radius. As shown in figure 7.5(n), the temperature profile show monotonic decrease from 12 keV to 4 keV from the center to the outskirt, which is consistent with the previous X-ray studies (Boehringer et al. 1998).

6.1.13 CIZA2242: Akamatsu & Kawahara 2011

Deep X-ray observations provide informations about the temperature and density of ICM across the shock fronts, which allows us to investigate the dynamical feature of this strongest shock. To examine the global X-ray properties of CIZA 2242, we attempted to reproduce the observed XIS spectra by fitting the Apec model with the background components discussed in Sec 5.2. We extracted the spectrum within the radio relic ($\sim$ 1.2 Mpc= $6'5$), and the redshift value in the spectral fit was fitted to 0.192. The spectrum was well fitted with the above model ($\chi^2_\nu = 1.09$ for 632 degrees of freedom). We find the temperature and the metal abundance of $kT = 7.77 \pm 0.25$

keV and $Z = 0.23 \pm 0.03$, respectively. The unabsorbed flux and luminosity in the 0.5–10 keV band are $F_{0.5-10.0\ \mathrm{keV}} = 6.9\times10^{-12}$ erg cm^{-2} s^{-1} and $L_{0.5-10.0\ \mathrm{keV}} = 6.7\times10^{44}$ erg s^{-1}, respectively.

In order to confirm the existence of a shock front at the radio relic, we performed the spectral fitting for each annulus determined in Chap 4. Figure 7.5(j) shows the radial profile of the ICM temperature in CIZA2242. The temperature within 6.′5 (1.25 Mpc) from the cluster center shows a fairly constant value of ~ 7.5 keV. As mentioned in Chap 4, van Weeren et al. (2010) reported the existence of a very sharp radio relic at those radius. We confirm that the temperature profile across radio relic shows significant drop from 6.8 keV to 1.5 keV in this region. Those temperature drops are consistent with the prediction of numerical simulation by van Weeren et al. (2011). Figure 6.11(j) shows the radial profile of the thermal pressure P of ICM in CIZA2242. We see a clear pressure jump by a order across the radio relic. The spatial coincidence of the ICM parameter jumps and the radio relic strongly suggests the existence of shock fronts.

6.1.14 Zwcl2341N & Zwcl2341S

We extracted the spectrum within 3’ (~ 740 kpc) and performed the spectral fit with the fixed redshift value to 0.270. The spectrum was well fitted with the thermal model ($\chi^2_\nu = 1.04$ for 473 degrees of freedom). We find the temperature and the metal abundance of $kT = 5.16 \pm 0.32$ keV and $Z = 0.25 \pm 0.08$, respectively. The unabsorbed flux and luminosity in the 0.5–10 keV band are $F_{0.5-10.0\ \mathrm{keV}} = 1.03 \times 10^{-12}$ erg s cm^{-2} and $L_{0.5-10.0\ \mathrm{keV}} = 2.2 \times 10^{44}$ erg s^{-1}, respectively.

The radial profiles of the ICM temperature are shown in Fig. 7.5(e) and (f) for Zwcl2341N and Zwcl2341S, respectively. Our temperature profiles are almost consistent with the Chandra results in the central region. The temperature drops from 4keV to 1 keV toward the north direction or from 4 keV to 2 keV toward the south direction. Figure 6.2(e,f) and Figure 6.11(e,f) show the electron density and the pressure profiles of Zwcl2341N and Zwcl2341S, respectively.

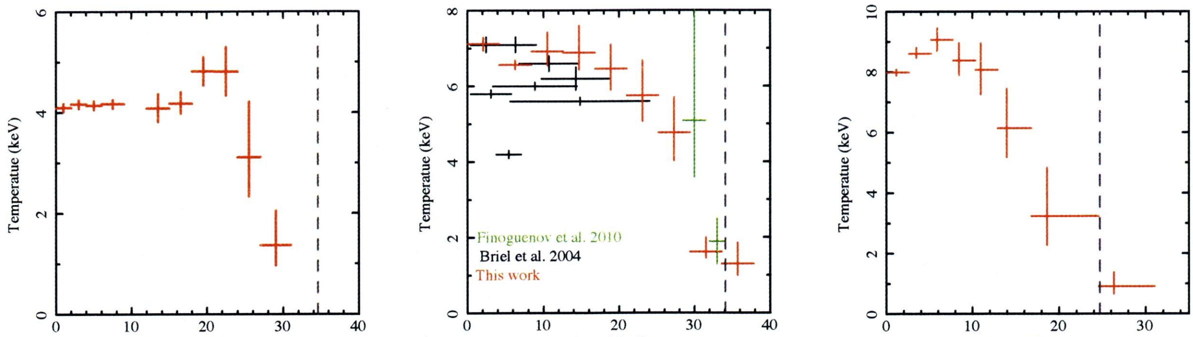
(a)Abell 3376 (b)Abell 3667 (c)Abell 2142

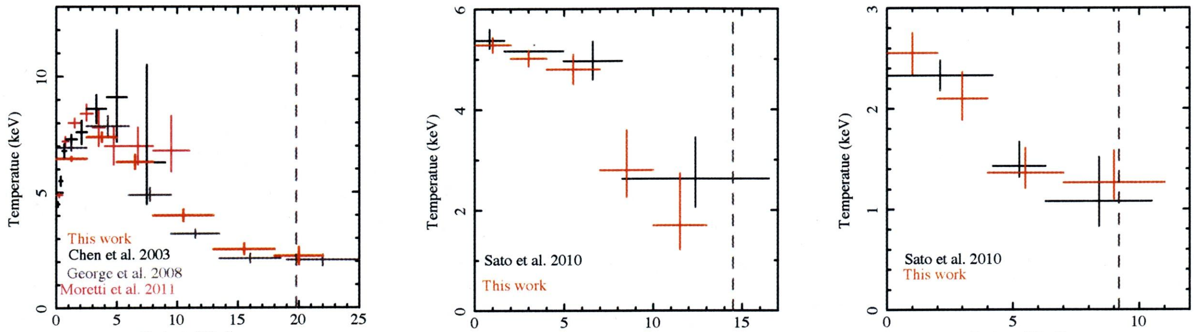
(d)PKS0745 (e)Abell 2811 (f)Abell 2801

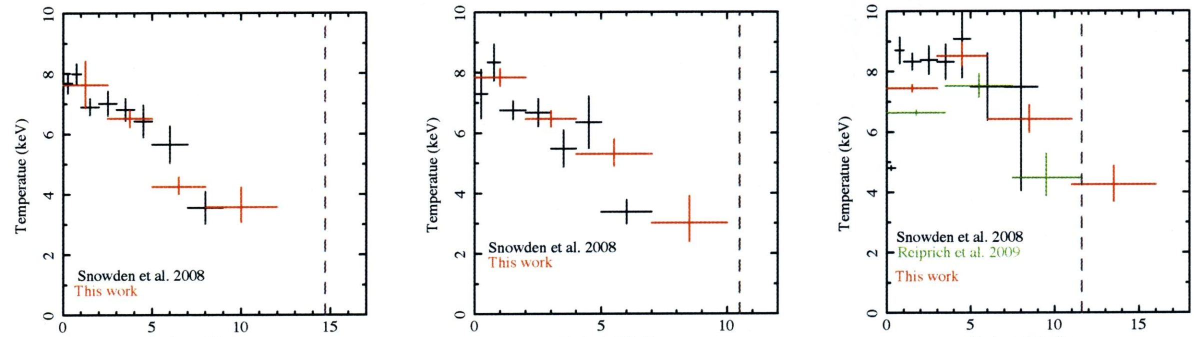
(g)Abell 1413 (h)Abell 2218 (i) Abell 2204

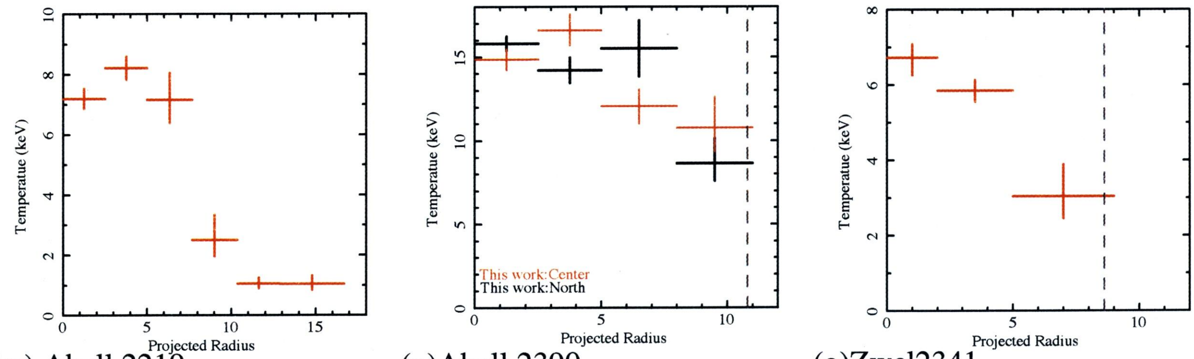
(j)CIZA2242 (k)Abell 2163 (l)Abell 963

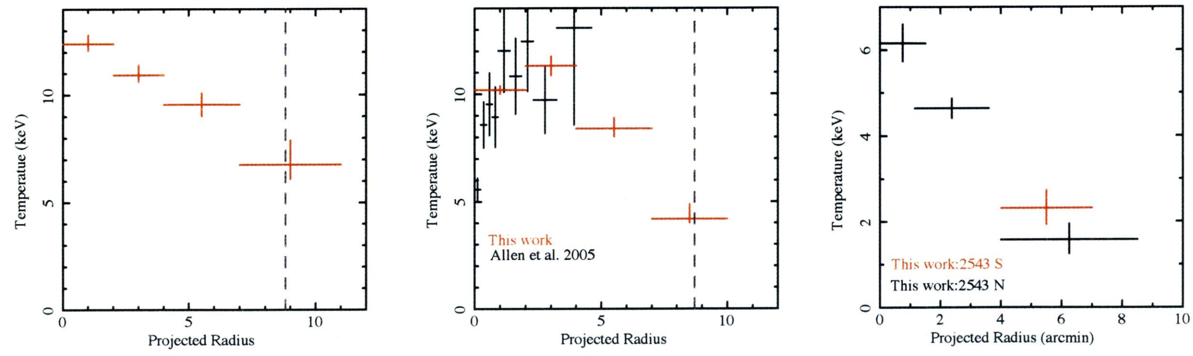
(m) Abell 2219 (n)Abell 2390 (o)Zwcl2341

Fig. 6.1: Radial profiles of ICM temperature obtained by Suzaku observations.

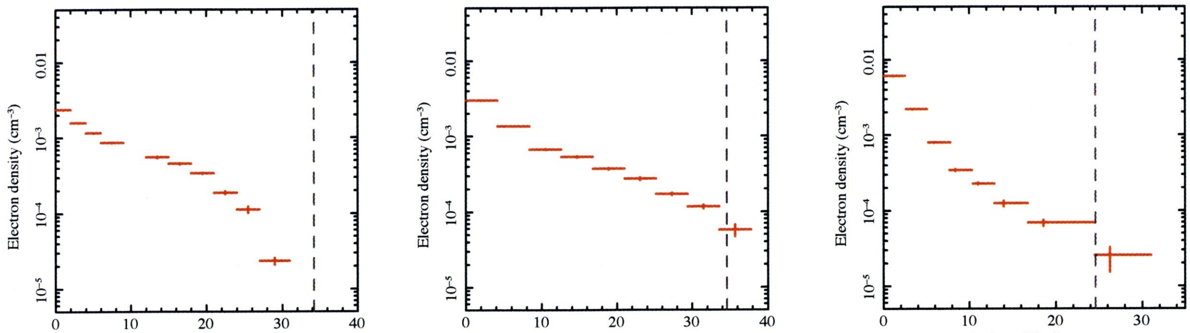
(a)Abell 3376 (b)Abell 3667 (c)Abell 2142

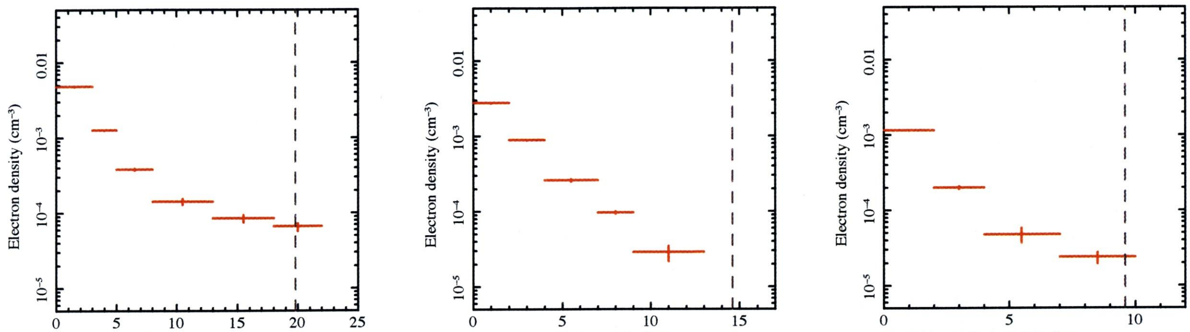
(d)PKS0745 (e)Abell 2811 (f)Abell 2801

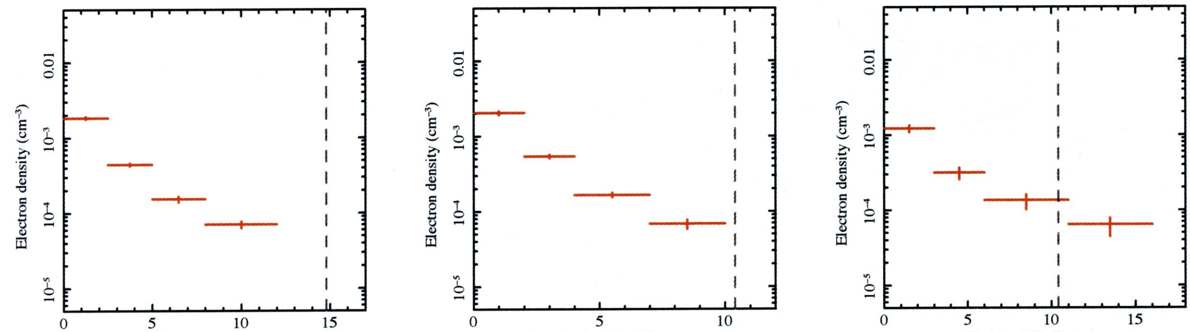
(g)Abell 1413 (h)Abell 2218 (i) Abell 2204

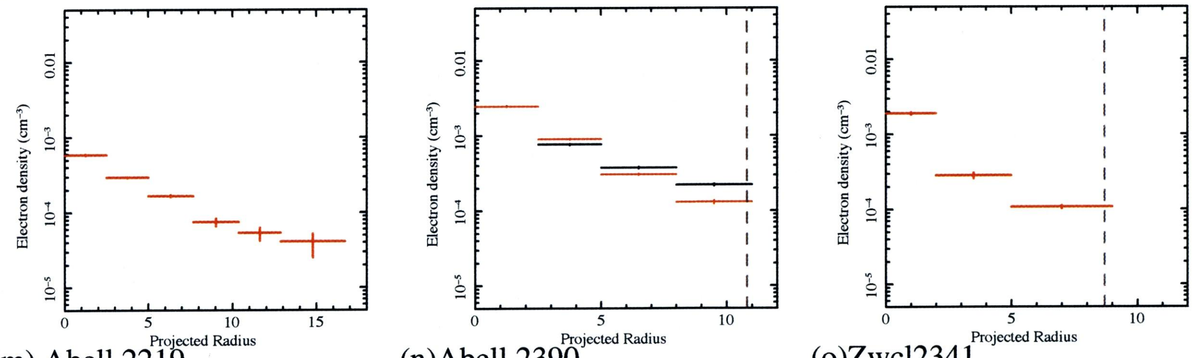
(j)CIZA2242 (k)Abell 2163 (l)Abell 963

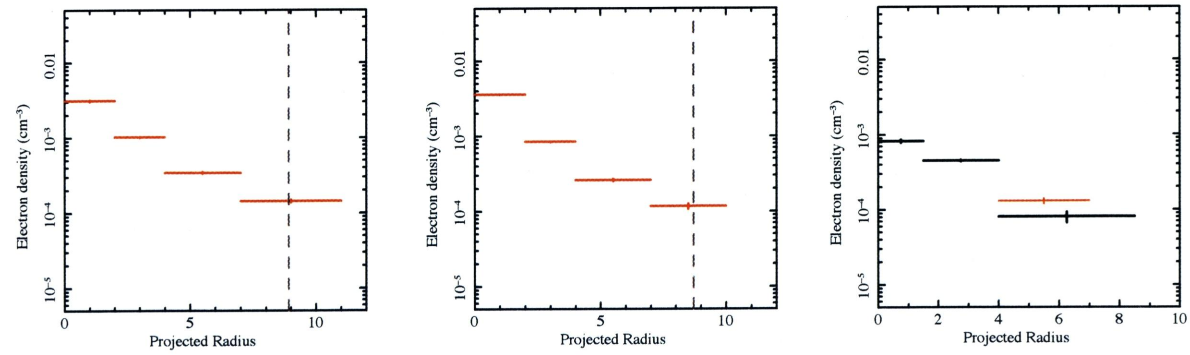
(m) Abell 2219 (n)Abell 2390 (o)Zwcl2341

Fig. 6.2: Radial profiles of deprojected electron density obtained by Suzaku observations.

(a)Abell 3376 (b)Abell 3667 (c)Abell 2142

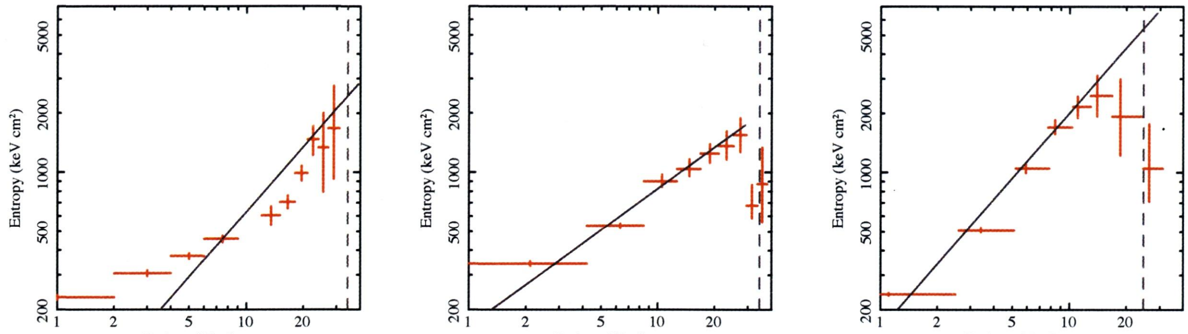

(d)PKS0745 (e)Abell 2811 (f)Abell 2801

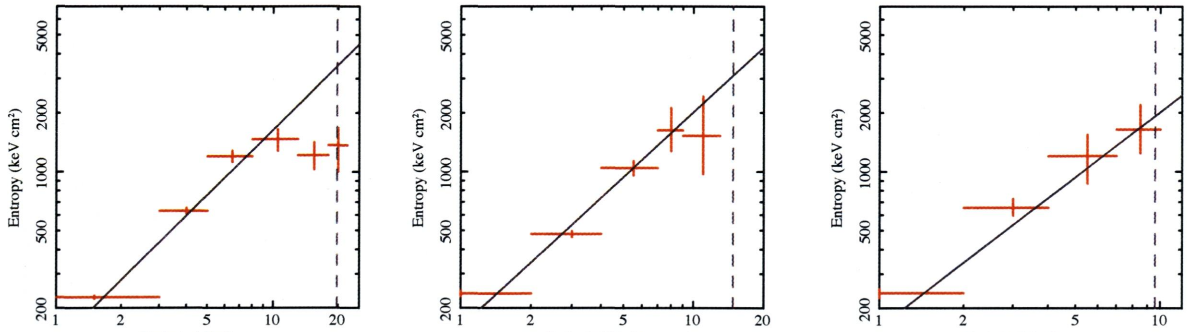

(g)Abell 1413 (h)Abell 2218 (i) Abell 2204

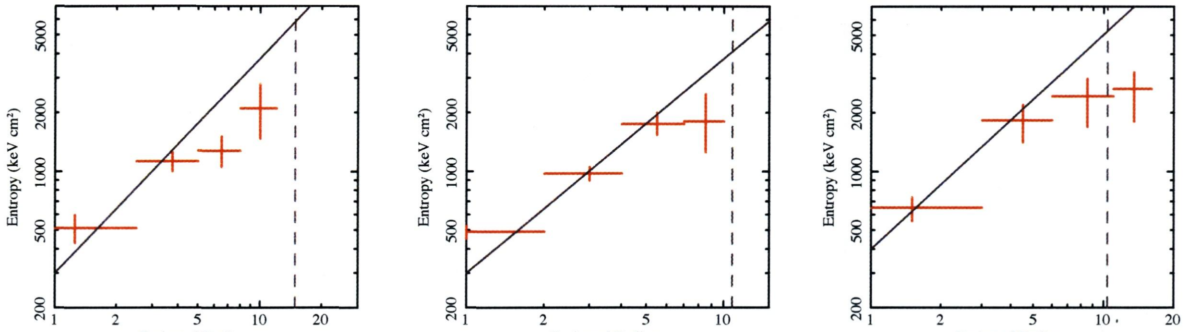

(j)CIZA2242 (k)Abell 2163 (l)Abell 963

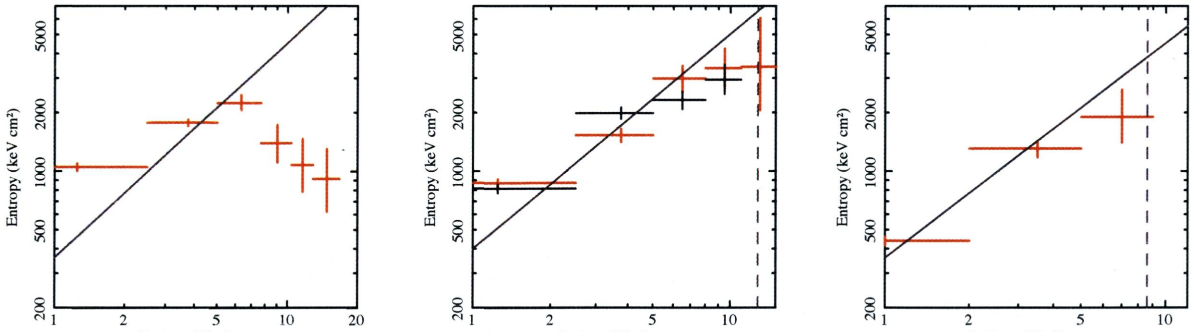

(m) Abell 2219 (n)Abell 2390 (o)Zwcl2341

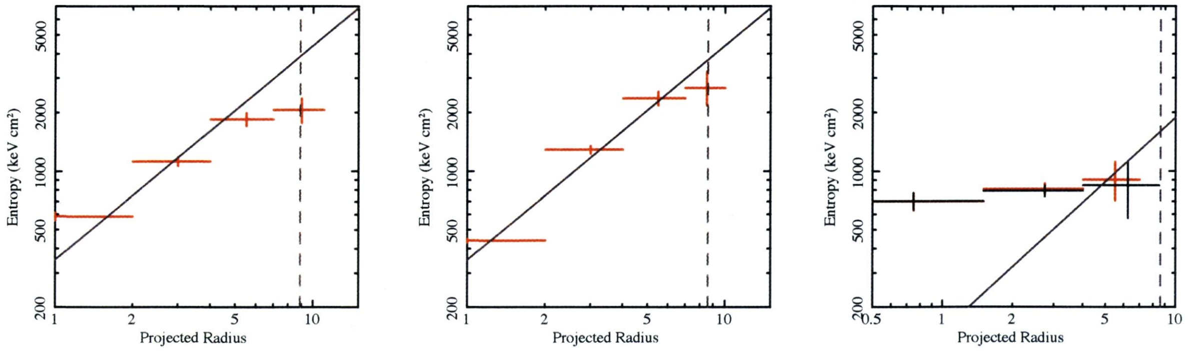

Fig. 6.3: Radial profiles of ICM entropy obtained by Suzaku observations.

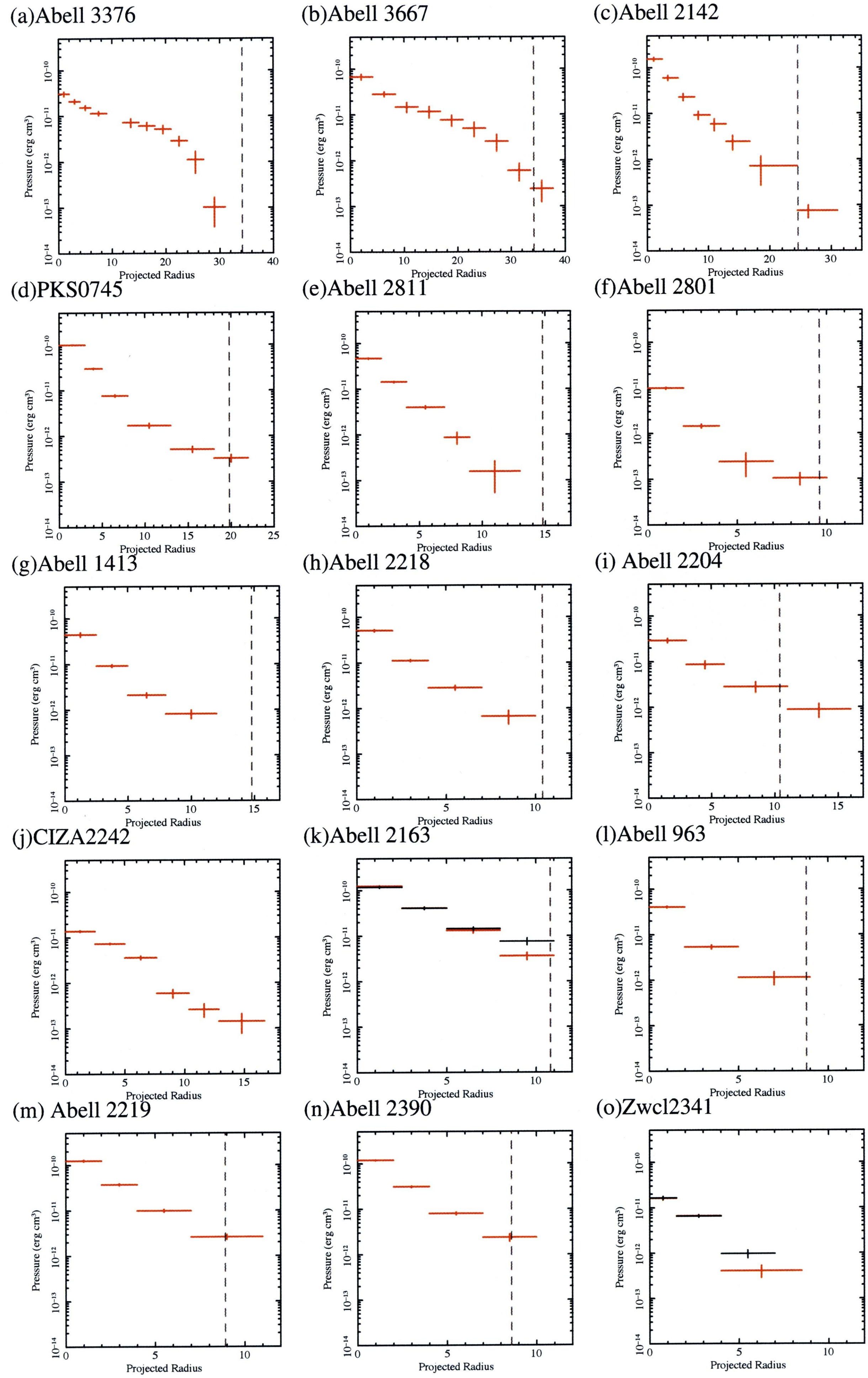
(a)Abell 3376 (b)Abell 3667 (c)Abell 2142

(d)PKS0745 (e)Abell 2811 (f)Abell 2801

(g)Abell 1413 (h)Abell 2218 (i) Abell 2204

(j)CIZA2242 (k)Abell 2163 (l)Abell 963

(m) Abell 2219 (n)Abell 2390 (o)Zwcl2341

Fig. 6.4: Radial profiles of ICM pressure obtained by Suzaku observations.

Table 6.1: Results of the Suzaku spectrum analysis. Column 4, emission weighted X-ray temperature with in 0.4 r_{200}. Column 5, metal abundance. Column 6, χ^2 and the degree of freedom (d.o.f) of the Apec model fitting.

ID	Cluster	D_L	k< T >	Z	Flux$_{2-10\mathrm{keV}}$	r_{500}	χ^2/d.o.f	
		[Mpc]	[keV]	[solar]	10^{-14} erg s^{-1}cm^{-2}/arcmin^2	erg s^{-1}	[arcmin(Mpc)]	[arcmin(Mpc)]
1	A3376	201.3	$4.10^{+0.04}_{-0.04}$	$0.25^{+0.01}_{-0.01}$	$5.28^{+0.80}_{-0.80}$	32.4 (1.74)	21.6 (1.13)	2926 / 2798
2	A3667	246.8	$6.68^{+0.09}_{-0.09}$	$0.31^{+0.02}_{-0.02}$	$10.66^{+0.02}_{-0.02}$	33.4 (2.21)	22.4 (1.45)	2792 / 2639
3	A2142	411.3	$8.57^{+0.10}_{-0.08}$	$0.29^{+0.01}_{-0.01}$	$33.17^{+0.51}_{-0.51}$	24.6 (2.47)	16.8 (1.64)	4045 / 3744
4	PKS0745	469.5	$6.61^{+0.07}_{-0.07}$	$0.38^{+0.01}_{-0.01}$	$36.23^{+-0.37}_{0.37}$	19.0 (2.15)	13.0 (1.44)	3578 / 3269
5	A2811	493.9	$5.15^{+0.10}_{-0.10}$	$0.30^{+0.03}_{-0.03}$	$6.37^{+0.20}_{-0.20}$	14.7 (1.90)	10.1 (1.27)	385 / 319
6	A2801	493.9	$2.29^{+0.21}_{-0.19}$	$0.39^{+0.14}_{-0.12}$	$0.50^{+0.03}_{-0.03}$	9.8 (1.27)	6.7 (0.85)	214 / 186
7	A1413	669.5	$6.69^{+0.38}_{-0.32}$	$0.40^{+0.09}_{-0.09}$	$21.84^{+0.28}_{-0.28}$	12.5 (2.13)	8.7 (1.45)	803 / 816
8	A2204	710.7	$7.70^{+0.12}_{-0.12}$					
10	A2218	841.6	$7.35^{+0.22}_{-0.22}$	$0.21^{+0.04}_{-0.04}$	$13.23^{+0.31}_{-0.31}$	10.4 (2.20)	7.4 (1.52)	394 / 319
9	A2163	986.9	$15.17^{+0.41}_{-0.42}$	$0.27^{+0.04}_{-0.04}$	$49.64^{+0.47}_{-0.47}$	12.8 (3.11)	9.2 (2.18)	3776 / 3145
10	CIZA2242	927.2	$7.58^{+0.24}_{-0.24}$	$0.23^{+0.03}_{-0.03}$	$5.14^{+0.57}_{-0.57}$	9.84 (2.23)	513 / 408	
11	A963	1003.3	$6.81^{+0.35}_{-0.27}$	$0.35^{+0.07}_{-0.07}$	$5.39^{+0.12}_{-0.12}$	8.4 (2.07)	6.0 (1.45)	753 / 809
12	A2219	1113.9	$11.93^{+0.32}_{-0.25}$	$0.24^{+0.03}_{-0.03}$	$8.78^{+0.12}_{-0.12}$	10.1 (2.73)	7.3 (1.93)	578 / 423
13	A2390	1125.0	$10.56^{+0.15}_{-0.15}$	$0.34^{+0.02}_{-0.02}$	$28.30^{+0.33}_{-0.33}$	9.4 (2.57)	6.8 (1.82)	3291 / 3061

6.2 Temperature profile

The ICM temperature is an important observational parameter which reflects the depth of the gravitational potential of the cluster. Their profiles also enable us to look into the history of the ICM heating and the growth of clusters. Some numerical simulations (Ettori et al. 2004; Borgani et al. 2004) predicted that the intracluster gas temperature drops to about 50% of the central temperature around r_{200} under hydrostatic equilibrium. Those results reproduced observed temperature profiles to about $0.5r_{200}$ (De Grandi & Molendi 2002; Vikhlinin et al. 2005; Pratt et al. 2007). In particular, recent XMM-Newton (Pratt et al. 2007) results showed temperature profiles out to $0.6r_{200}$. Based on the observed results shown in the previous chapter, we will discuss the physical properties of ICM in the outermost region of clusters, including cluster-scale shock fronts, and possible deviation from thermal equilibrium.

6.2.1 Averaged temperature profiles

We normalized the radial temperature profile by the average temperature determined within $0.4r_{200}$. Their temperature profiles are shown in figure 6.5. Our sample include 9 relaxed clusters and 5 merging clusters. Crosses shows the relaxed clusters and diamonds show the merging clusters. The r_{200} value are derived from Henry et al. (2009). Our temperature profiles are measured with considerable accuracy up to virial radius r_{200}. Figure 6.5 clearly shows different trend in relaxed and merging cluster samples. We will discuss each trend in the next section.

6.2.2 Relaxed cluster

In this section, we investigate the trend of the temperature profiles of relaxed clusters. As shown in the previous section, our measurement shows a clear trend; the cluster temperature profiles decline with distance from the center, which is consistent with the previous measurement and extends the temperature profiles up to the virial radii. The comparison of our temperature profiles with those obtained from Chandra and XMM-Newton are shown figure 6.6(a). We note that the definitions of the average temperature kT differ between those studies.

We first fit the scaled temperature profiles in the outer region ($r/r_{200} > 0.2$) with a simple linear line model as;

$$kT(r)/k < T >= A + Br. \tag{6.2}$$

The best fit model is shown in figure 6.6(a) by solid red line and those parameters are shown in table 6.2. A negative value of B indicates that the temperature profiles decline with radius. The resultant best-fit line is approximately consistent with the previous results by Chandra and XMM-Newton.

Next, we adopt a polytropic model discribed as below;

$$kT(r)/k < T >= A[1 + (\frac{r}{r_0})^2]^{-1.5\beta(\gamma-1)}. \tag{6.3}$$

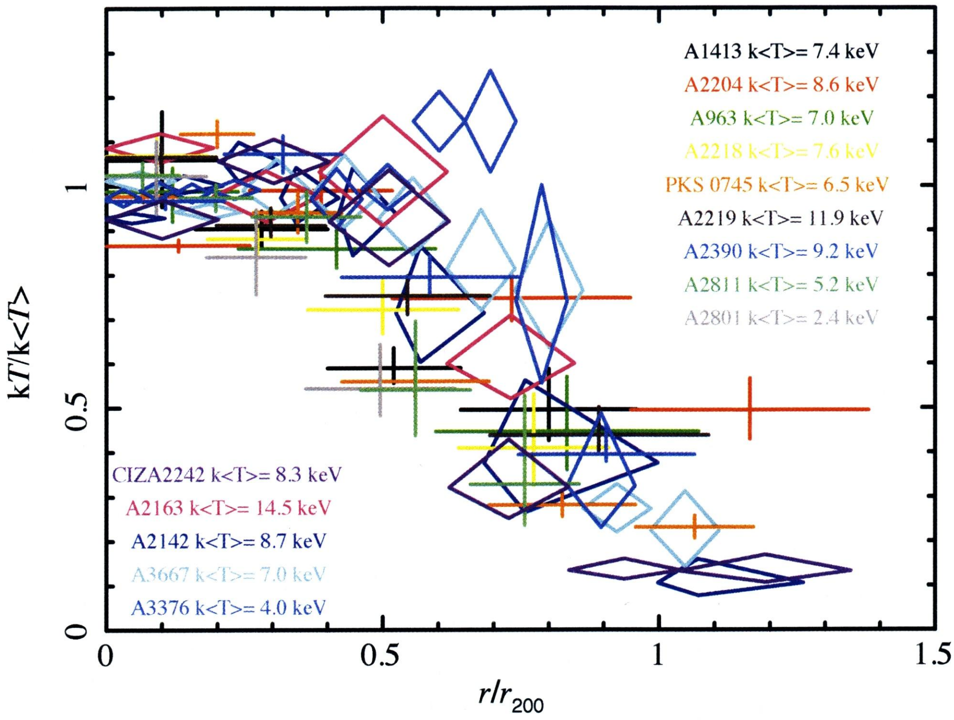

Fig. 6.5: Scaled projected temperature profiles. The profiles have been normalized to the mean temperature. Crosses show the relaxed clusters and diamond show the merging clusters. The r_{200} value are derived from Henry et al. (2009).

where r_0 is r_c and A is the scaled temperature at $r = 0$. r_0 and β are set equal to 0.08 and 0.58, which is the mean value of the β or double β model in our sample. We fit the scaled temperature profiles in the outer region ($r/r_{200} > 0.2$) and show the resultant best-fit model in figure 6.8(b) by blue curve. The resultant best-fit values are shown in table 6.2. The parameter of the polytropic model γ represents the condition of plasma; γ=1 represents the isothermal case and γ=5/3 is the adiabatic case.

Table 6.2: Best-fit parameters for liner and polytropic temperature profiles

	Liner		Polytropic	
	A	B	A	γ
This work	1.17±0.02	-0.81±0.03	1.94±0.07	1.27±0.02
Vikhlinin et al. 2005	1.22	-1.20	–	–
Pratt et al. 2007	1.19	-0.74	–	–
Markevitch et al. 1998	–	–	–	$1.24^{+0.20}_{-0.12}$

The resultant polytropic index γ is compared in figure 6.7 with the previous works (Markevitch et al. 1998; Finoguenov et al. 2001). Our best-fit value of the polytropic index γ is within the isothermal and adiabatic cases and is slightly closer to the isothermal case. Although the previous works have large error with $\gamma = 1.24^{+0.20}_{-0.12}$:(Markevitch et al. 1998), our result generally agrees with their value at about $\gamma \sim 1.25$.

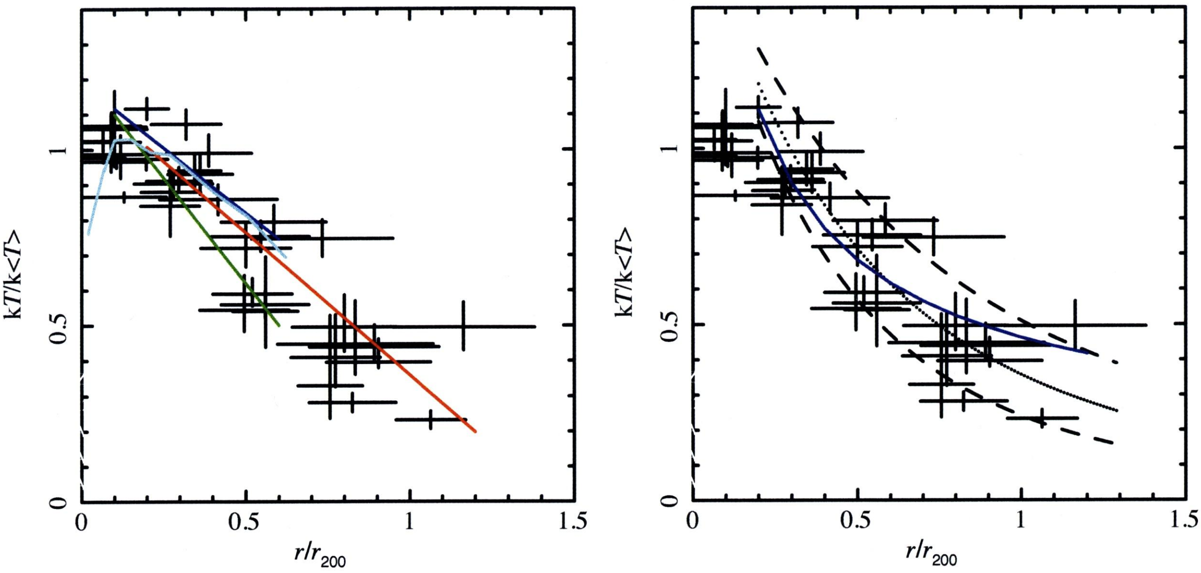

Fig. 6.6: (a) Scaled projected temperature profiles compared with the previous X-ray studies (Chandra, XMM, SWIFT:Vikhlinin et al. 2005; Pratt et al. 2007). The black crosses show our results for relaxed clusters in our sample (A1413, A2204,A963, A2218, PKS0745, A2219, A2390, A2811, A2801). Chandra and XMM-Newton results are shown by green and blue lines, respectively. (b) is same as (a), but compared with the results of numerical simulation by Burns et al. 2010 (dashed and dotted lines) and our polytropic model (blue line).

Burns et al. (2010) discuss a non-equilibrium effect on the temperature profile based on N-body + hydrodynamic simulations. Those simulations indicate a cluster temperature decline by a factor of ~ 3 at r_{200}, consistent with the feature observed for two nearby clusters, PKS 0745-191 and A 1795 (George et al. 2008; Bautz et al. 2009). Burns et al. (2010) approximated the average temperature profile by a function,

$$\frac{T}{T_{\rm avg}} = A\left[1 + B\left(\frac{r}{r_{200}}\right)\right]^{\beta}. \tag{6.4}$$

They obtained the best-fit values as $A = 1.74 \pm 0.03,\ B = 0.64 \pm 0.10 and\beta = -3.2 \pm 0.4$ for the two cluster data. In figure 6.6(b), we plotted the model prediction temperature profile. Black dotted curve shows the best-fit temperature profile, and dashed lines show 1σ error range reported by Burns et al. (2010). The relation of Burns et al. (2010) represents the temperature profiles for the our sample fairly well. This approximate "universal" temperature profile suggests that clusters generally hold self-similar relation even near r_{200}, where sometime dependent effects caused by infalling matter may be seen.

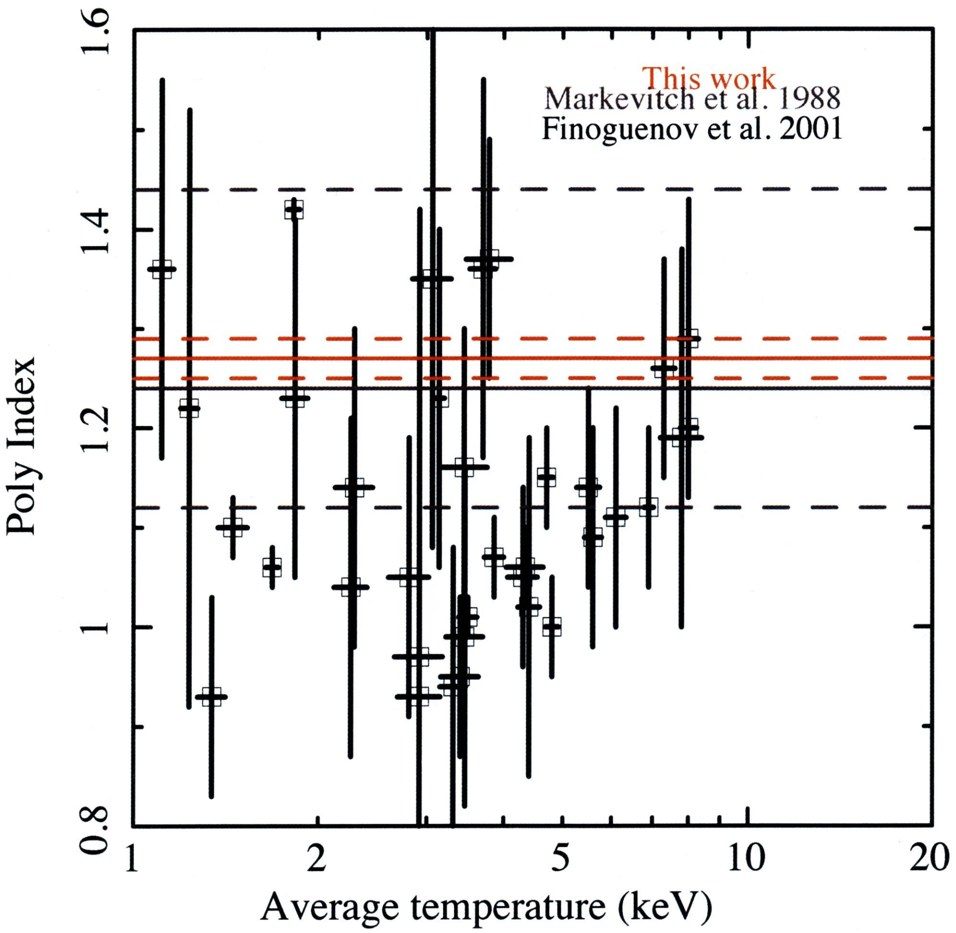

Fig. 6.7: Comparison between the previous works (Gray lines: Markevitch et al. (1998), open squre: Finoguenov et al. (2001)) and the observed values (red lines) of the polytropic index. The crosses with error bars which are drawn at the 68% confidence level.

6.3 Electron density

The electron density profile was calculated from the normalization parameter of the Apec model, defined by

$$Norm = \frac{10^{-14}}{4\pi D_A^2(1+z)^2}\int n_e n_H dV \tag{6.5}$$

with the unit of cm^{-5}, where D_A (cm) is the angular diameter distance to the source, n_e and $n_{\rm H}$ (cm^{-3}) are the number densities of electron and hydrogen, respectively. We note that the resultant normalization using an ARF generated by *xissimarfgen* needs the correction by a factor of SOURCE_RATIO_REG/Ω_e. See Ishisaki et al. 2007 Sec 5.3 for more information. Each annular region, projected in the sky, includes emission from different other annular regions with densities due to integration along the line of sight. We have de-convolved the electron density assuming spherical symmetry by successively calculating the values from the outermost regions. In this process, we assumed a constant temperature in each annular region. The uncertainty of the density due to this assumption is a few %.

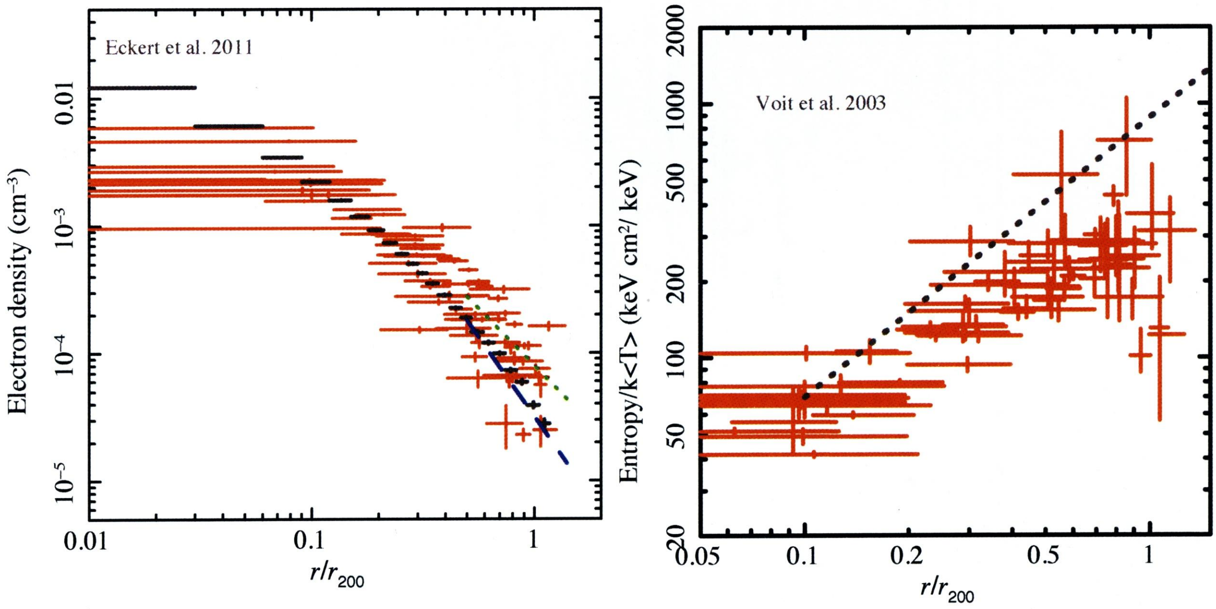

Fig. 6.8: Left: Comparison between the previous works (Gray crosses: Eckert et al. 2011a) and the observed values (red crosses) of the electron density. Blue dashed and green dotted line show the slope with $\propto r^{-2.0}$ and $\propto r^{-1.8}$, respectively. Right: Entropy profiles for each cluster. The profiles have been normalized to the mean temperature. The gray dotted line show the prediction of gravitational heating, $r^{1.1}$ (smoothed accretion) model (Tozzi & Norman 2001; Voit et al. 2003).

Figure 6.2 shows the resultant electron density profiles for individual clusters. To compare with the previous measurements, we normalize each profiles by their virial radius. Figure 6.8 left shows the normalized electron density profiles (red crosses) along with the ROSAT measurements (gray crosses: Eckert et al. 2011a). Our density profiles show a decrease down to

$\sim 10^{-5}$ cm^{-3} around the virial radius in agreement with the previous ROSAT results. We compared the slope of the density profile in the outskirts with the XMM-Newton results (Croston et al. 2008). Croston et al. (2008) report that the gas density slope continues to increase up to -2.0 (blue) with radius in the region 0.5 $r_{500} - r_{500}$ from the XMM-Newton observations, and their density profiles are in agreement with the result of numerical simulation (Borgani et al. 2004). Our results agree with the previous studies for other clusters, and with the predicted profile of $n_e \propto r^{-1.8}$ (blue) based on the β-model (β = 0.6) in the outer region. Our profiles are almost consistent with the ROSAT results, but there exist a large scatter because of the Suzaku HPD. In addition to the above reason, the large scatter comes from the sample selection in our analysis. Our sample includes the system which are in a significant merging state. Because of the radial electron density distribution in clusters is likely to be strongly affected by the dynamical state, merger events are expected to disrupt the density structure significantly.

6.3.1 Entropy profile

The entropy of ICM is used as an indicator of the energy acquired by the gas. We will refer to "entropy" of the ICM by $K = kTn_e^{-2/3}$ following the recent convention. Numerical simulations indicate that a self-similar growth of clusters commonly shows entropy profiles approximated by $r^{1.1}$ up to r_{200}, excluding the cool core region (Voit et al. 2003). Recent XMM-Newton results on the entropy profiles of 31 clusters showed a median slope of 0.98 out to about r_{500} which is approximately $0.5r_{200}$ (Pratt et al. 2010). The slope also showed positive correlation with the average temperature. They also found that morphologically disturbed clusters showed a large scatter (0.5–2.0) in the slope. Suzaku has extended the entropy measurement close to r_{200} for several clusters, and showed a flattening or even a decrease at $r \gtrsim 0.5r_{200}$ as mentioned earlier. Discussion has been made that the ICM may not be under equilibrium in the cluster outer regions (Hoshino et al. 2010).

Figure 6.3 shows the entropy profile for all the observed clusters based on the present Suzaku measurements. The gray line indicates the slope of 1.1, which represents the accretion shock heating model by Tozzi & Norman (2001); Voit et al. (2003). The entropy slope is consistent with this value in the radius range up to $0.5r_{200}$. The slope becomes flatter at $r > 0.5r_{200}$ or goes negative near r_{200}. Figure 6.3 right shows the normalized entropy profiles (red crosses) and the prediction of simulation (gray dotted line $\propto$ $r^{1.1}$). Most of the sample show the "flattening" profiles except for A2801, the low temperature sample. In particular, merging systems (A3376, A3667, A2142 and CIZA2242) show significant deviation from the simulation and some of those sample show sudden drops, which indicate the existence of the shock heating. Those "flattening" profiles are already reported for other several clusters (George et al. 2008; Bautz et al. 2009; Kawaharada et al. 2010; Hoshino et al. 2010; Simionescu et al. 2011; Akamatsu et al. 2011a).

As for the cause of the entropy drop relative to the predicted $r^{1.1}$ relation, three possibilities have been pointed out so far. One is the non-equilibrium effect (Hoshino et al. 2010), Another is the non-thermal pressure (Kawaharada et al. 2010) and the other is the clumpiness (Simionescu et al. 2011; Urban et al. 2011), all working only in the outer regions. These conditions are not mutually exclusive but may be closely related with each other. We will discuss the physical conditions of ICM in the cluster outskirts in the next chapter based on the observed entropy profiles.

6.4 Radio relic clusters: Akamatsu & Kawahara 2011

We normalized the radial temperature profile of each cluster by the flux-weighted average temperature. The resultant scaled temperature profiles are shown in Fig 6.9. We find that the temperature profiles of four samples, including the previous two results, exhibit significant discontinuity across the radio relic. The discontinuity can be interpreted as the shock front at the radio relics. For the other two samples (Zwcl2341N, S), the angular resolution was not good enough to check the presence of the discontinuity, unfortunately. Hereafter, we focus on the 4 samples in which the existence of the temperature discontinuity is confirmed.

Another remarkable point of the scaled temperature is their flatness within the radio relic. Recent X-ray observational results show that the ICM in relaxed clusters indicate the "universal" declining profile up to the virial radius (Markevitch et al. 1998; De Grandi & Molendi 2002; Vikhlinin et al. 2005; Pratt et al. 2007; Akamatsu et al. 2011a). The flatness of the temperature profile within the radio relic might need a heating mechanism, such as a shock heating.

As mentioned above, the temperature profiles of relaxed cluster show "universal" profile", and these clusters do not show a clear sign of dynamical evolution. It is natural that the flat temperature profiles of merging cluster will be settled to the universal profile in less than the cosmic time. In our sample, the locations of the radio relics are far from the cluster center at typically $r_{shock} \sim$ Mpc ($0.5r_{200}$). Because of low density (n_e = $10^{-3-\ -5}$ cm^{-3}) in the outskirts of clusters, the cooling time in those region exceeds the cosmic time. Thus, we have to consider other processes to achieve the "universal profile". Possible physical processes are diffusion and adiabatic expansion. We like to point out that observations along the non-merging axis are of special importance in understanding those processes. Compared with the merging axis, there is little information about the ICM properties in the outer regions along the non-merging axis. We expect that the ICM would be in an earlier stage of heating in the merger axis, and the processes of heating and thermal relaxation may be seen in a clearer manner. Therefore, comparison of the ICM properties between merging and non-merging axies would give us new insights about the formation and evolution process of clusters.

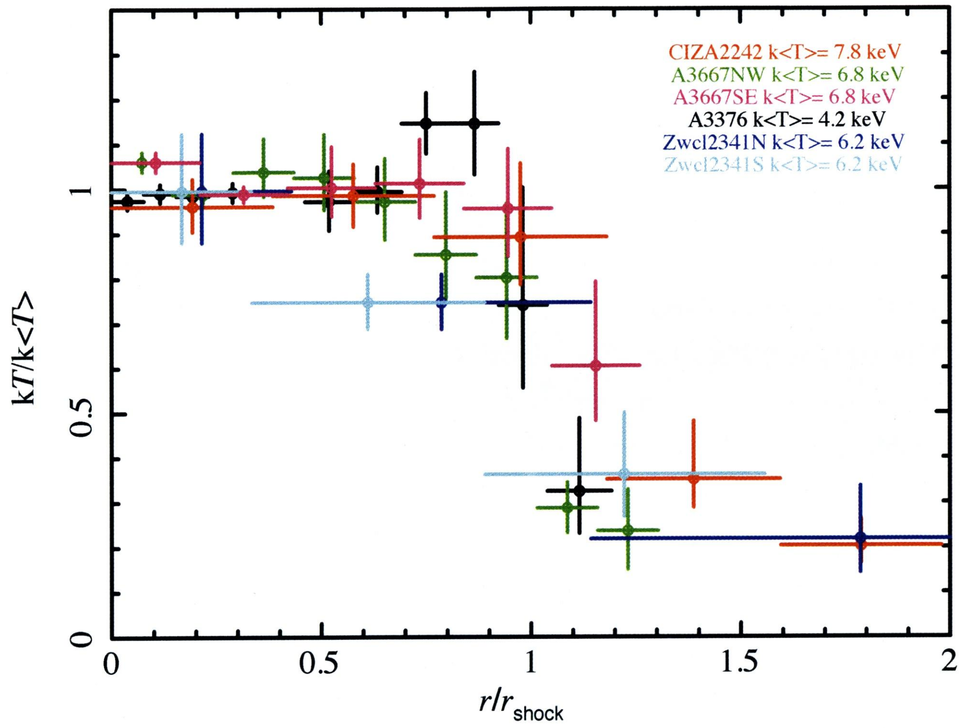

Fig. 6.9: Scaled projected temperature profiles. The profiles have been normalized to the mean temperature and the radius of radio relic r_{shock}. The r_{shock} value derived from the literatures are summarized in Table 7.1.

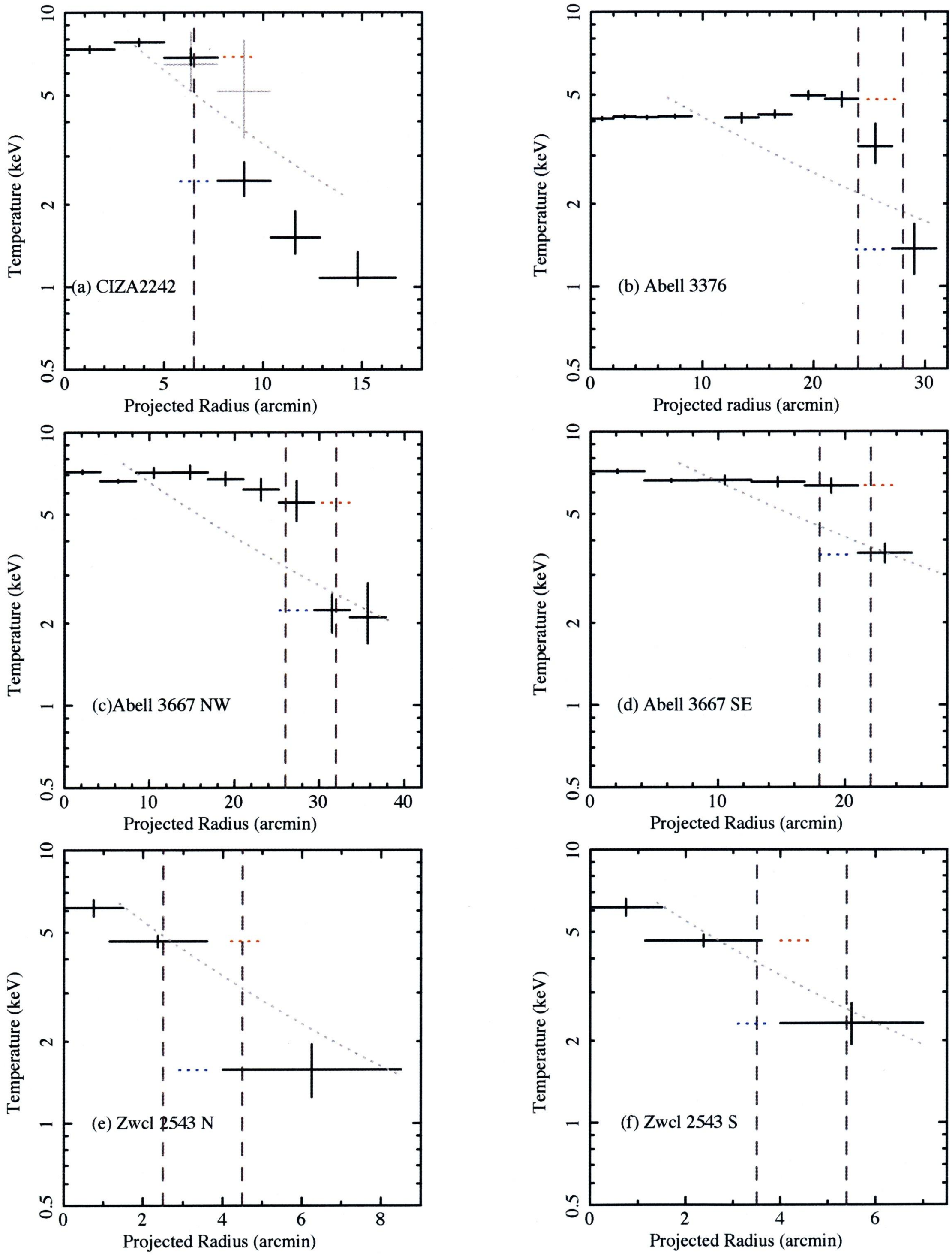

Fig. 6.10: X-ray temperature profiles for the six radio relics. Vertical dashed lines indicate the position the of radio relics. Gray dotted lines indicate the "universal" temperature profile expected from the scaled temperature profiles (Burns et al. 2010). The red and blue horizontal bars show the pre and post shock quantities we use to derive Mach number (Sec 7.1.1). The vertical bars indicate 1σ error. In (a)CIZA2242, the profile in a vertical direction of merging axis is plotted by gray error bars.

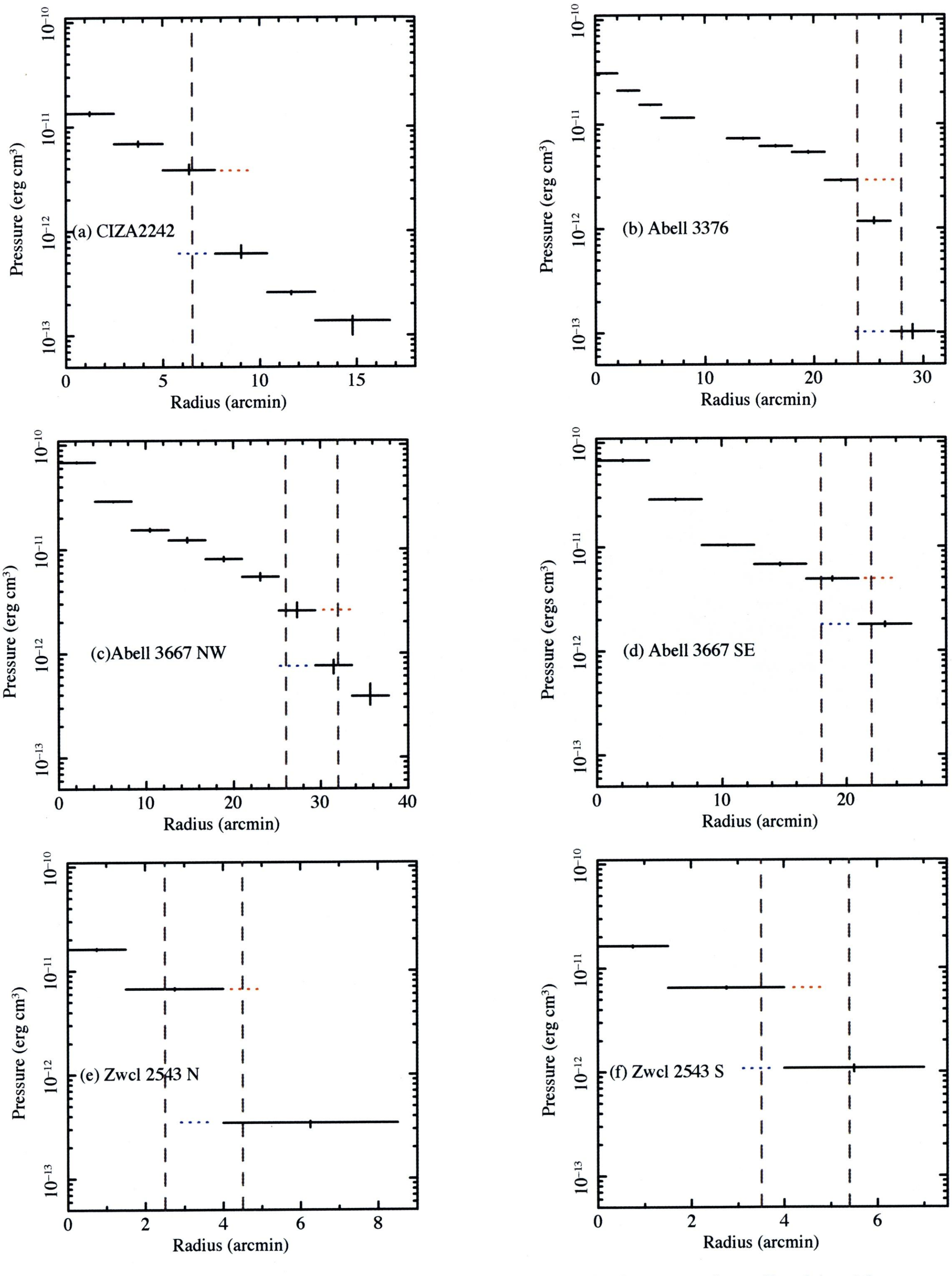

Fig. 6.11: Pressure profiles derived by the deprojection technique as described in Akamatsu et al. (2011a). Vertical dashed lines indicate the position of radio relics. The red and blue horizontal bars show the pre and post shock quantities we use to derive Mach number (Sec 7.1.1). The vertical bars are 1 σ errors.

Chapter 7

Discussion

7.1 Radio relic clusters

We will evaluate the Mach numbers based on the X-ray temperature and pressure with the Rankine-Hugoniot jump condition and compare with the Mach numbers from the radio spectral indeices. The resultant Mach numbers ($\mathcal{M} =$ 1.5-3) are almost consistent with each other, while the Mach number of CIZA2242 from X-ray data tends to be lower than that of the radio observation. These results of the systematic analysis suggested that the giant radio relics in merging clusters represent the strong shock structures, as suggested by the previous studies of the individual clusters. We will also discuss the non equilibrium state of the electron temperature and the average temperature at the radio relic.

7.1.1 Mach number corresponding to the radio relic

We estimate the Mach number using both temperature and pressure jumps across the relics. The Mach number can be obtained by applying the Rankine-Hugoniot jump condition, assuming the ratio of specific heats as $\gamma = 5/3$, as

$$\frac{T_2}{T_1} = \frac{5\mathcal{M}_{X,kT}^4 + 14\mathcal{M}_{X,kT}^2 - 3}{16\mathcal{M}_{X,kT}^2} \equiv f(\mathcal{M}_{X,kT}), \tag{7.1}$$

$$\frac{P_2}{P_1} = 1 + \frac{2\gamma}{\gamma+1}(\mathcal{M}_{X,P}^2 - 1) \tag{7.2}$$

T_1, T_2 and P_1, P_2 are the pre-shock and post-shock temperatures and pressures, and $\mathcal{M}_{X,kT}$ and $\mathcal{M}_{X,P}$ are the estimated Mach numbers by the temperature and pressure jumps. The post and pre quantities we use are marked by red and blue horizontal bars in Figure 7.5 and Figure 6.11.

We compare our results with the Mach numbers derived from the previous radio observations. Based on the Diffusive Shock Acceleration (DSA) theory, we can estimate the Mach number based on the radio spectrum, as

$$\alpha = -\frac{3\mathcal{M}_{\rm radio}^{-2} + 1}{2 - 2\mathcal{M}_{\rm radio}^{-2}}, \tag{7.3}$$

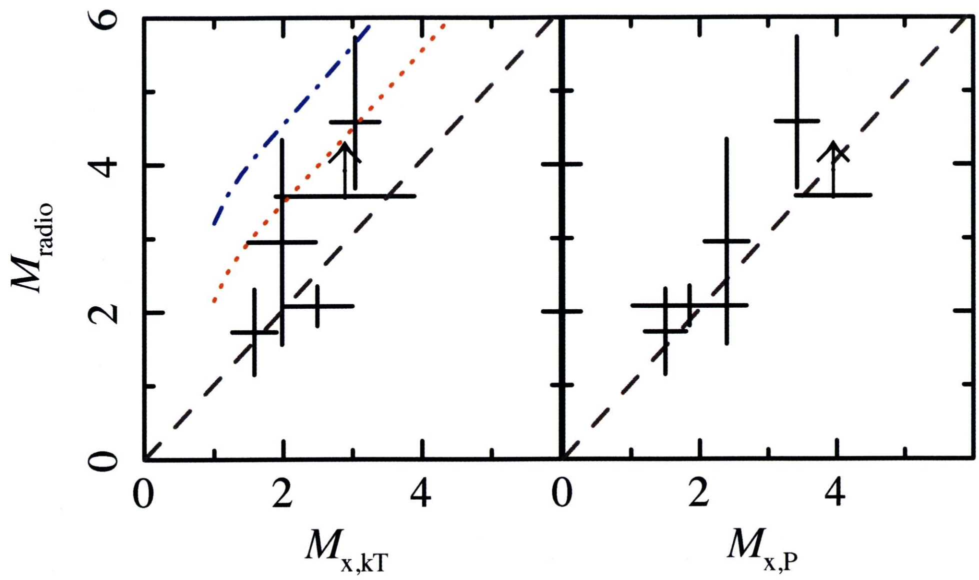

Fig. 7.1: The Mach number derived from radio ($\mathcal{M}_{radio}$) plotted against that from the ICM temperature ($\mathcal{M}_{X,kT}$) and pressure ($\mathcal{M}_{X,P}$). The gray dashed lines indicate linear correlation as a reference. The red dotted and blue dash-dotted lines indicate the theoretical model including the deviation between averaged and electron temperatures with $\epsilon \equiv T_e/\overline{T} = 2/3$ and $1/2$. (Eq. [7.5]) . The error bar of $\mathcal{M}_{X,kT}$ and $\mathcal{M}_{X,P}$ show 68 % confidence level.

where α is radio spectral index and $\mathcal{M}_{\text{radio}}$ is the Mach numbers from the radio observations. For strong shocks, the radio spectral index will be flat at about -0.5. We used the radio spectral indices from the previous radio observations summarized in Table 7.1.

The Mach numbers are listed in Table 7.1. Since we could not find any information of radio spectral index, we do not estimate $\mathcal{M}_{\text{radio}}$ for A3376.

Although Zwcl2341N and Zwcl2341S show no strong signs of temperature discontinuity as mentioned in Sec 6.4, we formally derived the Mach numbers from the X-ray data. Figure 7.1 displays the Mach number from the X-ray data compared with the radio relsults. As shown in this figure, we find that two different methods give consistent results within the current observational error, while the Mach number from the X-ray temperature $\mathcal{M}_{X,kT}$ tend to be lower than that from the radio $\mathcal{M}_{\text{radio}}$.

In the case of CIZA2242, if we assume the mach number from the radio observation is correct, the expected post shock temperature would reach kT = 12.5 keV. Although our results are well reproduced by the 1 temperature model, we fit with a 2 temperature model to the spectrum extracted from 5.′0– 7.′7 annulus, which is just after shock passage region. The metal abundances of the two apec components were tied to be the same, and only the temperature and normalization were set free. We then obtained an almost acceptable fit with χ^2/ d.o.f. = 266/261 compared with the single temperature case of 277/264. The rather low statics of the spectrum hampered us to distinguish between the 2kT and 1kT models. The hot component temperature was derived as $kT_{\text{high}} = 7.79^{+1.41}_{-0.88}$ keV, and the cool one as $kT_{\text{low}} = 1.38^{+0.91}_{-0.28}$ keV, respectiviley. The intensity of the cool component is about an order lower than the hot one. Based on this analysis, there were no signature of the presence of a very high-temperature component.

Based on the numerical simulations of the ICM in merging galaxy clusters, a non-equilibrium state and an electron-ion two-temperature structure have been predicted (Takizawa 2005; Rudd & Nagai 2009; Akahori & Yoshikawa 2010). The shock heating is effective for protons, and after the shock heating, electrons and protons equilibrate via Coulomb collisions on a timescale as shown below (Takizawa 1998);

$$t_{\rm ie} = 2 \times 10^8 \,{\rm yr} \left(\frac{n_e}{10^{-3}\,{\rm cm}^{-3}}\right)^{-1} \left(\frac{T_e}{10^8\,{\rm K}}\right)^{3/2} \left(\frac{\ln \Lambda}{40}\right), \tag{7.4}$$

where $\ln \Lambda$ denotes the Coulomb logarithm (Spitzer 1956). Using Eq. 7.4 and observational value, we estimate the electron-ion equilibration time t_{ie}. In the region just after shock passage, the equilibration time t_{ie} are 0.65 Gyr, 0.55 Gr, 0.41 Gyr and 0.46 Gyr for CIZA2242, A3667NW, A3667SE and A3376, respectively. Within this time-scale, these regions will stay in a non-equilibrium state. Future high resolution X-ray spectrometers, such as SXS on ASTRO-H (Mitsuda et al. 2010) and XMS on Athena, can detect the signs in those non-equilibrium state region.

Although shock velocities can be computed from the sound speed c_s and the shock compression $C = n_2/n_1$, we could not see any clear surface brightness jump in the Suzaku data. Therefore we cannot derive the typical physical scale of the shock structure to attain ion-electron equilibration, $l_{eq} = v_{shock} t_{ie}$. Instead of v_{shock} we use the sound speed c_s itself, and compute $l_s = c_s\, t_{ie}$ since $l_s \gtrsim l_{eq}$ ($l_{eq} = 1 - 4 l_s$). Using the sound speeds $c_s = 665 \pm 80$km/s (CIZA2242), 773 ± 117 km/s (A3667NW) , 981 ± 76 km/s (A3667SW) , and 601 ± 106 km/s (A3376), we derived $l_s = 0.44$ Mpc (CIZA), 0.43 Mpc (A3667NW), 0.41 Mpc (A3667SW) and 0.28 Mpc (A3376). Considering l_{eq} is 2-3 times larger than l_s, the ICM on the shock scale should still remain non-equilibrium state more or less. We introduce the electron and average temperature ratio $\epsilon \equiv T_e/\overline{T}$. Since X-ray temperature reflects the electron temperature, we can rewrite equation (7.1) as $T_2 \rightarrow T_2/\epsilon$. The simulation predicted $\epsilon \sim 0.2$-0.5 (?). If we may assume that $\mathcal{M}_{\rm radio}$ reflects the true Mach number, we can estimate ϵ by comparing $\mathcal{M}_{X,kT}$ with $\mathcal{M}_{\rm radio}$. Solving $f(\mathcal{M}_{\rm radio}) = (T_2/\epsilon)/T_1 = f(\mathcal{M}_{\rm X,kT})/\epsilon$, we obtain

$$\begin{aligned} \mathcal{M}^2_{\rm radio} &= \frac{1}{2\mathcal{M}^2_{X,kT}\epsilon} \left\{ \mathcal{M}^4_{X,kT} + 14\mathcal{M}^2_{X,kT}(1-\epsilon) - 3 \right. \\ &+ \left. \sqrt{12\mathcal{M}^4_{X,kT}\epsilon^2 + [\mathcal{M}^4_{X,kT} + 14\mathcal{M}^2_{X,kT}(1-\epsilon) - 3]^2} \right\}. \end{aligned} \tag{7.5}$$

This relation is plotted by red dotted and blue dot-dashed lines in Figure 7.1 for $\epsilon = 2/3$ and 1/2, respectively. Although we cannot determine the accurate value of ϵ due to the large error, $\epsilon \sim 2/3$ gives good agreement, and in principle the accurate measurement of $\mathcal{M}_{\rm X,kT}$ and $\mathcal{M}_{\rm radio}$ will enable to determine ϵ.

Table 7.1: Basic properties of the clusters

	$kT_{poste\ shock}$ (keV)	$kT_{pre\ shock}$ (keV)	$\mathcal{M}_{kT}$	$P_{post\ shock}$ ($\times10^{-12}$ erg cm^{3})	$P_{pre\ shock}$ ($\times10^{-12}$ erg cm^{3})	$\mathcal{M}_{P}$	α	$\mathcal{M}_{\rm radio}$
CIZA2242	6.73±0.45	1.65±0.20	3.04±0.35	5.65±0.06	0.39±0.06	3.42±0.31	-0.60±0.05	4.58±1.32
Abell3376	4.81±0.29	1.35±0.35	2.94±0.60	2.89±0.05	0.10±0.02	4.78±0.49	–	–
Abell3667NW	5.52±0.95	2.23±0.34	2.29±0.39	2.56±0.42	0.76±0.10	1.70±0.18	-1.10±0.20	2.08±0.27
Abell3667SE	6.34±0.38	3.59±0.28	1.75±0.13	4.92±0.20	2.01±0.25	1.55±0.06	-1.50 ±0.17	1.73±0.58
Zwcl2341N	4.64±0.23	1.57±0.35	2.60±0.44*	6.67±0.17	0.35±0.04	3.96±0.24*	-0.49±0.18	>3.57
Zwcl2341S	4.63±0.23	2.31±0.37	1.95±0.25*	6.67±0.17	10.81±0.07	2.26±0.09*	-0.76±0.17	2.95±1.39

$*$: Although there are no strong signs of temperature discontinuity as mentioned in Sec 6.4, we formality derived the Mach number from X-ray data.

7.1.2 Comparison with numerical simulations

Similation of merging clusters have been carried out for two cases. We will describe them and compare with our results.

CIZA2242: van Weeren et al. (2011) performed hydrodynamical simulations of idealized binary cluster mergers, based on standard hydrodynamics and gravity. They use passive tracer particles in the simulations to model the radio emission. They find that a merger with a mass ratio between 1.5 : 1 and 2.5 : 1 provides the best match to the observed distribution of the radio emission in this cluster. Those simulations predict that post/pre shock ICM temperatures are $kT_{\rm post} \sim 7.5$ keV and $kT_{\rm pre} \sim 1.5$ keV, respectively (See fig 8 in van Weeren et al. (2011)). Those predictions of post/pre shock ICM temperatures are well consistent with the present observational values $kT_{\rm post} \sim 6.75 \pm 0.45$ keV and $kT_{\rm pre} \sim 1.65 \pm 0.20$ keV (68% confidence), respectively.

A3376: Paul et al. (2011) demonstrate cosmological simulations of major mergers in galaxy clusters. They found striking similarities in the morphology and other physical parameters of A3376, and discussed properties of "symmetrical radio relics". They find that ICM temperature behind the shock front shows a slightly enhanced profile (see Paul et al. (2011) fig.6). The observed temperature profile of A3376 within20′ (1.2 Mpc corresponding to $0.6r_{200}$) is almost flat or rising with $kT \sim 4.0$ keV, which is explainable on the basis of those simulations.

From the simulations of the structure formation of the Universe (Enßlin & Brüggen 2002; Vazza et al. 2009), cosmological shock waves induced by hierarchical clustering around clusters of galaxies are expected. Those cosmological shocks typically show the Mach number up to $\sim 10^3$. Shocks in the ICM and cluster outskirts, in particular, are generated by merger events. Based on the numerical simulations (Miniati et al. 2000; Vazza et al. 2009), those merger shocks typically exhibit the Mach number < 3. The distribution of the Mach number in our results show a peak around $\mathcal{M} \sim 2$. This result is well consistent with the prediction of numerical simulations. Our sample, however, is still limited to 6 radio relics, which is not enough. Future X-ray, SZ and radio surveys can reveal large amount of shock structures in clusters of galaxies.

7.1.3 Possibility of the non-equilibrium ionization

Theoretical studies about the non-equilibrium state and the electron-ion two-temperature structure of the ICM in merging galaxy clusters have been carried out (Takizawa 2005; Rudd & Nagai 2009; Akahori & Yoshikawa 2010). Recent Suzaku results suggest non-equilibrium features characterized by a different electron and ion temperatures in the cluster outskirts (Wong et al. 2009; Hoshino et al. 2010). In merging clusters, shock heating and compression raise the X-ray luminosity in the outer regions, giving us a good opportunity to look into the non-equilibrium features and gas heating processes.

We examine the possibility of a deviation between ion and electron temperatures. Assuming that the shock propagates from the cluster center to the outer region, the region just behind the shock may have a higher ion temperature than the electron one, because the time is not enough to reach the equilibrium. We calculate the ion-electron equilibration time and the ionization timescale. The ion-electron equilibration time is estimated from the electron density and temperature of ICM as shown in eq 7.4. The ionization timescale can be estimated from relative line intensities. Because the lines are very weak in the cluster outer region, we adopt the timescale for equilibrium ionization as $n_e t = 3 \times 10^{12}$ cm^{-3} s given by Masai 1984; Fujita et al.(2008) indicating that the outer region attains ionization equilibrium.

In fig 7.2, solid diamonds show the ion-electron equilibration times of CIZA2242, A3376 and A3667 based on the observed temperature and density profiles. The dashed diamonds in fig 7.2 show the resultant values of ionization timescales for $n_e t = 3 \times 10^{12}$ cm^3 s. The horizontal axis of fig 7.2 is normalized by the radio relic radius. The solid curve shows the expected time after the shock heating assuming a constant shock speed. The relaxation and ionization timescales, considering ion-electron Coulomb collisions, are both longer than the expected elapsed time after the shock heating around $r > 0.5 - 0.7 r_{\rm shock}$. This suggests that the region near the radio relic would not have reached ion-electron equilibrium. This can be confirmed with future spectroscopic observations which will be able to determine ion temperature through line width measurements.

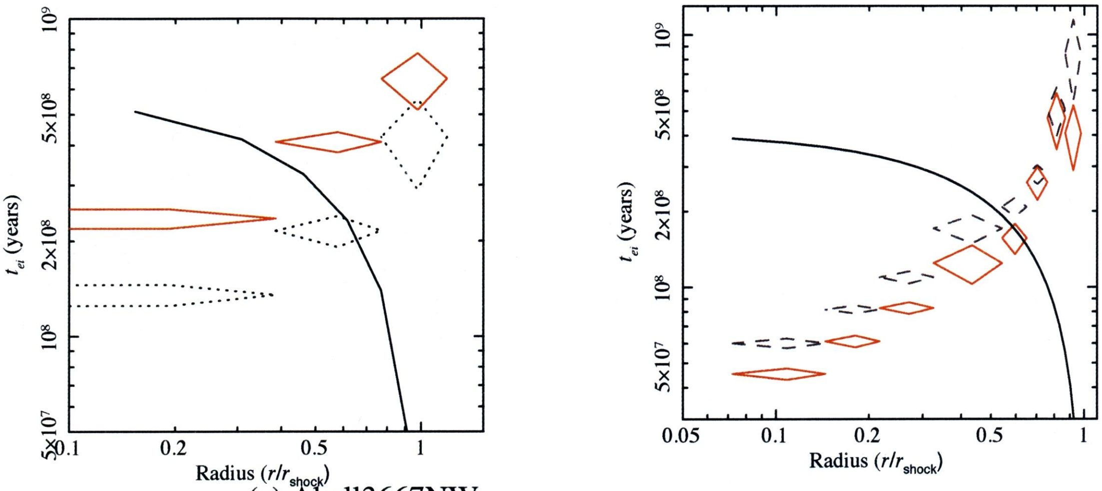
(a) CIZA2242

(b) Abell3376

(c) Abell3667NW

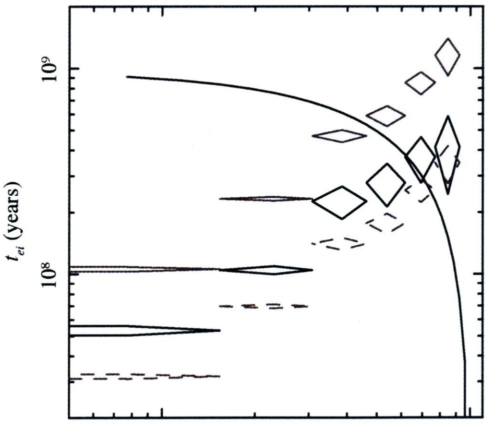

Fig. 7.2: Ion-electron equilibration time scale. Horizontal scale is normalized by the radius of the radio relic. The solid curve shows the time after a shock heating assuming a constant shock speed. Black diamonds show the ion-electron equilibration time calculated by equation 7.4. Gray solid and dashed diamonds show the ionization time for $n_e t = 3 \times 10^{12}$ cm^{-3} s.

7.2 Relaxed clusters: universal temperature profile

In this section, we discuss the temperature profile obtained by Suzaku. The temperature distribution in the ICM is the key information in the characterization of the thermal history and mass structure. Recent cosmological hydrodaynamical simulations in cold dark matter (CDM) model well reproduced declining temperature profiles in the cluster outer region (Ettori et al. 2004; Borgani et al. 2004). Those simulations show good agreement with recent observational results, e.g., ASCA, BeppoSax, Chandra and XMM-Newton (Markevitch et al. 1998; De Grandi & Molendi 2002; Vikhlinin et al. 2005; Pratt et al. 2007). Vikhlinin et al. (2005) reported that the observed temperature profiles by *Chandra* showed good agreement with numerical simulations employing the entropy conserving version of the smoothed particle dynamics (SPH) code (Springel & Hernquist 2002).

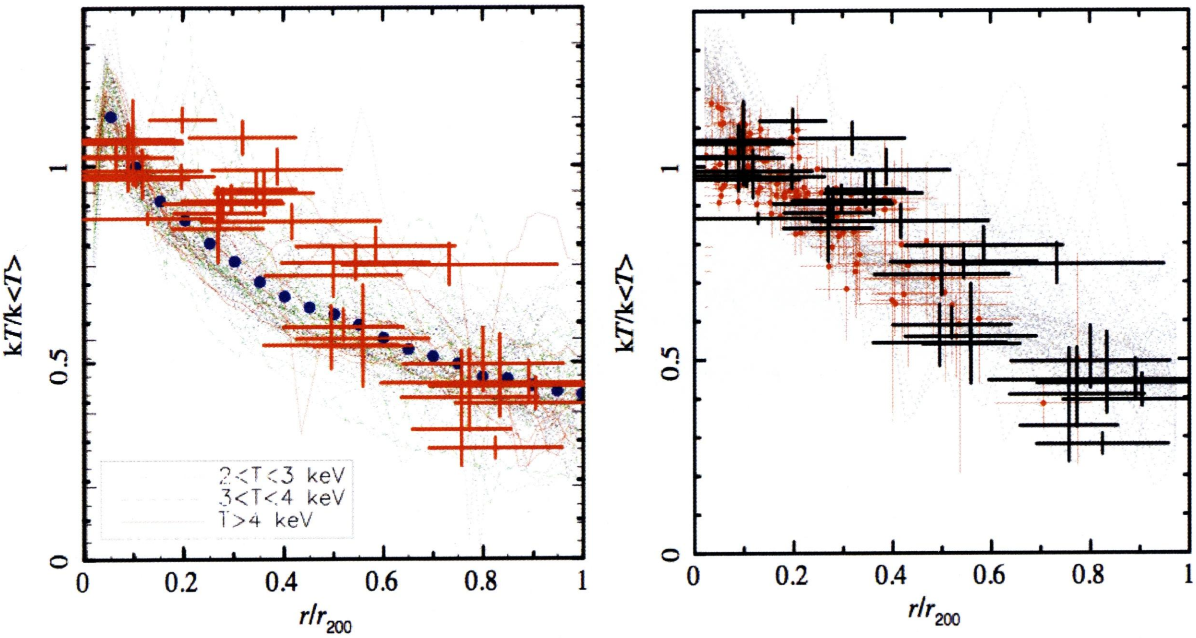

Fig. 7.3: Scaled projected temperature profiles (red crosses) compared with those from numerical simulations by Ettori et al. (2004) (left) and Borgani et al. (2004), respectively. In the left panel, blue dotted line shows the average of the simulated temperature profiles. In the right panel, small red filled circles show the temperature profiles obtained by XMM-Newton (Pratt et al. 2007). The simulated profiles by Borgani et al. (2004) are taken from Pratt et al. (2007).

We compare our observed temperature profiles with 2 numerical simulations by Ettori et al. (2004) and Borgani et al. (2004). In this simulation, Ettori et al. (2004) use the tree+SPH (smoothed particle hydrodynamic) code GADGET-2 for a cold dark matter (CDM) model. It includes radiative cooling, star formation and supernova feedback and allows the thermodynamic structure of clusters to be resolved radially up to redshift $z = 1$ in a way that is not yet completely accessible to observations. Borgani et al. (2004) used the Tree+SPH code GADGET to simulate a concordance CDM cosmological model within a box of 192 h^{-1} Mpc on a side,

480^3 dark matter particles and as many gas particles. The simulation includes radiative cooling assuming zero metallicity, star formation and supernova feedback.

Figure 7.3 shows the comparison. The simulated temperature profiles are scaled with the emission-weighted temperature. The observed temperature profiles are basically in good agreement with those simulation from $0.2r_{200}$ to the virial radius. ICM temperature gradually decreases by factor 2-3 from the center to the virial radius. From the previous works, the problem of discrepancy between simulations and observations in the central region was reported (Vikhlinin et al. 2005; Pratt et al. 2007). This discrepancy may be caused by the complex physical process in the central region. Because of the short cooling time in the central region, there is a significant large effect of radiative cooling. However, observed temperature profiles do not cool as expected (cooling flow paradigm) and the physical process to stop the cooling in the central region is still somewhat unclear. Although more detailed studies of the central region with observational and numerical studies are required, it is out of the scope of this thesis. In suumary, we show that those numerical simulations can describe the average temperature profile of observed clusters.

As shown in sec 6.2.1 and discussed in this section, ICM temperature profiles in relaxed clusters show "universal" decrease from $0.2r_{200}$ to the virial radius and this trend is in agreement with numerical simulations. However, temperature profiles of merging clusters show significant deviation from those profiles. In particular, A3376 shows flat temperature profile upto 0.8 r_{200} and a rise before the shock front. We regard this feature to be caused by the merger shock, which cause large impact on the ICM temperature via shock heating. In the A3376 case, we are probably observing the "fresh" state of the shock heating. This temperature excess will disappear after a cosmological timescale via conduction and dissipation, and eventually settle down to the "universal" temperature profile. Therefore, the temperature profiles of merging clusters offer us "snapshots" of various stage in the course of the dynamical evolution of cluster of galaxies.

7.3 Relaxed cluster: mass profile

In this section, we discuss the relation between the gravitational mass and the cluster average temperature, which is usually called as "$M-T$ relation". For X-ray mass estimation, we select 8 relaxed cluster of galaxies from our sample, which are A2801, A2811, A1413, A2204, A2218, A963, A2219 and A2390. We estimate the gravitational mass based on the observed temperature and density profiles. Here, we assume hydrostatic equilibrium and spherical symmetry, and calculate the gravitational mass within 3-demensional radius R with the following formula (Fabricant et al. 1980),

$$M_R = -\frac{R^2}{\rho_g G}\frac{dP_g}{dR} = -\frac{kTR}{\mu m_p G}\left(\frac{d\ln\rho_g}{d\ln R} + \frac{d\ln T}{d\ln R}\right), \tag{7.6}$$

where G is the gravitational constant, and μ (≈ 0.6) is the mean molecular weight of gas.

Next, we modeled the observed electron density and the projected temperature profiles based on the approach basically following the treatment by Vikhlinin et al. (2006). Vikhlinin et al. (2006) modeled the temperature profile to approximate the observed databy *Chandra*;

$$T(r) = T_0 \frac{(r/r_t)^{-a}}{[1+(r/r_t)^b]^{c/b}}, \tag{7.7}$$

$$T_{\rm cool} = \frac{x + T_{\rm min}/T_0}{x+1}, x = \left(\frac{r}{r_{\rm cool}}\right)^{a_{\rm cool}} \tag{7.8}$$

$$T_{3D}(r) = T_{\rm cool}T(r) \tag{7.9}$$

Here, $T(r)$ represents the temperature outside of the central cooling region approximated with broken power law, and $T_{\rm cool}$ represents the temperature decline in the central region in most clusters. Vikhlinin et al. (2006) used the above temperature model and showed that this model well reproduced the observed temperature profiles. Unfortunately, Suzaku XRT HPD is not as good as the Chandra resolution. Hence, we modified the above model to mach Suzaku observations with reduced number of parameters as below;

$$T(r)_{\rm Suzaku} = T_0 \frac{(r/r_{\rm t})^{-a}}{[1+(r/r_{\rm t})^b]^c}. \tag{7.10}$$

This model has many functional freedom (5 free parameters) and can adequately describe almost any type of smooth temperature distribution in the radial range of interest.

For the same reason, electron density profiles can be reproduced by a simple β-model;

$$n_e(r) = n_0 \left[1 + (\frac{r}{r_{\rm c}})^2\right]^{-3/2\beta}. \tag{7.11}$$

Using the above 2 equations, we modeled the observed temperature and electron density and evaluate entropy, pressure and mass. Table 7.2 shows the resultant values of the X-ray mass estimations and f_{gas} which is the ratio of gas mass $M_{g,500}$ to the total mass M_{500} within r_{500}.

Table 7.2: Masses, average temperatures, and gas fractions

	r_{500}	r_{200}	M_{500}	$M_{g,500}$	$f_{gas,500}$	K/K^*
cluster	kpc	kpc	($10^{14}M_\odot$)	($10^{14}M_\odot$)		
A2811	1270	1900	$6.29^{+2.32}_{-1.21}$	0.48±0.10	$0.076^{+0.028}_{-0.015}$	$0.765^{+0.149}_{-0.131}$
A2801	850	1270	$0.87^{+0.16}_{-0.11}$	0.10±0.01	$0.114^{+0.021}_{-0.015}$	$0.997^{+0.110}_{-0.066}$
A1413	1450	2130	$4.79^{+0.63}_{-0.47}$	0.80±0.04	$0.167^{+0.022}_{-0.016}$	$0.693^{+0.110}_{-0.065}$
A2204			$5.10^{+0.32}_{-0.27}$	0.75±0.04	$0.147^{+0.010}_{-0.009}$	$0.574^{+0.076}_{-0.112}$
A2218	1520	2200	$7.55^{+1.46}_{-1.05}$	1.32±0.06	$0.174^{+0.034}_{-0.024}$	$0.588^{+0.022}_{-0.027}$
A963	1450	2070	$4.81^{+0.93}_{-0.60}$	0.87±0.04	$0.181^{+0.035}_{-0.022}$	$0.547^{+0.071}_{-0.036}$
A2219	1930	2730	$11.53^{+1.00}_{-0.98}$	3.01±0.06	$0.262^{+0.023}_{-0.022}$	$0.538^{+0.014}_{-0.018}$
A2390	1820	2570	$12.68^{+1.41}_{-1.16}$	2.34±0.06	$0.184^{+0.021}_{-0.017}$	$0.652^{+0.023}_{-0.031}$

$*$: Entropy value expected from the extension of $r^{1.1}$ relation to 0.1~1 r_{200}.

Figure 7.5-7.12 show the resultant temperature, entropy, pressure and gravitational mass estimations. In the entropy profiles, the modeled observed entropy is shown with a red solid line and prediction of numerical simulation (Voit et al. 2003) is shown by a gray dotted line. We discuss physical conditions of ICM in the cluster outskirts in the next section.

In the X-ray observations of clusters of galaxies, the observed scaling relations are usually expressed in terms of the temperature T. However, basic physical properties such as radius, temperature, luminosity, etc. are functions of mass and redshift. The scaling relations are used as important tools to study the physics of cluster formation (Voit & Ponman 2003). To understand the real scaling relation of clusters of galaxies, we need to look into the relation between mass and temperature as $M - T$. We compare our mass estimations with the previous observational works (ASCA,Chandra, XMM-Newton Finoguenov et al. 2001; Vikhlinin et al. 2006; Arnaud et al. 2005), as shown in figure 7.4. The data are well fitted by a power law model (χ^2/d.o.f=7.2/6) as

$$M_{500} = A \times \left[\frac{kT}{5\ \mathrm{keV}}\right]^{\alpha}. \tag{7.12}$$

The resultant values are $A = 3.2 \pm 0.2 \times 10^{14}\ M_\odot$ and $\alpha = 1.58 \pm 0.10$, respectively. Our $M - T$ relation agrees with the previous X-ray study by Arnaud et al. (2005), which give $A = 4.1 \pm 0.2 \times 10^{14}\ M_\odot$ and $\alpha = 1.49 \pm 0.15$, respectively. Figure 7.4 left panel shows the $M - T$ relation for the present sample for which temperature profiles are measured within 0.4 r_{200}. Red crosses and dotted line show the estimated mass and best-fit $M - T$ relation in our sample.

We also compare our gas mass estimations with other works (Zhang et al. 2006; Zhang et al. 2007). Figure 7.4 right panel shows the resultant values of our gas mass estimation with the previous works. Our results are shown with red crosses and are consistent with the previous works (black and gray crosses). To compare with the prediction of self-similar relations, we fitted $M_{500,\mathrm{gas}} - T$ relation with the following formula;

$$M_{500,\mathrm{gas}} = A \times [kT]^{\alpha}. \tag{7.13}$$

The resultant best-fit values are $A = 0.014 \pm 0.002 \times 10^{14}\ M_\odot$ and $\alpha = 2.06 \pm 0.15$, respectively. Zhang et al. (2011) reported the slope of $M_{500,\mathrm{gas}} - T$ for their sample obtained by XMM-Newton to be 1.86 ± 0.19, which is consistent with our result within the margin of error. Zhang et al. (2011) also checked $M_{500,\mathrm{gas}} - T$ for the Vikhlinin et al. (2006) sample obtained by Chandra and found the slope of those sample to be 1.84.

Our mass estimations (gravitational mass and gas mass) agree well with those of other studies. This agreement support the scaling relations of clusters of galaxies (table 7.3).

Table 7.3: Best fit parameters for our $M - T$ relations

	$M_{500} = A \times [\frac{kT}{5\ \mathrm{keV}}]^{\alpha}$		$M_{500,\mathrm{gas}} = A \times [kT]^{\alpha}$	
	A [$10^{14}\ M_\odot$]	α	A[$10^{14}\ M_\odot$]	γ
Self similar	-	1.5	-	1.5
This work	3.2±0.2	1.58±0.10	0.014±0.002	2.06±0.15
Arnaud et al. 2005	4.1±0.2	1.49±0.15	–	–
Zhang et al. 2011	-	-	–	1.86±0.19

Based on our determination of the cluster mass (gravitational mass and gas mass), we estimate the ratio of the X-ray gas mass to the total gravitating mass as shown as a function of the average temperature in figure 7.4 bottom panel. The f_{gas} value are compared with the previous studies and agree with those estimations (Vikhlinin et al. 2006; Ettori et al. 2009). Except for A2219, A2801 and A2811, the resultant f_{gas} value are almost consistent with expected gas mass fraction (17%) from cosmological studies.

In the case of A2801 (2.3 keV) and A2811 (5 keV), the gas mass fractions show significantly lower value than this value. One possible explanation is that, since those two clustesr belong to the Sculptor supercluster, the gas may have escaped from the cluster to the supercluster space. This scenario was already suggested by Obayashi et al. (1998) from the ASCA observations of this supercluster. They found that gas mass fractions of A2801 and A2811 within 1 Mpc are 4.7 % and 5.2%, respectively.

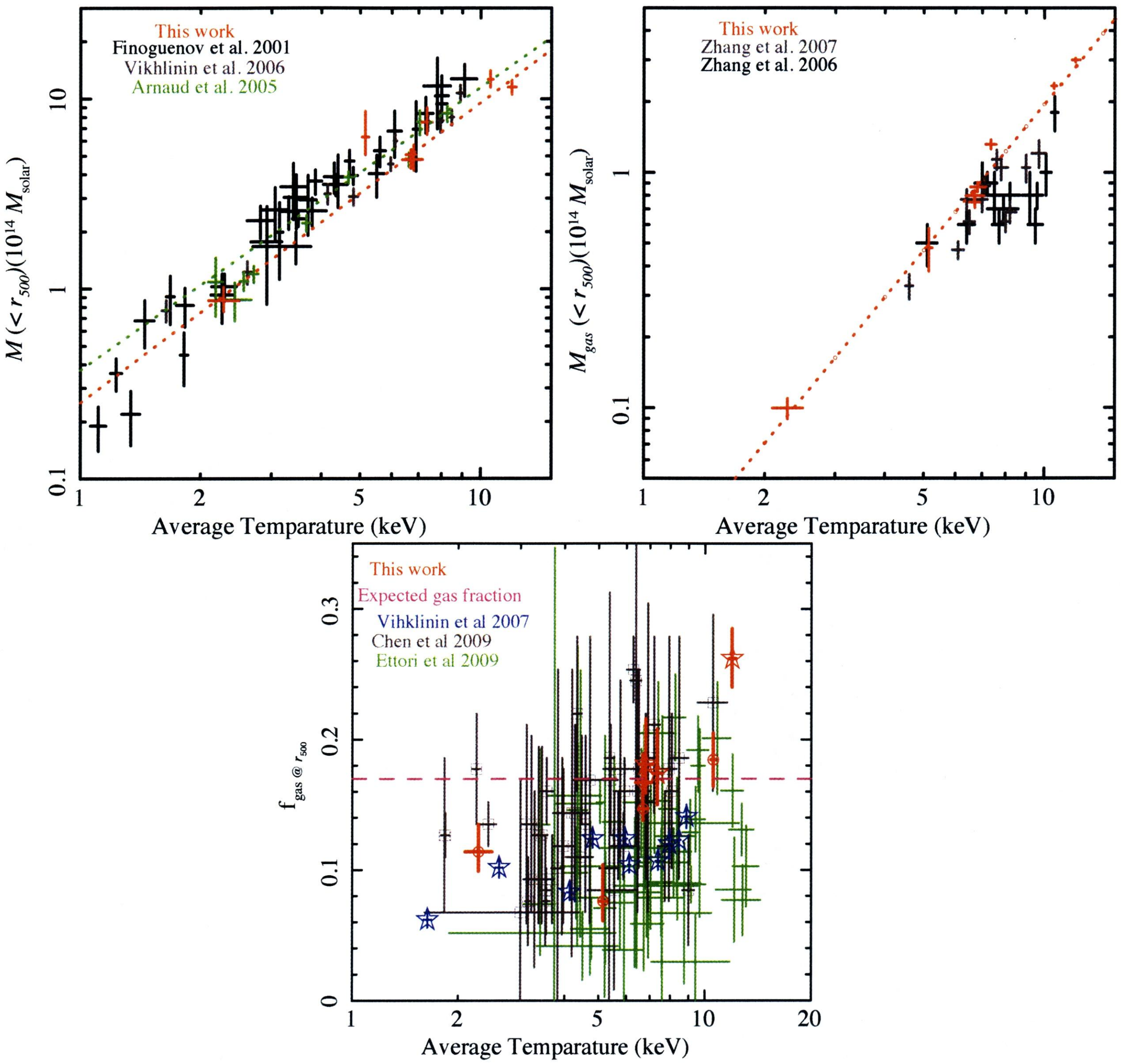

Fig. 7.4: (a) $M - T$ relation for the cluster samples with average temperature. Red crosses represent the mass determinations using observational values. Black and gray crosses are the previous works by ASCA and Chandra (Finoguenov et al. 2001; Vikhlinin et al. 2006). Red and green dotted lines show the best-fit $M - T$ relations for our sample and Chandra data (Arnaud et al. 2005). (b) $M_{gas} - T$ relation for different cluster samples with average temperature. Red crosses represent the mass determined from our observations. Red dotted line shows the best-fit $M_{500,gas} - T$ relation for our sample. Black and gray crosses are the previous works by XMM-Newton (Zhang et al. 2006; Zhang et al. 2007). (c) Observed gas fractions within r_{500} (red crosses). Blue, gray and green crosses are for the previous works by Chandra and XMM-Newton (Vikhlinin et al. 2006; Ettori et al. 2009). Magenta dashed lines show the expected gas mass fraction.

(a)Temperature profile of A2204

(b)Entropy

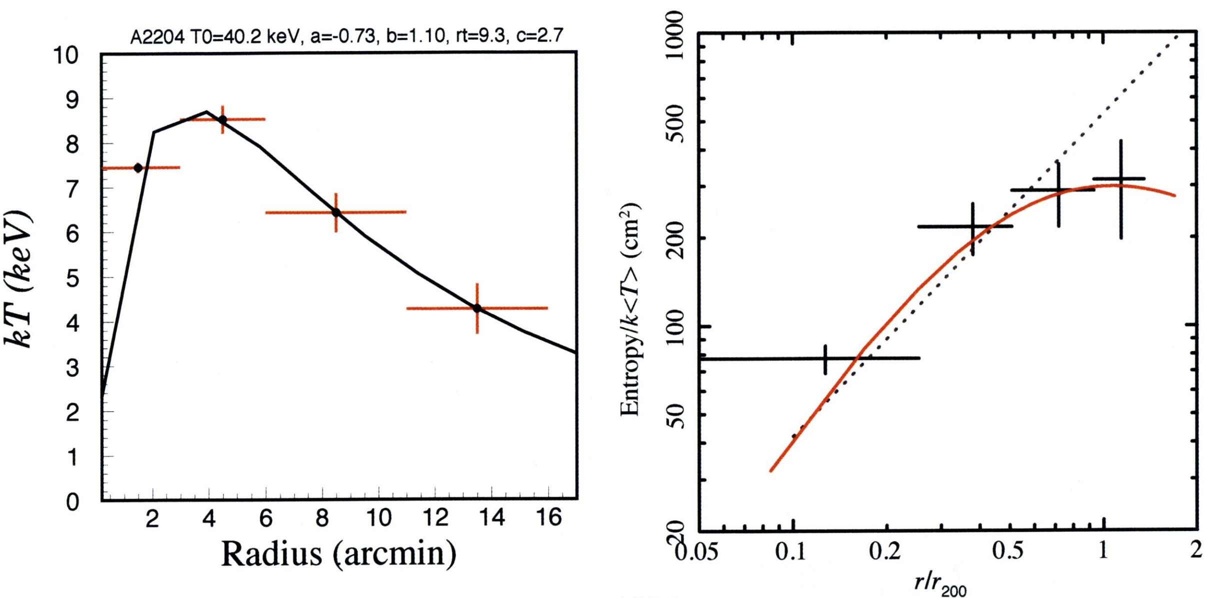

(c)Pressure

(d)Mass

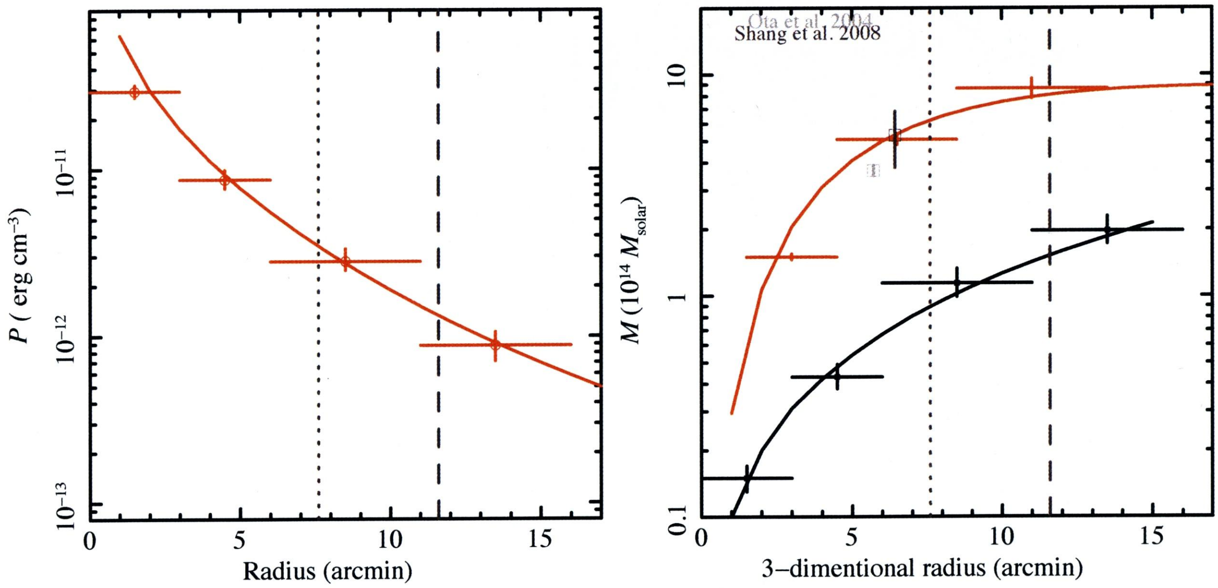

Fig. 7.5: (a) Temperature profile of A2204 with the best-fit model of eq 7.10 (black curve). The best-fit values of model parameters are shown in the figure. (b) Entropy profile divided by the average electron temperature (black crosses). Red solid line shows the model entropy profile estimated from eq 7.10 and eq 7.11. Gray dotted line indicates the prediction of accretion heating model, $r^{1.1}/kT$ (Tozzi & Norman 2001; Voit et al. 2003). (c) Pressure profile fitted with the model. (d) Gravitational mass and gas mass profiles of A2204. Red and black solid curves show the modeled mass profiles estimated from eq 7.10 and eq 7.11. In figure (c) and (d), gray dotted and dashed lines represent r_{500} and r_{200}, respectively.

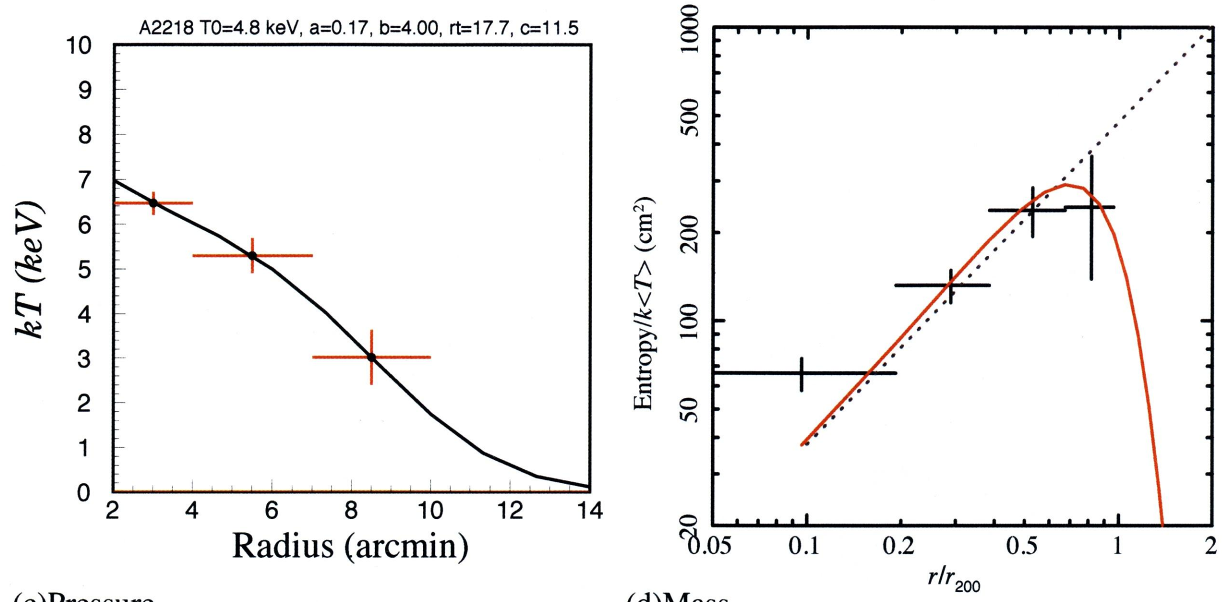

(a)Temperature profile of A2218

(b)Entropy

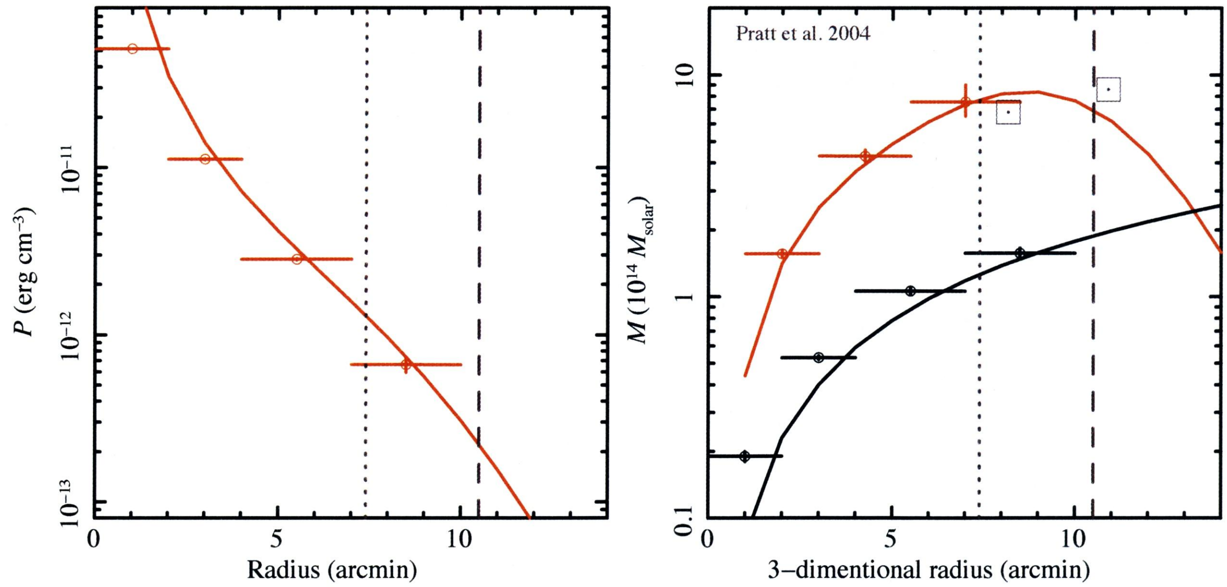

(c)Pressure

(d)Mass

Fig. 7.6:

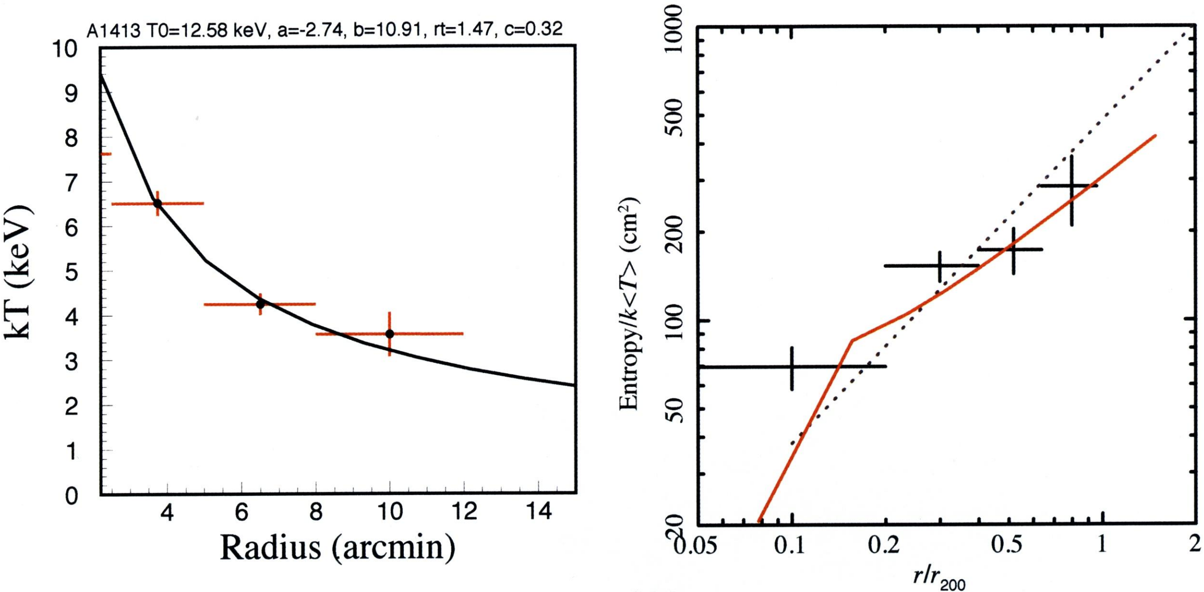

(a)Temperature profile of A1413

(b)Entropy

(c)Pressure

(d)Mass

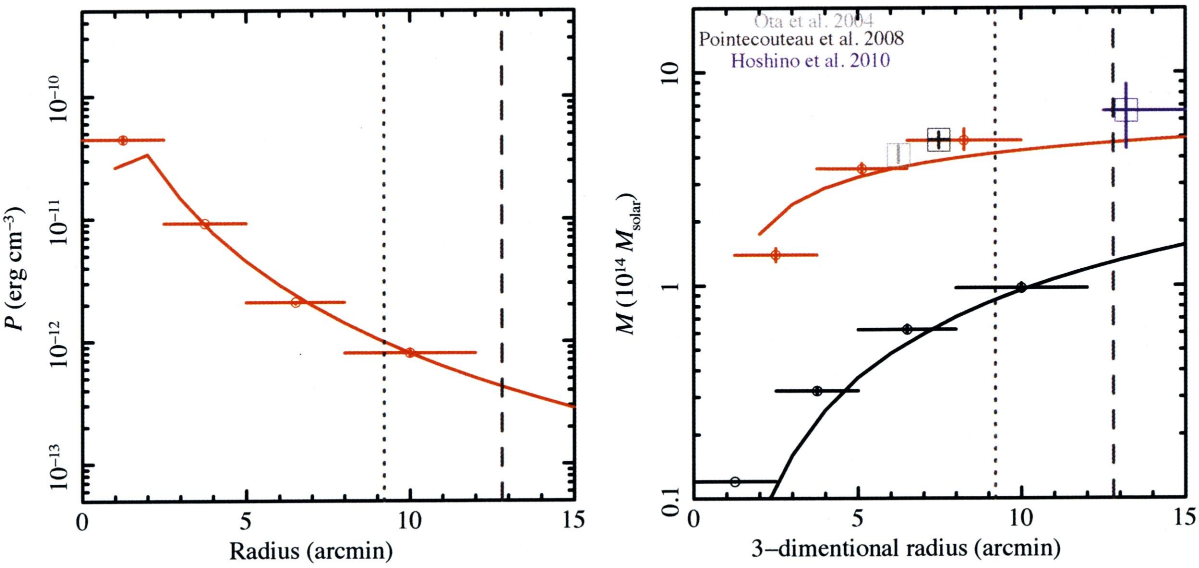

Fig. 7.7: A1413 continued.

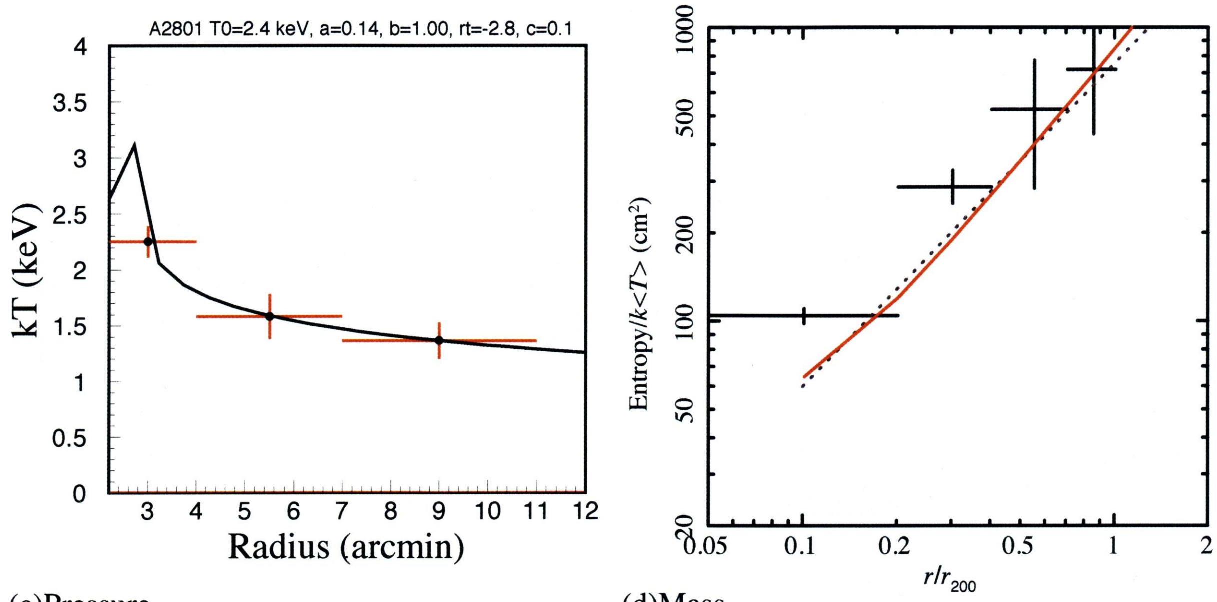
(a)Temperature profile of A2801

(b)Entropy

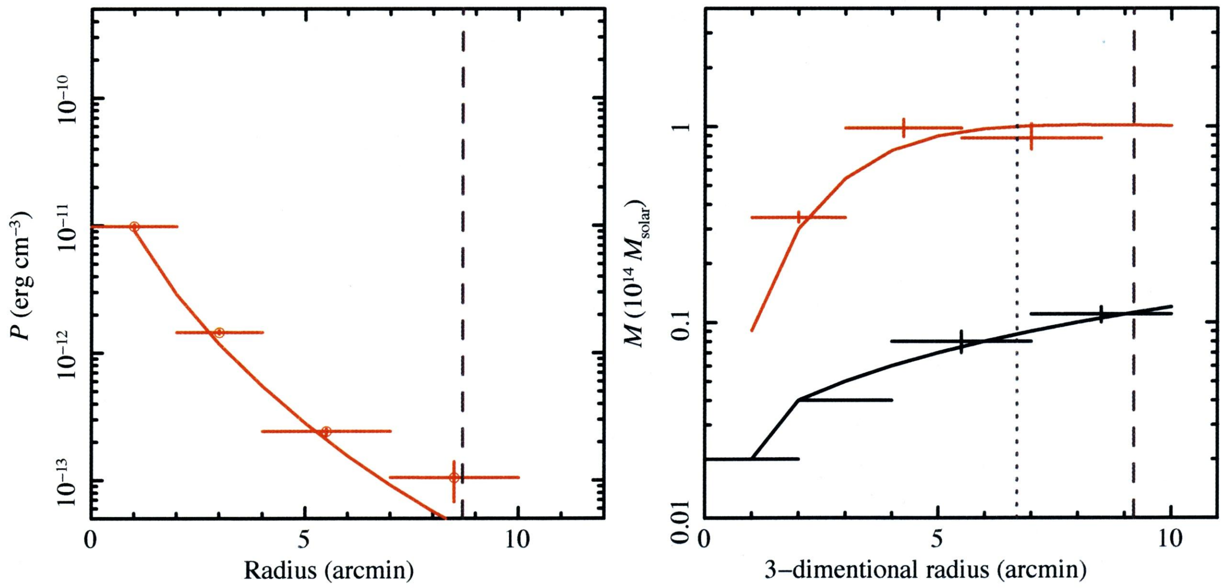
(c)Pressure

(d)Mass

Fig. 7.8: A2801 continued.

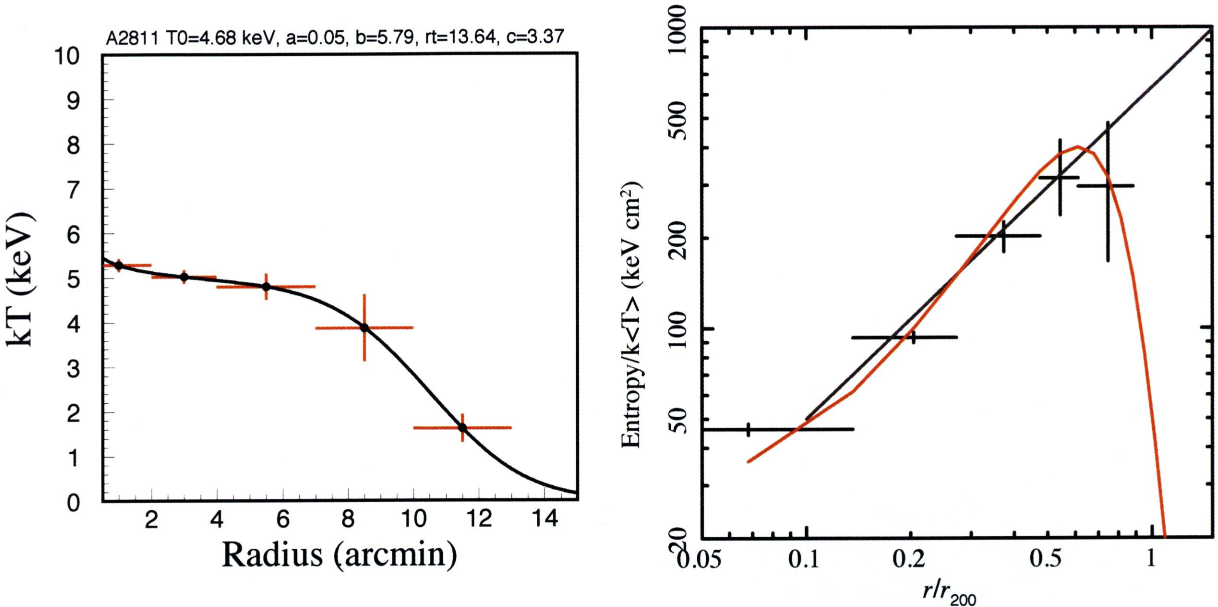

(a)Temperature profile of A2811

(b)Entropy

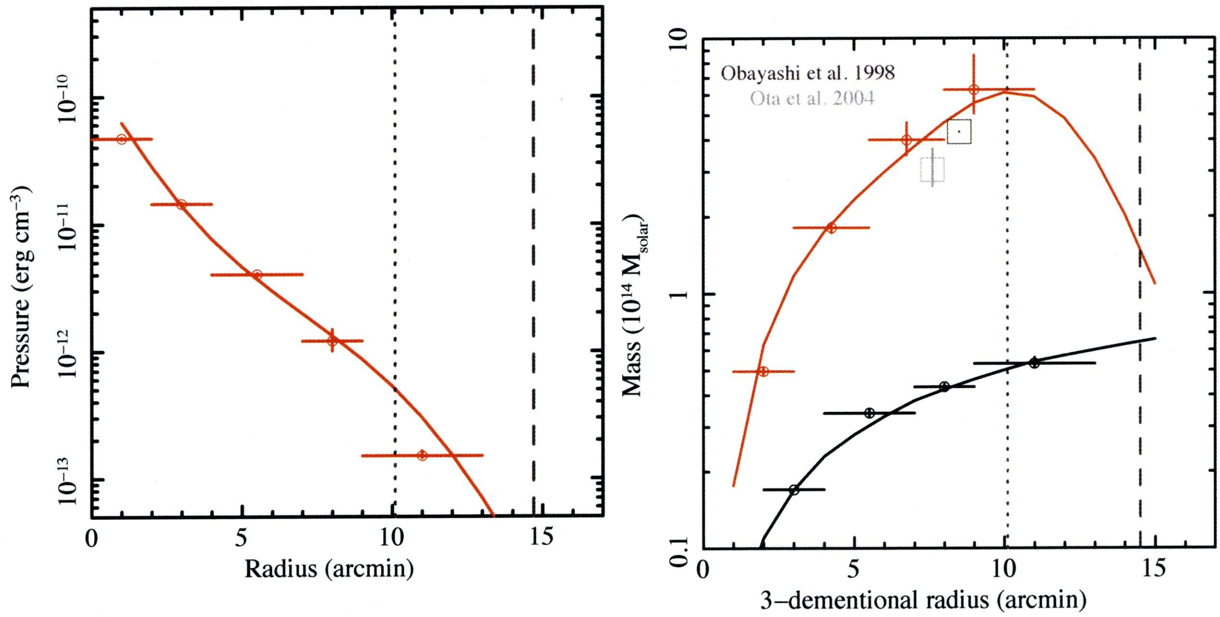

(c)Pressure

(d)Mass

Fig. 7.9: A1413 continued.

(a)Temperature profile of A963 (b)Entropy

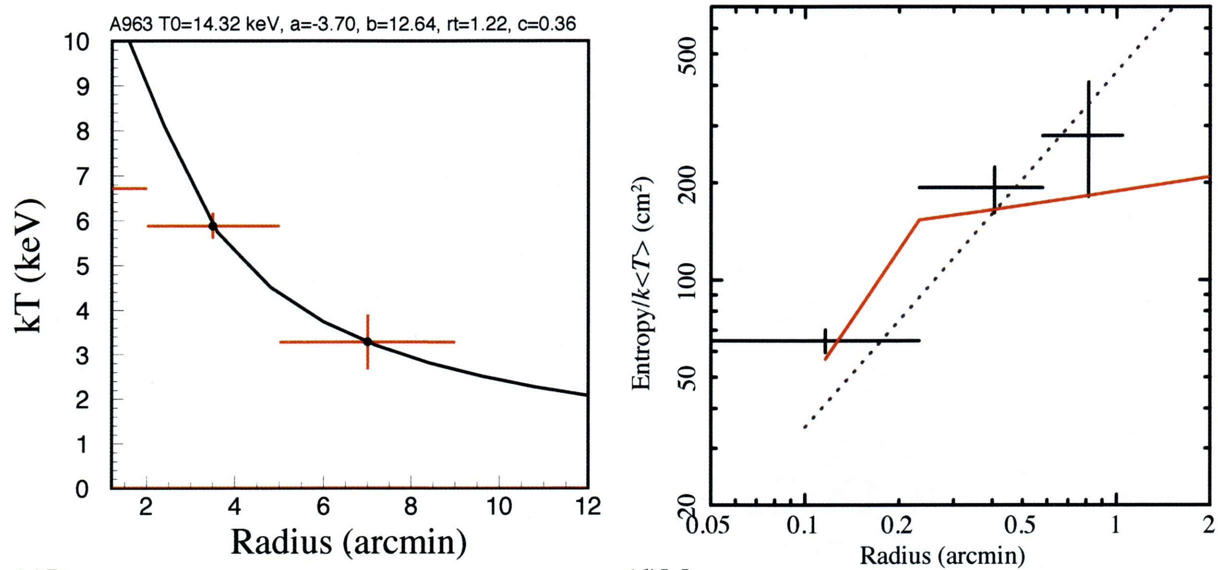

(c)Pressure (d)Mass

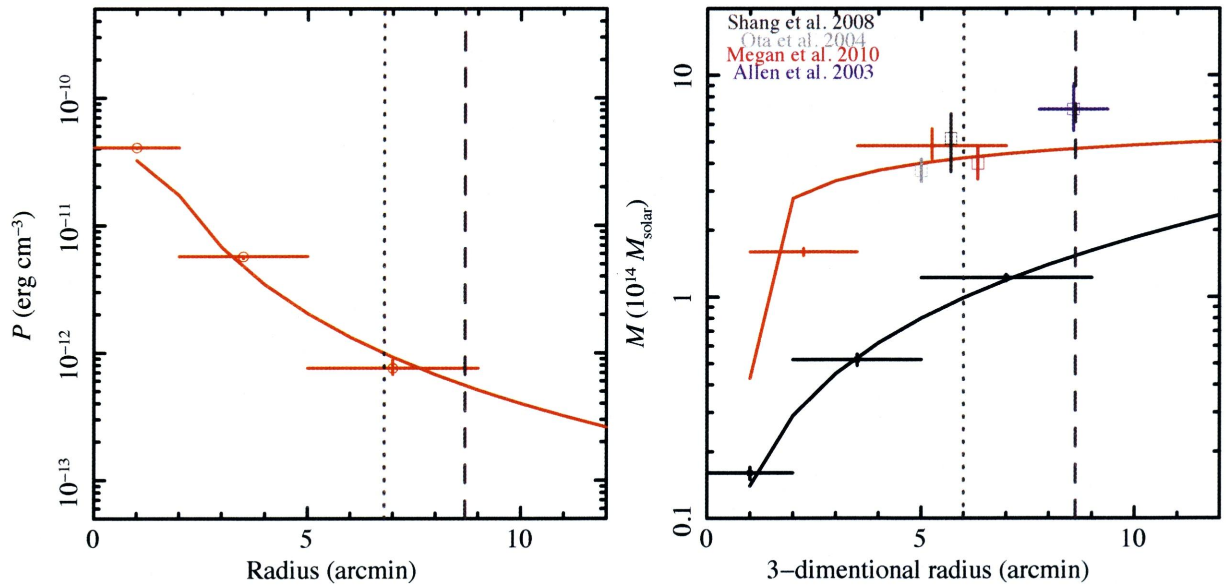

Fig. 7.10: A963 continued.

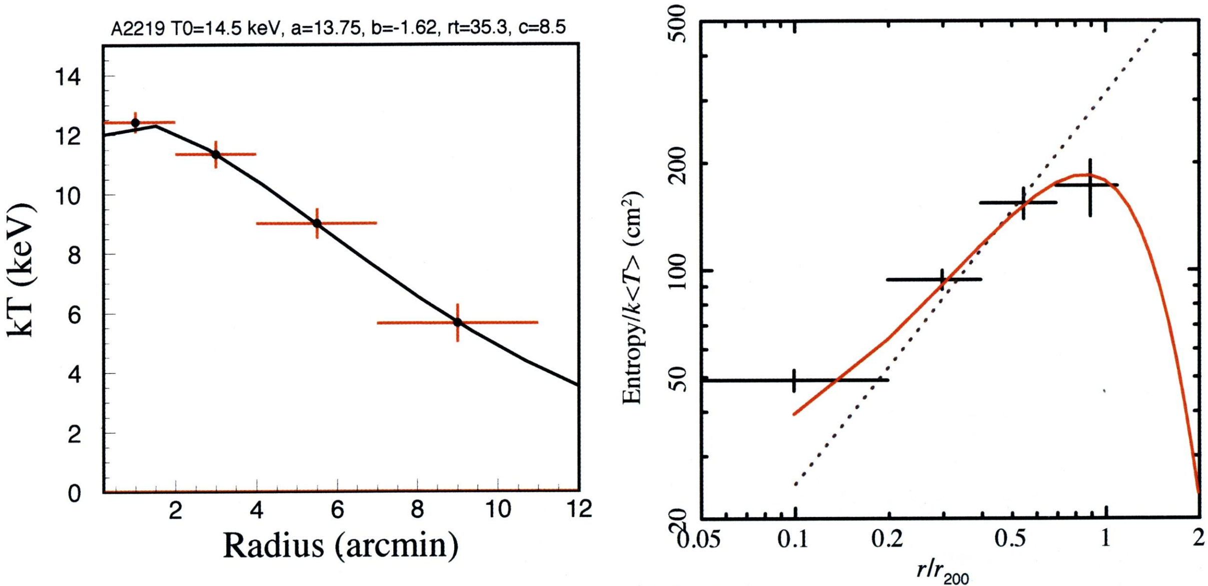

(a)Temperature profile of A2219

(b)Entropy

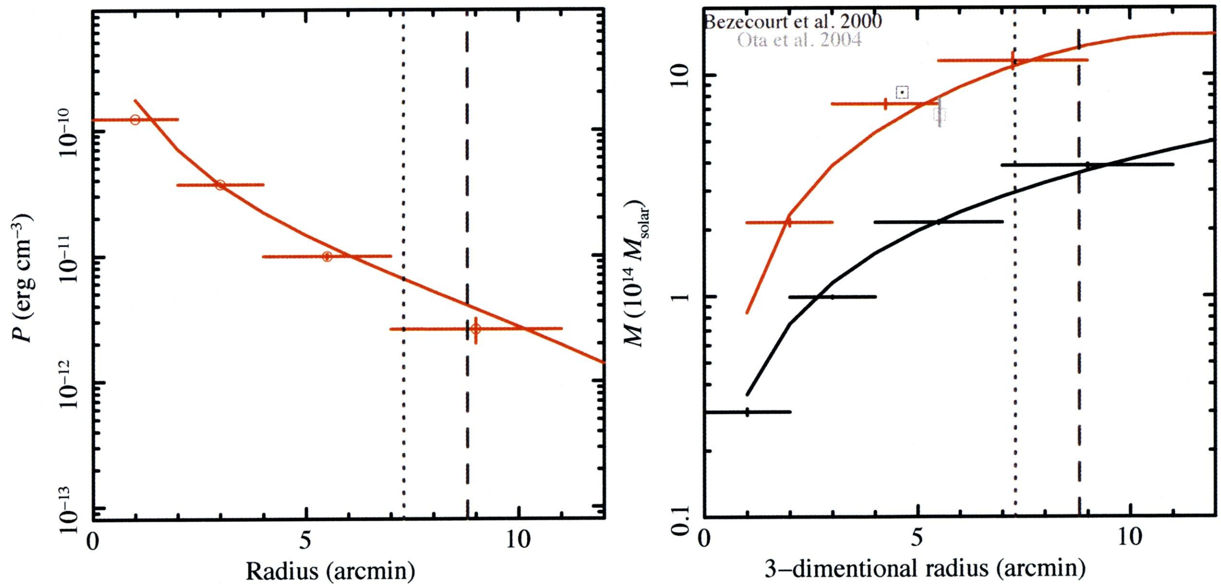

(c)Pressure

(d)Mass

Fig. 7.11: A2219 continued.

(a)Temperature profile of A2390

(b)Entropy

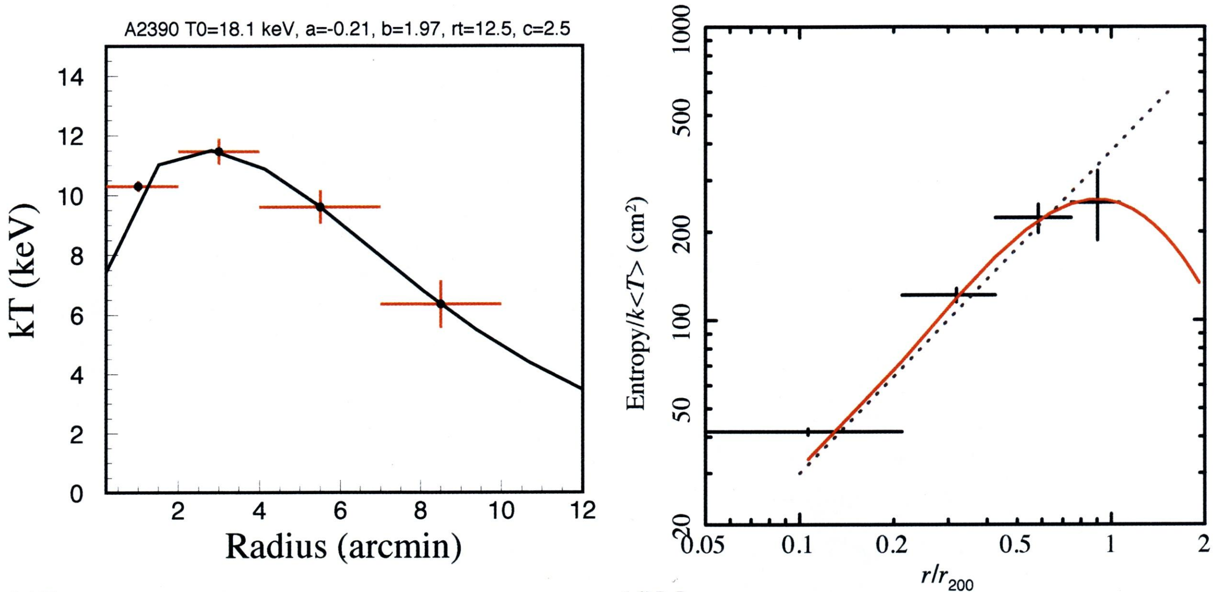

(c)Pressure

(d)Mass

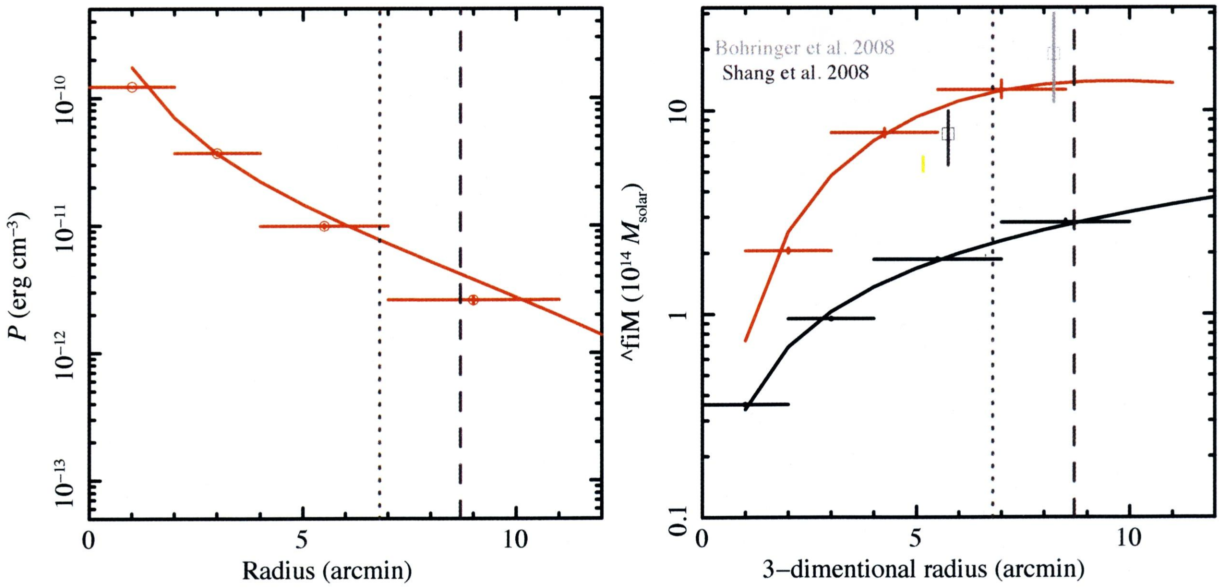

Fig. 7.12: A2390 continued.

7.4 Physical condition of the cluster outskirts

In this section, we discuss the physical conditions of ICM in the cluster outskirts based on the measured entropy profiles. The important aspect of studying the entropy structure in clusters is the distinction between heating by gravitational and non-gravitational processes. Recent X-ray studies of cluster outskirts (George et al. 2008; Reiprich et al. 2009; Bautz et al. 2009; Hoshino et al. 2010; Kawaharada et al. 2010; Simionescu et al. 2011; Akamatsu et al. 2011a) revealed that physical conditions of ICM in the cluster outskirts are not so simple as expected from the gravitational heating. A significant evidence of this problem is the deviation of the observed entropy from the relation of numerical simulations (Tozzi & Norman 2001; Voit et al. 2003; Borgani et al. 2006) in the outskirts. Voit et al. (2003) reported the entropy profile of ICM to follow $K \propto r^{1.1}$, if clusters grew through smooth mass accretion. Recent XMM-Newton (Pratt et al. 2010) and Chandra results on the entropy profile showed the slope within r_{500}, which is approximately 0.5 r_{200}, to be in agreement with the predictions from those numerical simulations. However, recent Suzaku observations of further outer region showed significant deviation from this profile ($K \sim r^{1.1}$), charatcterized by a flattening or a small drop after a monotonous increase with radius, around the outermost region. The deviation from the simulated entropy curve in the cluster outskirts is apparently common to many clusters including merging and non-merging systems. The origin of this deviation is still unclear, and is still a subject of active discussion. Currently, three main scenarios to explain the physical condition in the cluster outskirts have been proposed;

Gas clumpiness (Simionescu et al. 2011; Urban et al. 2011)

In the X-ray observations, the intensity of the bremsstrahlung emission follows the average of the square of the electron density $\langle n_e^2 \rangle$. If the density is not spatially uniform which is expected in the outskirts where fresh matter falls into the cluster, the average electron density estimated from the bremsstrahlung intensity will overestimate the true value. This will give low entropy value in the outer region.

Non-thermal pressure (Kawaharada et al. 2010)

From the X-ray and weak lensing mass analysis, Kawaharada et al. (2010) reported that the X-ray hydrostatic mass was lower than the spherical-lensing one, suggesting that non-thermal pressure may be significant. These small relative contribution of thermal pressure would be resulted from additional sources of pressure, such as bulk and or turbulent motions of the plasma.

Non-equilibrium (Hoshino et al. 2010; Akamatsu et al. 2011a):

Cluster outskirts are linked to be out of thermal equilibrium with the electron temperature lower than the ion temperatures, because these regions have not spent enough time to rise the electron temperature after the shock heating.

As shown in chapter 6, our cluster sample shows flattening in the entropy profiles in the outskirts, except for A2801 (kT = 2 keV) case. We, again, compared our entropy profiles the numerical simulation which only consider smooth accretion heatings (Voit 2005) as shown in figure 7.13 left panel. There are significant deviations between the observed and simulated entropy profiles beyond 0.5 r_{200}.

To investigate the physical condition of ICM in outskirt, we look at the degree of entropy deviation between the observation and simulation. We take the ratio of observation and simulation in 0.8-1r_{200} range in the sample described in 7.2 with an addition of A2142 and A3667 (Akamatsu et al. 2011a; Akamatsu et al. 2011b) for reference of merging clusters. The resultant entropy ratios are shown in figure 7.13 right panel together with other measurements (Humphrey et al. 2011a; Humphrey et al. 201111b; Rudd & Nagai 2009; Urban et al. 2011; Kawaharada et al. 2010; Simionescu et al. 2011). Open circles and stars denote difference of clusters of galaxies as relaxed and merging, respectively. Although the sample is small for low temperature systems (below 5 keV), there exists a clear dependence of the entropy deviation against average temperature. In particular, the ratios for merging clusters are smaller than those for relaxed clusters.

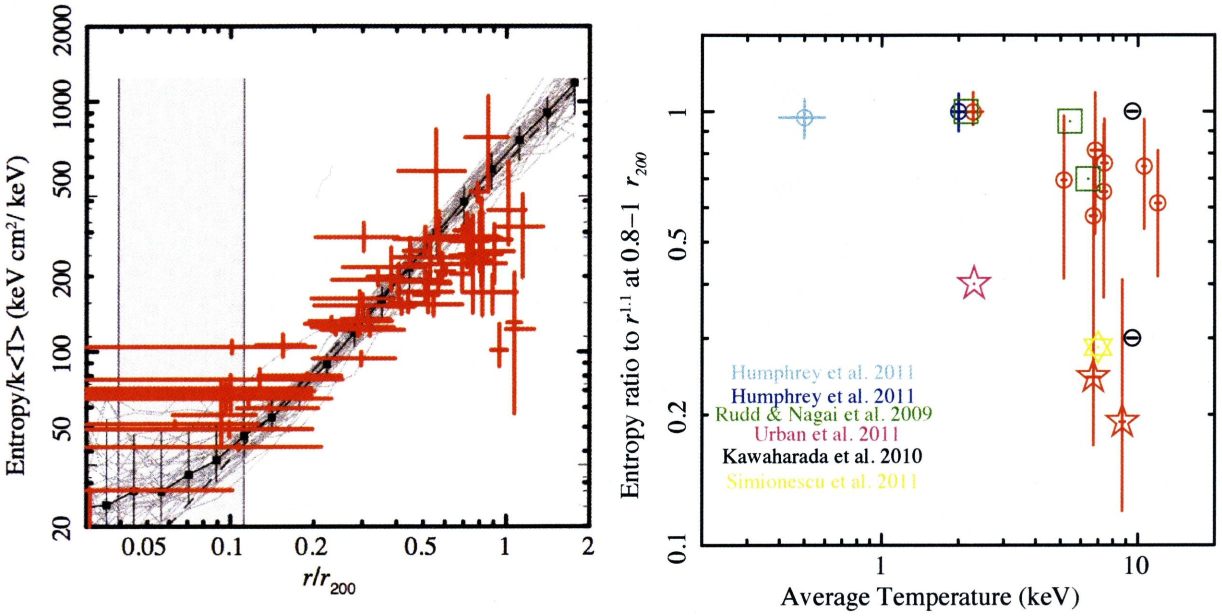

Fig. 7.13: left: Scaled projected entropy profiles (red cross) compared with the those from numerical simulations (gray) considering smooth accretion from Voit (2005). There exists significant deviation between simulation and observed entropy profiles. right: The ratio between the observed and simulated (Tozzi & Norman 2001; Voit et al. 2003) entropy value includeing $0.8 - 1 r_{200}$ with other measurments (Humphrey et al. 2011a; Humphrey et al. 201111b; Rudd & Nagai 2009; Urban et al. 2011; Kawaharada et al. 2010; Simionescu et al. 2011). Open circles and stars indicate the clusters of galaxies to be either relaxed or merging, respectively. Green squres show the simulated prediction of the degree of the non-equilibrium ionization by Rudd & Nagai (2009).

Recent numerical simulation of cluster of galaxies (Vazza et al. 2011) shows the time evolution of entropy profile. They confirmed that entropy profile of cluster shows a flattening and dropping trend in the outskirts just after a merger with sub-halo, and that after spending enough time the entropy from the sub-halo becames nearly identical to the entropy of the main cluster (fig.14 in Vazza et al. 2011).

In addition to the above simulation, Mitchell et al. (2009) reporedt the results of the production of cluster entropy in a binary clusters merger with FLASH simulations. Figure 2 in Mitchell et al. (2009) shows the resultant entropy distribution of a binary cluster merger at times, 0, 1, 2 , 3, 4, 5, 7 and 10 Gyr. Significant entropy generation occurs around the shock structure at t=2 Gyr when the core collides, and later on again when ICM re-accretes to the main body.

Based on the results of the above two simulations, the entropy profile will exhibit some flattening and dropping features during the formation of clusters of galaxies. Our observational results of merging clusters (A2142, A3667:Akamatsu et al. 2011a; Akamatsu et al. 2011b) support this scenario. Fig 7.14 shows, again, the observed entropy profiles of A2142 and A3667. In the A2142 case, we observed the cluster along its merger axis. The entropy profile of A2142 becomes flatter and finally shows a negative slope around r_{200}, which reflects the state that the outskirt of A2142 is still dynamical and in a non-equilibrium state. In the A3667 case, we found shock structures in the ICM temperature profile across the radio relic (two black dashed lines) in the cluster outskirt. This entropy profile is a good example to see the entropy generation by the shock heating, which is clearly recognised in figure 7.14 across the radio relic. The entropy profile of A3667 shows a sudden drop across the radio relic. This is a direct observational evidence of entropy generation by shock heatings.

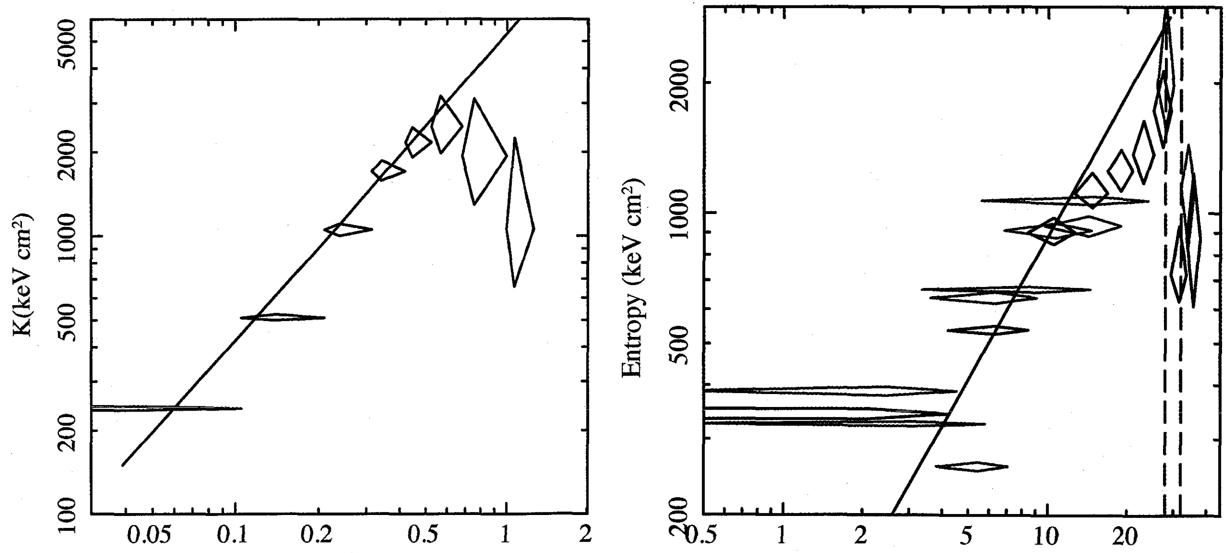
(a)Example of entropy under non-equilibrium state (b)Example of shock heating entropy generation

Fig. 7.14: Observed entropy profiles of merging clusters A2142 (left:Akamatsu et al. 2011a) and A3667 (right:Akamatsu et al. 2011b). The black solid line shows the predicted entropy profile $K \propto r^{1.1}$ by the smooth accretion model (Tozzi & Norman 2001; Voit et al. 2003).

Based on the above discussion, we interpret that the deviation between the observed and simulated entropy profiles is caused mainly by the non-equilibrium state of the plasma in the cluster outskirts. The temperature dependance of the entropy deviation (fig. 7.13 right panel) can be interpreted in the following way; (i) Smaller systems without recent merging activity are expected to be relaxed. So, those relaxed systems are reaching in equilibrium state considering the electron and ion temperatures. The entropy profile of those system will follow the prediction of the smoothed accretion model (Tozzi & Norman 2001; Voit et al. 2003). (ii) Larger systems grow up via accretion and major mergers. So, it is natural that those systems experienced recent merger activities and their outskirts still do not reach the thermal equilibrium state. (iii) Regardless of the size of the systems, merger activities cause bulk flows of ICM, which will cause negative entropy slope. Finally, we propose a very simple model for the entropy generation around the cluster outskirts as shown in figure 7.15.

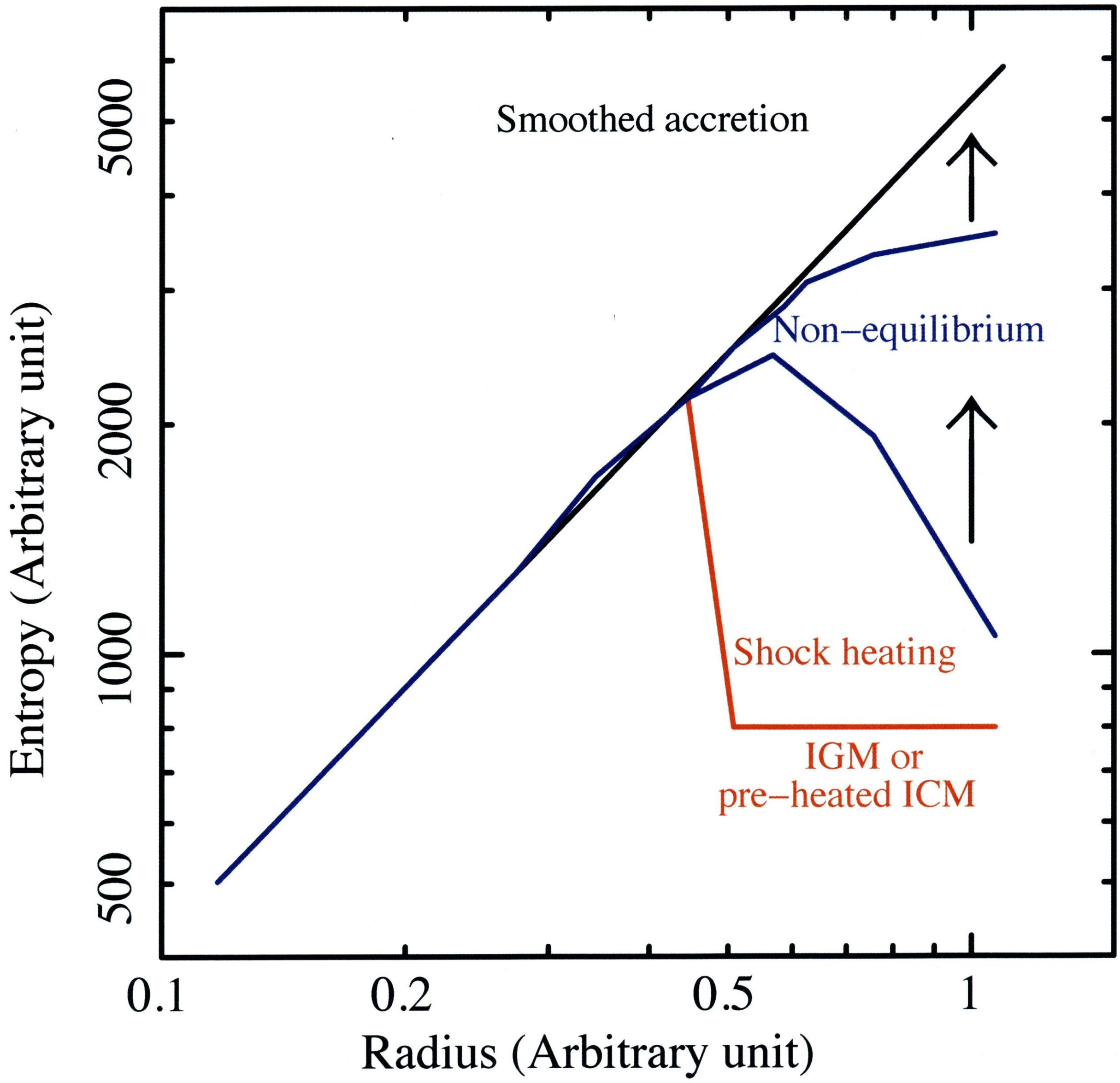

Fig. 7.15: The schematics illustrates pattern diagram of entropy profile for several conditions. The vertical and horizontal axises arbitrary scaled. The black solid line shows predicted entropy profile $K \propto$by smooth accretion model (Tozzi & Norman 2001; Voit et al. 2003).

7.5 Scenario of the cluster growth in their outskirts.

Finally, we will consider the scenario evolution in the outskirts of clusters of galaxies based on our results combined with the standard picture of the bottom-up structure formation. Again, we summarize the main features of our results of cluster outskirts as below;

1. The entropy profiles of smaller systems seem to follow the prediction of the smooth accretion model (Tozzi & Norman 2001; Voit et al. 2003).
2. Larger systems grow up via accretion and several episodes of major mergers. So, it is natural to expect that these systems have experienced recent merger activities and their outskirts still do not reach the thermal equilibrium state.
3. Regardless of the size of the system, merger activities always cause bulk flows of ICM, which will result in a negative entropy slope as we have seen in the previous sections.

These results indicate the following scenario for the cluster growth; the smaller systems such as groups or low-temperature clusters of galaxies are formed earlier than the massive high-temperature ones. The larger systems are still growing to more massive systems due to its large potential wall. Then, outskirts of such large systems are likely to be still in dynamic state.

This result can be recognized as a supporting evidence of the hierarchical clustering scenario, which predicts that larger objects in the Universe are take very long time to be formed time as shown in figure 7.16.

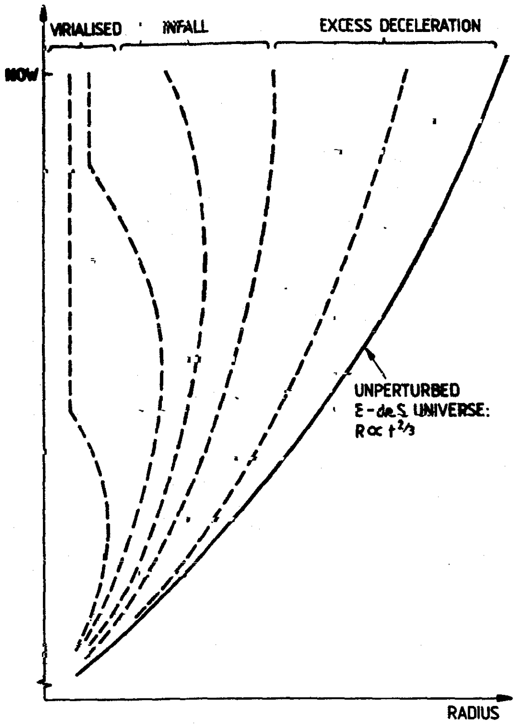

Fig. 7.16: The dynamics of over-dense spheres in the expanding universe. The amplitude of density fluctuations growth with the time as $R \sim t^{2/3}$ (Heavens 1992).

Chapter 8

Summary and Conclusion

In the present ΛCDM model, clusters of galaxies grow through gas accretion from large-scale filaments and mergers of subclusters. The temperature profiles of ICM give important information in studying the gravitational processes responsible for the cluster formation in the Universe.

We analyzed 15 clusters of galaxies, which included 8 merging clusters, 4 radio relic clusters and 9 relaxed clusters, observed with Suzaku and showing the ICM emission up to the virial radius. We derived radial profiles of temperature, electron density, and entropy, and compared these properties with the results of previous studies. We discussed the physical condition of the gas in the cluster outskirts based on those observed ICM parameters. We summarize the main results of the thesis as follows;

- The ICM temperature profiles for the relaxed clusters show "universal" trend, gradually decreasing toward the outer region by about 20-50% around the virial radius. The average temperature profile for relaxed clusters can be described by the formula by Burns et al. (2010) up to r_{200}, suggesting that non-thermal pressure support is significant in the outer regions.

- In the average temperature profile, we found significant difference between the relaxed and the merging clusters. The temperature profiles of merging clusters show significant deviation from the profile. In particular, A3376 shows a flat temperature profile upto 0.8 r_{200} following by a rise before the shock front. We expect that this temperature excess will disappear after a cosmological timescale via conduction and dissipation, and eventually settle down to the "universal" temperature profile. Therefore, the temperature profiles of merging clusters offer us "snapshots" of various stages in the course of the dynamical evolution of cluster of galaxies.

- The electron density decreases down to $1 - 10 \times 10^{-5}$ cm^{-3} at the virial radius and agrees with the previous ROSAT measurements (Eckert et al. 2011a).

- The scaled entropy profile within about $0.6r_{200}$ follows $r^{1.1}$, predicted by the accretion shock heating model. As one goes to outer region, the profile becomes flatter and finally shows a negative slope around r_{200}, except for the low temperature cluster such as Abell 2801 (kT=2.5 keV).

- We confirm that ICM temperature and pressure show significant drops across the radio relic region, which indicates the presence of the shock front at the radio relic. The estimated Mach numbers from the X-ray observations span the range 2-3, which agree with the nalues from the radio observation. Based on the estimations of the relaxation and ionization times needed after the shock heating, we found the indication of ion-electron non-equilibrium state in our sample of the radio relic clusters.

- The $M - T$ relation of the derived gravitational mass and gas mass at r_{500} of relaxed clusters shows good agreement with the previous studies.

- We have found that the ICM gas to the total mass ratio s f_{gas} at 0.5 r_{200} are consistent with a constant value.

- Compared with the observed entropy profiles and prediction of the numerical simulations, we found the deviation between those profiles had the dependence on the temperature. Based on the entropy generation theory and the bottom up scenario, we discuss that the possibility of the dynamical non-equilibrium state in the outer regions of massive clusters of galaxies.

Acknowledgement

I would express my best gratitude to Yoshikata Ishisaki, who is a my supervisor and a collaborator of the present work, for his genuine support and patient encouragement. He has supported me throughout five-years ph.D course. Special thanks as well to Takaya Ohashi for his warm help. I appreciate to Dr. Y. Ezoe, Dr. K. Shinozaki, Dr. Y. Takei and Dr. Y. Kawahara for many useful comments and his encouragement. I am indebted to Dr. Kuniaki Masai and Dr Sin Sasaki for their helpful suggestions. I wish to thank all (present and former) members of experimental and theoretical astrophysics group in Tokyo Metropolitan University. I thank many foreign collaborator as Dr. P. Luigi, Dr. C. Macculi, and Dr. L. Colasanti , who supported me when I visit INAF ROMA to work with them. Dr. J. Kaastra and Dr. J. de plaa helped me when I visit SRON institute with ASTRO-H Science team support. I deeply acknowledges hospitality in the SRON HEA group. I looking forward to continued excellent friendship with them. I thank all the Suzaku team members for their support of the Suzaku project.

Finally, I am grateful to my parents, brothers and friends for their hearty support and encouragement through my life.

This work was supported by Grant-in-Aid for Japan Society for the Promotion of Science (JSPS) Fellows (22·1582) and the MEXT program “Support Program for Improving Graduate School Education”.

Bibliography

Akahori,T., 2008, "Thermal and Dynamical Evolution of Galaxy Clusters", (Dissertation for a degree of doctor of science; Tokyo Metropolian University), 2008

Akahori, T., & Yoshikawa, K. 2010, PASJ, 62, 335

Akamatsu, H., Hoshino, A., Ishisaki, Y., Ohashi, T., Sato, K., Takei, Y., & Ota, N. 2011, arXiv:1106.5653

Akamatsu, H., de Plaa, J., Kaastra, J., et al. 2011, arXiv:1111.5162

Akamatsu, H., et al. 2011, submitted to PASJ (A3376)

Akamatsu, H., & Kawahara, H. 2011, arXiv:1112.3030 (CIZA2242)

Allen, S. W., Edge, A. C., Fabian, A. C., et al. 1992, MNRAS, 259, 67

Anders, E., & Grevesse, N. 1989, Geochim. Cosmochim. Acta, 53, 197

Anders, E., & Grevesse, N. 1989, Geochim. Cosmochim. Acta, 53, 197

Arnaud, M., Pointecouteau, E., & Pratt, G. W. 2005, A&A, 441, 893

Bagchi, J., Enßlin, T. A., Miniati, F., et al. 2002, *na*, 7, 249

Bagchi, J., Durret, F., Neto, G. B. L., & Paul, S. 2006, Science, 314, 791

Bautz,M.W., Miller, E.D., Sanders,J.S., Hayashida, K., Henry, J.P., Hughes, J.P., & Tamura,T, 2009, arXiv:0906.3515v1

Basu,K., ZhangY.-Y., Sommer,M.W., Bender, A.N., Bertoldi, F., Dobbs, M., Eckmiller,H., Halverson, N.W., Holzapfel, W.L., Horellou, C., Jaritz, V., Johansson, D., Johnson, B., Kennedy, J., Kneissl, R., Lanting,T., Lee, A.T., Menten, K.M., Navarrete, F.P., Pacaud, F., Reichardt, C.L., Reiprich, T.H., Richards,P.L., Schwan,D., & Westbroock, B., 2009, arXiv:0911.3905v1

Bezecourt, J., Hoekstra, H., Gray, M. E., et al. 2000, arXiv:astro-ph/0001513

Borgani,S., Diaferio,A.,Dolag,K.,& Schindler,S., 2007, EAS Publications Series, 24, 145

Borgani,S., & Guzzo,L., 2001, Nature, 409, 39-45

Borgani, S., et al. 2004, MNRAS, 348, 1078

Borgani, S., et al. 2006, MNRAS, 367, 1641

Boehringer, H., Tanaka, Y., Mushotzky, R. F., Ikebe, Y., & Hattori, M. 1998, A&A, 334, 789

Bourdin, H., Arnaud, M., Mazzotta, P., et al. 2011, A&A, 527, A21

Buote, D. A., & Tsai, J. C. 1996, ApJ, 458, 27

Burns, J. O., Skillman, S. W., & O'Shea, B. W. 2010, ApJ, 721, 1105

Briel, U. G., Finoguenov, A., & Henry, J. P. 2004, A&A, 426, 1

Brown, S., & Rudnick, L. 2011, MNRAS, 412, 2

Brüggen, M., Bykov, A., Ryu, D., Röttgering, H. 2011, Space Sci. Rev., 138

Cavagnolo, K. W., Donahue, M., Voit, G. M., & Sun, M. 2009, ApJS, 182, 12

Chen, Y., Ikebe, Y., Böhringer, H. 2003, A&A, 407, 41

Clarke, T. E., & Ensslin, T. A. 2006, AJ, 131, 2900

Clowe, D., Bradač, M., Gonzalez, A. H., Markevitch, M., Randall, S. W., Jones, C., & Zaritsky, D. 2006, ApJL, 648, L109

Croston, J. H., Pratt, G. W., Böhringer, H., et al. 2008, A&A, 487, 431

De Grandi, S., & Molendi, S. 2002, ApJ, 567, 163

De Grandi, S., Ettori, S., Longhetti, M., & Molendi, S. 2004, A&A, 419, 7

Dickey, J. M., & Lockman, F. J. 1990, ARA&A, 28, 215

Ebeling, H., Voges, W., Bohringer, H., et al. 1996, MNRAS, 281, 799

Eckert, D., Molendi, S., Gastaldello, F., & Rossetti, M. 2011, A&A, 529, A133

Eke,V.,R., Navarro,J.,F., & Frenk,C.,S., 1998, ApJ, 503, 569

Eke, V. R. and Navarro, J. F. and Steinmetz, M., 2001, ApJ, 554, 114

Enßlin, T. A., & Brüggen, M. 2002, MNRAS, 331, 1011

Ettori, S., Borgani, S., Moscardini, L., et al. 2004, MNRAS, 354, 111

Ettori, S., Morandi, A., Tozzi, P., et al. 2009, A&A, 501, 61

Fabricant, D., Lecar, M., & Gorenstein, P. 1980, ApJ, 241, 552

Ferrari, C., Govoni, F., Schindler, S., Bykov, A. M., & Rephaeli, Y. 2008, Space Sci. Rev., 134, 93

Finoguenov, A., Reiprich, T. H., Bohringer, H. 2001, A&A, 368, 749

Finoguenov, A., Jones, C., Böhringer, H., & Ponman, T. J. 2002, ApJ, 578, 74

Finoguenov, A., Sarazin, C. L., Nakazawa, K., Wik, D. R., & Clarke, T. E. 2010, apj, 715, 1143

Fujita, Y, Tawa, N., Hayashida, K., Takizawa, M., Matsumoto,H., Okabe, N., &, Reiprich,T., 2008, PASJ, 60, S343

Gehrels,N. and Williams, E.D., 1993, ApJL, 418, 25

George,M.R.,Fabian, A. C., Sanders,J. S., Young., A. J., and Russell, H. R., 2008, MNRAS, 395, 657

Henry, J. P., & Briel, U. G. 1996, ApJ, 472, 137

Henry, J. P., Evrard, A. E., Hoekstra, H., Babul, A., & Mahdavi, A. 2009, ApJ, 691, 1307

Heavens, A. 1992, The Observatory, 112, 292

Hoshino, A., et al. 2010, PASJ, 62, 371

Humphrey, P. J., Buote, D. A., Canizares, C. R., Fabian, A. C., & Miller, J. M. 2011, ApJ, 729, 53

Humphrey, P. J., Buote, D. A., Brighenti, F., et al. 2011, arXiv:1106.3322

Ishizaka, C., & Mineshige, S. 1996, PASJ, 48, L37

Ishisaki, Y., et al. 2007, PASJ, 59, 113

Smail, I., Hogg, D. W., Blandford, R., et al. 1995, MNRAS, 277, 1

Jones, C., & Forman, W. 1984, ApJ, 276, 38

Kaastra, J. S., Mewe, R., & Nieuwenhuijzen, H. 1996, UV and X-ray Spectroscopy of Astrophysical and Laboratory Plasmas, 411

H. Kawahara, H. Yoshitake, T. Nishimichi, and T. Sousbie. 2011, ApJL, 727, L38

Kawaharada, M., et al. 2010, ApJ, 714, 423

Kawano, N., et al. 2009, PASJ, 61, 377

King, I. 1962, AJ, 67, 471

Kocevski, D. D., Ebeling, H., Mullis, C. R., & Tully, R. B. 2007, ApJ, 662, 224

Knopp, G. P., Henry, J. P., & Briel, U. G. 1996, ApJ, 472, 125

Koyama, K., et al. 2007, PASJ, 59, 23

Kushino, A., Ishisaki, Y., Morita, U., Yamasaki, N. Y., Ishida, M., Ohashi, T., & Ueda, Y. 2002, PASJ, 54, 327

Landau, L. D., & Lifshitz, E. M. 1960, Energy Conversion Management,

Lavery, R. J., & Henry, J. P. 1988, ApJL, 329, L21

Machacek, M. E., Bautz, M. W., Canizares, C., & Garmire, G. P. 2002, ApJ, 567, 188

Markevitch, M., Forman, W. R., Sarazin, C. L., & Vikhlinin, A. 1998, ApJ, 503, 77

Markevitch, M., Ponman, T. J., Nulsen, P. E. J., et al. 2000, ApJ, 541, 542

Markevitch, M., & Vikhlinin, A. 2001, ApJ, 563, 95

M. Markevitch, A. H. Gonzalez, L. David, A. Vikhlinin, S. Murray, W. Forman, C. Jones, and W. Tucker. 2002, ApJL, 567,L27–L31

Markevitch, M., Govoni, F., Brunetti, G., & Jerius, D. 2005, ApJ, 627, 733

Markevitch, M. 2006, The X-ray Universe 2005, 604, 723

Metcalfe, L., Kneib, J.-P., McBreen, B., et al. 2003, A&A, 407, 791

Mathis, H., Lavaux, G., Diego, J. M., & Silk, J. 2005, MNRAS, 357, 801

Masai, K. 1984, Ap&SS, 98, 367

Miniati, F., Ryu, D., Kang, H., et al. 2000, ApJ, 542, 608

Miralda-Escude, J., & Babul, A. 1995, ApJ, 449, 18

Mitchell, N. L., McCarthy, I. G., Bower, R. G., Theuns, T., & Crain, R. A. 2009, MNRAS, 395, 180

Misaki, K., Kunieda, H., Maeda, Y., Haba, Y., Itoh, K., Mori, H., Iizuka, R., Itoh, A., Inoue, H., Okada, S., Yokoyama, Y., Ogasaka, Y., Tamura, K., Furuzawa, A., Shibata, R., Tanaka, T., Naitou, M., Ishida, M., Hayakawa, A., Inoue, C., Hayashi, A., Shimizu, T., Serlemitsos, P. J., Soong, Y., Chan, K.-W., Okajima, T., & Lehan, J. P. 2004, in Optics for EUV, X-Ray, and Gamma-Ray Astronomy. Edited by Citterio, Oberto; O'Dell, Stephen L. Proceedings of the SPIE, Volume 5168, pp. 294-305 (2004)., ed. O. Citterio & S. L. O'Dell, 294–305

Mitsuda, K., Bautz, M., Inoue, H., et al. 2007, PASJ, 59, 1

Mitsuda, K., et al. 2010, Proc. SPIE, 7732,

Mori, H., Iizuka, R., Shibata, R., Haba, Y., Hayakawa, A., Hayashi, A., Inoue, C., Inoue, H., Ishida, M., Itoh, A., Itoh, K., Kunieda, H., Maeda, Y., Misaki, K., Naitou, M., Okada, S., Shimizu, T., & Yokoyama, Y. 2005, PASJ, 57, 245

Nakazawa, K., et al. 2009, PASJ, 61, 339

Nevalainen, J., Oosterbroek, T., Bonamente, M., & Colafrancesco, S. 2004, ApJ, 608, 166

Neumann, D. M., Bohringer, H. 1999, ApJ, 512, 630

Obayashi, H., Makishima, K., & Tamura, T. 1998, PASJ, 50, 537

Ota, N., & Mitsuda, K. 2003, Astronomische Nachrichten, 324, 172

Ota, N., Murase, K., Kitayama, T., et al. 2008, A&A, 491, 363

Parrish, I. J., McCourt, M., Quataert, E., & Sharma, P. 2011, arXiv:1109.1285

Paul, S., Iapichino, L., Miniati, F., Bagchi, J., & Mannheim, K. 2011, ApJ, 726, 17

Pratt, G. W., & Arnaud, M. 2002, A&A, 394, 375

Pratt, G. W., Böhringer, H., & Finoguenov, A. 2005, A&A, 433, 777

Pratt, G. W., Böhringer, H., Croston, J. H., Arnaud, M., Borgani, S., Finoguenov, A., & Temple, R. F. 2007, A&A, 461, 71

Pratt, G. W., et al. 2010, A&A, 511, A85

Peterson, J. R., & Fabian, A. C. 2006, Phys. Rep., 427, 1

Reiprich, T. H., et al. 2009, A&A, 501, 899

Ricker, P. M., & Sarazin, C. L. 2001, ApJ, 561, 621

Röttgering, H. J. A., Wieringa, M. H., Hunstead, R. W., & Ekers, R. D. 1997, MNRAS, 290, 577

Rudd,D.H., & Nagai,D., 2009, ApJ, 701, L16

Russell, H. R., Sanders, J. S., Fabian, A. C., Baum, S. A., Donahue, M., Edge, A. C., McNamara, B. R., & O'Dea, C. P. 2010, MNRAS, 406, 1721

Takei, Y., Akamatsu, H. et al. 2011, Suzaku Conference

Tawa, N., et al. 2008, PASJ, 60, 11

Sanders, J. S., Fabian, A. C., & Taylor, G. B. 2005, MNRAS, 356, 1022

Sanders, J. S., Fabian, A. C., & Taylor, G. B. 2009, MNRAS, 393, 71

Sarazin,C.L., 1988, "X-ray emission from clusters of galaxies", (Cambridge: Cambridge University Press), ch2, 4, 5

Sato, K., Kelley, R. L., Takei, Y., et al. 2010, PASJ, 62, 1423

Sasaki, S. 1996, PASJ, 48, L119

Shan, H. Y., Qin, B., & Zhao, H. S. 2010, MNRAS, 408, 1277

Serlemitsos, P. J., et al. 2007, PASJ, 59, 9

Simionescu, A., et al. 2011, Science, 331, 1576

Snowden, S. L., Mushotzky, R. F., Kuntz, K. D., & Davis, D. S. 2008, A&A, 478, 615

Swarup, G. 1991, IAU Colloq. 131: Radio Interferometry. Theory, Techniques, and Applications, 19, 376

Sugawara, C., Takizawa, M., & Nakazawa, K. 2009, PASJ, 61, 1293

Spitzer,L.Jr., 1956, Physics of Fully Ionized Gases, New York: Interscience

Springel, V., & Hernquist, L. 2002, MNRAS, 333, 649

Squires, G., Neumann, D. M., Kaiser, N., et al. 1997, ApJ, 482, 648

Takei, Y., Ohashi, T., Henry, J. P., et al. 2007, PASJ, 59, 339

Takahashi, T. e. a. 2007, PASJ, 57, 743

Takizawa,M., 1998, ApJ, 509, 579

Takizawa, M. 2005, ApJ, 629, 791

Takizawa, M. 2008, ApJ, 687, 951

Takizawa, M., & Naito, T. 2000, ApJ, 535, 586

Tamura, T., Hayashida, K., Ueda, S., & Nagai, M. 2011, PASJ, 63, 1009

Tawa, N., et al. 2008, PASJ, 60, 11

Tozzi, P., & Norman, C. 2001, ApJ, 546, 63

van Weeren, R. J., Röttgering, H. J. A., Bagchi, J., et al. 2009, A&A, 506, 1083

van Weeren, R. J., Röttgering, H. J. A., Brüggen, M., & Hoeft, M. 2010, Science, 330, 347

van Weeren, R. J., Brüggen, M., Röttgering, H. J. A., & Hoeft, M. 2011, MNRAS, 1445

Vazza, F., Brunetti, G., & Gheller, C. 2009, MNRAS, 395, 1333

Vazza, F., Dolag, K., Ryu, D., et al. 2011, MNRAS, 418, 960

Vikhlinin, A., Markevitch, M., & Murray, S. S. 2001, ApJL, 549, L47

Vikhlinin, A., Markevitch, M., Murray, S. S., Jones, C., Forman, W., & Van Speybroeck, L. 2005, ApJ, 628, 655

Vikhlinin, A., Kravtsov, A., Forman, W., Jones, C., Markevitch, M., Murray, S. S., & Van Speybroeck, L. 2006, ApJ, 640, 691

Vikhlinin, A., Kravtsov, A. V., Burenin, R. A., et al. 2009, ApJ, 692, 1060

Voit, G. M., Balogh, M. L., Bower, R. G., Lacey, C. G., & Bryan, G. L. 2003, apj, 593, 272

Voit, G. M., & Ponman, T. J. 2003, ApJL, 594, L75

Voit,G,M.,2005,RvMP,77,207

Yoshino, T., Mitsuda, K., Yamasaki, N. Y., et al. 2009, PASJ, 61, 805

Wik, D. R., Sarazin, C. L., Finoguenov, A., et al. 2009, ApJ, 696, 1700

Wong, K.-W., & Sarazin, C.L., 2009, ApJ, 707, 1141

Zhang, Y.-Y., Böhringer, H., Finoguenov, A., et al. 2006, A&A, 456, 55

Zhang, Y.-Y., Finoguenov, A., Böhringer, H., et al. 2007, A&A, 467, 437

Zhang, Y.-Y., Finoguenov, A., Böhringer, H., et al. 2011, A&A, 527, 3

Urban, O., Werner, N., Simionescu, A., Allen, S. W., Böhringer, H. 2011, MNRAS, 546

Appendix A

Individual cluseters

Table A.1: Best-fit parameters of the ICM in PKS0745-191

	0′−2.′5	2.′5-5.′0	5.′0-8.′0	8.′0-13.′0	13.′0-18.′0	18.′0-22.′0
kT(keV)	$6.47^{+0.07}_{-0.07}$	$7.43^{+0.20}_{-0.20}$	$6.35^{+0.29}_{-0.29}$	$5.19^{+0.80}_{-0.51}$	$2.53^{+0.25}_{-0.21}$	$2.25^{+0.37}_{-0.38}$
Z	$0.37^{+0.02}_{-0.02}$	$0.31^{+0.03}_{-0.03}$	$0.36^{+0.06}_{-0.06}$	0.2 (fix)	0.2 (fix)	0.2 (fix)
norm*	$2867.7^{+29.3}_{-29.3}$	$185.6^{+2.7}_{-2.7}$	$38.6^{+1.2}_{-1.2}$	$3.2^{+0.2}_{-0.3}$	$1.4^{+0.3}_{-0.2}$	$0.5^{+0.2}_{-0.2}$
χ^2/d.o.f	2845 / 2747	1643 / 1565	704 / 622	1199 / 798	607 / 554	413 / 386

Table A.2: Best-fit parameters of the ICM in A2811

	0′−2.′0	2.′0-4.′0	4.′0-7.′0	7.′0-10.′0	10.′0-13.′0
kT(keV)	$5.29^{+0.15}_{-0.14}$	$5.08^{+0.15}_{-0.15}$	$5.10^{+0.31}_{-0.30}$	$3.87^{+1.08}_{-0.75}$	$1.62^{+0.75}_{-0.31}$
Z	$0.30^{+0.05}_{-0.05}$	$0.28^{+0.04}_{-0.04}$	0.2 (fix)	0.2 (fix)	0.2 (fix)
norm*	$588.7^{+11.0}_{-10.9}$	$99.6^{+2.0}_{-2.0}$	$14.2^{+0.4}_{-0.4}$	$1.6^{+0.2}_{-0.2}$	$0.3^{+0.1}_{-0.1}$
χ^2/d.o.f	333 / 319	336 / 319	354 / 320	392 / 320	206 / 127

Table A.3: Best-fit parameters of the ICM in A2801

	0′−2.′0	2.′0-4.′0	4.′0-7.′0	7.′0-11.′0
kT(keV)	$2.64^{+0.12}_{-0.13}$	$2.25^{+0.19}_{-0.14}$	$1.58^{+0.21}_{-0.20}$	$1.37^{+0.32}_{-0.16}$
Z	$0.48^{+0.11}_{-0.10}$	$0.54^{+0.15}_{-0.12}$	0.2(fix)	0.2(fix)
norm*	$63.0^{+4.7}_{5.3}$	$3.4^{+0.7}_{0.5}$	$0.4^{+0.1}_{0.1}$	$0.1^{+0.0}_{-0.0}$
χ^2/d.o.f	191 / 188	267 / 188	198 / 189	104 / 75

Table A.4: Best-fit parameters of the ICM

	0′-2′	2′-4′	4′ – 6′	6′ – 9′	12′ – 15′	15′ – 18′	18′ – 21′	21′ – 24′	24′ – 27′	27′ – 31′
kT (keV)	$4.09^{+0.08}_{-0.08}$	$4.16^{+0.09}_{-0.09}$	$4.14^{+0.09}_{-0.09}$	$4.17^{+0.09}_{-0.09}$	$4.08^{+0.29}_{-0.27}$	$4.17^{+0.23}_{-0.19}$	$4.81^{+0.29}_{-0.28}$	$4.68^{+0.48}_{-0.48}$	$3.11^{+1.10}_{-0.78}$	$1.34^{+0.69}_{-0.39}$
Z	$0.33^{+0.03}_{-0.03}$	$0.28^{+0.03}_{-0.03}$	$0.26^{+0.03}_{-0.03}$	$0.25^{+0.03}_{-0.03}$	$0.21^{+0.09}_{-0.08}$	$0.18^{+0.06}_{-0.06}$	$0.11^{+0.06}_{-0.06}$	0.2 (fix)	0.2 (fix)	0.2 (fix)
norm*	$164.8^{+3.2}_{-3.2}$	$108.3^{+1.9}_{-1.9}$	$75.0^{+1.1}_{-1.1}$	$64.7^{+1.3}_{-1.3}$	$46.4^{+2.3}_{-2.3}$	$25.5^{+0.9}_{-0.9}$	$15.3^{+0.5}_{-0.5}$	$6.7^{+0.3}_{-0.3}$	$2.1^{+0.2}_{-0.2}$	$0.3^{+0.2}_{-0.2}$
χ^2/d.o.f	322 / 307	314 / 307	388 / 307	342 / 307	362 / 307	352 / 307	348 / 307	351 / 308	345 / 308	361 / 308

Table A.5: Best-fit parameters of the ICM

	0′-4.′2	4.′2-8.′4	8.′4 – 12.′6	12.′6 – 16.′8	16.′8 – 21.′0	21.′0 – 25.′2	25.′2 – 29.′4	29.′4 – 33.′6	33.′6 – 37.′8
kT(keV)	$7.14^{+0.17}_{-0.17}$	$6.57^{+0.13}_{-0.12}$	$6.93^{+0.50}_{-0.36}$	$6.94^{+0.71}_{-0.50}$	$6.49^{+0.65}_{-0.56}$	$5.70^{+0.94}_{-0.66}$	$5.36^{+1.11}_{-0.91}$	$1.92^{+0.39}_{-0.37}$	$1.58^{+0.62}_{-0.41}$
Z	0.29 ± 0.03	0.33 ± 0.03	0.26 ± 0.09	0.20 ± 0.11	0.22 ± 0.12	0.26 ± 0.22	0.2 (FIX)	0.2 (FIX)	0.2 (FIX)
norm*	631.2 ± 6.3	209.1 ± 1.8	66.2 ± 1.9	45.7 ± 2.0	27.3 ± 1.4	16.3 ± 1.4	5.0 ± 0.5	2.9 ± 0.4	1.0 ± 0.3
χ^2/d.o.f	386 / 311	391 / 311	323 / 311	498 / 404	371 / 330	348 / 330	404 / 347	388 / 347	454 / 347

Table A.6: Best-fit parameters of the ICM in A2142

	0′–2.′5	2.′5-5.′0	5.′0-7.′8	7.′8-10.′3	10.′3-12.′9	12.′9-16.′8	16.′8-24.′6	24.′6-31.′1	31.′1-38.′8
kT(keV)	$8.16^{+0.10}_{-0.10}$	$9.02^{+0.19}_{-0.19}$	$9.50^{+0.38}_{-0.38}$	$8.47^{+0.65}_{-0.48}$	$7.79^{+0.81}_{-0.79}$	$6.14^{+1.30}_{-0.95}$	$3.42^{+2.14}_{-1.22}$	$1.01^{+0.44}_{-0.29}$	$1.08^{+0.28}_{-0.37}$
Z	$0.33^{+0.02}_{-0.02}$	$0.28^{+0.02}_{-0.02}$	$0.24^{+0.05}_{-0.05}$	$0.31^{+0.09}_{-0.09}$	$0.19^{+0.13}_{-0.12}$	0.2 (fix)	0.2 (fix)	0.2 (fix)	0.2 (fix)
norm*	1.82 ± 0.01E5	3.90 ± 0.01E4	7.50 ± 0.01E3	2.09 ± 0.07E3	8.30 ± 0.32E2	6.70 ± 0.40E2	1.35 ± 0.22E2	2.00 ± 0.11E1	1.00 ± 0.50
χ^2/d.o.f	712 / 604	691 / 604	681 / 604	309 / 270	338 / 270	381 / 358	272 / 217	238 / 223	299 / 223

Table A.7: Best-fit parameters of the ICM of A1413

	0′-2′.0	2′.0-5′.0	5′.0 – 8′.0	8′.0 – 12′.0
kT(keV)	$7.92^{+0.20}_{-0.24}$	$6.50^{+0.29}_{-0.28}$	$4.38^{+0.32}_{-0.25}$	$3.88^{+0.69}_{-0.55}$
Z	$0.30^{+0.05}_{-0.05}$	$0.32^{+0.07}_{-0.07}$	$0.21^{+0.11}_{-0.10}$	0.2(fix)
norm	$395.8^{+9.2}_{-9.2}$	$43.6^{+1.0}_{-0.9}$	$10.0^{+0.1}_{-0.1}$	$4.5^{+0.1}_{-0.1}$
χ^2/d.o.f	1086 / 1024	1066 / 978	1153 / 979	1294 / 1018

Table A.8: Best-fit parameters of the ICM of A2218

	0′-2′.0	2′.0-4′.0	4′.0 – 7′.0	7′.0 – 9′.0
kT(keV)	$7.85^{+0.29}_{-0.28}$	$6.47^{+0.26}_{-0.26}$	$5.30^{+0.49}_{-0.39}$	$3.01^{+0.89}_{-0.62}$
Z	$0.20^{+0.05}_{-0.05}$	$0.23^{+0.06}_{-0.06}$	$0.21^{+0.11}_{-0.10}$	0.2(fix)
norm	$520.8^{+9.2}_{-9.2}$	$65.0^{+1.4}_{-1.4}$	$10.1^{+0.4}_{-0.4}$	$1.8^{+0.2}_{-0.2}$
χ^2/d.o.f	356 / 319	404 / 319	313 / 319	384 / 320

Table A.9: Best-fit parameters of the ICM of CIZA2242

	0′-2′.5	2′.5-5′.0	5′.0 – 7′.7	7′.7 – 10′.4	10′.4 – 12′.9	12′.9 – 16′.7
kT(keV)	$7.25^{+0.34}_{-0.33}$	$8.37^{+0.49}_{-0.39}$	$7.45^{+1.08}_{-0.93}$	$4.06^{+1.51}_{-0.84}$	$1.53^{+0.53}_{-0.38}$	$1.42^{+0.50}_{-0.24}$
Z	$0.00^{+0.00}_{0.00}$	$0.00^{+0.00}_{0.00}$	$0.00^{+0.00}_{0.00}$	$0.00^{+0.00}_{0.00}$	$0.00^{+0.00}_{0.00}$	$0.00^{+0.00}_{0.00}$
norm						
χ^2/d.o.f	325 / 309	361 / 309	461 / 316	203 / 156	121 / 96	142 / 118

5

Table A.10: Best-fit parameters of the ICM of A2163center

	0′-2.′5	2.′5-5.′0	5.′0 – 8.′0	8.′0 – 11.′0	11.′0 – 15.′0
kT(keV)	$15.80^{+0.44}_{-0.44}$	$14.21^{+0.76}_{-0.76}$	$15.51^{+1.67}_{-1.68}$	$8.64^{+1.52}_{-1.04}$	$8.42^{+4.39}_{-1.92}$
Z	$0.29^{+0.04}_{-0.04}$	$0.17^{+0.06}_{-0.06}$	$0.10^{+0.13}_{-0.10}$	$0.21^{+0.16}_{-0.16}$	0.2 (fix)
norm	$1125.3^{+0.0}_{0.0}$	$151.9^{+4.0}_{-4.0}$	$24.7^{+0.9}_{-0.9}$	$7.8^{+0.3}_{-0.3}$	$3.0^{+0.4}_{-0.4}$
χ^2/d.o.f	3458 / 2982	1892 / 1936	1117 / 1091	829 / 839	826 / 877

Table A.11: Best-fit parameters of the ICM of A2163ne

	0′-2.′5	2.′5-5.′0	5.′0 – 8.′0	8.′0 – 11.′0
kT(keV)	$14.86^{+0.63}_{-0.63}$	$16.58^{+0.97}_{-0.88}$	$12.04^{+1.02}_{-1.02}$	$10.76^{+1.85}_{-1.44}$
Z	$0.29^{+0.05}_{-0.05}$	$0.23^{+0.08}_{-0.08}$	$0.24^{+0.09}_{-0.09}$	0.2(fix)
norm	$1091.3^{+24.8}_{-24.8}$	$167.0^{+4.1}_{-4.1}$	$47.9^{+0.9}_{-0.9}$	$13.8^{+0.6}_{-0.6}$
χ^2/d.o.f	2262 / 2138	1627 / 1565	1205 / 1043	490 / 484

Table A.12: Best-fit parameters of the ICM of A963

	0′-2.′0	2.′0-5.′0	5.′0 – 9.′0
kT(keV)	$6.71^{+0.20}_{-0.17}$	$5.90^{+0.29}_{-0.29}$	$4.18^{+0.98}_{-0.72}$
Z	$0.37^{+0.04}_{-0.04}$	$0.18^{+0.05}_{-0.05}$	0.2(fix)
norm	$476.7^{+10.1}_{-10.0}$	$28.8^{+8.4}_{-7.9}$	$6.2^{+1.0}_{-0.9}$
χ^2/d.o.f	1775 / 1819	1217 / 1219	567 / 526

Table A.13: Best-fit parameters of the ICM of A2219

	0′-2.′0	2.′0-4.′0	4.′0 – 7.′0	7.′0 – 11.′0
kT(keV)	$12.42^{+0.36}_{-0.36}$	$11.34^{+0.46}_{-0.47}$	$9.01^{+0.53}_{-0.51}$	$5.66^{+0.65}_{-0.64}$
Z	$0.25^{+0.04}_{-0.04}$	$0.24^{+0.04}_{-0.04}$	0.2(fix)	0.2(fix)
norm	$786.6^{+7.7}_{-7.7}$	$145.2^{+2.1}_{-2.1}$	$29.4^{+0.8}_{-0.8}$	$5.8^{+0.4}_{-0.4}$
χ^2/d.o.f	564 / 399	485 / 399	506 / 400	389 / 400

Table A.14: Best-fit parameters of the ICM of A2390

	0′-2′.0	2′.0-4′.0	4′.0 – 7′.0	7′.0 – 11′.0
kT(keV)	$10.31^{+0.18}_{-0.18}$	$11.47^{+0.43}_{-0.44}$	$9.61^{+0.56}_{-0.56}$	$6.34^{+1.04}_{-0.79}$
Z	$0.37^{+0.03}_{-0.03}$	$0.28^{+0.04}_{-0.04}$	0.2(fix)	0.2(fix)
norm	$961.2^{+9.6}_{-9.6}$	$97.0^{+1.0}_{-1.1}$	$15.9^{+0.5}_{0.6}$	$3.2^{+0.2}_{-0.2}$
χ^2/d.o.f	2770 / 2482	1901 / 1916	1199 / 1262	669 / 688

Table A.15: Best-fit parameters of the ICM of Zwcl2341

	0′-1′.5	1′.5-4′.0	4′.0 – 7′.0	4′.0 – 7′.0
kT(keV)	$6.16^{+0.42}_{-0.44}$	$4.64^{+0.22}_{-0.23}$	$1.57^{+0.32}_{-0.38}$	$2.62^{+0.42}_{-0.38}$
Z	$0.27^{+0.05}_{-0.05}$	$0.21^{+0.11}_{-0.1}$	0.2(fix)	0.2(fix)
norm	$62.0^{+3.2}_{-3.3}$	$26.3^{+1.2}_{-1.2}$	$3.2^{+0.2}_{-0.2}$	$6.3^{+0.4}_{-0.7}$
χ^2/d.o.f	133 / 169	102 / 105	356 / 394	

Appendix B

Stray light

B.1 Image

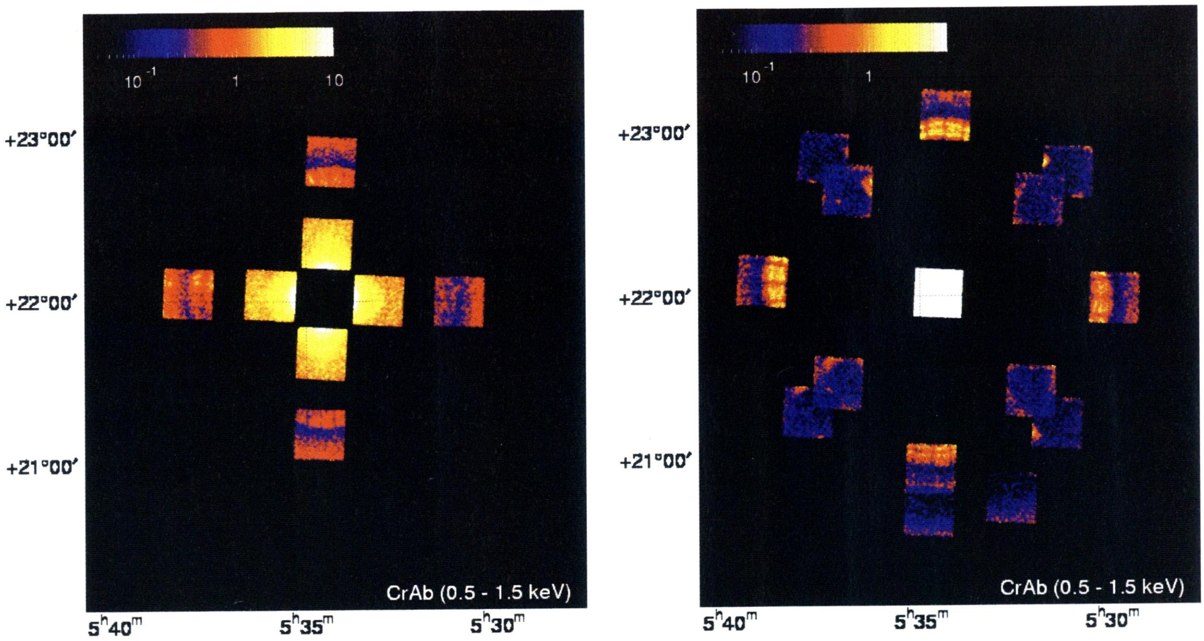

(a) SWG

(b) AO5

Fig. B.1: NXB subtracted image for 0.5_1.5 keV band.

Image:20off_0deg

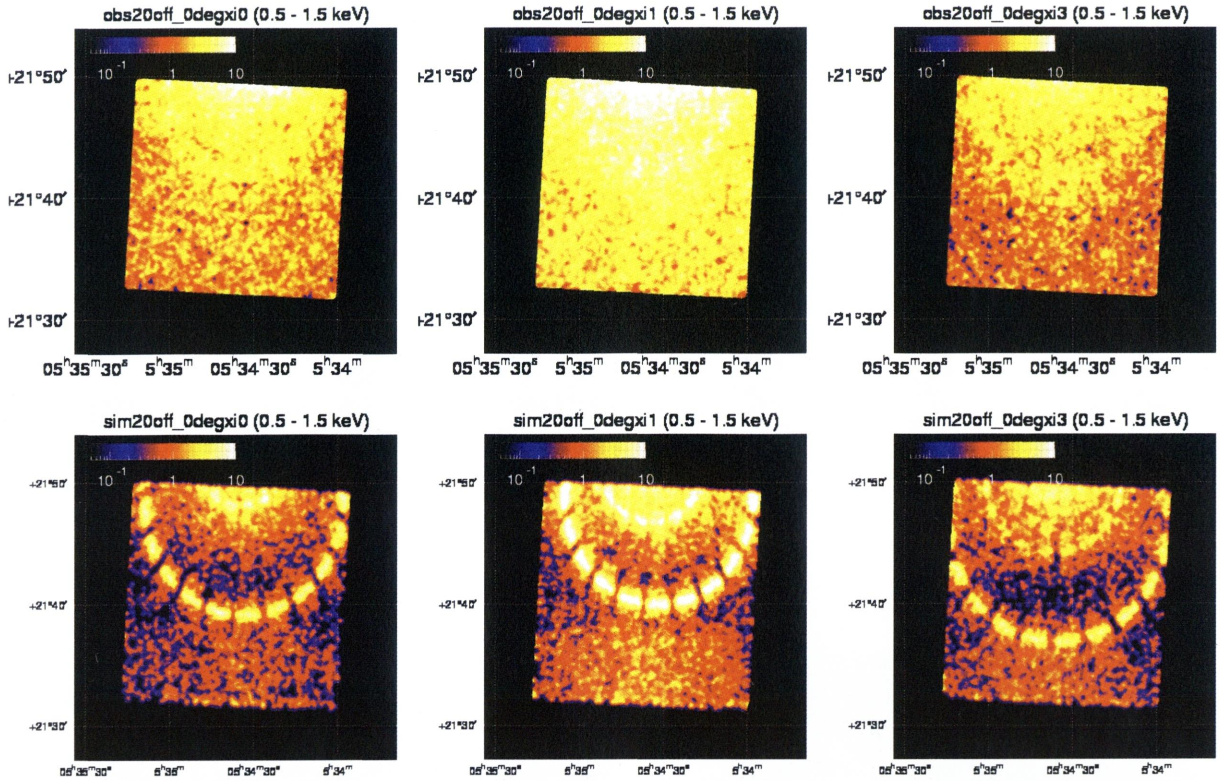

Image:20off_90deg

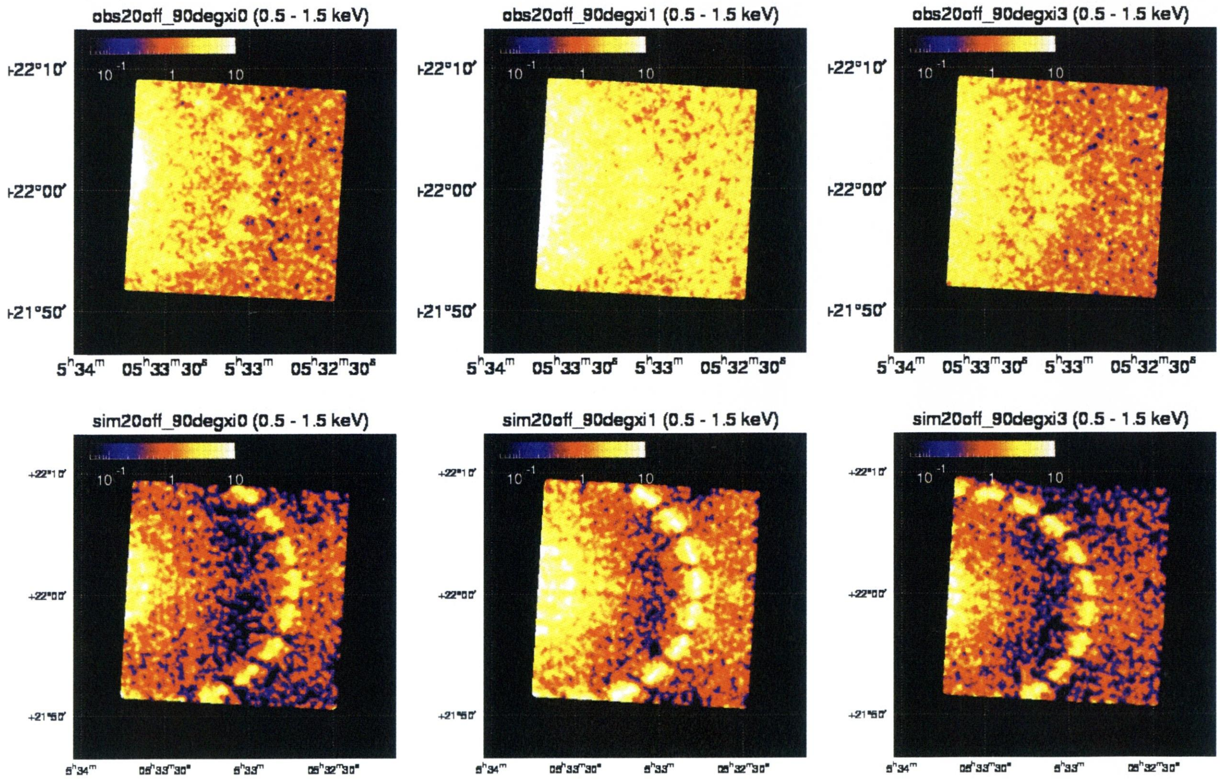

Image:20off_180deg

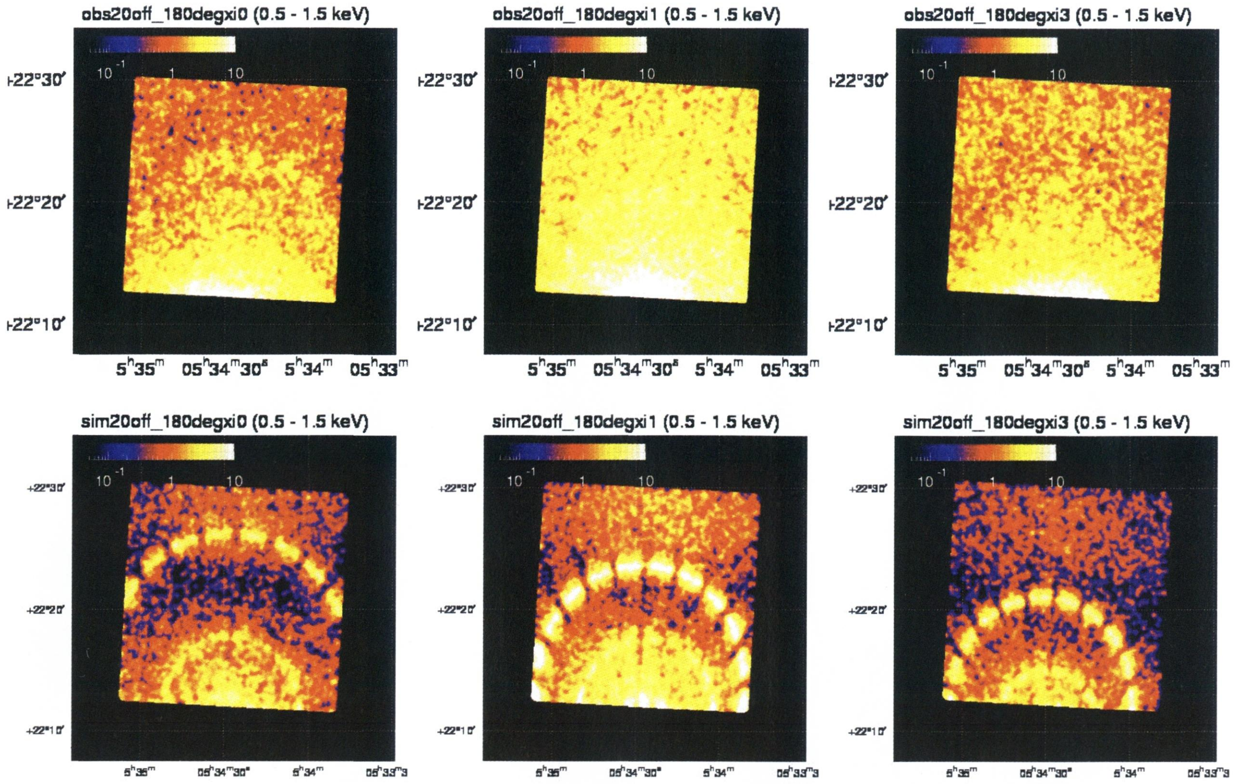
obs20off_180degxi0 (0.5 - 1.5 keV)
obs20off_180degxi1 (0.5 - 1.5 keV)
obs20off_180degxi3 (0.5 - 1.5 keV)
sim20off_180degxi0 (0.5 - 1.5 keV)
sim20off_180degxi1 (0.5 - 1.5 keV)
sim20off_180degxi3 (0.5 - 1.5 keV)

Image:50off_0deg

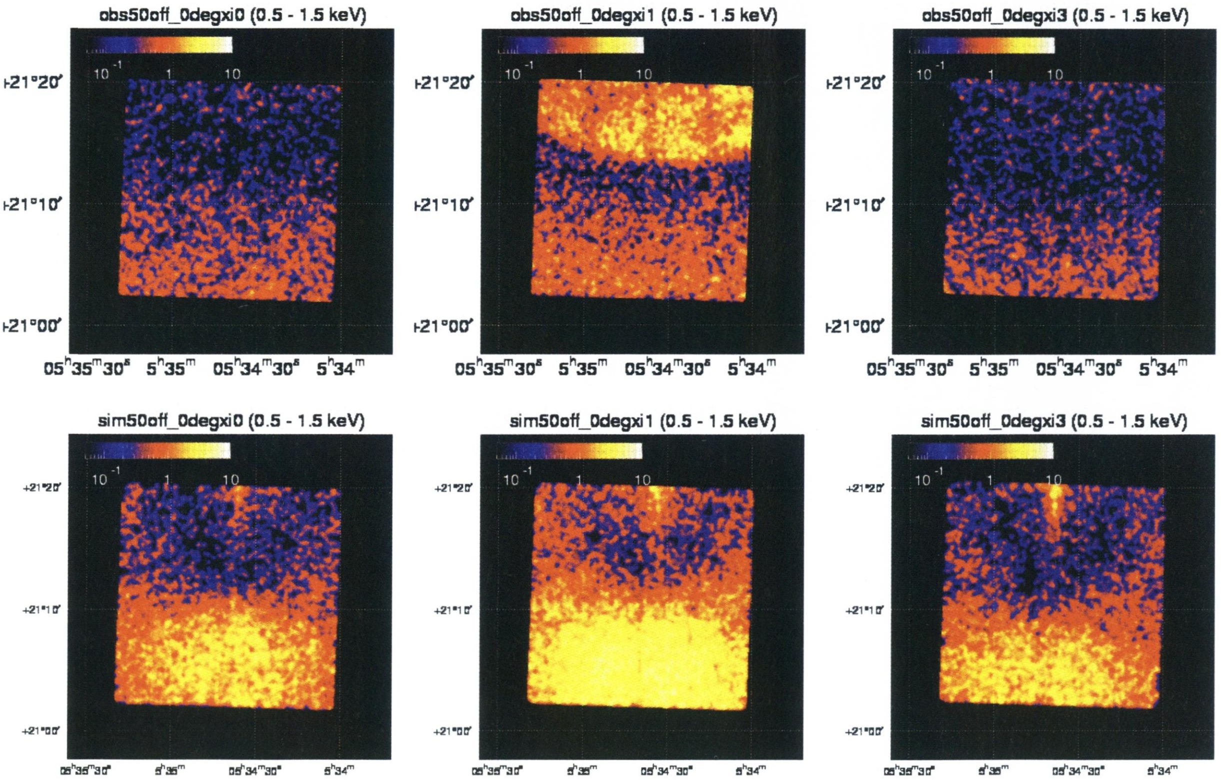
obs50off_0degxi0 (0.5 - 1.5 keV)
obs50off_0degxi1 (0.5 - 1.5 keV)
obs50off_0degxi3 (0.5 - 1.5 keV)
sim50off_0degxi0 (0.5 - 1.5 keV)
sim50off_0degxi1 (0.5 - 1.5 keV)
sim50off_0degxi3 (0.5 - 1.5 keV)

Image:50off_90deg

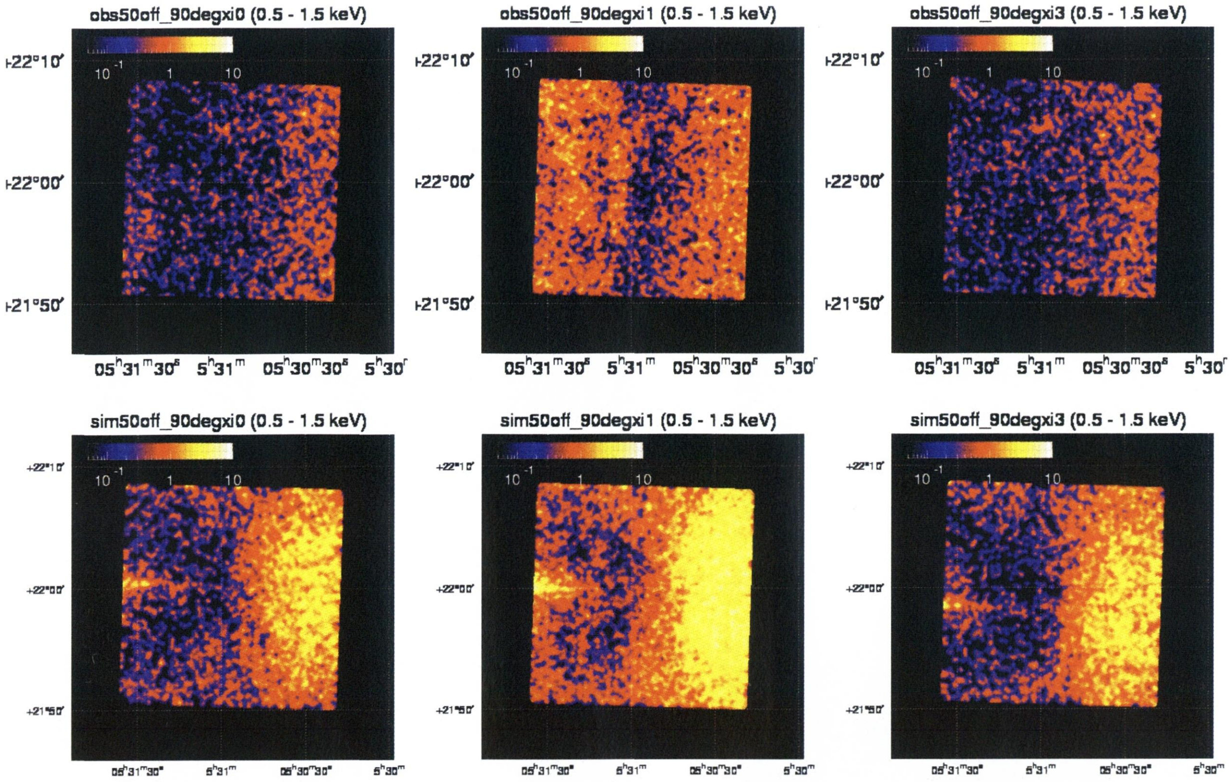

Image:50off_270deg

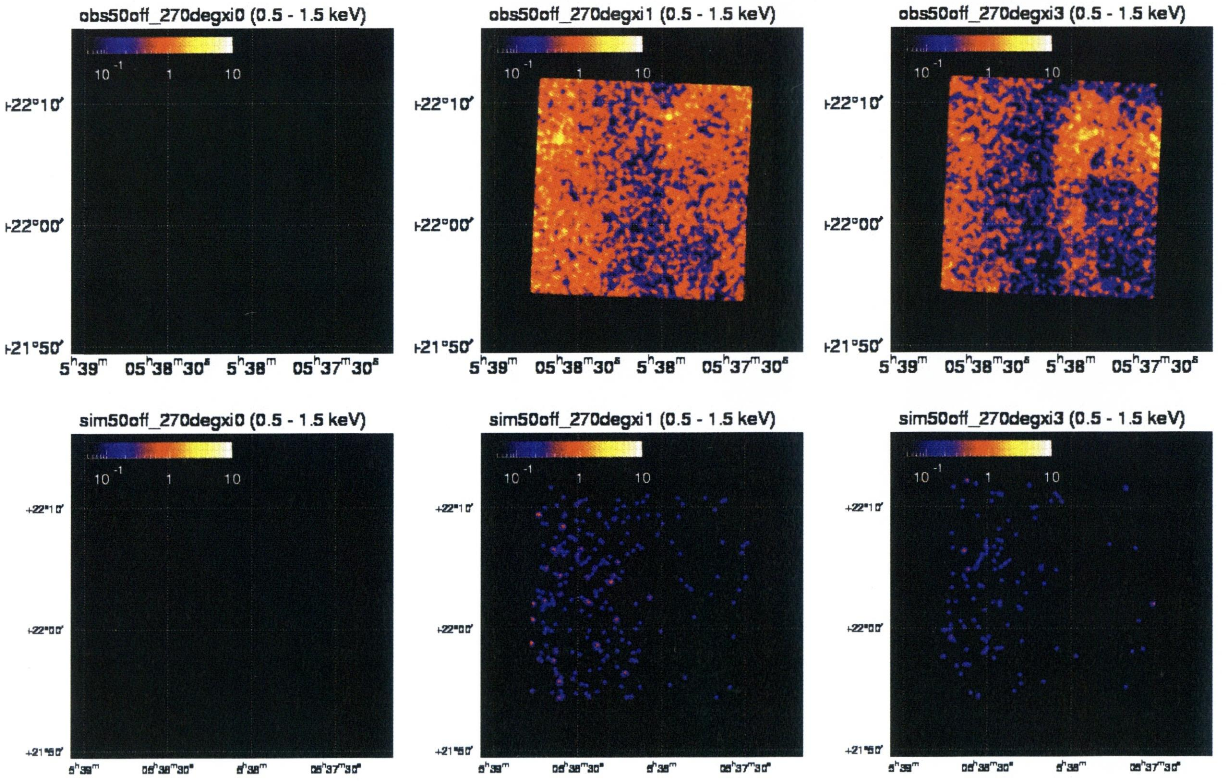

Image:50off_45deg

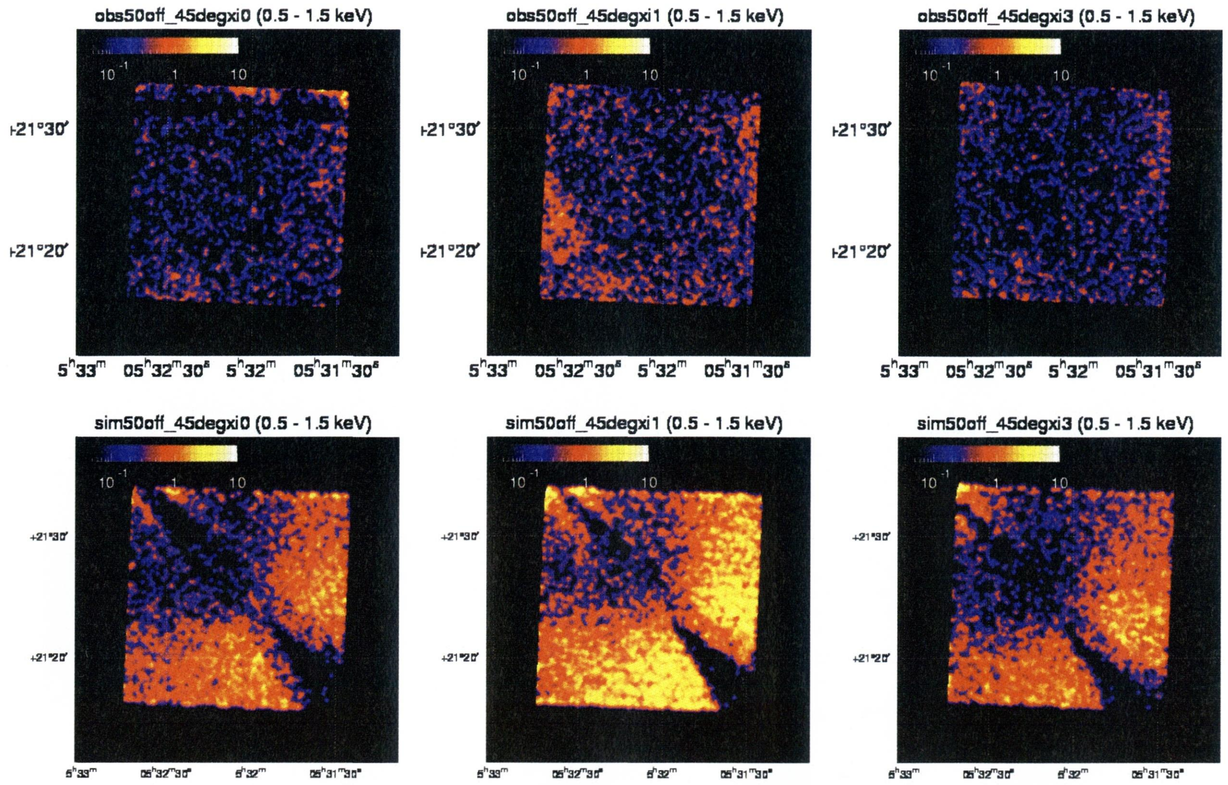

Image:50off_135deg

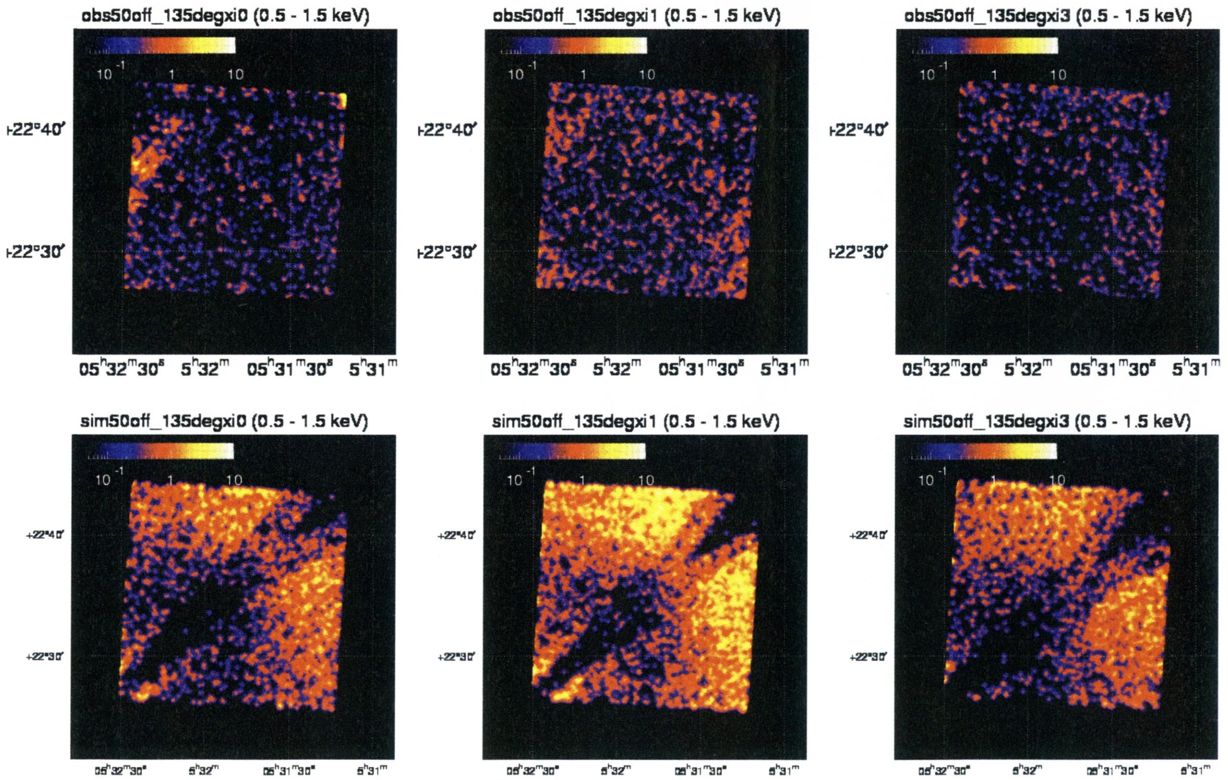

Image:50off_225deg

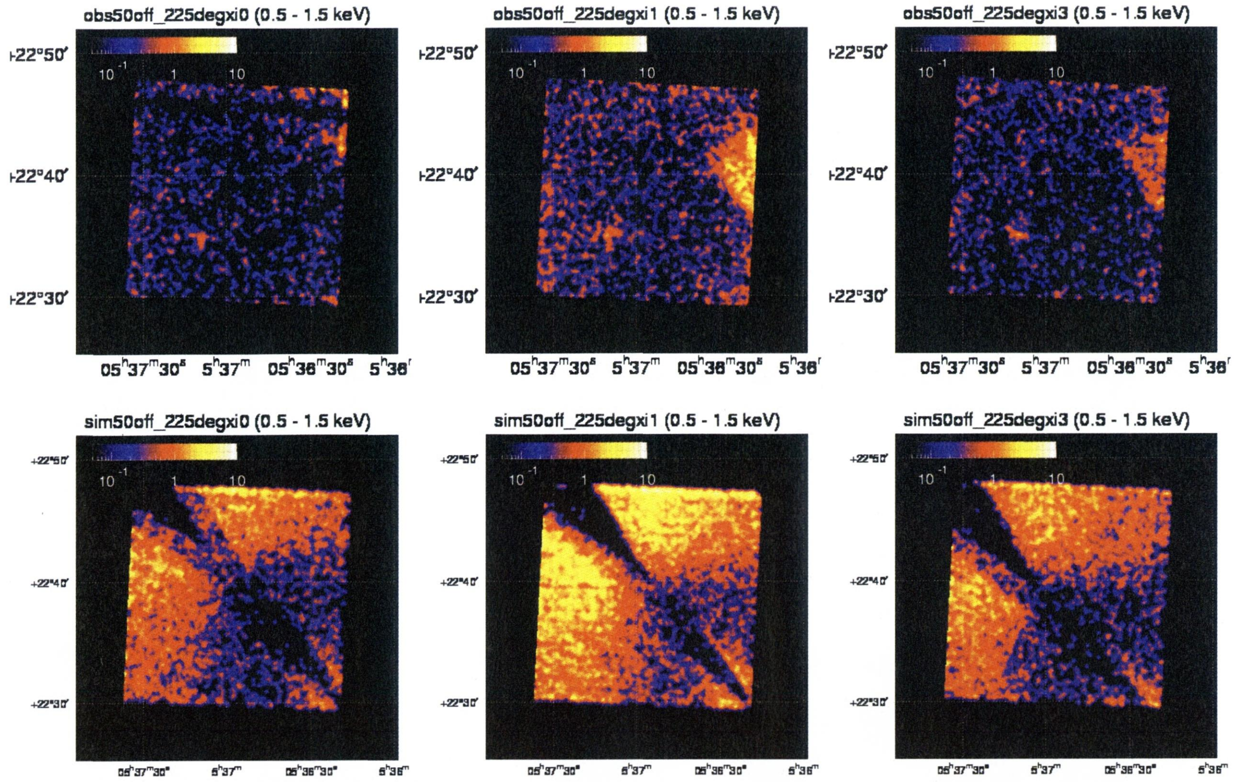

Image:50off_315deg

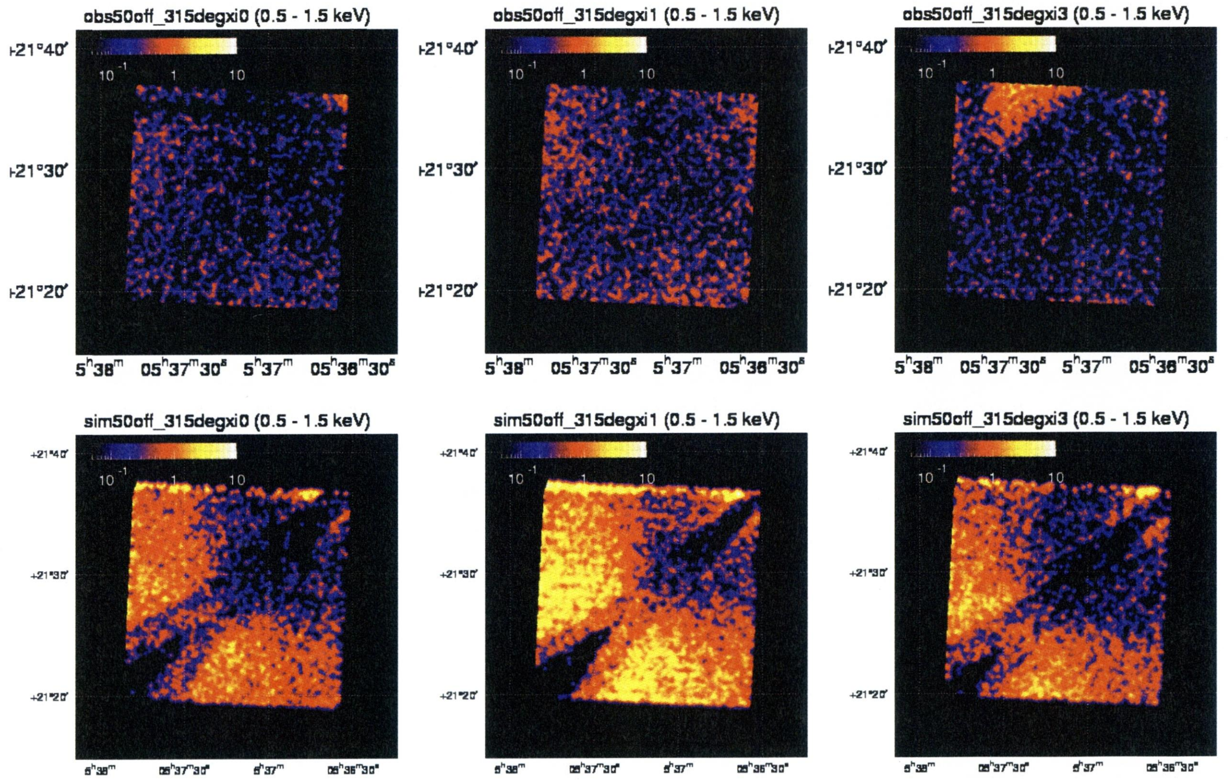

Image:65off_0deg

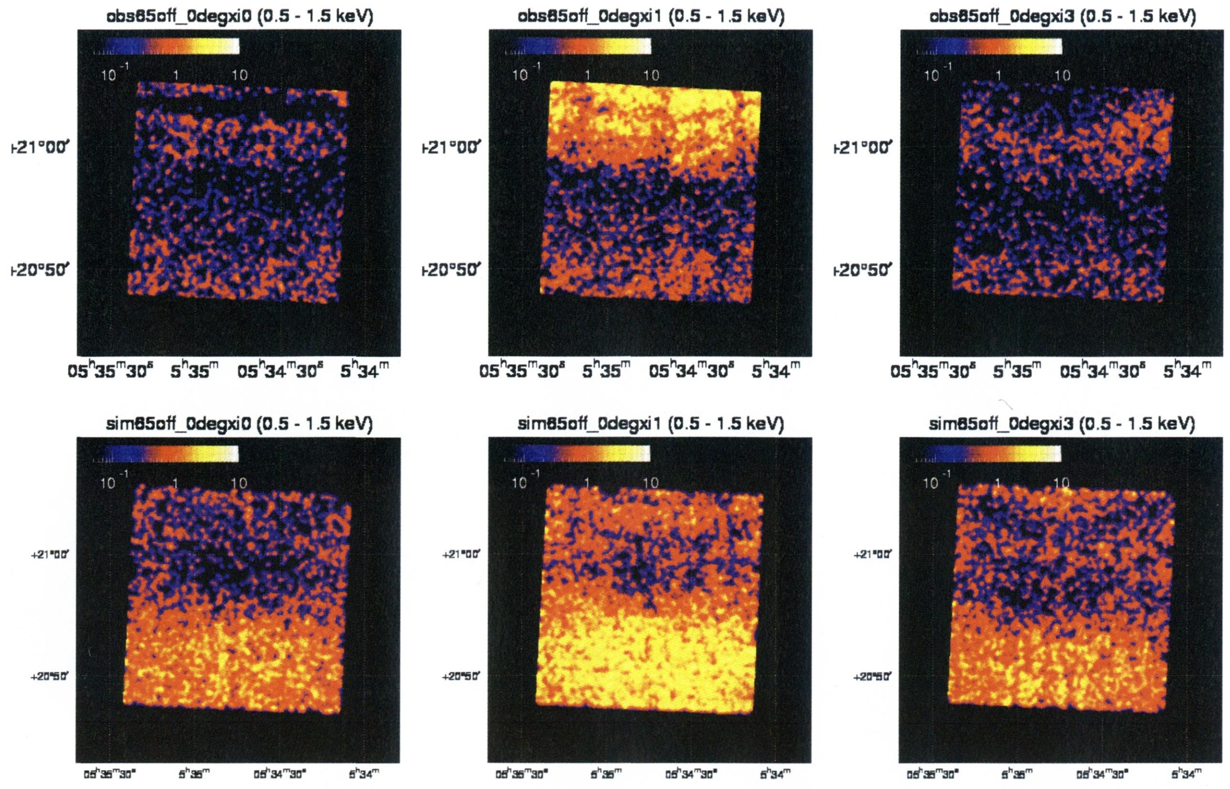

Image:80off_0deg

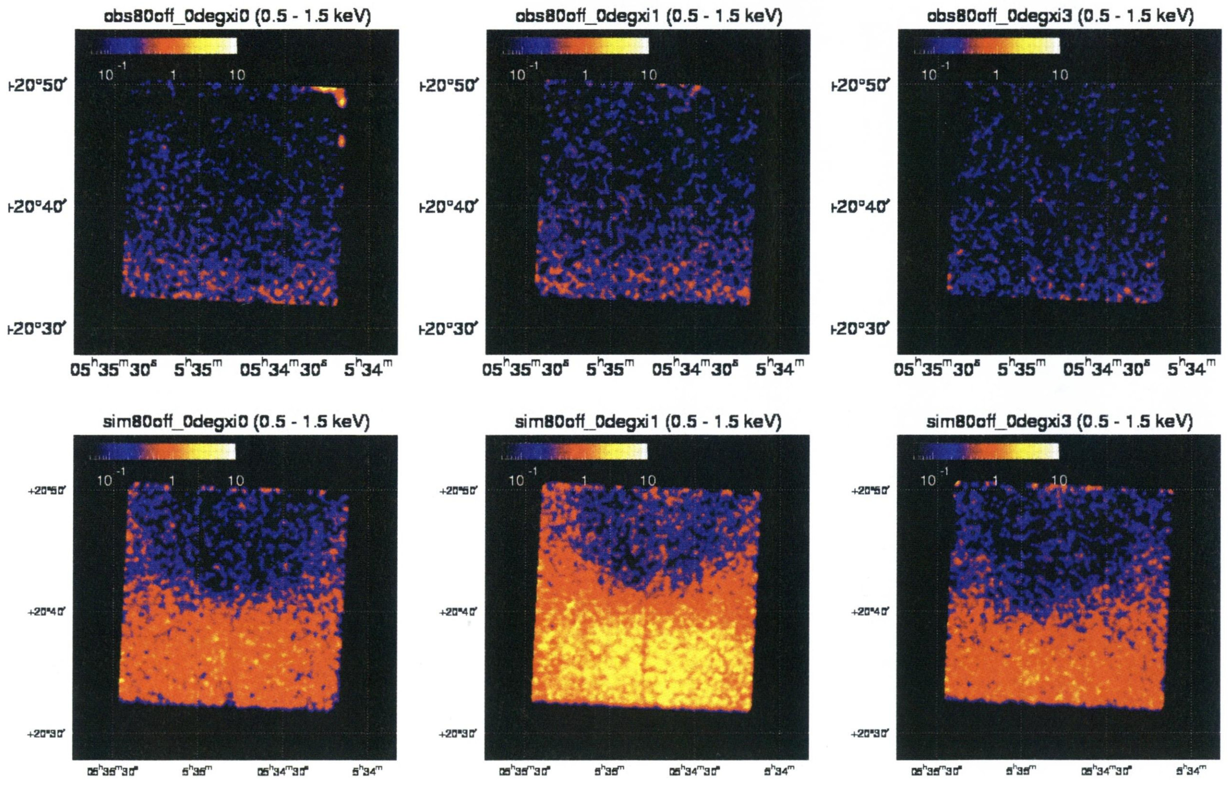

Image:65off_45deg

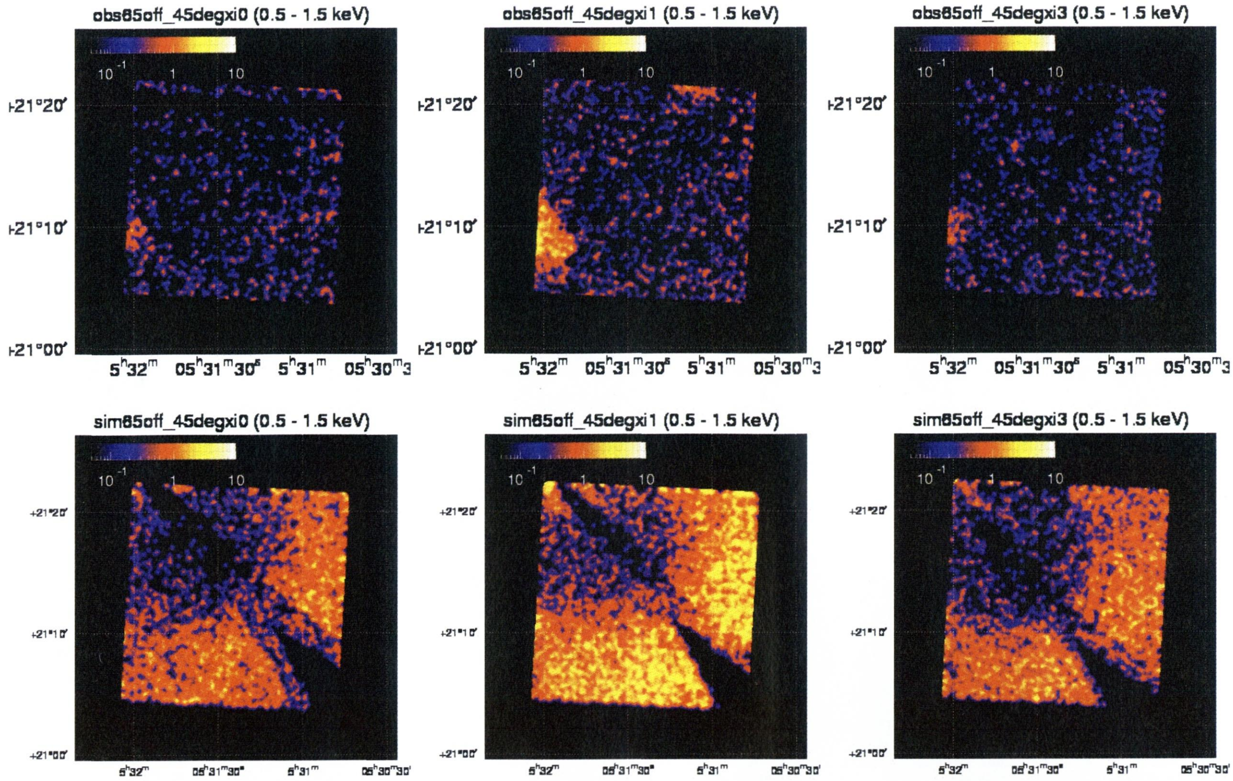

Image:65off_90deg

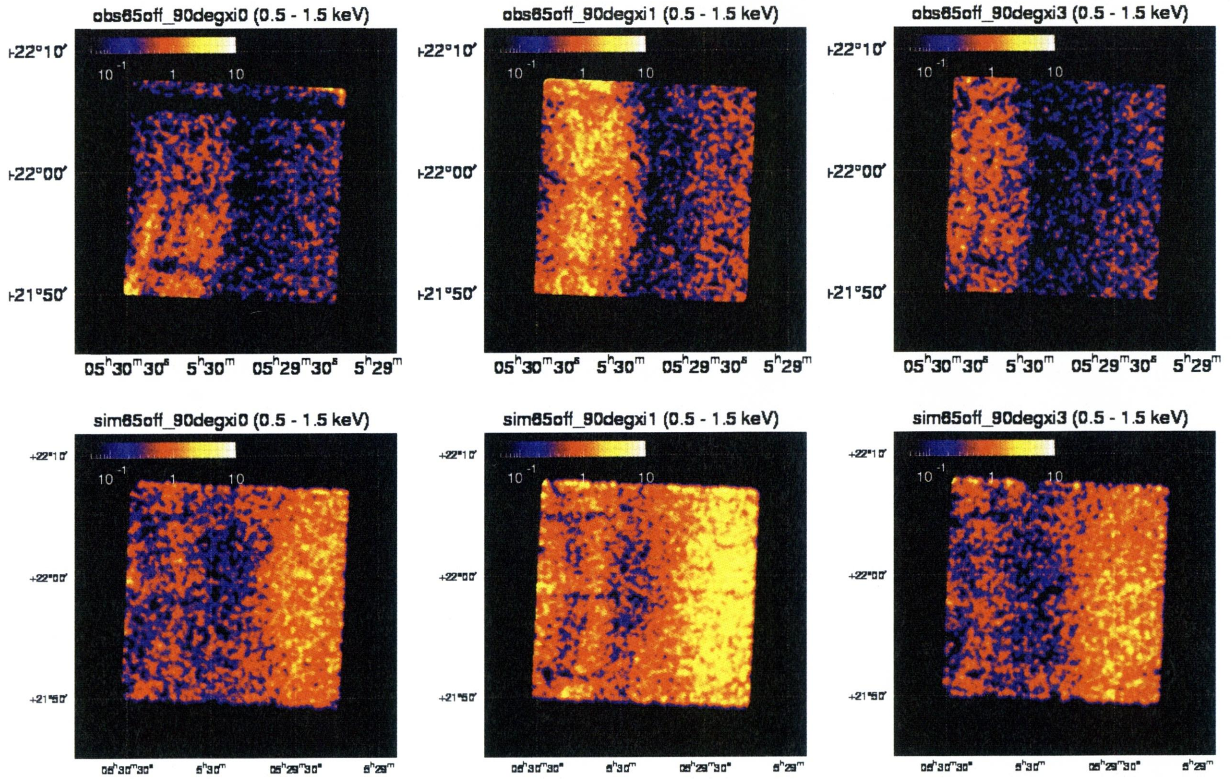

Image:65off_135deg

obs65off_135degxi0 (0.5 - 1.5 keV)

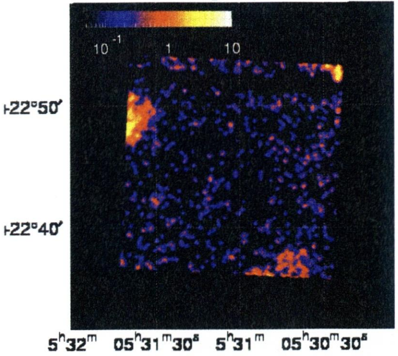

obs65off_135degxi1 (0.5 - 1.5 keV)

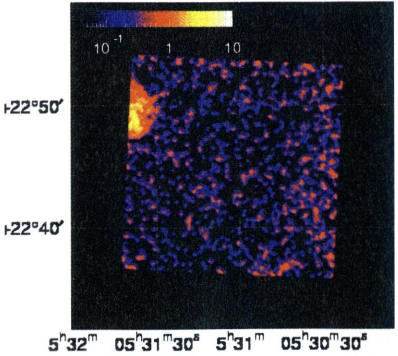

obs65off_135degxi3 (0.5 - 1.5 keV)

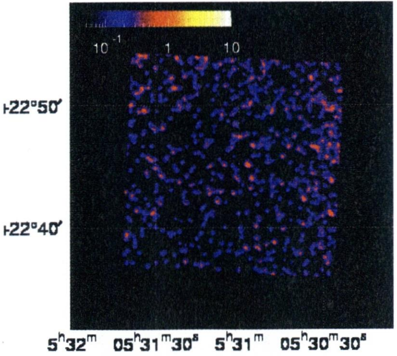

sim65off_135degxi0 (0.5 - 1.5 keV)

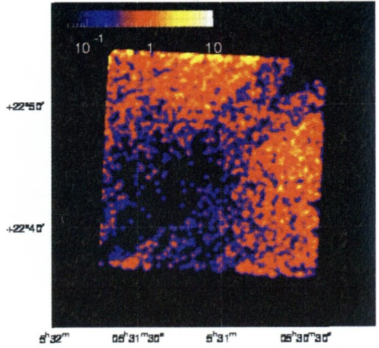

sim65off_135degxi1 (0.5 - 1.5 keV)

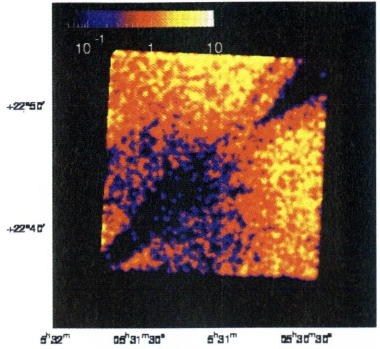

sim65off_135degxi3 (0.5 - 1.5 keV)

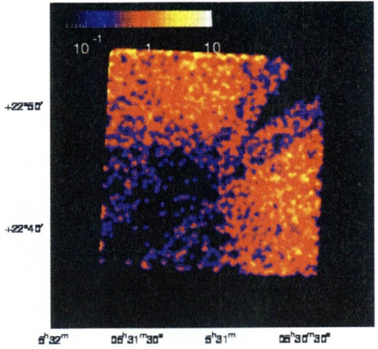

Image:65off_180deg

obs65off_180degxi0 (0.5 - 1.5 keV)

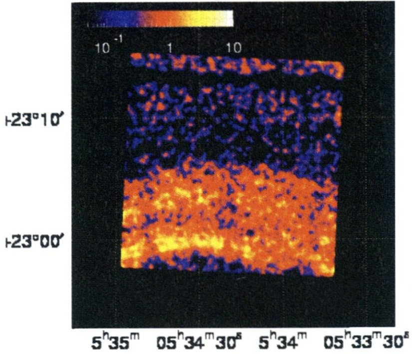

obs65off_180degxi1 (0.5 - 1.5 keV)

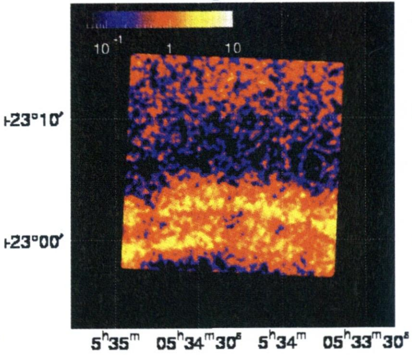

obs65off_180degxi3 (0.5 - 1.5 keV)

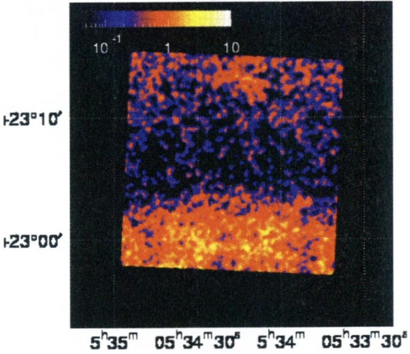

sim65off_180degxi0 (0.5 - 1.5 keV)

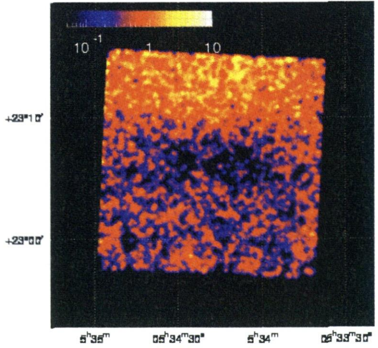

sim65off_180degxi1 (0.5 - 1.5 keV)

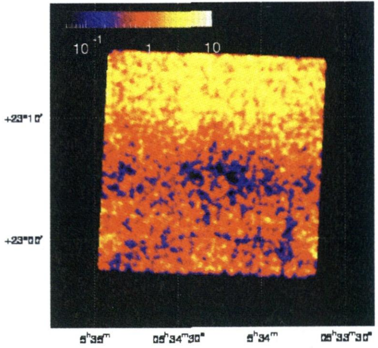

sim65off_180degxi3 (0.5 - 1.5 keV)

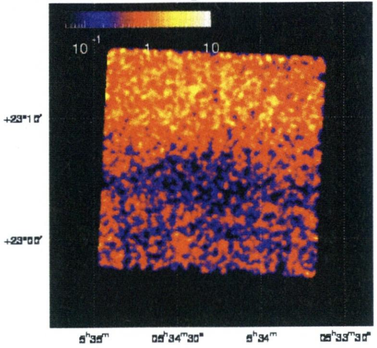

Image:65off_225deg

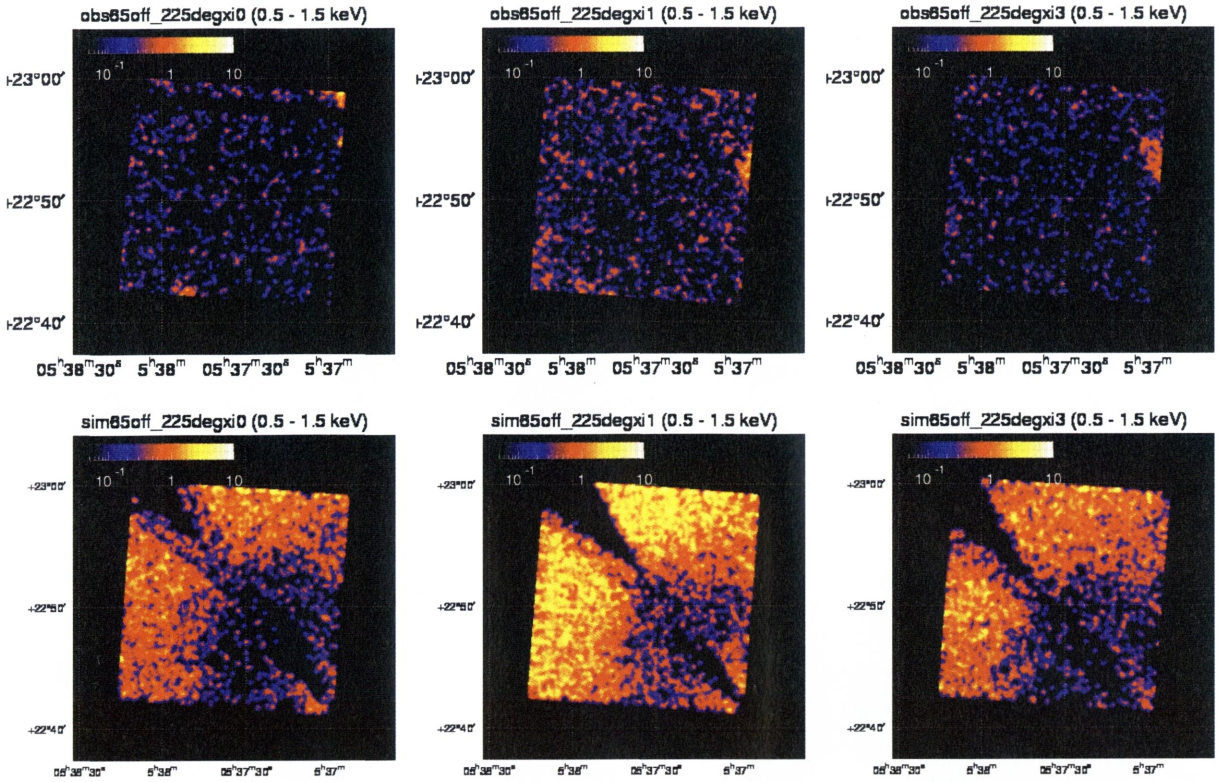

Image:65off_270deg

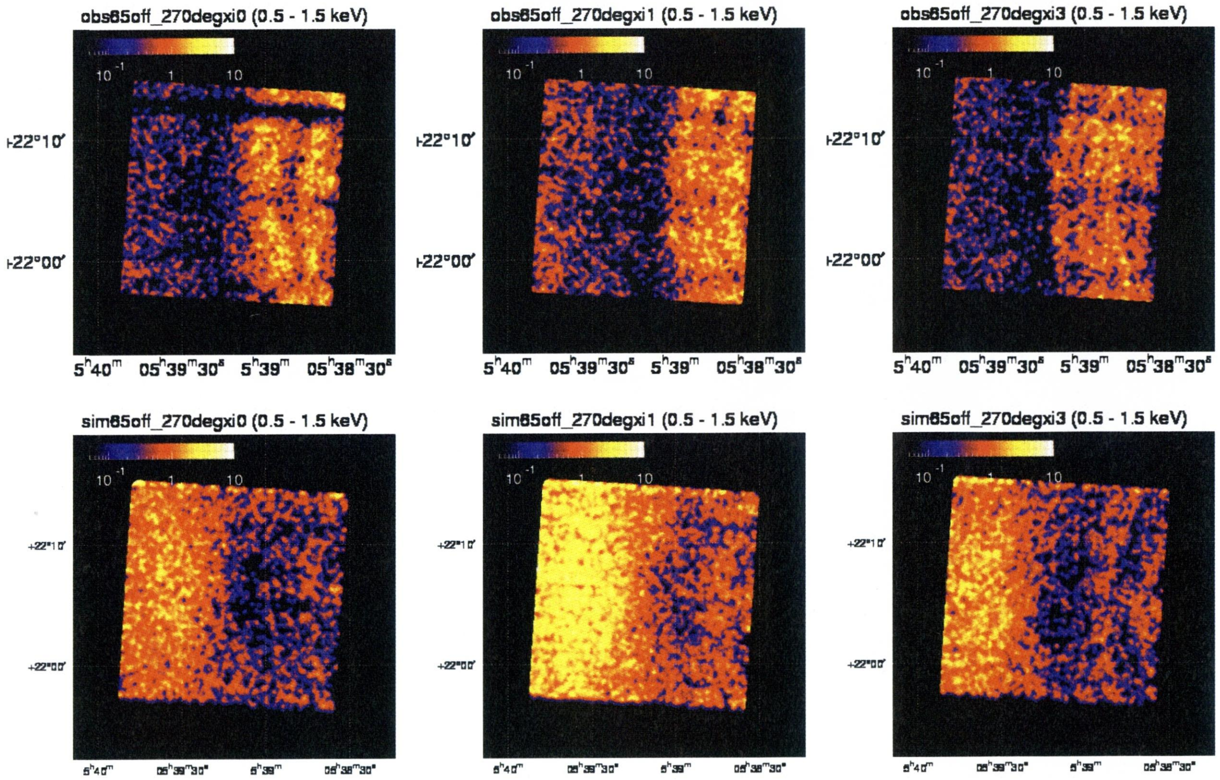

Image:65off_315deg

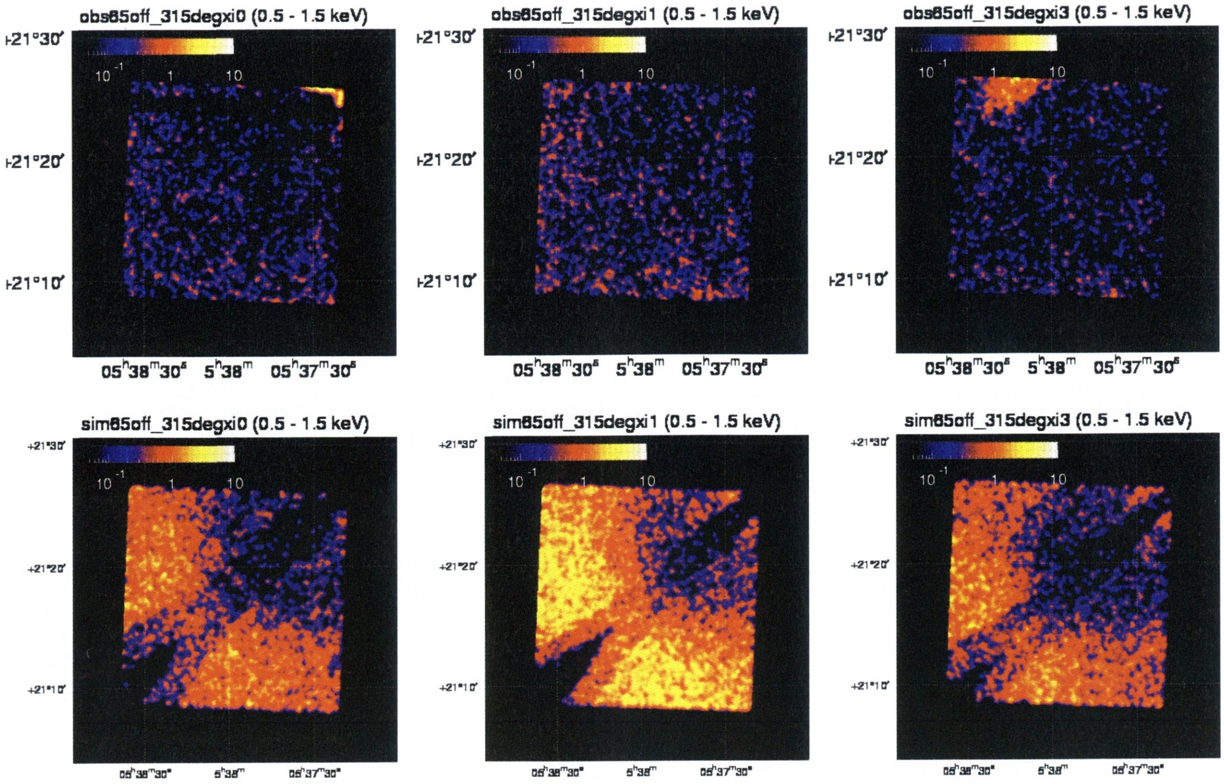

Radial:20off_0deg

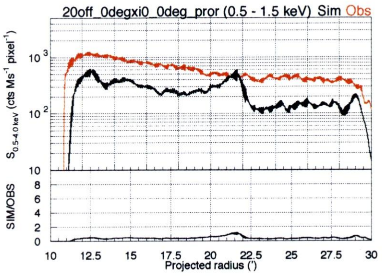

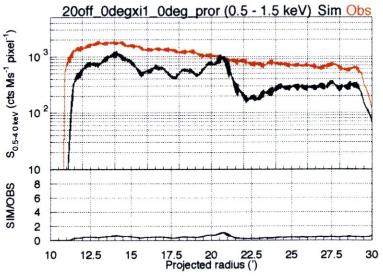

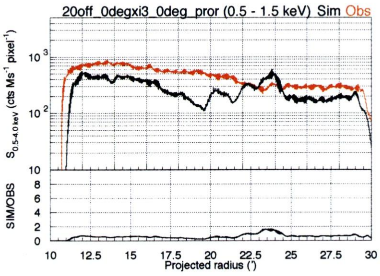

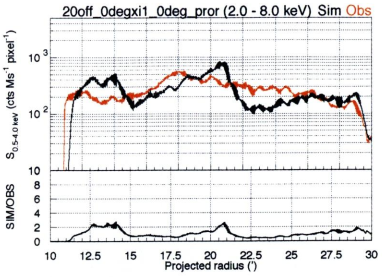

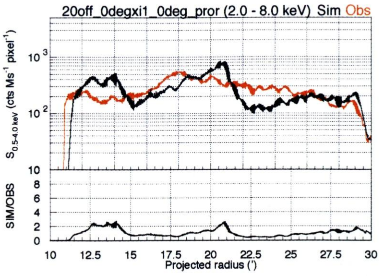

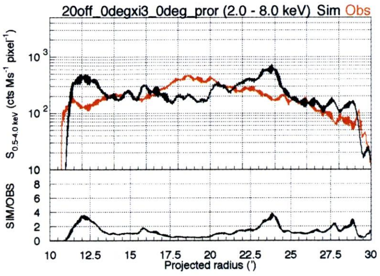

Radial:20off_90deg

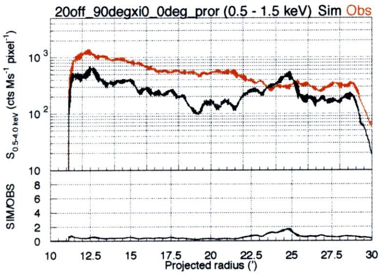

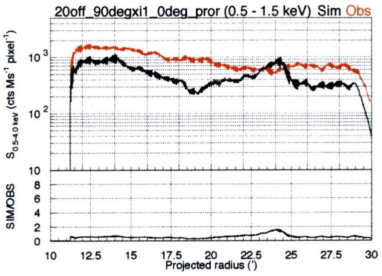

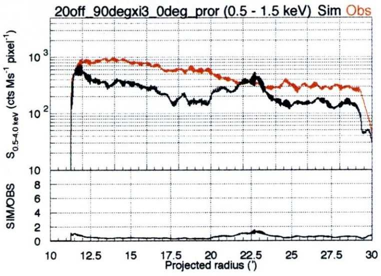

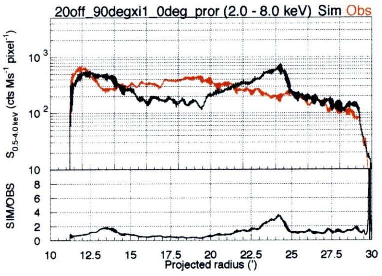

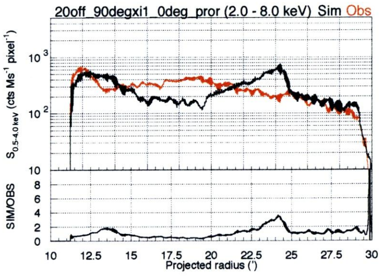

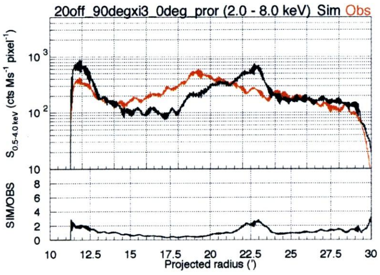

Radial:20off_180deg

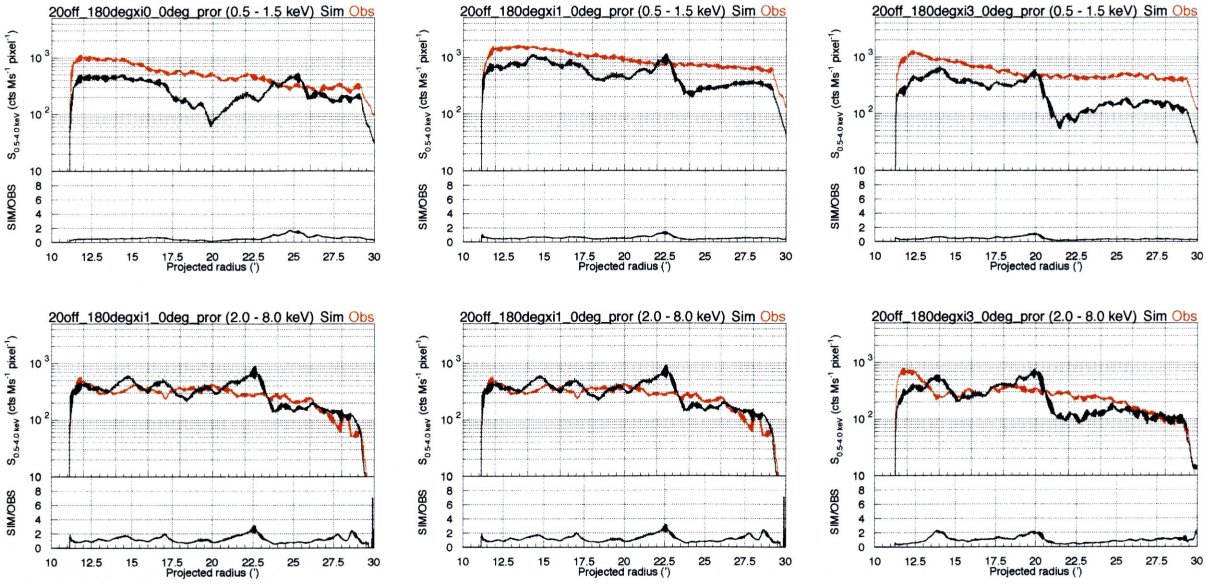

Radial:50off_0deg

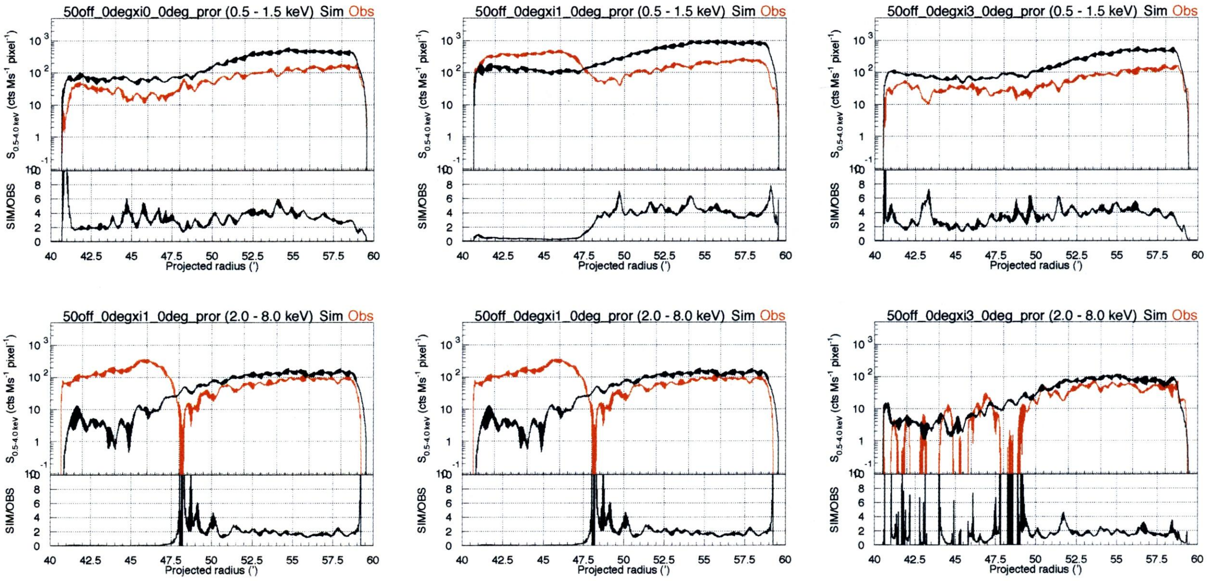

Radial:50off_90deg

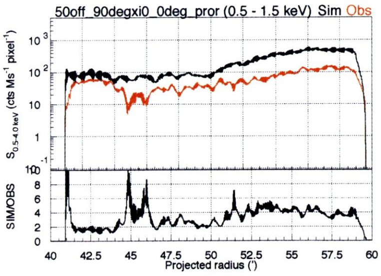

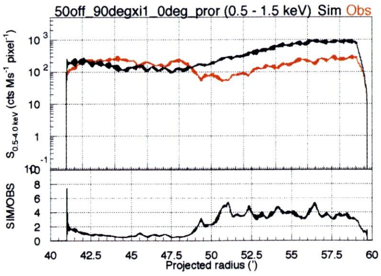

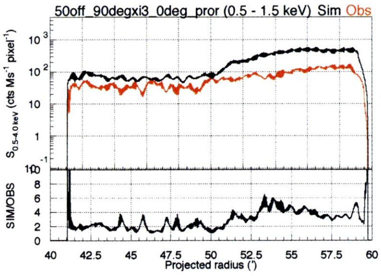

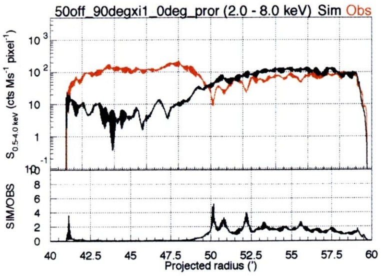

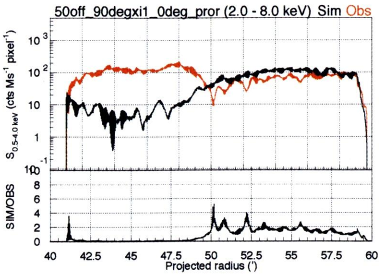

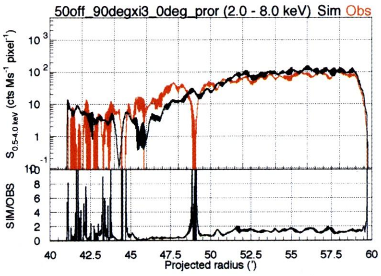

Radial:50off_270deg

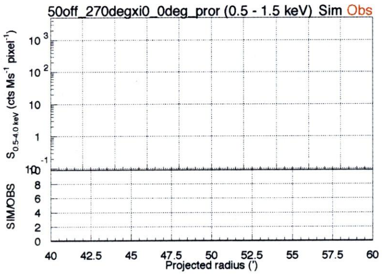

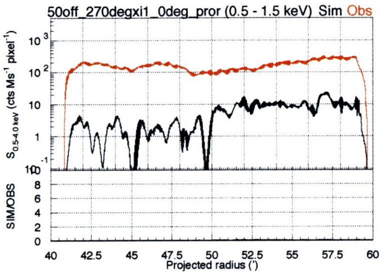

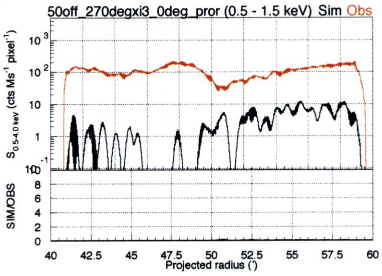

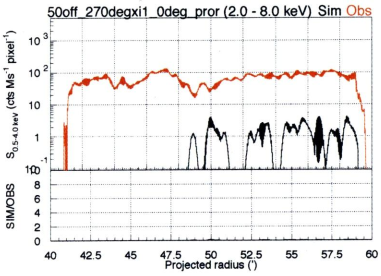

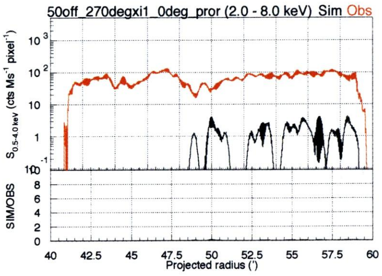

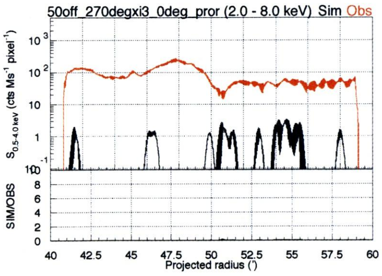

Radial:50off_45deg

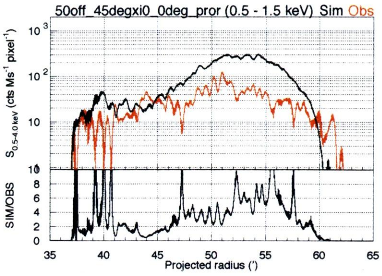

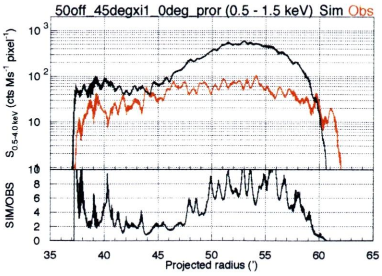

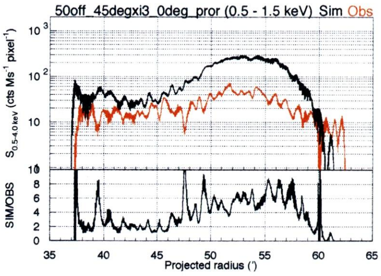

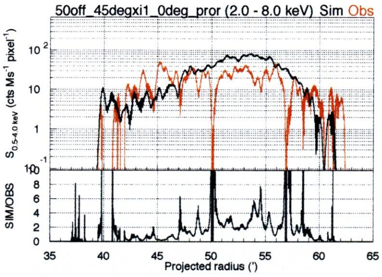

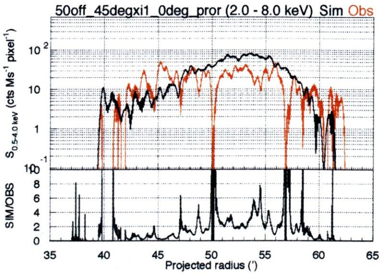

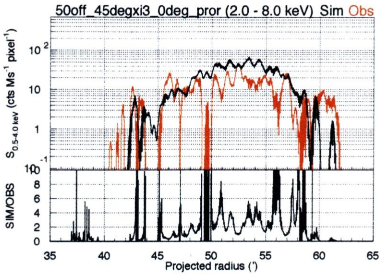

Radial:50off_135deg

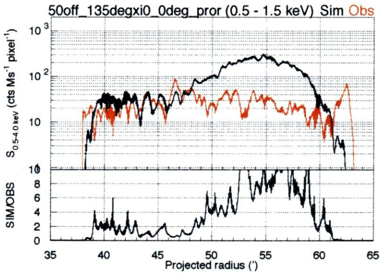

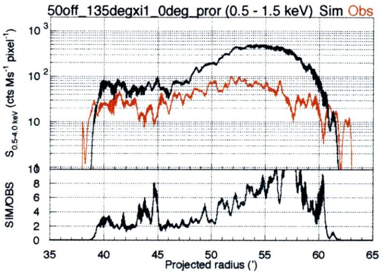

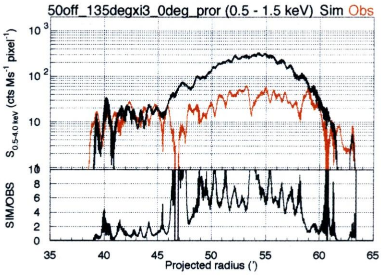

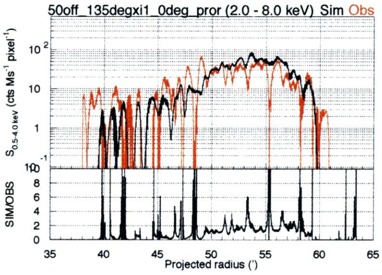

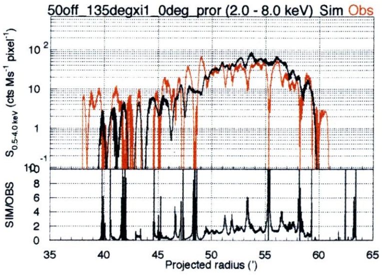

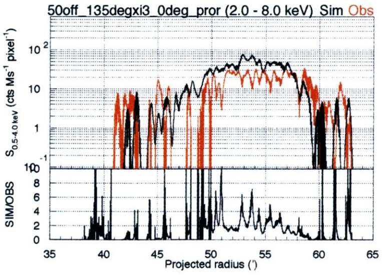

Radial:50off_225deg

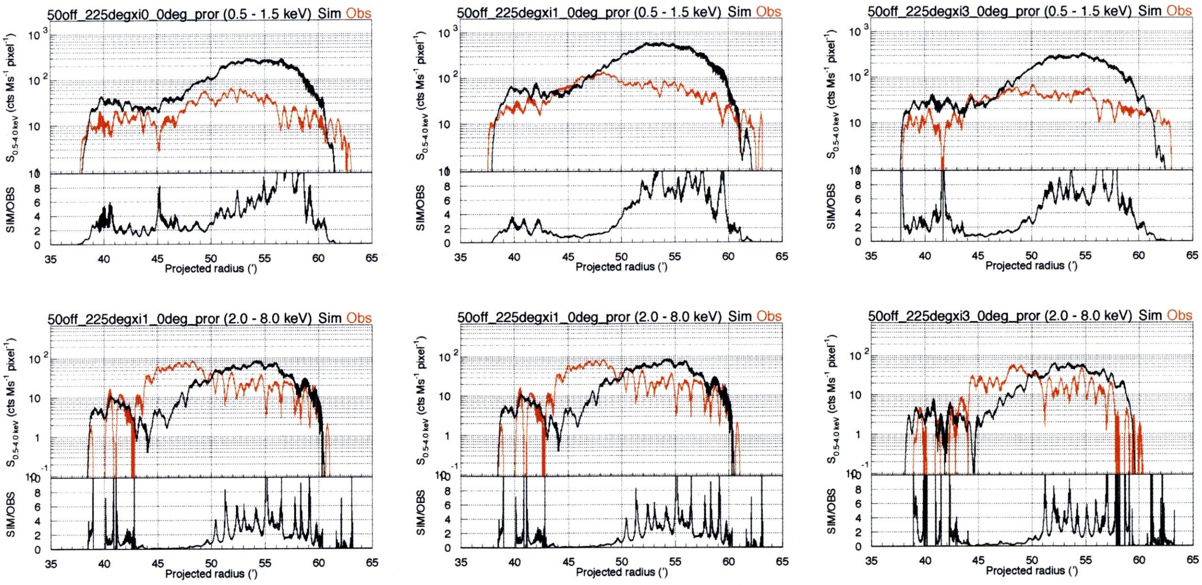

Radial:50off_315deg

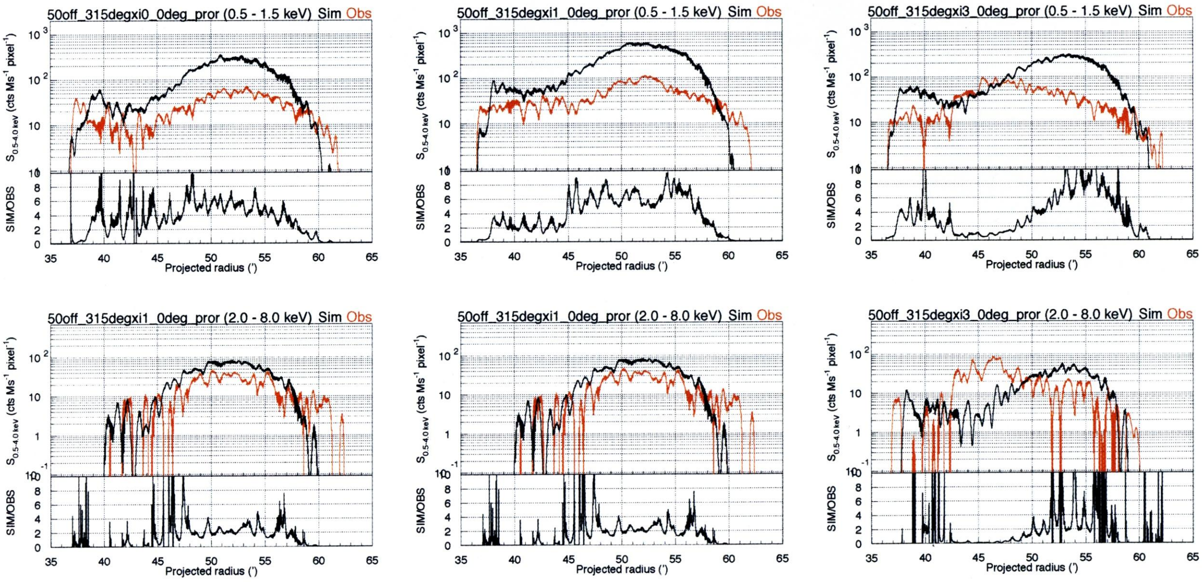

Radial:65off_0deg

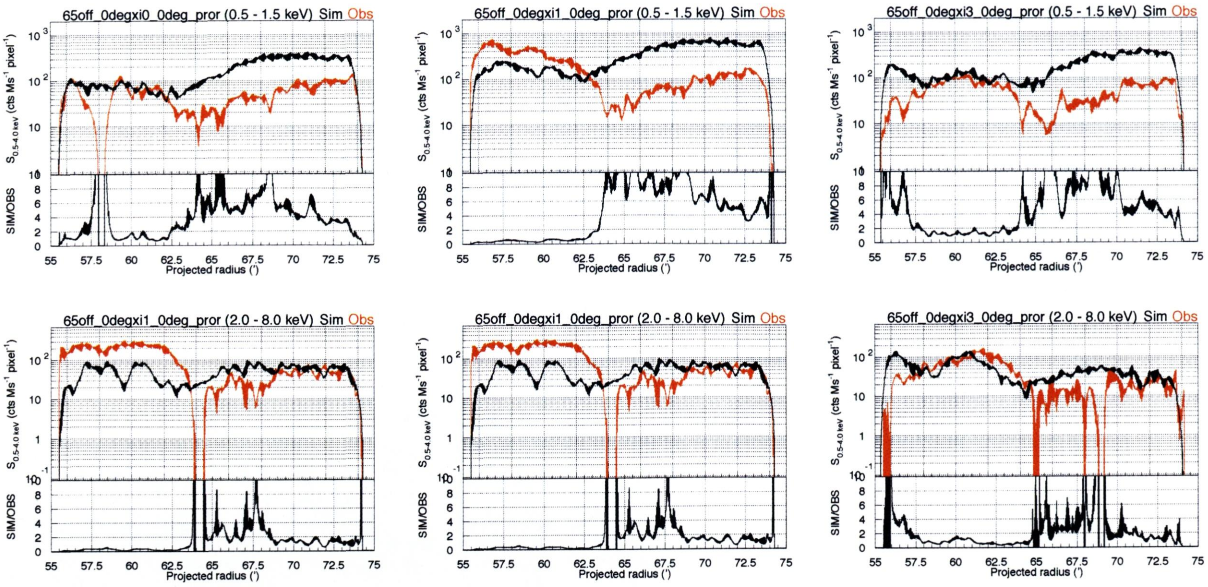

Radial:80off_0deg

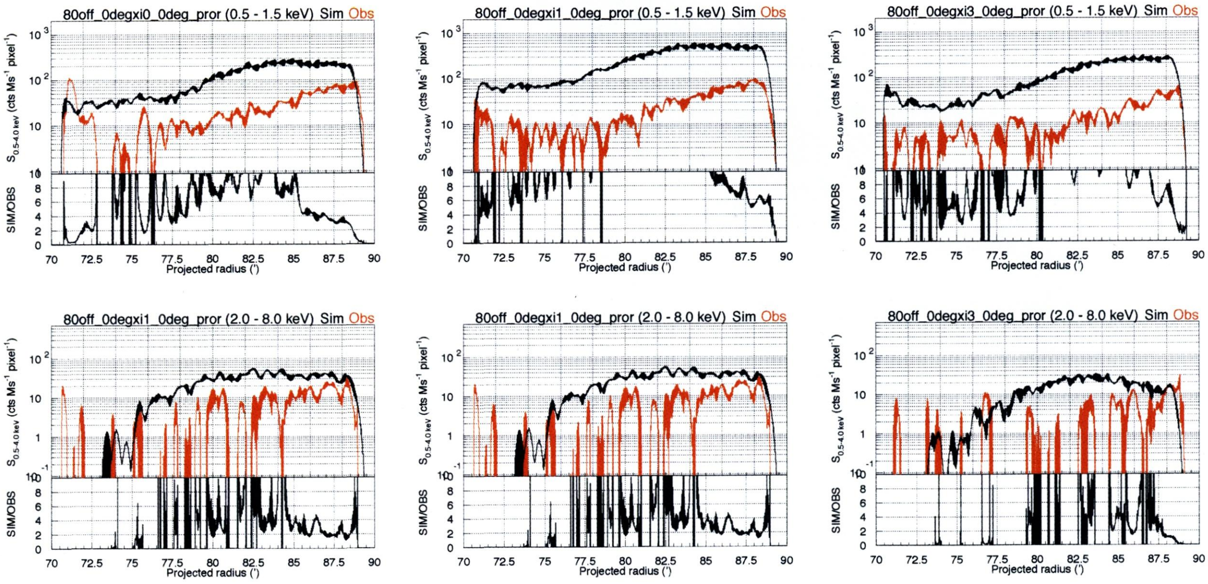

Radial:80off_22.5deg

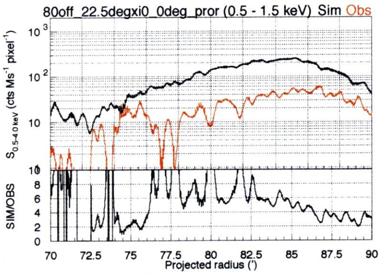

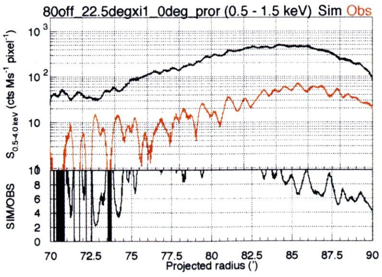

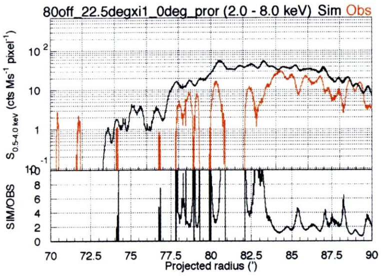

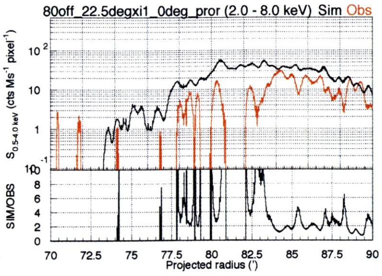

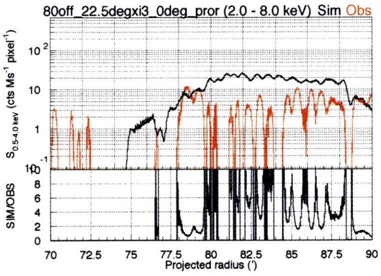

Radial:65off_45deg

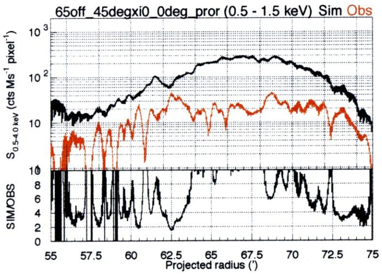

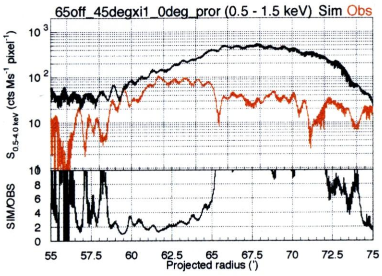

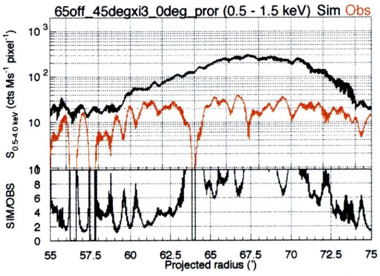

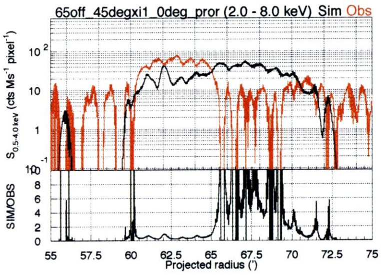

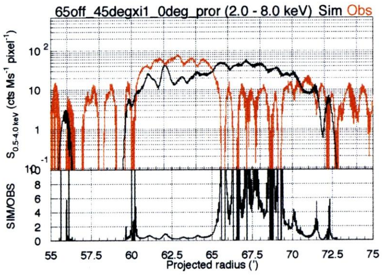

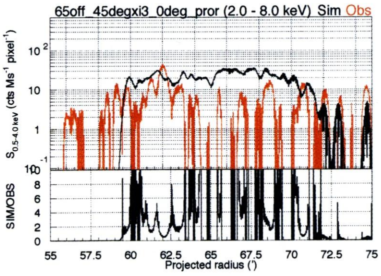

Radial:65off_90deg

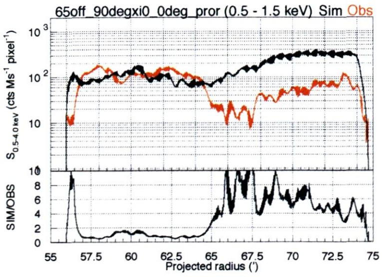

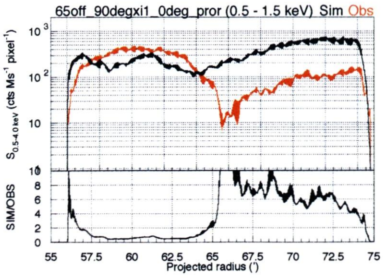

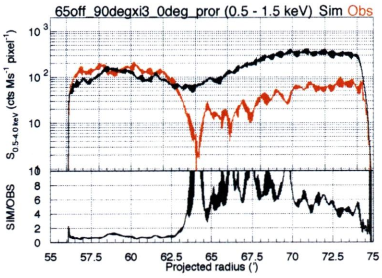

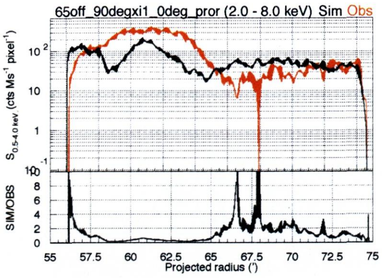

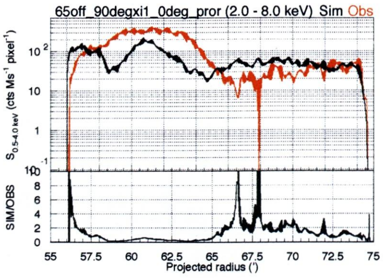

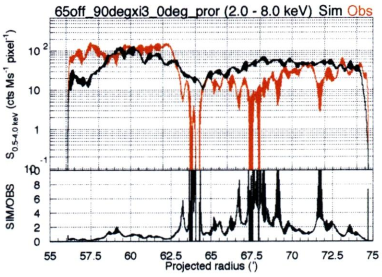

Radial:65off_135deg

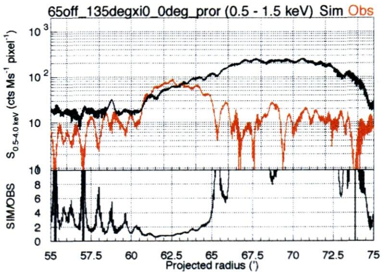

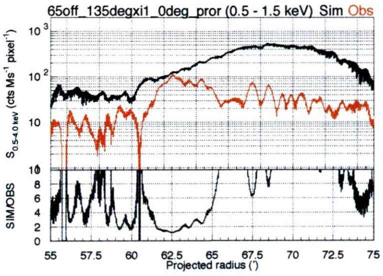

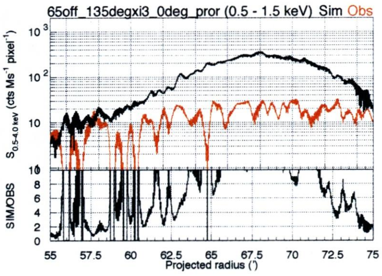

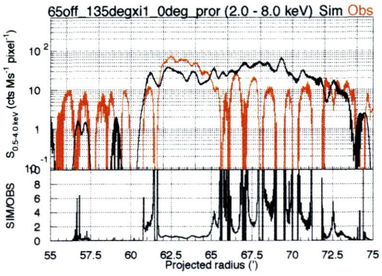

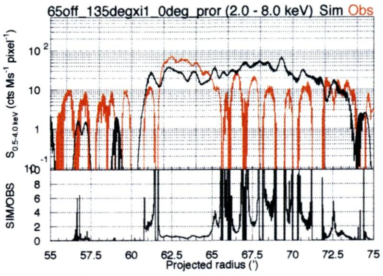

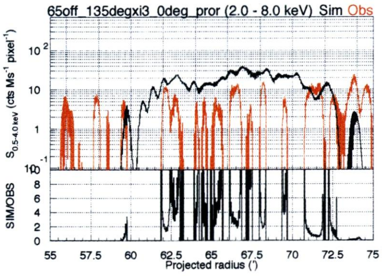

Radial:65off_180deg

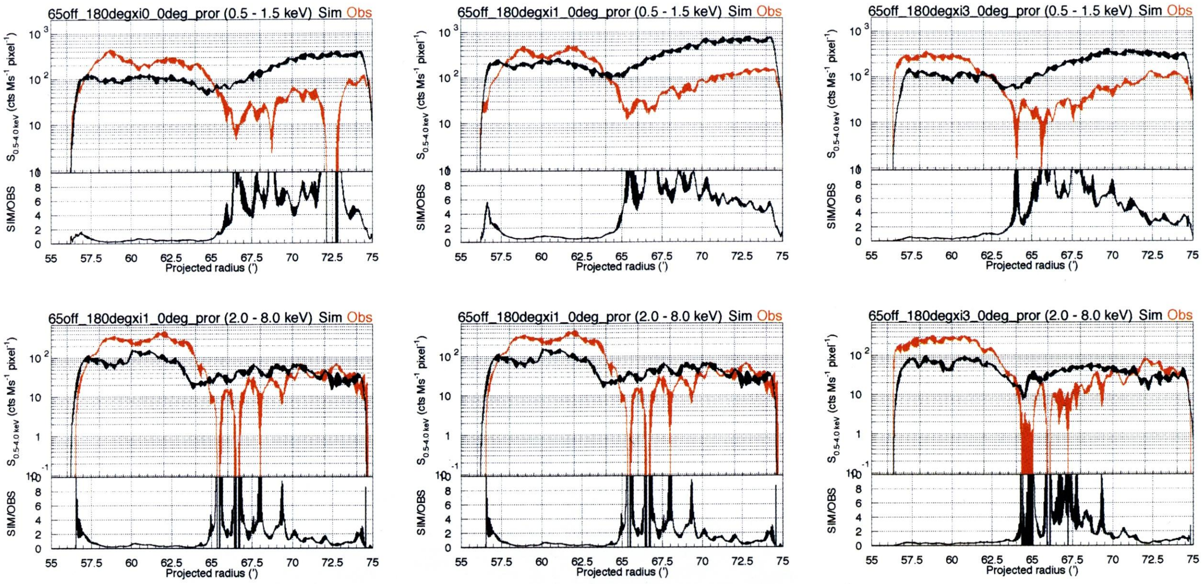

65off_180degxi0_0deg_pror (0.5 - 1.5 keV) Sim Obs

65off_180degxi1_0deg_pror (0.5 - 1.5 keV) Sim Obs

65off_180degxi3_0deg_pror (0.5 - 1.5 keV) Sim Obs

65off_180degxi1_0deg_pror (2.0 - 8.0 keV) Sim Obs

65off_180degxi1_0deg_pror (2.0 - 8.0 keV) Sim Obs

65off_180degxi3_0deg_pror (2.0 - 8.0 keV) Sim Obs

Radial:65off_225deg

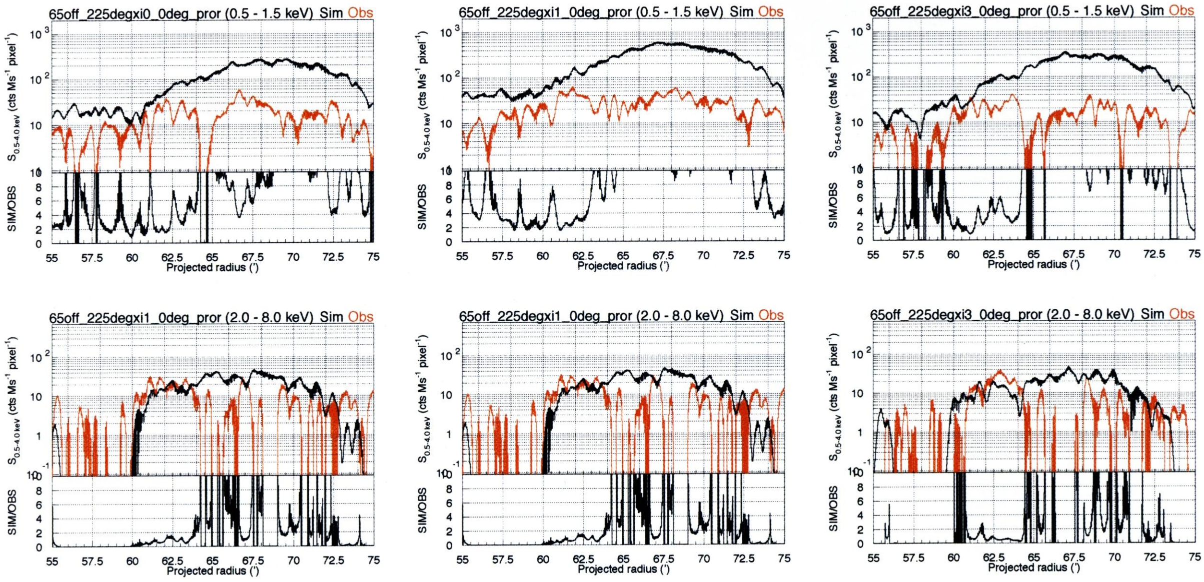

65off_225degxi0_0deg_pror (0.5 - 1.5 keV) Sim Obs

65off_225degxi1_0deg_pror (0.5 - 1.5 keV) Sim Obs

65off_225degxi3_0deg_pror (0.5 - 1.5 keV) Sim Obs

65off_225degxi1_0deg_pror (2.0 - 8.0 keV) Sim Obs

65off_225degxi1_0deg_pror (2.0 - 8.0 keV) Sim Obs

65off_225degxi3_0deg_pror (2.0 - 8.0 keV) Sim Obs

Radial:65off_270deg

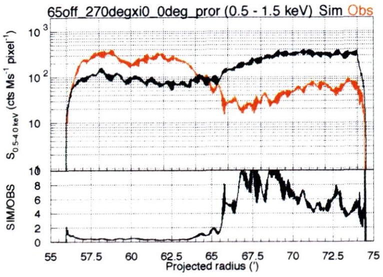

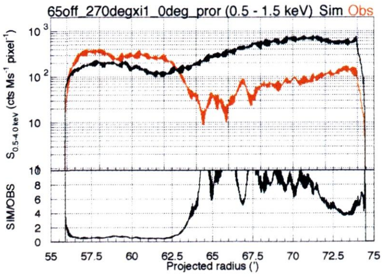

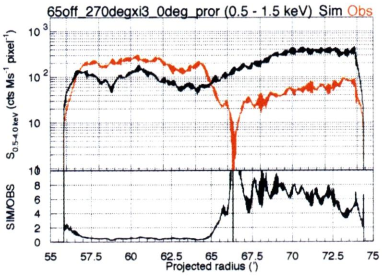

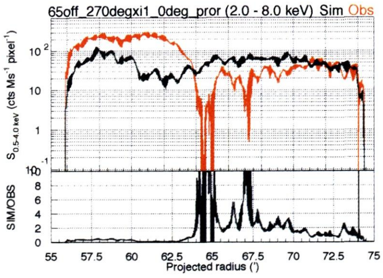

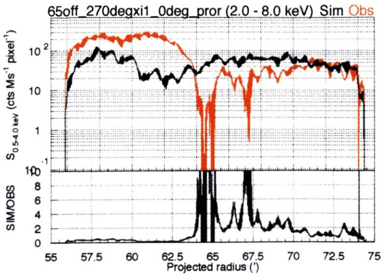

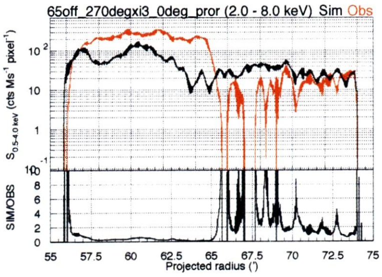

Radial:65off_315deg